Università degli Studi di Torino
Scuola di Dottorato

UNIVERSITÀ
DI TORINO

Development of eco-friendly gas mixtures for Resistive Plate Chambers

Luca Quaglia

Università degli Studi di Torino
Scuola di Dottorato

Dottorato in Fisica

Development of eco-friendly gas mixtures for Resistive Plate Chambers

Author: Luca Quaglia

Reviewers:
Andrea Alici
Jose ”Chilo” Garabatos Cuadrado

Supervisor: Martino Gagliardi

Title:	Development of eco-friendly gas mixtures for Resistive Plate Chambers
Author:	Luca Quaglia
Reviewers:	Andrea Alici Jose ”Chilo” Garabatos Cuadrado
Supervisor:	Martino Gagliardi
Study programme:	PhD in Physics
Institution:	Physics Department, University of Torino
Year:	2023
Keywords:	High energy Physics, Detectors, Resistive Plate Chambers, Fluorinated Gases, Alternative gas mixtures, ALICE, CERN

"Pretending you know what you're doing is almost the same as knowing what you are doing, so just accept that you know what you're doing even if you don't and do it"

Article D of the *Cult of Done Manifesto*

Contents

Abstract

ALICE (A Large Ion Collider Experiment) studies heavy-ion (mainly Pb-Pb), proton-ion and proton-proton (pp) collisions at the CERN Large Hadron Collider (LHC). In central heavy-ion collisions, a deconfined state of matter, known as Quark-Gluon Plasma (QGP), is formed. In the forward rapidity region, ALICE is equipped with a muon spectrometer, detecting quarkonia (e.g. J/Ψ, Υ) and open heavy flavour via their muonic decays. Quarkonia are key probes of the QGP properties: the suppression of J/Ψ has been one of the first proposed signatures for the formation of QGP in heavy-ion collisions.

The identification of muons in ALICE is performed by two stations of Resistive Plate Chambers (RPCs) placed downstream of two hadron absorbers. Particles tagged as muons are tracked by a set of ten stations of multi-wire proportional chambers. The correct operation of RPCs is ensured by the choice of the proper gas mixture and currently the ALICE RPCs are operated with a mixture of $C_2H_2F_4$, i-C_4H_{10} and SF_6.

Starting from 2016, new European Union regulations enforced a progressive phase-out of $C_2H_2F_4$ and, although its use for scientific purposes may still be allowed, CERN has adopted a policy of reduction of its greenhouse gases consumption, to which RPC operation by the LHC experiments contributes for about 80%. Most importantly, the ban on industrial usage of $C_2H_2F_4$ will make it difficult and costly to purchase. The work described in this thesis is devoted to the detailed study and characterization of alternative eco-friendly gas mixtures for the ALICE muon RPCs.

Preliminary tests with cosmic rays, reported in literature, have indicated that mixtures where $C_2H_2F_4$ is fully replaced by a combination of CO_2 and $C_3H_2F_4$ (HFO-1234ze) in variable proportions are promising, hence mixtures of this type were chosen for this work. The next crucial steps are the detailed in-beam characterization of such mixtures, the study of their performance under increasing irradiation levels, and their stability over time and as a function of the integrated charge.

The Gamma Irradiation Facility (GIF++) at CERN, equipped with a 12.5 TBq ^{137}Cs source able to induce counting rates up to several kHz/cm^2 and

located along a secondary beam line of the CERN accelerator complex, is an ideal tool for these studies, allowing one to to study the RPC performances in a high background radiation environment and to accumulate the integrated charge expected in a few years of operation at the LHC in a much shorter time span.

This thesis describes the methodology and results of a set of beam and aging tests carried out at the GIF++ with ALICE-like RPC prototypes, operated with several mixtures with varying proportions of CO_2 and $C_3H_2F_4$. In both cases, the RPC standard gas mixture has been used to establish the baseline behavior of the RPC.

The tested mixtures have been fully characterized, in terms of absorbed current, efficiency, prompt charge, cluster size and time resolution, using the muon beam provided to the GIF++ in dedicated beam time periods. Both digitized (for detailed shape and charge analysis) and discriminated signals (using the same front-end electronics as employed in ALICE) were analyzed. Throughout the test periods, the irradiation from the GIF++ source was used to simulate a high background radiation on the RPCs, to test their rate capability. The role of the new components in the RPC mixture has been analyzed and, in light of the obtained results, the most promising mixtures have been pinpointed.

Outside of the allocated beam time, a (still ongoing) long-term irradiation campaign at GIF++ was started, to study the stability of the detector response (so far only in terms of absorbed current) if exposed to intense radiation for a prolonged period of time, thus obtaining the first important indications on the long-term behavior of RPC detectors operated with HFO-based mixtures.

Preface

The contents of this thesis are presented in the following order: Chapter 1 contains an introduction to the CERN Large Hadron Collider (LHC, in Section 1.1), together with a brief description of its injector chain (complex of smaller pre-accelerators which feed the particles to the LHC) in 1.1.1. Section 1.2 reports a detailed description of A Large Ion Collider Experiment (ALICE), one of the four main experiments located at the LHC. A summary of its physics goals is reported in 1.2.1 and a short description of its sub-detectors is provided in 1.2.2.

Chapter 2 is devoted to the description of the Resistive Plate Chambers (RPCs), main subject of this thesis. Section 2.1 describes the physical processes that lead to the formation of a detectable signal in gaseous detectors, together with an historical overview of the process which led to the invention of RPCs, which are described in great detail in Section 2.2. The two main modes of operation of these detectors are described therein, together with an overview of the main RPC working parameters. The influence of environmental parameters on the detector response and the role of the gas mixture in RPC operation are described in 2.2.3 and 2.2.4. The subject of RPC aging (degradation in RPC performance, following their long-term operation) is briefly introduced in 2.2.5. Section, 2.3 describes the RPC-based ALICE Muon IDentification (MID) system, discussing first its physical layout (2.3.1), the process which led to the choice of the currently employed RPC gas mixture (2.3.2) and, last, the expected running conditions during the upcoming LHC physics runs (2.3.3). Lastly, in Section 2.4, the possibility that some mild aging effects might be appearing in some of the MID RPCs, and how this has been investigated, is discussed.

Chapter 3 contains a brief review of the studies that have been carried out, prior to this thesis, for the search of eco-friendly alternatives to the current RPC gas mixture. Section 3.1 describes the status of the progressive greenhouse gas usage phase-out plan, being enforced by the European Union and how this might affect RPC operation at CERN. Section 3.2 describes the results of studies, with cosmic muons, that have been carried

out by the Turin ALICE group and the Rome ATLAS group. These works have been chosen since the HFO-based gas mixtures investigated by the two groups have a different i-C_4H_{10} concentration and the effects of this choice are analyzed.

Chapter 4 reports an extensive discussion of the beam test studies that have been carried out at the CERN Gamma Irradiation Facility (GIF++). Section 4.1 reports the motivation behind the beam test studies described in this chapter, together with a description of all the gas mixtures tested (4.1.1). The description of the GIF++ is reported in Section 4.2, both in terms of the ^{137}Cs source (4.2.1) and muon beam (4.2.2). Section 4.3 describes the experimental setup used for data taking: 4.3.1 contains a description of the detectors and services (gas and high voltage) installed at GIF++, 4.3.2 briefly describes the software used for the data-acquisition and 4.3.3 outlines the procedure that was followed to develop the trigger used both to trigger on the muon beam and to measure the gamma-induced background on the RPCs. The two following subsections (4.3.4 and 4.3.5) are dedicated to a description the specific set-up used when signals are processed by the ALICE front-end electronics or by a digitizer. Section 4.4 reports the main steps of the data analysis process, complemented by what is reported in Appendix A. The analysis description is interspersed with figures to visualize each of the described steps. The results of the beam test studies are divided into two sections, 4.5.1 and 4.5.2. This division has been chosen to reduce the occupation of the figures but also to divide between mixtures with a working point lower and higher than the standard gas mixture, respectively.

Chapter 5 reports the preliminary results obtained from the aging studies carried out so far at the GIF++. The experimental setup and monitoring system have already been introduced in the previous chapter, hence Section 5.1 provides a general description of aging studies and it outlines the strategy that was followed by the ECOgas@GIF++ collaboration to perform this kind of studies. Section 5.2 contains the results of the aging tests and it is divided into three subsections: 5.2.1, 5.2.2, 5.2.3. These report respectively the results obtained with the standard gas mixture and with two eco-friendly alternatives. The subsection, 5.2.3.2 contains the description of an investigation that was carried out after an anomalous current increase was observed in the ALICE RPC, during the aging studies.

Chapter 6 contains a summary of the results shown in the previous chapter, together with an outlook for possible future developments of this work

Chapter 1

The ALICE detector at LHC

This chapter contains a description of the ALICE (A Large Ion Collider Experiment) detector at the CERN Large Hadron Collider (LHC), both in terms of detector and physics goals. Section 1.1 introduces the LHC, the largest particle accelerator at CERN, and its injector chain. Section 1.2 describes the ALICE detector, providing a summary of its physics goals (in 1.2.1) as well as describing its sub-detectors (in 1.2.2).

1.1 The Large Hadron Collider (LHC) at CERN

The Large Hadron Collider (LHC[1]) is a two-ring superconducting hadron accelerator and collider, located at the CERN laboratory in Geneva. It lays in a 26.7 km long tunnel and it is the largest and most powerful particle accelerator ever built and it is used to accelerate protons and lead ions, although also other elements, such as oxygen[2], are being considered and xenon has been used in a short test run in 2017[3].

The LHC accelerates two counter-rotating particle beams, which circulate in two different beam pipes. For cost-saving reasons, the accelerator was built in the same tunnel that hosted the Large Electron Positron (LEP[4]) Collider up to 2001 and, due to the space constraints imposed by this choice, it was impractical to build two separate proton rings. This led to the adoption of the so-called twin-bore magnet design[5], meaning that the magnet windings for the two beam pipes are accommodated in a common cold mass and cryostat, with magnetic flux circulating in the opposite sense through the two magnets. All the LHC magnets (dipoles, quadrupoles etc.) are superconductive and are operated at a temperature of 1.9 K, thanks to liquid helium cooling[6]. A total of 1232 main dipoles and 392 quadrupoles cover a total of $\sim$ 19 km of the total LHC circumference.

Figure 1.1 shows a schematic layout of the LHC. This figure shows that

the circumference is divided in 8 sections (referred to as *octants*); each octant accommodates a straight and a curved section of the accelerator. The reason behind this shape is that the LEP accelerator, being an electron-positron machine, was subjected to high synchrotron radiation loss which led to the installation of many accelerating elements (radio-frequency cavities) to compensate the losses. The above mentioned straight sections hosted said cavities.

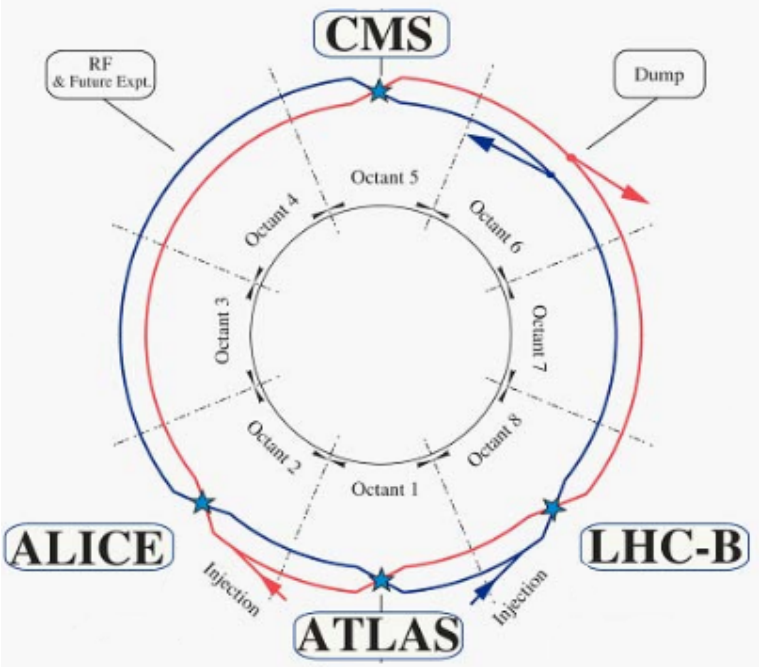

Figure 1.1: Schematic layout of the LHC. Highlighted are the 8 access points and the location of the four experimental areas. Figure taken from [1]

Since the LHC is a hadron accelerator, the synchrotron radiation losses are negligible, hence it was decided to install the accelerating elements[7] (RF cavities) in a single section of the circumference (referred to as point 4); which consist of two independent RF systems, one for each circulating beam. The two beams are collided in correspondence of four experimental caverns, in each of which a detector is installed: ATLAS[8] (A Toroidal LHC Apparatus) in point 1, ALICE[9] (A Large Ion Collider Experiment) in point 2, CMS[10] (Compact Muon Solenoid) in point 5 and LHCb[11] (LHC beauty) in point 8. Point 6 contains the beam dump, i.e., the infrastructure needed to extract the circulating beams from the accelerator and send them on composite graphite blocks[12] to absorb the beam energy and empty the machine. Point 3 contains beam monitoring systems and point 7 hosts one of the LHC cooling plants, to keep the superconductive magnets at the correct temperatures. The injection points will be discussed in 1.1.1.

1.1.1 LHC Injector chain

Protons and ions are not injected directly into the LHC, rather they go through a series of smaller accelerators, before finally being injected into the LHC. The path for protons and ions is similar in some parts and different in others. The main acceleration steps are listed here, together with Figure 1.2, which graphically shows the accelerator chain.

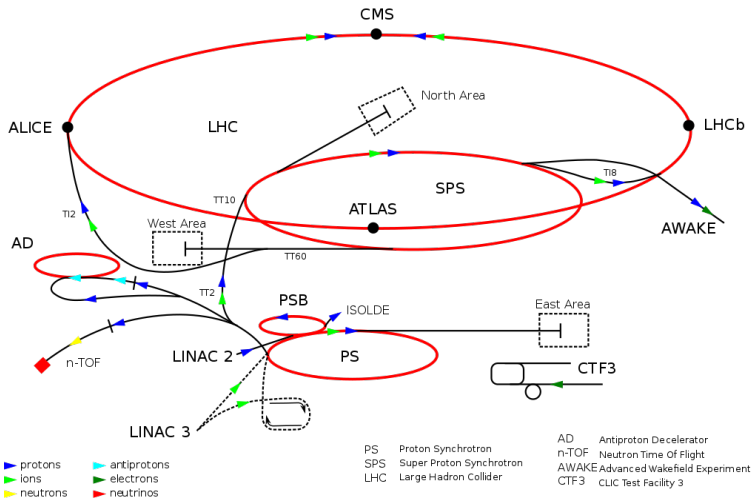

Figure 1.2: Schematics of the protons/ions acceleration chain. Figure taken from [1]

Protons are produced by stripping the electrons off of hydrogen molecules and are firstly accelerated by the LINAC 4[13] (a linear particle accelerator) up to 160 MeV. They are then sent to the Proton Synchrotron Booster[14] (PSB), where they are accelerated up to 2 GeV. The following step is the Proton Synchrotron[15] (PS), which pushes the beam energy to 26 GeV. The last step before the injection into LHC is the Super Proton Synchrotron[16] (SPS), which accelerates the protons up to 450 GeV. The two lines marked as "Injection" in Figure 1.1, represent special beam lines, which are used to transfer the beams from SPS to LHC. There are two injection lines (one per beam) and the injection points are close to point 2 and 8.

The lead ions originate from a heated Pb filament: a few electrons are stripped and the resulting ions travel through the LINAC3 [17] linear accelerator, reaching an energy of 4.5 MeV per nucleon. Next, the ions are accumulated and accelerated to 72 MeV per nucleon in the Low Energy Ion Ring, or LEIR[18]. After leaving the LEIR, the ions share the same path as the protons, going through the PS (up to 5.9 GeV per nucleon) and then, after the final stripping stage, the SPS (reaching 177 GeV per nucleon). Last, they are injected into the LHC by means of the same transfer lines, as for protons, mentioned above. At the time of writing, the maximum beam energies

reached by the LHC are 6.8 TeV for protons and 2.68 TeV for lead ions.

1.2 The ALICE detector

ALICE is a general purpose, heavy-ion, detector, located at the LHC. It is mainly focused on the study of heavy-ion collisions, specifically investigating the formation and evolution of the quark-gluon-plasma (QGP), a state of nuclear matter where the quarks and gluons are not confined in hadrons anymore[19]. Data in proton-proton, as well as proton-lead, collisions are also collected, mainly (but not only) to provide baseline values for some of the observables under study in heavy-ion collisions.

During the LHC RUN3 (which started in 2022) and RUN4, the ALICE detector will collect data in proton-proton (pp) collisions at an interaction rate ranging from 0.5 to 1 MHz, as well as lead-lead (Pb-Pb) collisions, with an interaction rate up to 50 kHz. Up to RUN2, these values were (typically) 200 kHz for pp and 8 kHz for Pb-Pb. In order to cope with the increased interaction rates, the ALICE detector has undergone a major upgrade, during the long-shutdown 2 (a three-year scheduled stop for accelerator and detectors maintenance, from 2019 to 2022)[20,21]. The most notable change, with respect to RUN2, is the new continuous (trigger-less) readout mode, meaning that all events are read out by most of the ALICE detectors. The raw data from the detectors are transmitted to newly-installed computer farms, which perform an online (synchronous) reconstruction of all the collisions. The output of this synchronous reconstruction is stored for an asynchronous (offline) reconstruction with improved detector calibration and the output of this reconstruction will be used for the selection of interesting events to be permanently stored and, eventually, for physics analysis. All the mentioned data processing steps are carried out thanks to the new ALICE analysis framework, named O^2, which stands for *online-offline*, meaning that the same software is used for online reconstruction and physics analysis[22].

1.2.1 The physics of ALICE

As anticipated in the previous section, the ALICE detector focuses on the study of the strongly interacting nuclear matter and the deconfined medium of QGP. This is a state of nuclear matter where quarks and gluons are not confined in hadrons and form a hot and dense medium, which behaves like a plasma. This section contains a short introduction to the most important theoretical and experimental aspects of the physics of QGP, and a concise

description of some of the observable physics quantities that can be used to describe it.

1.2.1.1 Quantum chromodynamics (QCD) and phase transition

Since the physics studied by ALICE regards nuclear matter, the strong interaction is at play. Quantum chromodynamics (QCD) is the gauge theory, within the standard model, which describes this kind of interaction. The quantum numbers of QCD are flavour (up, down, strange, charm, top and bottom) and colour (red, green, blue). The exchange particles of the strong interactions are gluons and they carry a colour charge. The strong interaction is governed by the coupling constant α_s, which expresses the strength of the coupling of quarks and gluons. A key aspect of α_s is that its value depends on the transferred momentum (q^2) in a given interaction. Specifically, it decreases as q^2 increases. For low values of q^2, QCD is a non-perturbative theory and it is responsible of quark-gluon confinement in hadrons, while, as q^2 increases, α_s decreases, allowing one to treat QCD with a perturbative approach. The only rigorous way to treat QCD at low values of q^2 is the so-called lattice QCD[23], which studies the properties of nuclear matter as a function of macroscopic quantities, such as temperature and baryonic density. Lattice QCD calculations have shown that for a temperature of ~ 170 MeV (critical temperature, T_C), the colour field becomes too weak to confine quarks and gluons into hadrons, leading to a new phase of matter with partonic degrees of freedom: the Quark-Gluon Plasma. It is believed this was the state of matter $\sim 10^{-6}$ s after the Big-Bang. Figure 1.3 shows, in the left panel, the above mentioned behavior of α_s as a function of q^2; while the right panel shows the phase diagram of nuclear matter, as a function of the temperature and net baryonic density.

According to the nuclear matter phase diagram, the transition between confined and de-confined matter (referred to as phase transition) can be reached either by increasing the temperature while keeping a low baryonic density (so-called hot QGP), or by keeping a low temperature and increasing the net baryonic density (cold QGP), or by a combination of both. Since a hot QGP can be created in high-energy heavy-ion collisions, these will be described in the next sub-section. Note that also other (phenomenological) models, beside lattice QCD, can predict the phase transition: a simple example is the MIT bag model[26]. This model provides a value of critical temperature of ~ 145 MeV, reasonably close to the estimation provided by lattice QCD.

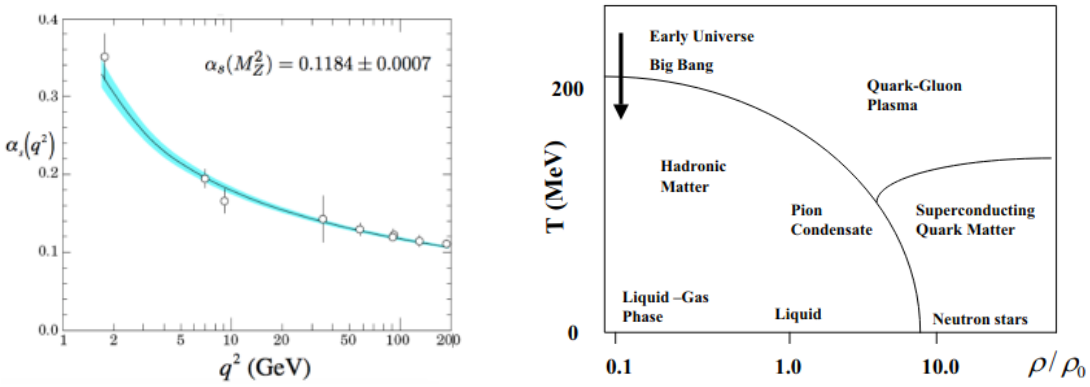

Figure 1.3: Left panel: measured values of α_s as a function of q^2, Figure taken from [24]. Right panel: phase diagram of nuclear matter as a function of the temperature and the normalized baryonic density. Figure taken from [25]

A useful quantity in the description of the QGP is the energy density, which can be related to the temperature through the laws of relativistic ideal gases, as explained in Reference [27]. The formula reported therein has a Stefan-Boltzmann-like dependence from T^4: in the case of the critical temperature provided by lattice QCD, one gets a value of energy density (for a two-flavour QGP) equal to about 0.9 GeV/fm^3.

1.2.1.2 Heavy-ion collisions as a way to create QGP

To study QGP in a laboratory, the system has to exhibit certain properties: it has to be a spatially extended and long-lived system of strong interacting particles. The spatial extension is required since it has to be studied using macroscopic variables and it has to be long-lived because, in order to define thermodynamic observables, it has to reach thermal equilibrium. Moreover, smaller systems such as pp and e^+e^- collisions do not provide a high enough particle multiplicity to reach the energy density needed to observe the phase transition. Hence, more extended objects (such as heavy nuclei) have to be collided.

Nucleus-nucleus collisions (A-A for short) are a physical process in which extended objects (nuclei) are collided with one another. In a given collision, multiple nucleons (protons/neutrons) can interact. The number of interacting nucleons depends on the impact parameter (b), which is defined as the distance between the centers of the two colliding nuclei. The smaller the impact parameter, the more nucleons will interact (central collision). On the contrary, the larger the impact parameter, the less nucleons will interact (peripheral collision). The energy density for a central collision is obviously greater than for a peripheral one. At the LHC, lead nuclei are collided at en-

ergies never before reached at a particle collider. At the beginning of RUN3, in 2022, an energy of 5.36 TeV per nucleon pair in the center of mass ($\sqrt{s_{NN}}$) was reached during a short pilot run. The aim of these high-energy collisions is the creation and the study of the QGP; which is itself short-lived, hence it cannot be studied directly, rather one studies observables related to the particles produced in a collision, to determine if and how their production is affected by the presence of the QGP. These particles/observables are usually referred to as *probes*.

A semi-classical model, called the Glauber model (described in details in Reference [28]), allows one to mathematically describe a collision between extended objects. Among other variables, it provides the number of elementary collisions (between nucleons) in a nuclear collision at a given impact parameters, considering the number of nucleons in the two colliding objects, the inelastic nucleon-nucleon cross section and the so-called nuclear overlap function, which expresses the probability to have one nucleon from each of the colliding nuclei in the same space region. The number of colliding and spectator nucleons (the former take part in the collision while the latter do not), which follow from the calculated number of elementary collisions, is also used to characterize heavy-ion collisions.

Space-time evolution of heavy-ion collision The space-time evolution of a heavy-ion collision is a complex phenomenon that goes through different stages; Figure 1.4 graphically shows this process, using a z-t diagram (z is the direction along which the particle beam travels and t is the time). Before the collision, the colliding nuclei appear as disks, due to Lorentz contraction, and it is assumed that the time at which the collision takes place is equal to t = 0. For t $\lesssim$ 1 fm/c the system is in what is referred to as the "pre-equilibrium" phase, where parton-parton hard scatterings mainly happen, depositing a large amount of energy in the medium, and the system is not yet at thermal equilibrium. In this phase mostly high p_t[1] partons and heavy quarks are created. If the system has reached critical values of energy density and temperature, quarks and gluons become deconfined and QGP is formed. Because of pressure gradients, the fireball system expands following hydrodynamics laws[29].

Following the QGP phase, the system hadronizes (when it reaches temperature T_C in Figure 1.4), meaning that free quarks and gluons combine to form hadrons and become, once again, confined (the system now behaves

[1] p_t = transverse momentum, i.e., the component of the particle momentum perpendicular to the beam direction

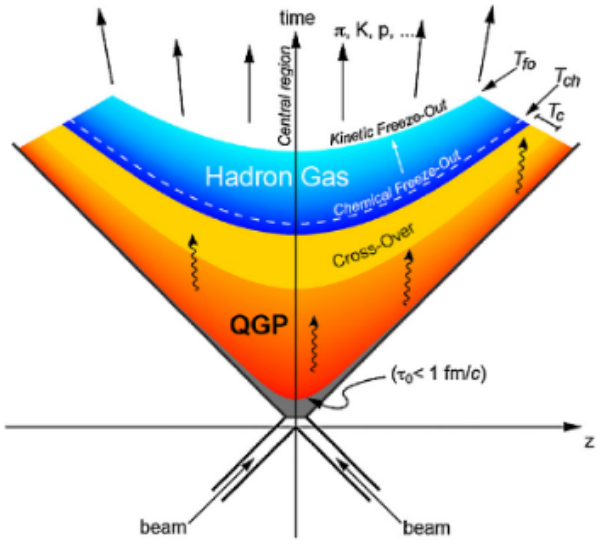

Figure 1.4: Space-time evolution of a heavy-ion collision. The z-axis represents the longitudinal position of the colliding beams and t is the time. The collision happens at z = 0 and t = 0. Figure taken from [29]

like a hadron gas). The system continues to expand and cool down, reaching two different freeze-out phases: 1) chemical freeze-out: inelastic interactions between the particles stop, so the chemical composition of the system is fixed (at temperature T_{ch} in Figure 1.4) 2) kinetic freeze-out: elastic interactions cease to occur, the particle kinematical distributions are fixed and the momentum spectra of the particles are established (at temperature T_{fo} in Figure 1.4). To provide some numerical values (using the Bjorken approximation[30] to calculate the energy density) at the thermalization time, one finds that at LHC (in Pb-Pb collisions at the RUN1 energy $\sqrt{s_{NN}}$ = 2.76 TeV) the thermalization time (t_{therm}) is somewhere between 0.6 and 1 fm/c[29] and energy density (ϵ_{th}) between 25 and 40 GeV/fm^3[31].

Since the QGP life-time is very short (around 5-10 fm/c at LHC), its direct observation is not possible and experiments must study the particles, produced after the chemical and kinetic freeze-out, looking for signatures of QGP.

1.2.1.3 QGP observables

The observables used to study QGP are usually divided into two categories, according to the transferred momentum in the given process: soft probes (low momentum transfer) and hard probes (high momentum transfer). These processes are studied and the results are compared to those observed in other colliding systems (for example proton-proton or proton-nucleus collisions), where the QGP is not expected to form, to have a baseline with

which to compare what is observed in the heavy-ion case.

Soft probes

Soft probes are produced in the last phases of the collision, where the typical q^2 of interactions is relatively low, so they cannot be studied in terms of perturbative QCD and phenomenological models are required. Two examples of soft probes are described here: collective flow and strangeness enhancement.

Collective flow Collective flow reflects the presence of pressure gradients in the QGP fireball, arising from the strong interaction among its constituents (partons). If the collision is not central, the fireball has an initial spatial anisotropy, which is translated by the collective flow into an azimuthal anisotropy in the kinematic distributions of produced particles. A sketch of a non-central nucleus-nucleus collision is shown in Figure 1.5, which highlights the asymmetry of the overlap region.

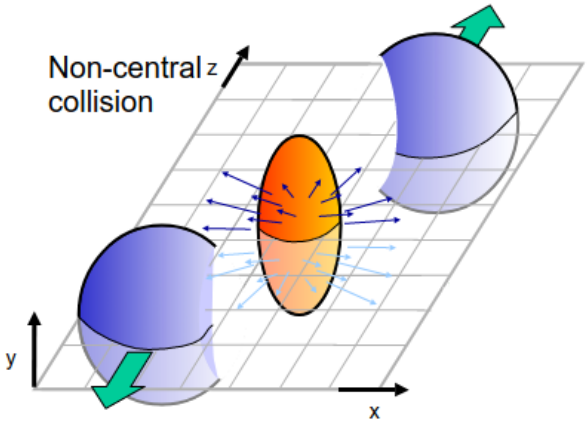

Figure 1.5: Sketch of a non-central nucleus-nucleus collision. The collisional axis is denoted as z while the transverse region is defined by x and y. Figure taken from [32]

The azimuthal distribution of the produced particles can be expressed in terms of a Fourier decomposition (as explained in Reference [33]) with coefficients v_n. The second order flow coefficient (v_2, elliptic flow) is the largest contributor to the asymmetry of non-central collisions, as reported in References [34–36]. Figure 1.6 reports the trend of the v_2 coefficient for various identified particles and centrality classes, as a function of their p_t. The wording "centrality class" is a definition of the collision centrality. As an example, the centrality class 0-5% contains the 5% most central events analyzed. These results have been obtained by the ALICE collaboration in Pb-Pb collisions at $\sqrt{s_{NN}}$ = 5.02 TeV.

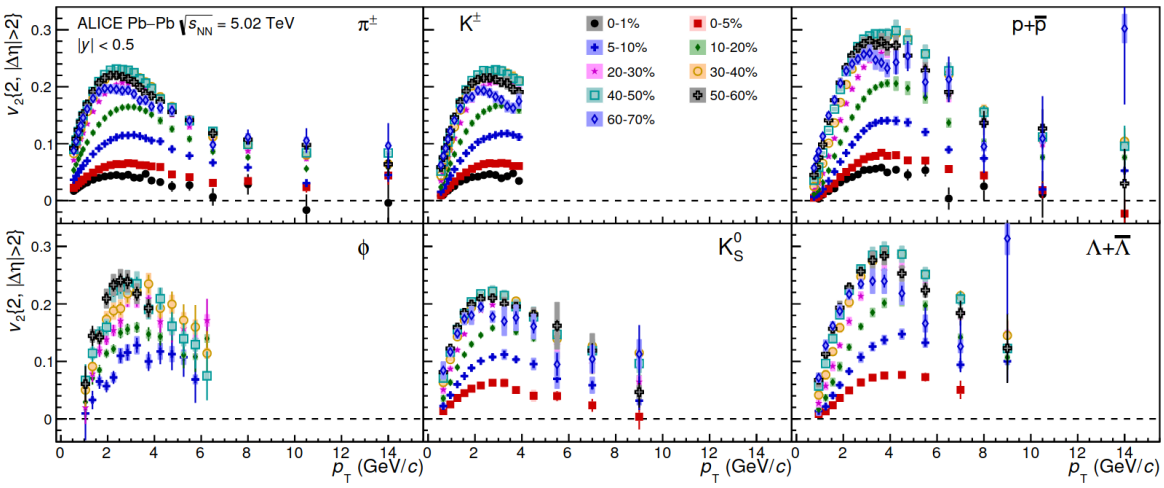

Figure 1.6: v_2 coefficient as a function of the particle p_t for different centrality classes and various particles ($\pi^{\pm}$, $K^{\pm}$, p+$\bar{p}$, ϕ, K^S_0 and Λ+$\bar{\Lambda}$. Figure taken from [34]

The v_2 coefficient is shown for different identified particles: $\pi^{\pm}$, $K^{\pm}$, p+$\bar{p}$, ϕ, K^S_0 and Λ+$\bar{\Lambda}$. All the identified particles show the largest v_2 for the centrality classes above 40-50%. For more peripheral collisions, the v_2 decreases, suggesting that the lifetime of the system becomes shorter and shorter and the asymmetry effects tend to become less pronounced.

The higher order coefficients (v_3 and v_4) define the triangular (generated by fluctuations of nucleons and gluons in the overlap region) and quadrangular (generated both by initial geometry fluctuations and by the non-linear hydrodynamic response of the medium) flows respectively[34]. Results from the ALICE collaboration on these coefficients are also shown in Reference [34].

Strangeness enhancement The mass of hadrons is only partly due to the mass of the constituent valence quarks; simply speaking, the quarks *dress-up* due to the strong interaction that keeps them confined in hadrons. Hence, in proton-proton collisions the production of strange hadrons is suppressed by their large mass (with the possible exception of very high-multiplicity collisions, as reported in Reference [37]). In a QGP, strange quark pairs are abundantly produced via gluon fusion (with a production threshold equal to twice the bare quark mass), and combine into strange hadrons at hadronization[38], increasing the ratio between strange particles (containing at least one strange quarks) and non-strange ones, such as pions, with respect to a non-QGP scenario. The ALICE collaboration has measured this ratio in all colliding systems, from pp at $\sqrt{s}$ = 7 TeV[39,40] to Pb-Pb at $\sqrt{s_{NN}}$ = 2.76 TeV[41] as well as p-Pb[42] at $\sqrt{s_{NN}}$ = 5.02 TeV. Figure 1.7 shows the ratio of multi-

strange baryons (Ξ and Ω) with respect to pions ($\pi^+ + \pi^-$) as a function of multiplicity (a proxy for the centrality classes discussed above). Note that different multiplicities are associated to different colliding systems, including pp at $\sqrt{s}$ = 900 GeV [43].

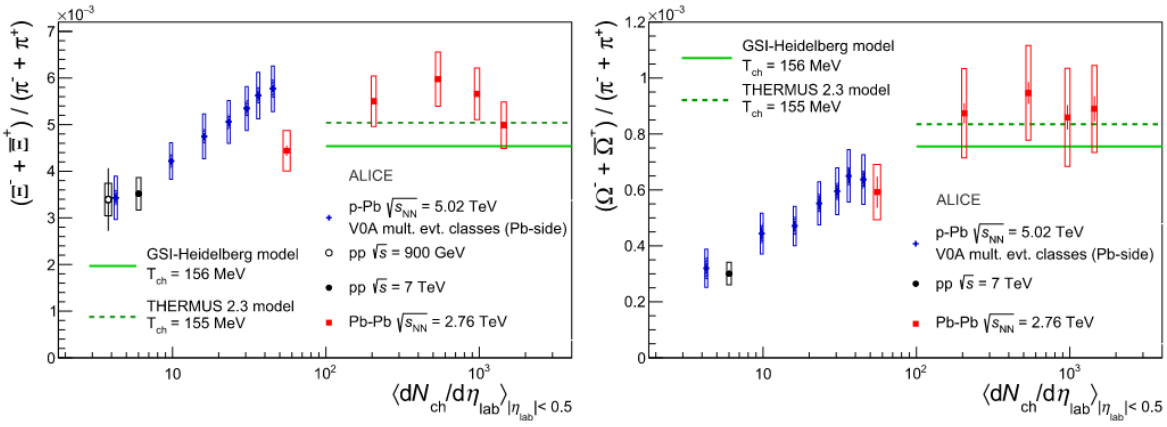

Figure 1.7: Ratio of multi-strange particles (Ξ and Ω) to pion production for different charged particle multiplicity and different colliding systems. The Pb-Pb points represent, from left to right, the 60-80%, 40-60%, 20-40% and 10-20% and 0-10% centrality classes. Figure taken from Reference [42]

The strangeness enhancement can be observed as the increase of the ratio of strange to non-strange particles with increasing multiplicity. A comparison with the other colliding systems reveals that the ratio for the highest p-Pb multiplicity (blue markers) is compatible with the measurements in Pb-Pb collisions in the multiplicity range corresponding 0-60% centrality range for the Ξ, while it is slightly lower for the Ω. It is also interesting to note that the values obtained for low p-Pb multiplicity are similar to the ones measured in minimum bias pp collisions. In general, the ratios seem to be increasing smoothly, with the charged particle multiplicity, from pp to Pb-Pb collisions.

Hard probes

Hard probes are produced in the first moments ($0 < t \lesssim 0.3$ fm/c [29]) of the collision, when the available energy is not yet degraded. Since they happen with a large q^2 transfer, their production rate can be treated in terms of perturbative QCD. Moreover, considering that they are produced shortly after the collision, they experience the full evolution of the hot and dense QGP medium and are affected by it.

The main observables related to hard processes are: high p_t hadrons, open heavy flavour (particles containing an heavy quark such as bottom/charm,

together with lighter quarks), and quarkonia (bound states of a heavy quark and its anti-quark).

Generally speaking, one would expect the number of high p_t particles to scale with the number of elementary nucleon-nucleon collisions (binary scaling) but it has been observed that this basic rule is broken in nucleus-nucleus collisions[44]. This can happen either for initial or final state effects. Initial state effects are expected to be present also in cases where QGP is not created, while final state effects are considered signatures of QGP formation (expected only in heavy-ion collision). A description of initial state effects can be found, for example in Reference [45]. Since final state effects are a signature of QGP formation, they will be briefly described in the following. An important quantity to be defined is the so-called nuclear modification factor (R_{AA}), defined as the ratio between the yields of a given particle (and, possibly, in a given transverse momentum and rapidity range) in nucleus-nucleus and pp collisions, divided by the number of elementary collisions in a nucleus-nucleus collision.

Energy loss High p_t partons are produced in the initial stages of the collision ($0 < t \lesssim 0.3$ fm/c) and they traverse the hot QGP medium. Partons can lose their energy in two ways: elastic scattering with the other partons in the medium (collisional energy loss) and gluon radiation (gluonstrahlung, similar to the electromagnetic bremsstrahlung). These phenomena lead to a reduction, relative to proton-proton collisions, of the yield per elementary collision of high p_t particles.

By studying the R_{AA} in central Au-Au collisions at the RHIC heavy-ion collider[46] at the Brookhaven National Laboratory (BNL), the STAR and PHENIX collaborations found that the production of hadrons with $p_t > 4$ GeV/c was suppressed by a factor ~ 5 with respect to pp collisions[47,48]. To be sure that this suppression is actually QGP-related, measurements were performed in d-Au collisions (deuterum-gold, where no QGP is expected) and indeed no suppression was observed in that case, showing that the effect observed in Au-Au collisions has to be attributed to QGP. More recent results have been obtained by the ALICE collaboration, in Pb-Pb collisions at $\sqrt{s_{NN}} = 2.76$ TeV [49] and $\sqrt{s_{NN}} = 5.02$ TeV in [50] and they are summarized in the following. The left panel of Figure 1.8 shows the R_{AA}, for the primary charged particles, obtained by the ALICE collaboration at $\sqrt{s_{NN}} = 2.76$ TeV, in the most central events, compared to the results obtained by the STAR and PHENIX collaborations in Au-Au collisions at $\sqrt{s_{NN}} = 200$ GeV (at similar centralities), as a function of p_t. The right panel shows the R_{AA} for

central ad peripheral events at $\sqrt{s_{NN}}$ = 5.02 TeV, with a comparison to the R_{pPb} (nuclear modification factor in p-Pb collisions). The R_{AA} is smaller than unity, which provides evidence for strong parton energy loss and large medium density at the LHC.

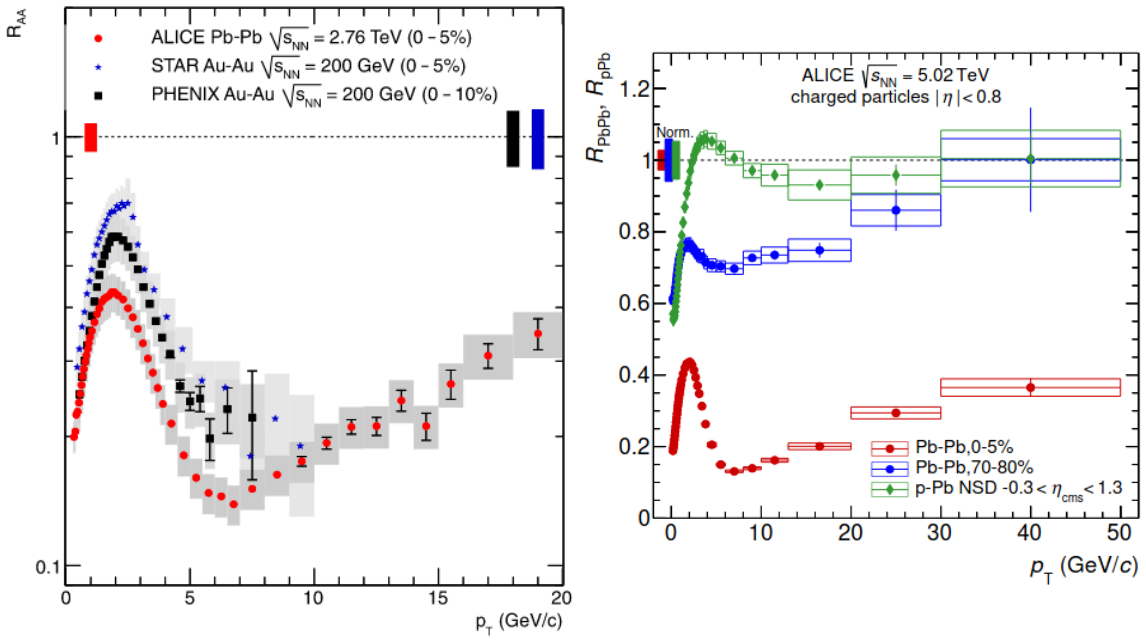

Figure 1.8: Left panel: R_{AA} for primary charged particles produced in central Pb-Pb collisions at $\sqrt{s_{NN}}$ = 2.76 TeV compared to results obtained by STAR [47] and PHENIX [48] in central Au-Au collisions at$\sqrt{s_{NN}}$ = 200 GeV; figure taken from [49]. Right panel: R_{AA} for primary charged particles produced in central and peripheral Pb-Pb collisions at $\sqrt{s_{NN}}$ = 5.02 TeV compared to results obtained in p-Pb collisions at the same $\sqrt{s_{NN}}$; figure taken from [50]

In the p_t range common to RHIC and LHC ($0 < p_t < 7$ GeV/c) a similar trend of the R_{AA} is observed, with a maximum around 2 GeV/c but the suppression seems to be higher for the collisions in LHC. This could be explained by assuming that the medium produced at LHC is much denser than at RHIC.

The comparison between the Pb-Pb and p-Pb colliding systems (right panel of Figure 1.8) is interesting since for $p_t > 8$ GeV/c the R_{pPb} is consistent with unity, meaning that the observed suppression in Pb-Pb collision is due to the formation of QGP and not to initial state effects. The bump at low p_t observed in all collision systems is a feature generally referred to as the Cronin effect[51].

Another observable related to the energy loss of partons while traversing QGP is the so-called jet quenching. This happens when two partons are produced in opposite directions (back-to-back) close to the border of the QGP fireball. If one of the two partons moves away from the expanding fireball, the other (due to momentum conservation) will move in the oppos-

ite direction (inside the fireball). The former will hadronize in a high p_t jet while the latter will lose its energy traversing the medium, leading to the production of low p_t particles. This phenomenon is analyzed, for example, in Reference [52]. Figure 1.9 shows the measured particle production as a function of a variable referred to as $\Delta\Phi$, which is defined as the angular difference of a particle, with respect to the direction of the highest p_t jet in any event. In pp collisions (black markers), a secondary peak (at $\Delta\Phi \sim 180°$) is observed, since the back-to-back jets contribute to it. In the case of central Au-Au collisions (blue markers), instead, the suppression of the particle production at $\Delta\Phi \sim 180°$ is clearly visible. Note that in d-Au (a smaller colliding system, represented by the red markers) collisions, the jet quenching is not observed. This is a good indication that this phenomenon is a final state effect, related to QGP.

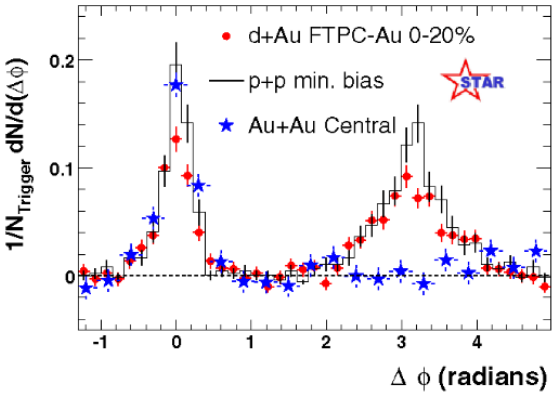

Figure 1.9: Particle production as a function of the angular difference with respect to the highest p_t jet in pp, Au-Au and d-Au collisions. Figure taken from [52]

Lastly, heavy quarks (charm and bottom) can be produced only in high q^2 processes in the initial stages of the collision and are also subject to energy loss. The difference with lighter partons is the so-called dead-cone effect[53], which causes particles with higher mass to lose less energy while traversing the QGP. This creates a hierarchy in R_{AA} values according to the particle mass, in particular one expects $R_{AA}^{\pi} < R_{AA}^{D} < R_{AA}^{B}$, where D and B denote the charmed (D) and bottom (B) open-heavy-flavour mesons, respectively. This was experimentally shown by the ALICE collaboration, as reported in Reference [54].

Quarkonium suppression Quarkonia are bound states of heavy quarks and their corresponding anti-quark ($b\bar{b}$, also known as bottomonium and $c\bar{c}$, also known as charmonium). The suppression of quarkonia production has been proposed as a possible signature of QGP formation in heavy-ion collisions,

as reported by Reference [55]. Quarkonia are usually studied through their di-leptonic decay channels, as is the case for the ALICE muon spectrometer (whose muon identification system will be extensively discussed throughout this thesis). The quarkonium bounding potential in vacuum can be described as the sum of two terms: a Coulomb-like ($\propto 1/r$) one plus a constant term k*r (confinement term) that represents QCD confinement (r is the radial distance between quark and anti-quark). When dealing with deconfined quarks immersed into a partonic medium, the confinement term vanishes and the free color charges reduce the binding strength of the confinement term by a factor $\propto e^{-r/\lambda_d}$, where λ_d is the so-called Debeye screening radius (maximum distance at which two color charges can form a bound state in QGP). Different bound states of charmonium and bottomonium exist and they have different binding energies: the greater this value, the smaller the binding radius. It has been predicted that, as the temperature of the system increases, the value of λ_d tends to decrease, meaning that different quarkonia are suppressed at different temperatures, in a sequential way (sequential suppression)[56]. Works such as [57] and [58], report measured values for the nuclear modification factor of quarkonia by the ALICE experiment, in Pb-Pb collisions at $\sqrt{s_{NN}}$ = 5.02 TeV. Figure 1.10 shows, in the left panel, the value of R_{AA} as a function of the collision centrality, for the J/Ψ ($c\bar{c}$ bound state). In the same chart, the results for a center-of-mass energy of 2.76 TeV are also reported. The right panel of Figure 1.10 shows instead the R_{AA} as a function of the collision centrality for the Υ ($b\bar{b}$ bound state), both for $\sqrt{s_{NN}}$ = 2.76 and 5.02 TeV .

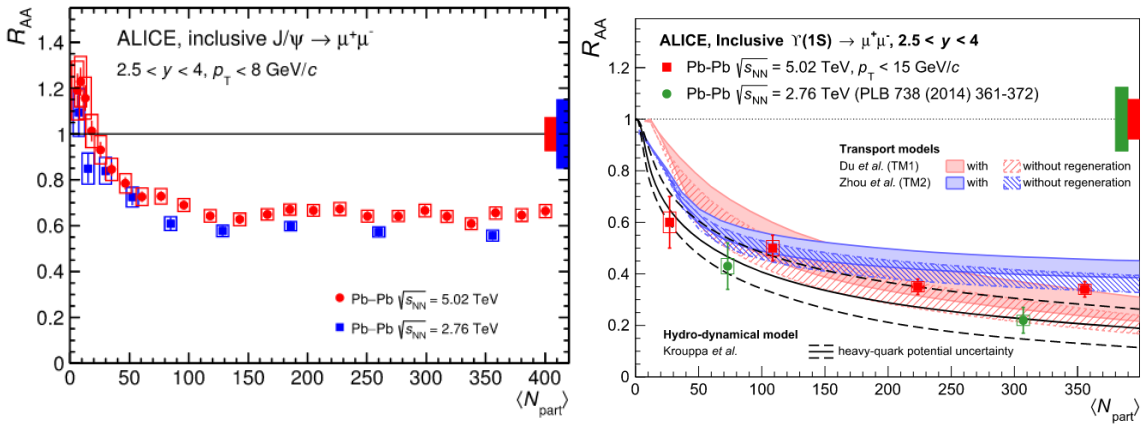

Figure 1.10: Left panel: R_{AA} for J/Ψ as a function of the collision centrality for Pb-Pb collisions at $\sqrt{s_{NN}}$ = 2.76 and 5.02 TeV, measured by the ALICE collaboration; figure taken from [57]. Right panel: R_{AA} for Υ as a function of the collision centrality for Pb-Pb collisions at $\sqrt{s_{NN}}$ = 2.76 and 5.02 TeV, measured by the ALICE detector; figure taken from [58]

The J/Ψ suppression increases (R_{AA} decreases) up to $N_{part} \sim 100$ and

then it becomes approximately constant at a compatible value between the two center-of-mass energies shown in the chart. For more peripheral collisions ($N_{part} \lessapprox 50$), an excess of very low p_t J/Ψ was observed in Pb-Pb collisions, which might originate from the J/Ψ photo-production[59] and could explain the increase of the R_{AA} for peripheral collisions. Moreover, Reference [60] reports that the J/Ψ suppression measured by the ALICE detector, at LHC energies, is less pronounced (at low-to-intermediate p_t and for large centralities) than what had previously been measured at RHIC [61] in Au-Au collisions at $\sqrt{s_{NN}}$ = 200 GeV. This can be explained by considering that at higher colliding energies (as is the case at the LHC), a higher number of $c\bar{c}$ pairs are created[62,63], which may form a J/Ψ at the phase boundary or in the hadronization phase, leading to an increase of J/Ψ production and a greater R_{AA}.

For what concerns the Y (1S) suppression, it was shown that R_{AA} decreases with the centrality of the collision, as can be seen in the right panel of Figure 1.10, which also shows how the suppression is similar at $\sqrt{s_{NN}}$ =2.76 and 5.02 TeV.

1.2.2 The ALICE detectors

Figure 1.11 shows a sketch of the ALICE detector as of the start of RUN3[20]. ALICE is spatially divided into two detection regions, namely the central barrel, which covers the pseudo-rapidity region $|\eta| < 0.9$, and the forward muon spectrometer, covering the pseudo-rapidity range range $-4 < \eta < -2.5$. The central barrel is embedded in a room-temperature solenoid magnet, which generates a field of ~ 0.5 T and it contains detectors which provide efficient tracking in the high track-density environment of heavy-ion collisions, covering transverse momenta from $\sim$ 100 MeV/c to $\sim$100 GeV/c with excellent hadron and electron identification capabilities. The forward muon spectrometer uses a set of absorbers to remove hadrons and identify muons originating from the decays of quarkonia and open heavy flavour.

1.2.2.1 Central barrel detectors

Starting from the interaction point and moving outwards, the first sub-detector is the Inner Tracking System (ITS) which is used for the extrapolation of tracks to the primary vertex. Up to RUN2, it was composed by six layers of silicon detectors, with different detection technologies (pixels, drift and strips) and its readout speed was limited to 1 kHz. The new ITS (ITS2)[64] is composed by seven layers of Monolithic Active Pixel Sensors (MAPS),

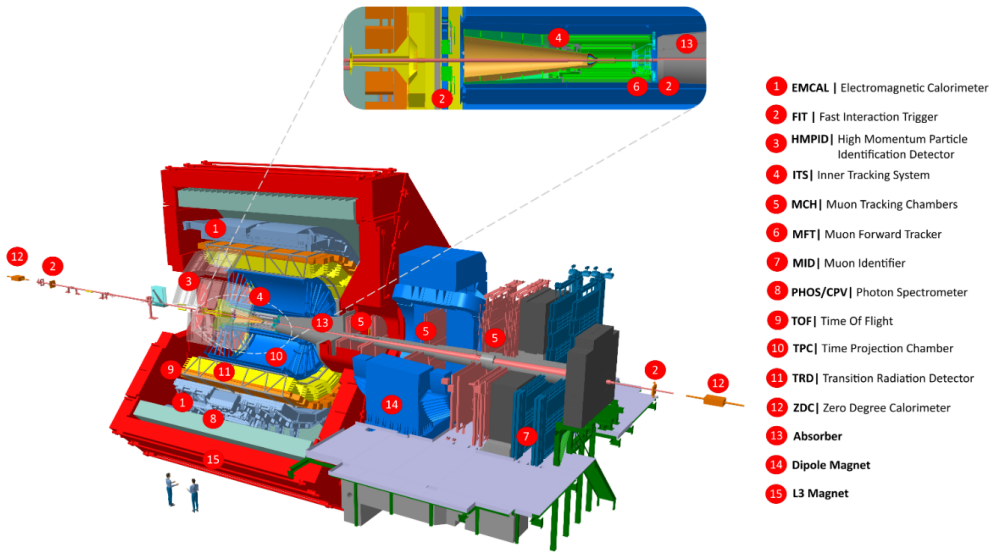

Figure 1.11: ALICE detector layout during the LHC RUN3. Figure taken from [20]

which provide better pointing resolution (considering also that its first layer is closer to the beam pipe) as well as the capability to cope with the higher expected readout rate. The Time Projection Chamber (TPC), is the next detector following the ITS. It is a 90 m^3 time projection chamber, filled with a mixture of Ne-CO_2-N_2 which provides tracking of charged particles and particle identification. Up to RUN2, the TPC readout was carried out using multiwire proportional chambers, which needed an active-gate ion backflow suppression, limiting the readout speed. To overcome this limitation, the readout system was upgraded[65] and Gas Electron Multipliers (GEMs) have been installed, to reduce the ion backflow, making the detector able to work at the foreseen 50 kHz Pb-Pb interaction rate. Surrounding the TPC is a Transition Radiation Detector (TRD), which exploits the fact that when an electron crosses an inhomogeneous material it produces a transition radiation (TR), while other particles (such as pions) do not. The TRD is composed by a radiator followed by a multiwire proportional chamber, filled with a mixture of Xe-CO_2. The different behavior of electrons and pions, when crossing the TRD, can be exploited to distinguish the two. Following the TRD, an array of multi-gap Resistive Plate Chambers (MRPCs) constitutes the Time Of Flight (TOF) detector of ALICE. These RPCs are operated with a mixture of R134a and SF_6 (see 2.2.4 for more details on this gases) and they are used to measure the particle time of flight, for particle identification purposes, with a system (detector, front-end electronics and calibrations) time resolution of the order of $\sim$ 60 ps. Portions of the central barrel are covered by an electromagnetic calorimeter (EMCal) and a photon calor-

imeter (PHOS), coupled with a Charged-Particle Veto (CPV). EMCal uses Pb-scintillator sampling calorimeters to measure highly energetic photons, electrons, neutral pions, and jets of particles. The acceptance of EMCal is completed by the presence of the Di-Jet Calorimeter (DCal), which allows the measurement of hadron-jet and di-jet correlations (same detector technology as EMCal). PHOS employs $PbWO_4$ crystals to detect photons, as well as to measure the hadron spectra via their radiative decay. The CPV is made up of a set of proportional chambers to suppress charged-particles contamination in PHOS. Finally, the High Momentum Particle Identification Detector (HMPID), a ring-imaging Cherenkov detector operated with C_6F_{14}, enables hadron identification at large transverse momenta.

1.2.2.2 Forward detectors in ALICE

This section describes the detectors located at forward rapidity in ALICE and it is divided into two paragraphs. The first one describes the newly installed Fast Interaction Trigger (FIT) detectors, together with the Zero Degree Calorimeters (ZDC). The second one provides an overview of the muon spectrometer.

FIT and ZDC

The FIT detector[66] is composed by three different sub-systems: FV0, FT0A/C and FDDA/C. FV0 ($2.2 < \eta < 5$) is a scintillator-based disk-shaped detector, readout by means of optical fibers and placed on the opposite side of the muon spectrometer. Its role is to measure multiplicity, centrality and event plane in Pb-Pb collisions. FT0A and C ($3.5 < \eta < 4.9$ and $-3.3 < \eta < -2.1$ respectively) are two arrays of quartz Cherenkov radiators, readout by microchannel plate photomultipliers, placed on both sides of the interaction point. The role of FT0 is to precisely measure the collision time and to provide the instantaneous and integrated luminosity measurement, as well as a minimum-bias trigger for detectors that require it. The FDDA and C ($4.8 < \eta < 6.3$ and $-7 < \eta < -4.9$ respectively) detectors are also placed on both sides of the interaction point and they are plastic scintillator pads which are mainly used to tag diffractive events.

The ZDC detectors are located on both sides of the interaction point, inside the LHC tunnel at a distance of $\sim$ 115 m from the ALICE interaction point. They are made up of four quartz-fiber spaghetti calorimeters with silica optical fibers as active material embedded in a dense absorber, two for protons (ZPA/C) and two for neutrons (ZNA/C). Two electromagnetic

calorimeters (ZEM1/2), placed closer to the interaction point, complete the ZDC. Its main functions are the collision centrality estimation in Pb-Pb and p-Pb collisions (by detecting the spectating nucleons which did not take part in the interaction), as well as the event plane orientation. Furthermore they are used for luminosity determination in Pb-Pb collisions. The calorimeters are placed in such a way that their acceptance fully covers the region where spectator nucleons accumulate (due to their different charge/mass ratio with respect to Pb ions).

The ALICE muon spectrometer

The main goal of the ALICE muon spectrometer[67] is to study the muonic decay of hard probes, such as quarkonia and open heavy flavours (described in 1.2.1.3). Both charmonium (J/Ψ and $\Psi^{'}$) and bottomonium (Y,$Y^{'}$ and $Y^{''}$) bound states are studied in the muon spectrometer. The resonances can be detected down to zero transverse momentum and the mass resolution is $\sim$ 70 MeV in the J/Ψ and $\sim$ 100 MeV in the Y regions, respectively[68,69]. The ALICE muon spectrometer has undergone significant upgrades during the long shutdown 2 as well and they will be described in the following.

Figure 1.11 shows the muon spectrometer as of RUN3. Up to RUN2 the first element of the spectrometer (moving away from the interaction point) was the front absorber, a cone made of composite material (carbon and concrete) of 4.13 m length (10 λ_{int}, 60 X_0) which reduces the flux of primary hadrons from the collisions. The materials were chosen to minimize the muon multiple scattering inside the absorber itself and not degrade the spatial resolution of the spectrometer. In view of RUN3, the Muon Forward Tracker (MFT)[70] has been installed upstream of the absorber. This is a high-resolution silicon tracker, using the same technology as the new ITS, which enhances the tracking capabilities of the muon spectrometer, improving its vertexing capabilities thanks to the matching of tracks before and after the absorber. Downstream of the absorber, a set of ten cathode pad/strip chambers provide muon tracking. They have a spatial resolution $\sim$ 100 μm and more than 10^6 channels to limit the occupation rate to a maximum of 5% of the full set of chambers[71]. One of the tracking stations is embedded into a room-temperature dipole magnet, which produces a field of 0.7 T, to bend the muon tracks according to their sign. An iron wall, of 120 cm thickness (7.2 λ_{int}), is located behind the tracking chambers, to absorb any residual hadron which escaped the concrete absorber and traversed the spectrometer. Finally, a set of 72 single-gap Resistive Plate Chambers (RPCs) is

located behind said iron wall. These detectors are arranged in two stations, of two planes of 18 RPCs each, at $\sim$ 16 and 17 m from the interaction point. Until RUN2, this sub-system was addressed to as the Muon TRigger (MTR) but from RUN3 onward, since ALICE is running in trigger-less mode, it has become a Muon IDentifier (MID). The muon identification is performed by matching reconstructed tracks with track segments in the MID system. Since the search for an eco-friendly gas mixture to operate the MID RPCs is the subject of this thesis, a more detailed description of the system will be given in Section 2.3, in the next chapter.

1.2.3 Improved physics studies in RUN3

The main ALICE physics goals driving the upgrade requirements aim at extending the sensitivity of the experiment down to very low p_t and at the collection of the minimum bias data at the highest rate possible. These goals are discussed extensively in the letter of intent for the ALICE upgrade, reported in Reference [72] and are here briefly summarized.

- Heavy flavour: measurements of the production and azimuthal anisotropy of several charm and beauty hadrons, over a broad momentum range, as well as b-tagged jets.
- Quarkonia: precise measurements (starting from 0 p_t) of (prompt and non-prompt) J/Ψ yields and azimuthal anisotropy, Ψ(2S) and Υ yields both at forward and mid-rapidity.
- Jets: jet structure and di-jet imbalance (jet quenching) at TeV energies, b-tagged jets and jet correlation with photons and Z^0 bosons.
- Low mass dileptons and thermal photons: reconstruction down to 0 p_t in both the di-electron and di-muon channel.

Chapter 2

Resistive Plate Chamber detectors and the ALICE Muon IDentifier

This chapter contains an introduction to the Resistive Plate Chamber (RPC) detectors, which constitute the main subject of this thesis work. Section 2.1 introduces the principles behind particle detection in gaseous detectors, and the steps that led to the invention and developments of RPCs. Section 2.2 describes the RPC detector, highlighting the importance of the resistive electrodes and discussing the two main RPC operation modes (avalanche and streamer), together with the basics of signal formation and charge distribution. The discussion will then move on to the RPC main operational parameters, such as current, efficiency, time and position resolution. They key role of the gas mixture, to grant proper detector operation, is discussed in 2.2.4 and the issue of RPC aging will be introduced in 2.2.5. Section 2.3 is dedicated to the RPC-based ALICE Muon Identification system (MID). It contains a description of the system (2.3.1) and a summary of the steps that led the collaboration to the adoption of the current gas mixture (2.4). Finally, Section 2.4 is devoted to the analysis of possible signs of mild aging observed in some of the MID RPCs.

The search for an eco-friendly alternative to the gas mixture currently employed by the MID RPCs is the main subject of this thesis. The final goal of this search effort is to replace the gas mixture employed in the MID RPCs by the start of the LHC RUN4 in 2029.

2.1 Gas ionization principle

The basic physical phenomenon that governs particle detection in gaseous detectors is the ionization of the gas molecules. When a charged particle crosses the gas, it interacts with its molecules, losing fractions of its energy in every collision. If the energy lost in an interaction is above the ioniza-

tion energy of the gas molecule, a primary electron-ion pair can be formed (primary ionization). The number of primary electron-ion pairs created in the gas depends on the nature and on the energy of the incoming particle, as well as, of course, on the gas properties. If the energy of the primary electrons is high enough, they can further ionize the gas, until the available energy goes below the ionization energy (secondary ionization). The amount of energy transferred from the incoming particle to the gas molecules is the key parameter that governs the ionization process. Figure 2.1 reports a table taken from Reference [73]: it contains typical values of ionization energy for some gases of common use in gaseous detectors, as well as the mean energy loss by a minimum ionizing particle and the number of primary (N_P) and total (N_T, which includes secondary ionization) electron-ion pairs per cm of gas traveled.

Gas	Density mg cm^{-3}	E_x eV	E_I eV	W_I eV	$dE/dx\|_{min}$ keV cm^{-1}	N_P cm^{-1}	N_T cm^{-1}
Ne	0.839	16.7	21.6	30	1.45	13	50
Ar	1.66	11.6	15.7	25	2.53	25	106
Xe	5.495	8.4	12.1	22	6.87	41	312
CH_4	0.667	8.8	12.6	30	1.61	37	54
C_2H_6	1.26	8.2	11.5	26	2.92	48	112
iC_4H_{10}	2.49	6.5	10.6	26	5.67	90	220
CO_2	1.84	7.0	13.8	34	3.35	35	100
CF_4	3.78	10.0	16.0	54	6.38	63	120

Figure 2.1: Ionization parameters for some gases of common use in gaseous detectors. Parameters of interest are the gas density, primary ionization energy (E_1), average energy to create an electron-ion pair (W) and energy loss by ionizing particle per cm of gas travelled (dE/dx). Number of primary and total electron-ion pairs per cm (N_p and N_t) are also reported. Table from [73]

Note that, together with the ionization energy, the table reports the parameter W, which is the average energy per electron-ion pair creation, slightly higher than the ionization energy due to concurring energy-exchange processes.

When an external electric field is applied to the gas, the free ions and electrons start drifting along the field lines and are accelerated by the electric field. In this situation, a new phenomenon, called charge multiplication, can take place and it is of fundamental importance in the description of gaseous detectors. During its accelerated motion in the field, the electron is subjected to multiple interactions with other gas molecules and, if the energy gained by the electron between two collisions is higher than the gas ionization energy, the gas molecule can be ionized, leading to the formation of a new electron-ion pair in the gas. This is an exponential phenomenon,

described by the following law:

$$dn_e = \alpha n_e dx \quad \rightarrow \quad n_e = e^{\alpha d} \tag{2.1}$$

which describes the amount of new free electrons in the gas (dn_e) for a path dx travelled by an electron in the gas. The term α is the first Townsend coefficient, which expresses the average number of new electron-ion pairs per unit length; its value depends mainly on the electric field and the gas pressure. The second equality in equation 2.1 only holds for constant α (i.e., uniform electric field), which is the case for RPCs due to their planar geometry. The parameter d is the distance across which the charge multiplication, also called *avalanche*, develops. Note that if n_0 initial electrons are released in the gas, the total number of electrons will be proportional to it, according to $n_e = n_0 \exp(\alpha d)$ and the parameter $A = \exp(\alpha d)$ is referred to as the gas gain.

The drift velocity (average velocity along the electric field direction of charges in the gas) for electrons is $\sim$ 1000 times higher than for ions [74]. As a result, considering also the lateral diffusion, the avalanche develops a typical drop-like shape, with a fast moving head, constituted by electrons, and a slow-moving tail of positive ions. For RPC detectors, usual values of electron collection time (the time at which all electrons reach the anode) is a few ns, while for ions is a few μs (exact number depends on detector geometry and on the employed gas).

During the avalanche development, other effects can take place: de-excitation of excited atoms can lead to the emission of photons, which can ionize gas molecules in the space surrounding the avalanche, freeing other electrons (electron-photon feedback process). Those electrons can then start secondary, de-localized, avalanches.

If these secondary processes start to become dominant, each primary electron is accompanied by one or more secondary avalanches, called sometimes successors. If the process is not stopped in some way (as it will be described in the following) the free charges in the gas continue to grow until eventually a continuous discharge between the electrodes appears. It was observed that, for some critical value of total charge in the avalanche, the transition to a spark usually appears. In particular it was found that if the avalanche content approaches the Raether limit[75] (total charge content $An_0 > 10^8$ electrons), the electric field generated by the separation of positive and negative charges in the avalanche body, becomes comparable with the external field. As Figure 2.2 shows, the external electric field is bent in the vicinity of the positive body of the avalanche and secondary avalanches ini-

tiated close to the volume of the primary avalanche start drifting towards it and get strongly amplified because of the enhanced electric field nearby. The ionic column thus grows quite rapidly towards the cathode, leading to the formation of a thin plasma channel, usually referred to as streamer. Once the streamer reaches both electrodes, the transition to a spark is observed.

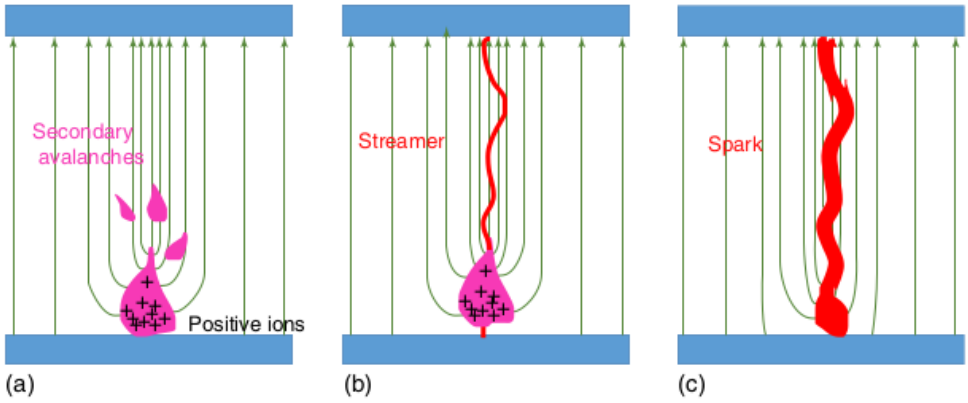

Figure 2.2: Stages of charge multiplication evolution and degeneration to a spark when the avalanche charge approaches the Raether limit. (a) field lines close to the avalanche experience a focusing effect and some secondary avalanches start moving toward the positive ions avalanche body (b) a thin plasma filament – a streamer is created (c) when the streamer reaches the electrodes, a spark happens through the channel. Figure taken from [74]

Moreover, when an ion approaches the cathode, it gets neutralized by detaching an electron from the cathode itself. If the energy of the ion is higher than the work function of the cathode (energy needed to extract an electron from a given material), a free electron can be emitted from the cathode (ion-induced feedback). The probability that this happens is called second Townsend coefficient (γ, with typical values in the range 10^{-3}-10^{-2}). Because of this type of phenomena, the spark develops earlier than predicted by the Raether condition and, if no quenching component is added to the gas mixture, the gain is limited to $A \sim 1/\gamma$.

2.1.1 From the ionization chamber to the RPC

Historically speaking, the first gaseous detectors to be employed were ionization chambers[74]. Various types of geometries were adopted (such as planar or cylindrical) but the general design consisted in two metallic electrodes (anode and a cathode) with a potential difference applied between them and filled with different gas mixtures. When ionizing radiation crosses the active volume, it ionizes the gas and the drift of the liberated charges produces a current, which can be measured to detect the passage of a particle. The de-

tection capability of this design was initially limited by the precision with which the current could be measured (relatively low at the time of development of these detectors in the early 1900's), and, more substantially, by the relatively small output signal, making them not suitable for particle-by-particle measurements and limiting their application to the measurement of particle flux only.

The successor of ionization chambers was the single-wire cylindrical counter[74], invented by Rutherford and Geiger in 1908. Figure 2.3 shows a sketch of this detector (left panel), which consisted of a metallic cylinder with a radius of 2-3 cm and a thin metallic wire (diameter $\sim$ 0.1 mm) stretched inside. The right panel of Figure 2.3 shows the typical response of such a detector in terms of current as a function of the applied high voltage.

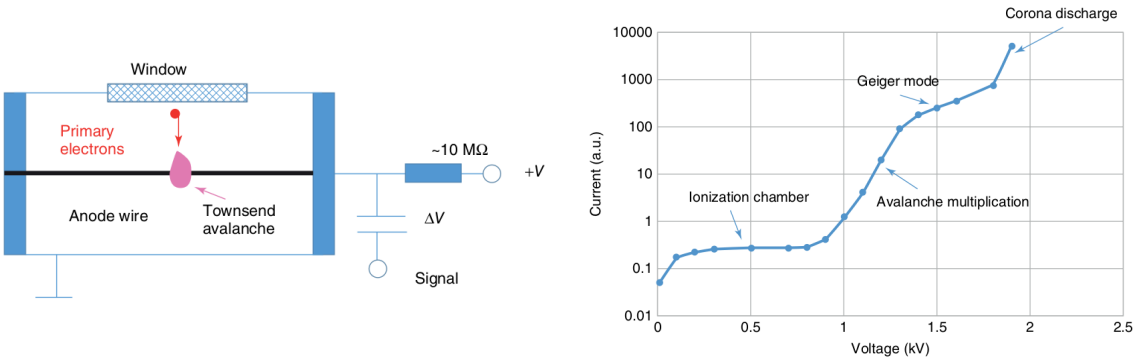

Figure 2.3: Left panel: sketch of single-wire cylindrical counter Right panel: typical response of single-wire counter in terms of current as a function of the applied high voltage. Figures taken from [74]

By looking at the detector current response, different regions can be observed. The first portion of the chart represents the so-called ionization chamber: if the electric field is not strong enough the charge recombination processes (electrons and ions recombining and neutralizing, effectively reducing free charges in the gas) have the upper hand on the ionization and not all the primary charge is collected; at higher voltages all the released charges are collected and a plateau is reached. If the high voltage is further increased, the charge multiplication processes start to appear. This regime is known as avalanche (or proportional) mode. Recall that those processes follow Equation 2.1, which states that the total number of created electrons is proportional to the number of primary electrons released in the gas. This means that the output signal of the detector is proportional to the number of primary electrons, i.e. to the energy loss of the ionizing particle. This is ensured by the cylindrical geometry: multiplication develops only in a small region near the anode, where the electric field is high enough and the

gain is independent of the ionization point. If one continues to increase the applied high voltage, the proportionality between primary electrons and detector response is lost and the signal amplitude of all pulses becomes almost equal to each other. In this case the feedback phenomena (photon and ion-induced) highlighted in the previous section become more relevant. Finally, if the high voltage is increased even more, a continuous discharge appears between the electrodes.

When a spark occurs in the gas, the high voltage drops and no further particle can be detected until the discharge is removed. In the past, many techniques have been employed to quench (absorb) the discharge in the gas. For example, as reported in [74], single-wire cylindrical counters were operated at voltages in the discharge region and a high value resistor ($\sim$ 100 MΩ) was inserted in series with the high voltage. With this precaution, if a discharge takes place in the gas, the current generated by said discharge (few μA) produces a voltage drop across the resistor, leading to a reduction of the applied voltage and to a self-quench of the discharge (since the high voltage is not enough to sustain it). Moreover, as it will be discussed in 2.2.4, some gases exhibit intrinsic quenching properties and can be used to obtain the required quenching effect.

The charge multiplication process allows one to detect radiation at the single particle level, since even a modest charge deposition in the gas can be detected, thanks to its amplification. The simplest geometry that can be adopted is the parallel-plate one, although this proved to be quite difficult to develop. In the planar geometry the proportionality is lost because the gain depends on the primary ionization point. Also, for avalanches initiated close to the cathode (which travel a long way in the gas) the transition from avalanche to spark is easily reached. Moreover, if any imperfections are present on the cathode material (i.e. sharp tips), those can lead to the emission of electrons, which travel the whole gas gap and are greatly amplified by the electric field, resulting in sparks.

A possible workaround was to use a spark counter[76]. In this type of detector, a planar geometry is adopted and a constant "low" voltage is applied; a triggering system is built using other detectors (such as scintillators or Geiger counters), installed around the spark chamber. When ionizing particles cross the detector, they ionize the gas along their path and the constant low electric field keeps ions and electrons separate. The trigger signal activates a pulsed high voltage generator, which produces a fast ($\sim$ μs) high voltage spike across the chamber electrodes, leading to the production of avalanches which rapidly translate to a spark. The position of the spark

is recorded by means of photographic methods and a stack of spark chambers can be employed to visualize a particle track. The high voltage then automatically goes back to lower values and the discharge is quenched. The drawback of this system is that the dead time between HV pulses is ~ 0.01 s.

A new frontier in gaseous detectors development was reached with the invention of the multi-wire proportional chamber (MWPC)[77], which consists of two parallel cathode planes, with an array of thin parallel wires stretched in the middle. When a charged particle crosses the gas volume, it produces primary electrons, which drift towards the anodic wires; as they approach the wires the strength of the electric field increases and charge multiplication starts at a distance of few anode radius. The movement of these charges induces negative signals on the wires and positive signals on the cathode planes. If one segments the cathodes in strips or pads, the two dimensional coordinates of the impinging particle can be determined with a space resolution on the order of 100 μm and, opposite to spark chambers, these detectors operate in the proportional regime and sparks rarely appear during operation. The main issue with this type of detectors is that the time resolution is on the order of few μs since, in principle, electrons can be released anywhere in the gas and have to drift all the way to the anode wires: this creates a jitter, that is compatible with the drift time of the detector.

The employment of planar geometry removes this element of time jitter, providing a good time resolution, but one has to find a way to reduce sparks and to operate the detector with an acceptable dead time. A solution was proposed by Santonico and Cardarelli in the 1980's[78]. They invented a detector with planar geometry, which employed resistive electrodes: the Resistive Plate Chamber was born.

2.2 The Resistive Plate Chamber

RPCs and spark counters share the same planar geometry design with a fundamental difference: RPCs employ high resistivity (10^9-10^{12} Ω·cm) bakelite[79] or glass electrodes. The outer surface of the electrodes is coated with a low-resistivity layer (usually graphite painting) to grant a proper high voltage connection. The applied electric field is strong enough to allow charge multiplication to happen anywhere in the gas, reducing the time jitter problem highlighted for proportional counters and MWPCs. The avalanche development follows the same process described in Section 2.1 but, if it degenerates into a streamer, when it touches the resistive cathode, this is not able to feed the streamer with further electrons, since resistive materials are not efficient

electron emitters[74]. Moreover, and most importantly, due to the resistive anode, the charges deposited by an avalanche or streamer are not immediately evacuated and this leads to a local reduction of the electric field, which quenches the charge multiplication processes, killing the streamer. Figure 2.4 shows a simplified circuit model for an RPC detector. The detector has the structure of a capacitor (C_g in the figure) and the two electrodes can be represented as capacitors with resistors in parallel (C_b and R_b).

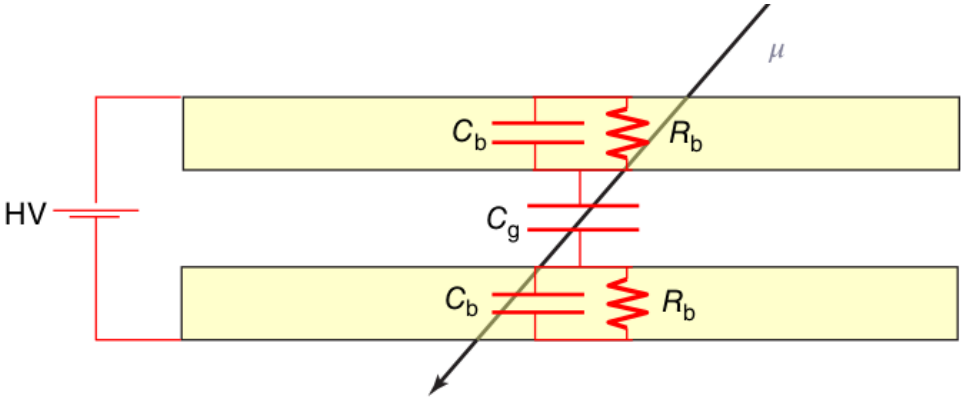

Figure 2.4: Simplified circuit representation of an RPC detector when crossed by an ionizing particle. C_b and C_g represent the capacitance of the bakelite and the gas; R_b is the resistance of the bakelite. Figure taken from [74]

When no particle is crossing the gas, the applied high voltage is supplied to the gas and no current is circulating; when an ionizing particle crosses the detector, the local discharge can be modelled as a current generator, which discharges the capacitor C_g. The system then behaves essentially like an RC circuit, restoring the original configuration with a time constant τ given by:

$$\tau = 2R_b\left(\frac{C_b}{2} + C_g\right) = 2\rho_b\frac{d}{S}\left(\frac{1}{2}\epsilon_0\epsilon_r\frac{S}{d} + \epsilon_0\frac{S}{g}\right) = \rho_b\epsilon_0\left(\epsilon_r + 2\frac{d}{g}\right) \qquad (2.2)$$

Where ρ_b is the resistivity of the bakelite, g and d are the thicknesses of the gas gap and electrodes respectively and S is the electrode surface interested by the discharge. With typical values for bakelite RPCs, τ is around 10 ms, which is much more than the avalanche collection time ($\sim$ 10 ns). This means that during the recovery time the voltage across the gap is reduced and the discharge cannot be sustained. The localized discharge is such that the detector remains sensitive to incoming particles on the whole active area, except for the region where the localized discharge took place. After a few τ's, the voltage is restored and the detector becomes efficient in that spot once again.

Mechanically speaking, the original RPC designed by Santonico and Cardarelli is quite simple, as shown in Figure 2.5. It is relatively cheap, if compared to other particle detectors, and easy to build. This makes the detector suitable to cover large areas, such as the muon systems in the big CERN experiments[8–10]. The gas gap is constituted by two bakelite sheets, whose distance is maintained constant by means of plastic spacers (made of polycarbonate), to grant a uniform electric field and constant gas amplification. The electrodes are coated with a thin graphite layer to distribute the high voltage across the surface and create the electric field in the detector. A layer of insulating material (usually Mylar) separates the graphite from the readout strips, usually made of copper. Since the resistive electrode is transparent to electric signals, the charge movement inside the gas induces a current in the readout strips, which pick-up the signal inductively. One end of the strips is usually connected to the readout (analog or digital) while the other end is terminated with a resistor to match the strip impedance (usually 50 Ω) and avoid reflections. The gas gap is sealed with a PVC frame and the gas inlets and outlets are inserted into the frame. The detector can be read out on both sides of the gas gap and, by using two strip planes with perpendicular orientation (one per RPC side), a 2D information on the impact point of the particle can be obtained.

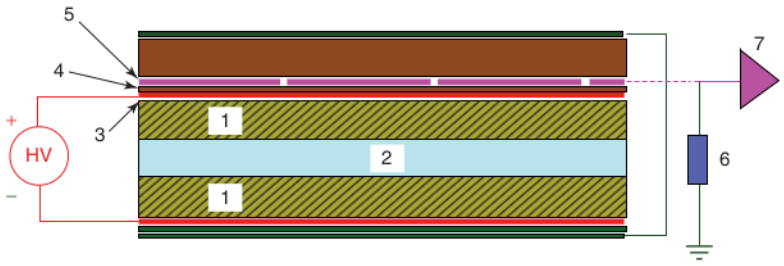

Figure 2.5: Cross section of an RPC detector. 1 = bakelite electrodes, 2 = gas gap, 3 = HV electrodes, 4 = Mylar insulating layers, 5 = readout strips, 6 = resistor, 7 = readout electronics. Figure taken from [74]

The inner surface of the bakelite can exhibit some imperfection (roughness of the surface or bumps), which would lead to electric field disuniformities and possible discharges. To overcome this problem, a thin layer of linseed oil[80], using pentane as a solvent, is applied to the inner layers of the bakelite and left to dry. The pentane evaporates and the linseed oil polymerizes, leaving the bakelite surface smoother.

2.2.1 Avalanche and streamer modes of operation

Two operation modes for RPC detectors can be adopted: streamer and avalanche. A brief description of both will be given in the following.

Streamer mode The RPCs were originally designed to exploit the streamer signal. Indeed, if the RPC response is analyzed (as shown in Figure 2.6), one can see that, following the appearance of a small precursor signal (related to the avalanche collection), after some delay time τ_b, a much more intense peak appears. This secondary signal is related to the appearance of streamers[81]. Note that the delay between the signals tends to be reduced if the high voltage is increased (as is the case from panel a to panel d of Figure 2.6).

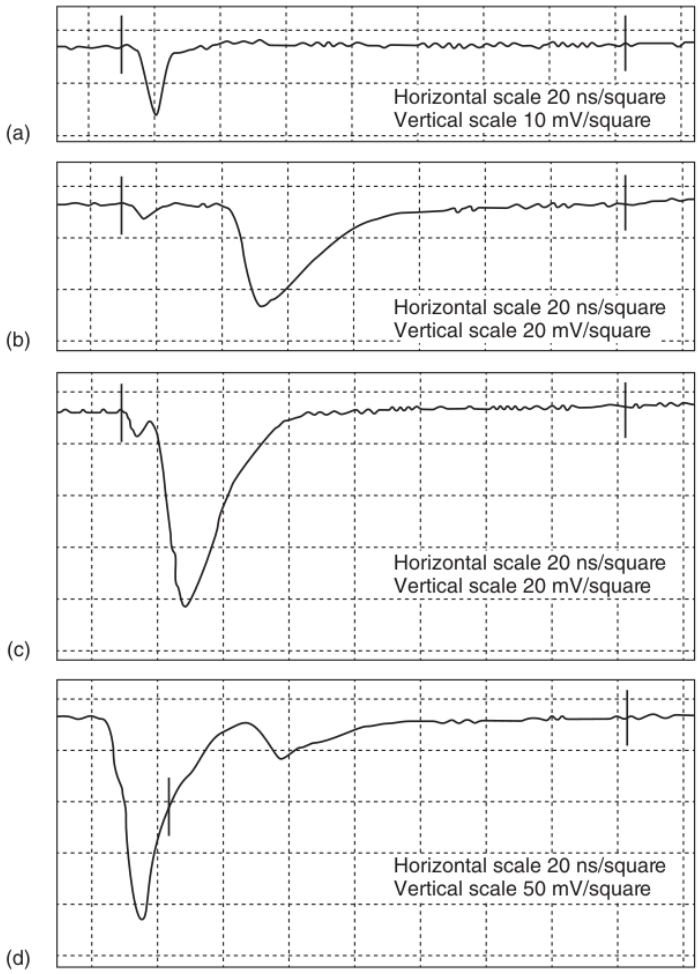

Figure 2.6: Evolution of signal waveform measured with an RPC filled with Ar/n-C_4H_{10}/$C_2H_2F_4$ with fractions 10/7/83 in volume. Going from top to bottom, the high voltage is increased and the delay between precursor and streamer signals is reduced, until they get superimposed (panel c and d). This is defined as streamer mode of operation. Figure taken from [81]

Works such as the one reported in Reference [81] have analyzed the RPC

behavior in terms of signal waveform and (prompt) charge released in the gas (using an RPC operated with Ar/n-C_4H_{10}/R134a with ratio 10/7/83) as a function of the applied high voltage. It was observed that, up to a certain voltage (of $\sim$ 9.2 kV) only the precursor signal described above was present. Above this "threshold" voltage, streamer signals started to appear (in a fraction close to 100% of the events[81]). The (prompt) charge for each detected particle was calculated by integrating the signal waveform in time and the results of this procedure are shown in Figure 2.7, as a function of the applied high voltage.

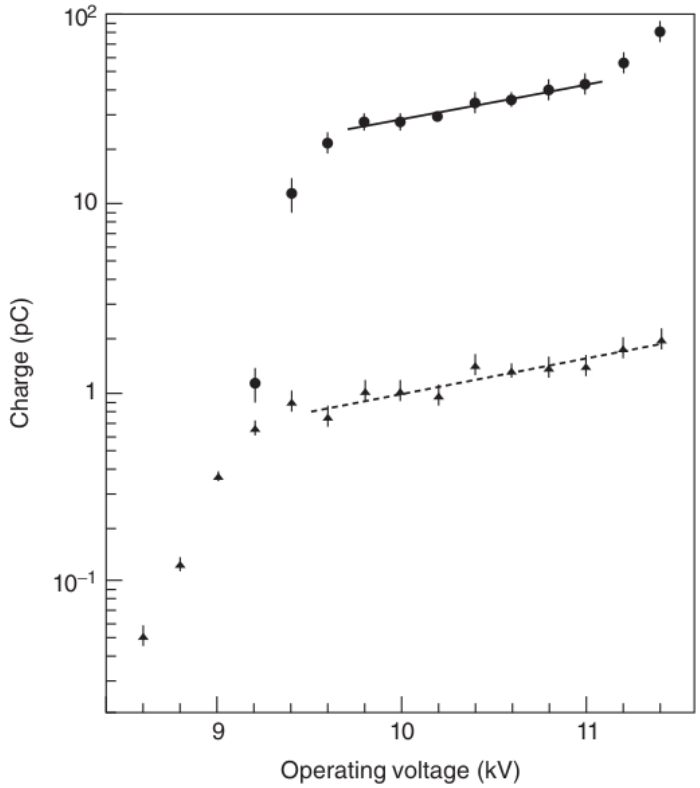

Figure 2.7: Trend of the prompt signal charge from an RPC operated in streamer mode. Triangular markers represent the precursor charge while the circular ones refer to the total charge (precursor plus streamer). Up to 9.2 kV the precursor charge increases exponentially. After this point a knee appears and the slope becomes lower and streamer signals start to appear (upper curve). Figure taken from [81]

Figure 2.7 shows two different (prompt) charge trends: the one with triangular markers refers to the charge of the precursor signal while the circular markers represent the total charge (precursor plus streamer). One can observe that up to 9.2 kV the precursor charge grows exponentially up to 1 pC. After this point, a knee is present and the slope starts to change, showing a saturation effect (most probably due to space charge effects). Together with the slope change, the streamers start to appear (upper curve)

and similar saturation effects are observed. The term prompt-charge (also called fast-charge) has been used; this is because the charge signal induced on the readout electrodes has two components: the fast one, induced by the electrons, and a slower one induced by the slow-moving ions (due to their smaller drift velocity, hence greater collection time). The collection of the total signal charge requires a more complicated circuit (as will be shortly discussed in 3.2.1.2), so the prompt charge can be used as a proxy for this quantity.

Avalanche mode The main issue with RPC operation in streamer mode is the reduced rate capability of detector, meaning that the detection efficiency is drastically reduced if the RPC is exposed to a high flux of ionizing particles.

In the case of RPC detectors, the rate capability is dominated by the fact that when the charge liberated by an ionizing particle crossing the gas reaches the electrodes, it creates a local reduction of the electric field, making the detector inefficient in that particular region. The voltage then returns back to the nominal value with a time constant approximately given by Equation 2.2. During this time the RPC cannot detect other particles impinging in that region and, if the detector is subjected to a higher particle rate, the probability that one crosses an inefficient region is non-negligible and the efficiency decreases. This issue can be overcome with two approaches[82]: by decreasing the electrode resistivity (to reduce τ) or by reducing the charge content of each signal to decrease the localized voltage discharge, leading to a faster recovery time. It was found that a decrease in electrodes resistivity could lead to a less stable RPC operation[82]. Instead, a reduction of the average charge per hit can be obtained by inserting a fraction of electronegative gas (as discussed in Reference [82]), which can absorb the free electrons in the gas, reducing the signal charge content.

The drawback of the avalanche operation mode is that the amplitude of the output signals is also reduced, making the use of sensitive pre-amplifiers a necessity, hence more sophisticated front-end electronics are needed. When a detector is operated in pure avalanche mode, no streamer contamination is visible but, of course, if the applied high voltage is increased, mild discharges can appear also in this case, indicating the end of the pure avalanche mode. Figure 2.8 reports the prompt charge spectra for three different gas mixtures of argon-isobutane with the addition of an electronegative gas (CF_3Br) which captures free electrons and reduces the number of events which degenerate into streamers.

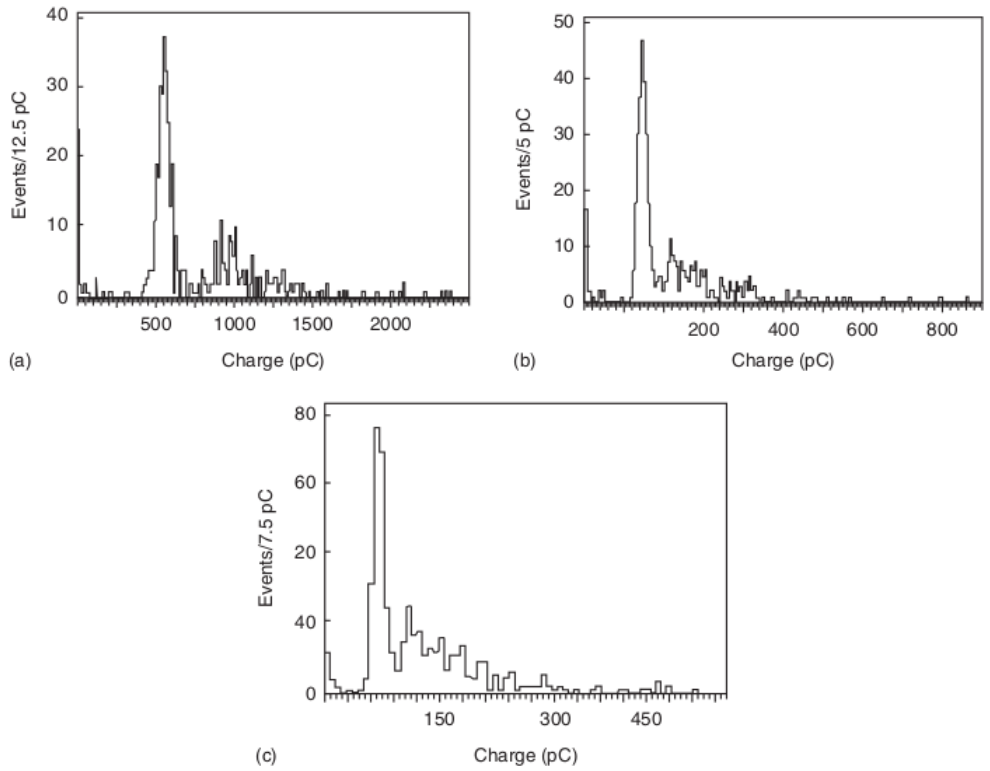

Figure 2.8: Charge distribution for argon-isobutane with different concentrations of CF_3Br: (a) 0%, (b) 4%, (c) 8% (note the different horizontal scale). Figure taken from [82]

An increasing percentage of CF_3Br in the mixture reduces the size of the signal induced on the electrodes, as reported from the three panels of Figure 2.8 where the CF_3Br concentration is increased going from panel a to panel c. The importance of the gas mixture to establish one or the other operation mode (avalanche and streamer) will be discussed in more detail in 2.2.4.

A comparison of the detector rate capability in avalanche and streamer mode is shown in Figure 2.9, where the efficiency for an RPC operated in the two modes is reported as a function of the impinging particle rate. One can clearly see that, for a given rate, the efficiency reduction for the RPC operated in streamer mode is greater than for the avalanche mode.

To conclude, operating an RPC in avalanche mode leads to a smaller charge per hit, producing a smaller voltage drop and a smaller recovery time (time needed to restore the critical voltage for multiplication after the localized drop due to the passage of an ionizing particle), hence the efficiency reduction will be smaller. Another factor that plays an important role in the determination of the recharge time is the electrodes resistivity, which appears in Equation 2.2. Typical values for bakelite range anywhere from 10^9 to 10^{11} Ω·cm. If left exposed to air, over time, the bakelite resistivity increases (as reported in Reference [83]). In order to avoid changes in resistivity (as well as in rate capability), the gas mixture employed in bakelite

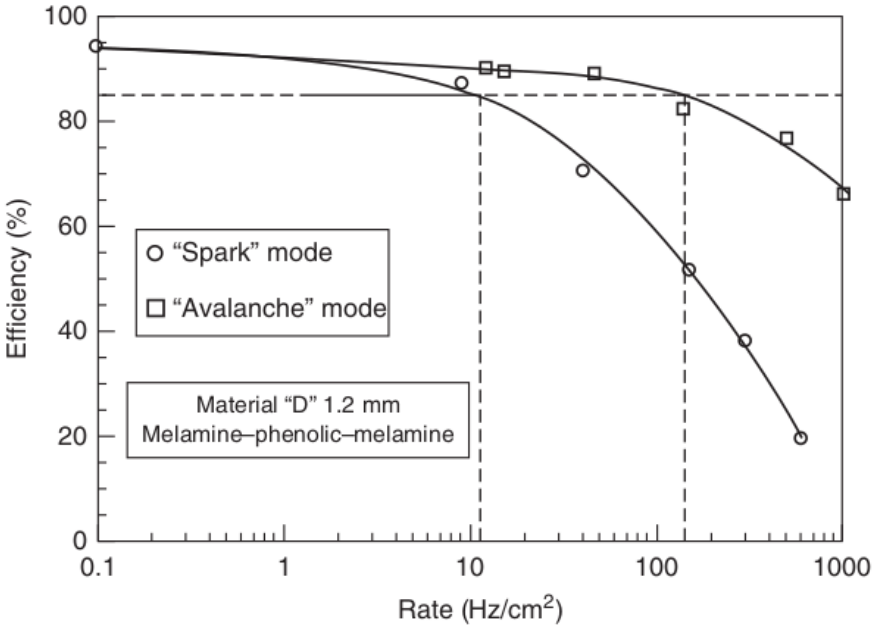

Figure 2.9: Efficiency as a function of the impinging particle rate for streamer and avalanche mode of operation. A better rate capability is visible for the RPC operated in avalanche mode. Figure taken from [74]

RPCs contains water vapour: 35 to 40% relative humidity is typically added to the gas mixture[74,83].

2.2.2 Signal formation and RPC working parameters

This section starts from a simplified analytical introduction to the signal formation process and tries to extract from this information the most significant detector working parameters. This discussion summarizes what is described in details in Reference [74].

Signal formation As it was outlined at the beginning of this chapter, when the gas is crossed by an ionizing particle, this creates ionization clusters (in number n_{cl}) along its path. What is meant with cluster is the primary electron-ion pair together with the additional pairs that can be created by the primary electron in case it has sufficient kinetic energy to re-ionize the gas.

The number of clusters is a stochastic variable, with an average that will be indicated by λ. Values of λ have been measured experimentally (e.g. in pure Ar, λ = 2.5 clusters/mm). For a mixture of different gases, a weighted average of λ values for each gas provides an acceptable estimation (weights are given by the volume fraction of each gas). If one can assume that the energy lost by an ionizing particle traversing the gas is small with respect to its

initial energy, one can neglect the dependence of λ from the particle energy. This is indeed a reasonable approximation for minimum ionizing particles. Last, if the particle enters the detector at an angle ϕ with respect to the perpendicular direction, the effective average number of clusters is defined as $\lambda_{eff} = \lambda/\cos\phi$. The probability to observe n_{cl} ion-electron clusters, if the particle traverses a thickness of gas g, is given by a Poisson distribution with average value $g\lambda_{eff}$, and the probability to have zero clusters is

$$P_{cl}(n_{cl} = 0) = e^{-g\lambda_{eff}} \tag{2.3}$$

This expresses the intrinsic inefficiency of the RPC and it imposes a lower limit to the gas gap thickness, depending on the gas mixture. For example, for λ_{eff} = 5.5 clusters/mm, a gas gap of 0.2 mm would have an intrinsic inefficiency of $\sim$ 33%.

The number of electron-ion pairs in a single cluster depends on the gas and experimental values, as reported in References [73, 74], show that a probability distribution $\propto 1/n^2$ can be used as a reasonable approximation (with n being the number of electron-ion pairs in a cluster).

The discussion so far concerned only the primary clusters. If an external electric field is also considered, charge multiplication phenomena start to appear. Once the charges start to drift (due to the electric field) they start to induce a signal on the readout electrodes. Since the ion drift velocity is $\sim$ 1000 times smaller with respect to the electron one, the time needed to collect the whole ionic charge (induced by ions) is order of magnitudes greater than what is needed to collect the electron signal. To exploit the precise time of the fast electron signal, this is recorded by an appropriate current amplifier[74]. For this reason, the discussion will focus on the electron signal in the following.

The charge contained in the avalanche can be expressed as:

$$q(x) = \sum_{j=1}^{n_{cl}} q_e n_{0,j} M_j e^{\alpha^*(x-x_{0,j})} \tag{2.4}$$

where the sum runs over all clusters, $n_{0,j}$ and $x_{0,j}$ are the number of primary electrons and the distance (from the cathode) of production of the j-th cluster, α^* is the effective first Townsend coefficient and the term M_j is used to take into account stochastic fluctuations in the avalanche process. The effective first Townsend coefficient has been introduced because, together with charge multiplication processes, attachment of the free electrons to the gas molecules can also take place. This phenomenon is de-

scribed by the attachment coefficient (η) which expresses the probability (per unit length) for an electron to undergo attachment. The effective first Townsend coefficient is defined as $\alpha^* = \alpha - \eta$. The stochastic nature of the charge multiplication process is expressed by the Polya distribution[84], which allows one to compute the probability to have n_e electrons in the avalanche after a length $l = g - x_0$ (g = gas gap thickness and x_0 = position of the initial cluster) as:

$$P_P(n_e) = \left[\frac{n_e}{N}(1+\theta)\right]^{\theta} exp\left[-\frac{n_e}{N}(1+\theta)\right] \tag{2.5}$$

where $N = e^{\alpha^*(g-x_0)}$ and θ is a parameter of difficult theoretical estimation. A typical value for the mixtures used in gaseous detectors is ~ 0.5.

At this point, the discussion can be shifted to the signal induced by the free moving charges on the readout electrodes. Calculations reported in Reference [74] show that the average induced charge (by the electrons) on the readout electrodes can be expressed as:

$$q_{ind} = \frac{\epsilon_r g}{\epsilon_r g + 2d}\frac{q_e}{\alpha^* g}\sum_{j=1}^{n_{cl}} n_{0,j} M_j [e^{\alpha^*(g-x_{0,j})} - 1] \tag{2.6}$$

where ϵ_r is the electrode relative dielectric constant, d is its thickness, g is the gas thickness, α^* is the effective first Townsend coefficient.

Charge distribution Starting from Equation 2.6, one can calculate the expected shape of the induced charge distribution (spectrum), when the detector is exposed to a flux of ionizing particles. This is a complicated calculation, involving many stochastic variables, so a more phenomenological approach can be followed. Figure 2.10 shows the charge distribution for two RPCs with different gap thickness (2 and 9 mm).

The two distributions differ significantly: in the case of 2 mm (narrow-gap) the number of entries grows as $q_{ind} \to 0$, while for the 9 mm one (wide-gap) it goes to zero. This means that, even if the average value of induced charge is roughly the same, small-charge events are more likely in a narrow-gap RPC, with respect to the wide-gap case. For the 9 mm RPC there also appears to be an excess of events in the right tail of the distribution, while this region is not as populated in the narrow-gap case. Since events with small charge are bound to be confused with the intrinsic noise of the detector/electronics, the shape of the charge distribution close to 0 is essential to predict the (in)efficiency of the detector.

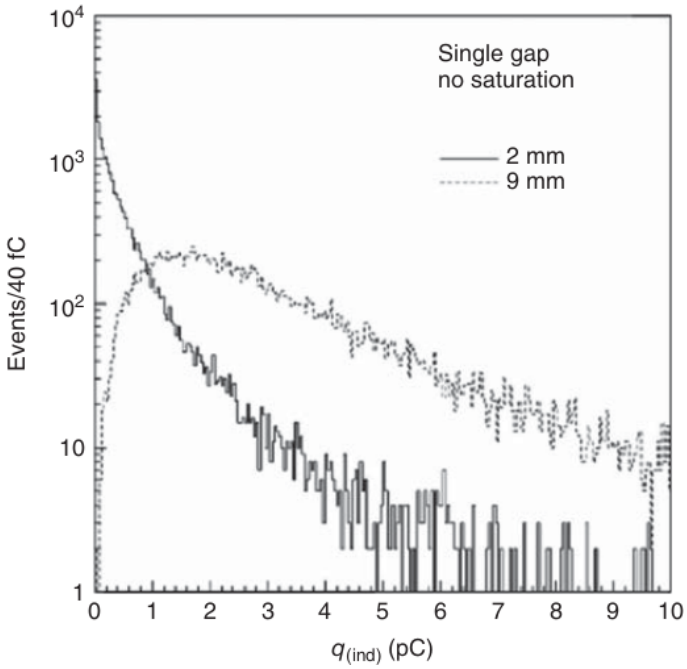

Figure 2.10: Induced charge spectra for two different gas gap thicknesses, 2 and 9 mm. Figure taken from [74]

If some assumptions are made, as described in Reference [74], one finds that the charge distribution shape essentially depends on the ratio λ/α^* between the density of primary ionization clusters and the effective Townsend coefficient. Depending on the value of the ratio, three cases can be distinguished:

- $(\lambda/\alpha^*) < 1$: the charge distribution is strictly decreasing (as is the case for the 2 mm RPC shown in Figure 2.10)
- $(\lambda/\alpha^*) \sim 1$: the charge distribution is constant around $q_{ind} \sim 0$
- $(\lambda/\alpha^*) > 1$: the charge distribution is strictly increasing around $q_{ind} = 0$ (as is the case for the 9 mm RPC shown in Figure 2.10)

Current The current flowing in a RPC detector is composed by two components. When the applied high voltage is too low to start the charge multiplication process, ideally, the current should be very close to zero. In real-life RPCs, almost always, a current is flowing even at this reduced values of high voltage. This current is not flowing through the gas, rather it can take other conductive paths, such as the plastic spacers, the gas gap seal or, in general, through any conductive path between anode and cathode. This current shows a linear behavior with the applied voltage, hence it is usually addressed to as Ohmic current.

When the high voltage is increased, charge multiplication processes start to appear and the current does not increase linearly with the high voltage but the trend becomes more exponential-like. The magnitude of the circulating current strongly depends on the gas mixture employed in the detector, together with the environmental parameters, such as temperature and pressure

If a high voltage is applied to the RPC without exposing it to a particle flux, the current flowing through it is only determined by the Ohmic component and by the intrinsic detector noise counts, and is defined as *dark* current. The typical example of intrinsic detector noise is a signal initiated by the detachment of an electron from the cathode. Imperfections on the inner electrode surface enhance the intrinsic noise, since the electric field is larger around a tip. If, on the other hand, the detector is exposed to a higher flux of ionizing particles, the current circulating through it strongly depends on the particle rate. Note that, for increasing currents, the voltage drop across the bakelite electrodes is no longer negligible. Indeed, the high voltage applied is split between the gas and the bakelite electrodes. This effect is extensively discussed in Section 4.5.1.4 and the effects on the detector efficiency are there discussed.

Electrodes resistivity As discussed at the beginning of Section 2.1, the characteristic feature of RPC detectors are the resistive electrodes. On the one hand, this feature is of key importance for the suppression of streamers but, at the same time, it is the limiting factor for the detector rate capability. Indeed, as explained in Section 2.2, the time needed to restore the electric field in the avalanche or discharge area is directly proportional to the resistivity of the bakelite electrodes. It is important to maintain this value as stable as possible over time and the addition of water vapor to the gas mixture serves this purpose. Different techniques, highlighted for example in Reference [83], can be adopted to measure the resistivity of the bakelite planes when the RPC is not assembled.

Once the detector is built, a non-invasive technique involving the use of pure Ar can be adopted. It is well known (as reported for example by Reference [85]) that if an RPC detector is flushed with pure argon and the high voltage is switched on, a plasma is created in the gas gap and this can be exploited to calculate the resistance (and from there the resistivity), as shown in the following. The left panel of Figure 2.11 shows the current of the ALICE-like RPC prototype, which will be described in 4.3.1, that has been used for the beam tests (that will be described in Chapter 4) and for

part of the aging studies (Chapter 5), as a function of the high voltage, when the detector is filled with pure argon.

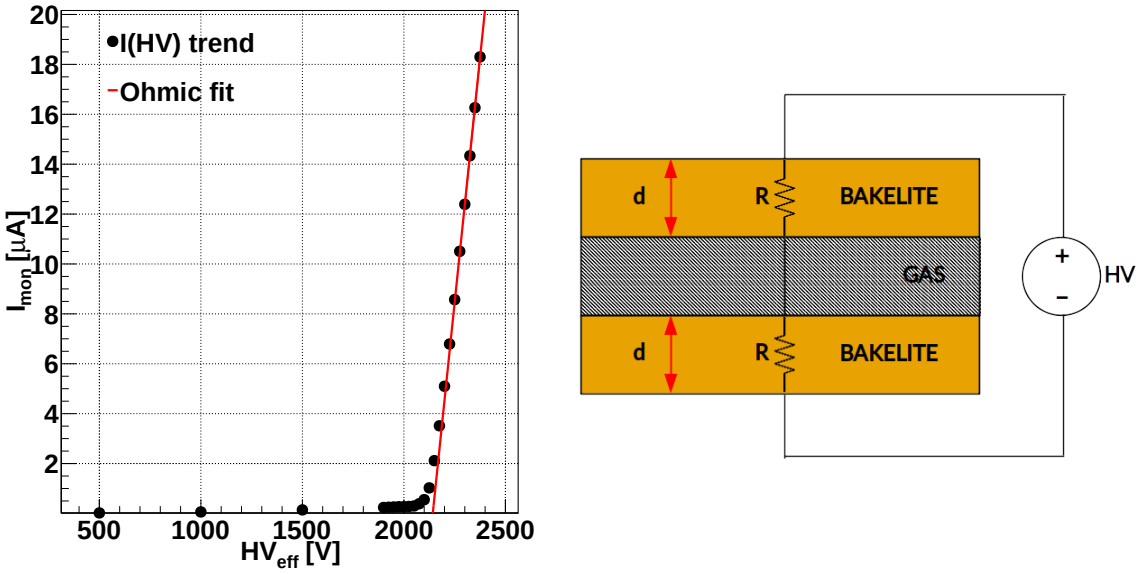

Figure 2.11: Left panel: I(HV) trend of the ALICE RPC if operated with pure Ar. Right panel: circuit model of the RPC if operated with pure Ar. The shaded pattern in the gas region symbolizes a short circuit

Up to ∼ 1.9 kV the current absorbed is negligible but, once this threshold is reached, a a steep rise in the absorbed current is observed. If the voltage is increased further, the current starts to have an Ohmic behavior, meaning that it increases linearly with the high voltage. This can be explained by considering that the plasma behaves like a short circuit between the two bakelite electrodes and the RPC can be considered as two resistors (the electrodes) in series with the high voltage, as reported in the right panel of Figure 2.11.

By performing a linear fit (y = bx + c) to the I(HV) curve in the linear region one can determine the resistance and resistivity of as follows:

$$R = \frac{1}{b} \rightarrow \rho = R\frac{S}{2d} \rightarrow \rho = \frac{1}{b}\frac{S}{2d} \tag{2.7}$$

Where the second Ohm law was also used. S is the bakelite electrode area and d is its thickness. Note that the equation assumes electrodes of equal resistivity, which is not always the case as, while producing bakelite sheets, the output resistivity can only be tuned within some tolerance. In case of electrodes with significantly different resistivity, Equation 2.7 provides the average resistivity of the two electrodes.

Typical values for the bakelite resistivity are around 10^9 - 10^{11} Ω·cm. The choice of electrode resistivity is a trade-off between rate capability and

streamer suppressing power. Indeed, a higher resistivity value leads to a stronger streamer suppression but at the same time it increases the time needed to restore the electric field after the passage of a particle. Low-resistivity electrodes are typically associated to a larger intrinsic noise[82].

Efficiency Information on the detector efficiency can be extracted by looking at the charge distribution (reported for example in Figure 2.10) close to zero, bearing in mind that the number of events with charge below a given threshold (as set in the front-end electronics) are lost. As a first approximation, only the charge induced by the first cluster (the one generated closest to the cathode) can be considered. In order to be detected, the charge induced by the movement of this cluster has to be greater than a fixed threshold, q_{thr}. If Equation 2.6 is truncated at cluster (j = 1) and is inverted, one finds that, in order to release a charge greater than the threshold, the cluster has to be generated at a distance from the cathode given by:

$$x_0^1 < g - \frac{1}{\alpha^*} log\left(\frac{q_{thr}}{A_1} + 1\right) \tag{2.8}$$

where A_1 is a parameter that absorbs some constants from Equation 2.6. Finally, taking into account also the probability distribution for the distance of the first cluster from the cathode, as reported in Reference [74], one can compute the efficiency of the chamber as:

$$\epsilon_c = 1 - exp\left(-\lambda_{eff}\left[g - \frac{1}{\alpha^*} log\left(\frac{q_{thr}}{A_1} + 1\right)\right]\right) \tag{2.9}$$

More refined calculations show that, if the contribution of the other clusters is considered, the total induced charge is a factor 1.25 greater with respect to what is calculated using the first cluster only. Typical threshold values in 2 mm gap detectors are $\sim$ 130 to 200 fC[86].

Time and position resolution The intrinsic time resolution for an RPC detector can be computed by starting from the previously discussed formulas. In particular, following the approach shown in Reference [74], one can start by considering the signal, in terms of current, induced by a single primary electron somewhere in the gap. One can define the value of I_{thr} as the threshold in terms of current, leading to the following:

$$i_{ind}(t) = I_s e^{\alpha^* v_d t} \quad \rightarrow \quad t = \frac{1}{\alpha^*} log \frac{I_{thr}}{I_s} \tag{2.10}$$

where i_{ind} represents the induced current, v_d is the electron drift velocity and I_s is the signal current amplitude, which differs event by event and is exponentially distributed around a given mean value. Note that Equation 2.10 has been rewritten in terms of the electron drift velocity but the physical content is the same as all equations in previous paragraphs. The time t corresponds to the time when the current signal crosses over the threshold and it becomes detectable by the RPC (crossing time).

The time resolution of the detector is computed as the fluctuations around the crossing time and calculations provide the following expression for it:

$$\sigma_t = \frac{1.28}{\alpha^* v_d} \tag{2.11}$$

which does not depend on the threshold. For a 2 mm RPC, this formula provides a time resolution of ∼1 ns. More complex calculations can be carried out, which also consider the presence of electronegative gases in the mixture. More refined calculations, for example shown in Reference [87], show that the time resolution is a decreasing function of n_{av}, defined as the average number of initiated avalanches[74], which differs from the number of primary clusters because it includes the probability that a primary electron is absorbed by an electronegative gas. A dependence from $1/\sqrt{n_{av}}$ is found.

The RPC time resolution can be improved by considering a new detector design, namely the multi-gap RPC (MRPC). In these detectors, the gas gap is divided in smaller slices, by using a stack of resistive electrodes, with the two outermost ones connected to the high voltage and the internal ones left electrically floating (for a more complete description of the MRPCs, the reader can refer to [88]). This type of detectors showed excellent performance in terms of time resolution and, as an example, the Time Of Flight (TOF) detector of the ALICE experiment (briefly described in 1.2.2.1), composed by an array of MRPCs with stacks of 5, 250 μm thick gaps, reaches a time resolution $\sim$ 50 ps[89].

Usually RPCs are read out with centimeter-wide strips which provide a spatial resolution in the order of the $\sim$ mm. As a first approximation, the spatial resolution can be computed as the product between the cluster size (number of neighbouring strips which produce a detectable signal in an event) and the strip pitch[1], divided by $\sqrt{12}$.

In order to improve spatial resolution, smaller-pitched strips can be used and a more precise avalanche position can be determined by looking at the charge deposition profile. With this approach, using mm-wide strips, a posi-

[1]Pitch = distance between the center of neighbouring strips

tion resolution of 100 μm has been reached [90] while for muon tomography (that is, using the RPC to detect cosmic muons on big-area detectors to perform tomography of large structures), an accuracy of 0.5 mm over a 1 m^2 area has been reached [91].

2.2.3 Effects of temperature and pressure

Gases are affected by environmental parameters, such as temperature and pressure. Indeed their density (ρ_g in the following) varies according to the values of these quantities. Moreover, the resistivity of the bakelite is also affected by temperature variations. Works such as the one reported in [83], have shown that a temperature increase by 20°C, decreases the bakelite resistivity by $\sim$ one order of magnitude.

Since the parameters related to charge multiplication (such as the Townsend coefficient) depend both on the applied electric field (E) and ρ_g, to maintain RPC performance constant despite changes in environmental parameters, the ratio E/ρ_g has to be kept constant. If RPCs are operated at different temperatures, variations in absorbed current, noise rate, efficiency and time resolution are observed. Specifically, a temperature increase leads to an increase of current (since the bakelite resistivity is reduced) and noise counting rate. At the same time, the gas density is reduced and this implies an increase in the ratio E/ρ_g, meaning that, for the same value of applied voltage, the multiplication in the gas is increased and so is the efficiency. The opposite happens for a pressure increase. In order to compare data obtained in different environmental conditions, the concept of "effective" high voltage (ΔV_{eff}) can be introduced[74] and defined as follows:

$$\Delta V_{eff} = \Delta V_{app} \frac{T}{T_0} \frac{p_0}{p} \tag{2.12}$$

where T and p are the measured values of temperature and pressure while p_0 and T_0 are reference values (a typical example is T_0 = 20°C = 293.15 K and p_0 = 970 mbar) and ΔV_{app} is the high voltage applied to the detector. This follows from the dependence of the gas density (at constant volume) on temperature and pressure, as obtained from the gas equation of state. Figure 2.12 shows, in the left panel, efficiency curves taken at different temperatures, as a function of the applied high voltage. The efficiency variation for a fixed voltage value can be observed. The right panel contains the same efficiency curves as a function of the effective high voltage, calculated with Equation 2.12, which shows that the efficiency curves are superimposed and no temperature dependence is observed.

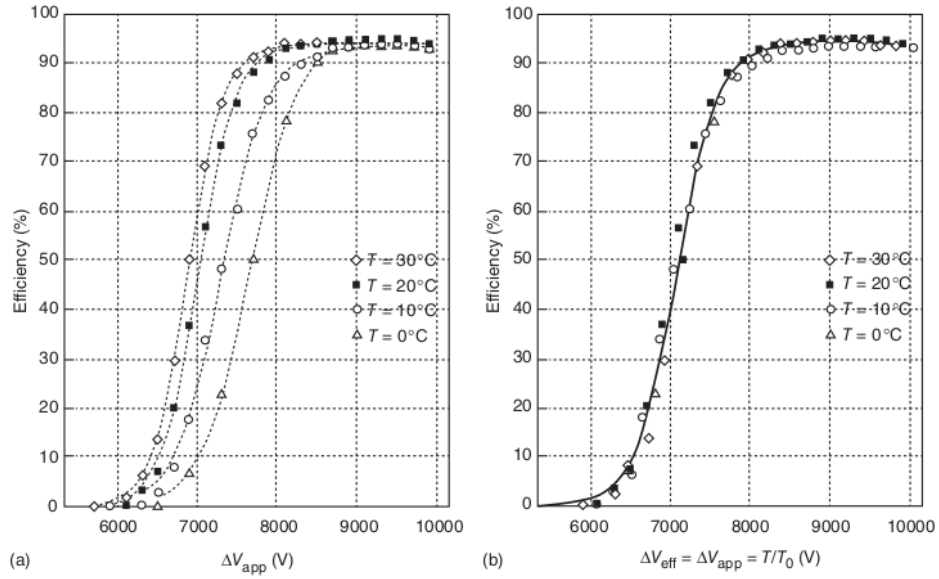

Figure 2.12: Effect of showing efficiency curves taken at different temperatures as a function of the applied high voltage (left panel) and as a function of the effective high voltage (right panel). Figure taken from [74]

The CMS collaboration introduced a slightly different, empirical, formula for the temperature and pressure HV correction, which assumes that the effective high voltage is determined partially by the T/p rescaled voltage and partially by the applied voltage alone[92]:

$$\Delta V_{app} = \left((1-\alpha) + \alpha \cdot \frac{P}{P_0} \cdot \frac{T_0}{T}\right) \cdot \Delta V_{eff} \tag{2.13}$$

This formula is the one adopted also in this thesis, as will be described in detail in 4.3.2.

2.2.4 The importance of the gas mixture

Having listed all the relevant parameters for RPC operation, the attention can be shifted to the gas mixture choice. The gas mixture has to fulfill a set of requests: it has to provide a high density of primary electron-ion pairs and a sufficiently high effective Townsend coefficient to ensure high detection efficiency; it has to exhibit relevant quenching properties, meaning that absorption of secondary photons should be maximized, and it also has to be electronegative, to capture free electrons and reduce the spatial size of the avalanche. Moreover, the processes taking place during charge multiplication should produce none to very little aggressive chemical species, which might attack the inner surfaces of the detector (most notably hydrofluoric acid, HF). Also the production of polymers should be kept to a minimum,

to minimize deposition of impurities on the electrode surface. Another important aspect to be considered is the availability and price of the adopted gases. As will be discussed later in this subsection and, more in detail, in Chapter 3, these are affected by the impact of the gas mixture on the environment, especially in terms of global warming and ozone layer depletion. Lastly, the RPC gas mixture must be harmless for men and as easy to handle as possible.

The first RPCs were operated in streamer mode and usually contained a mixture of argon, butane and some kind of chlorofluorocarbon[74]. Ar was present in fractions between 60 and 70% and it acted as the "active" component (main contributor to charge multiplication) of the gas mixture. The butane was used to absorb the photons produced in the streamer phase and the chlorofluorocarbon, being electronegative, to capture the free electrons. For a 2 mm gas gap, the working voltage is around 7.5 to 8.5 kV (depending on the gas mixture composition). Nowadays , RPCs are usually operated in avalanche mode and different gas mixtures are employed but they usually consist in the combination of three gases[73], in varying proportions: tetrafluoroethane ($C_2H_2F_4$ or R134a), which is a dense gas that provides a high density of primary ion-electron pairs; isobutane (i-C_4H_{10}), which is used because of its ability to absorb photons without ionizing, and sulphur hexafluoride (SF_6), a highly electronegative gas that absorbs free electrons, reducing the spatial size of the avalanche. The issue with R134a and SF_6 is that they are characterized by a high value of global warming potential (GWP). This figure is a pure number used to compare the effect of the emission of a ton of any given gas, if compared to the same mass of CO_2 (assumed to have GWP = 1). For instance, the GWP of R134a is $\sim$ 1488 (according to the 4^{th} Intergovernmental Panel on Climate Change [93]), which means that the emission of one ton of R134a absorbs 1488 times more heat than the same amount of CO_2. This poses a serious environmental threat, also considering the new European Union regulations of 2014 [94], which imposed a progressive reduction in the production and use of fluorinated greenhouse gases (meaning gases containing fluorine with damaging effects on global warming), leading to a reduced availability and increase in purchasing costs. A great effort is ongoing in the whole RPC community, to find a possible eco-friendly replacement for the currently employed gas mixtures. Chapter 3 provides a review of the possible strategies that are being adopted or proposed so far, to try and reduce both the cost and the environmental impact of RPC operation. Among these, the search for an alternative gas mixture, i.e., the main subject of this thesis.

2.2.5 Effects of long-term detector operation

The degradation of detector performance after being exposed to ionizing particles for a prolonged period of time (or even, sometimes, just with time, independently of operation) is defined as aging. Common aging effects include, in increasing order of severity: increased current (dark and/or under irradiation), increase of intrinsic noise and loss of efficiency. When the detectors that exhibit these signs are inspected, macroscopic imperfections can be observed and chemical analyses reveal the presence of various impurities that are not present in brand-new detectors, as reported by Reference [95]. Aging is a very complex phenomenon, that is not yet fully understood and where many chemical phenomena, regarding all the detector building blocks (materials, gas, high voltage) are intertwined with one another and often the relationships of cause and effect are difficult to disentangle. Reference [74] reports a detailed description of the aging effects observed in the first large experiments where RPCs were operated in streamer mode. These are indeed interesting observations, although not of key importance to this thesis. Nonetheless these were the first experiments where large scale RPCs were exposed to high particle fluxes and they have provided valuable lessons for the future experiments, since most of the aging effects were related to mistakes made during the detector construction and operation. Nowadays, the RPCs in big experiments are operated in avalanche (or maxi-avalanche, as is the case for the ALICE RPCs, described in Section 2.3) mode. This leads to a smaller charge released per hit and to more manageable aging effects, as reported by the CMS and ATLAS collaboration in References [96] and [97] respectively.

A more detailed discussion of ageing effects and how these are studied will be given in Section 2.3 of this chapter, when presenting the RPCs of the ALICE Muon Identification System. For these RPCs extensive long-term studies, using both streamer and avalanche mixtures, have been carried out. Moreover, as discussed in Section 2.4, some mild signs of aging are starting to appear for some of the RPCs in ALICE and a specific study, to investigate them, was carried out by the author of this thesis.

2.3 The ALICE Muon IDentifier (MID)

2.3.1 MID layout

As stated in 1.2.2.2, the ALICE Muon Identification (MID) system is composed by 72 single-gap RPCs arranged in two stations of two planes each (18 RPCs per plane). The RPCs have a 2 mm single gas gap, as well as 2 mm thick, low-resistivity (10^9 - 10^{10} Ω·cm) bakelite electrodes with a double linseed oil coating. The total area covered by the MID RPCs is $\sim$ 140 m^2 and the size of each detector plane is $\sim$ 6×6 m^2. To accommodate the LHC beam pipe, three different types of RPCs have been employed, namely "long" (rectangular shape, ~274×72 cm^2), "cut" (trapezoidal shape with similar size as the "long" RPC type) and "short" (rectangular shape 223×72 cm^2)[98]. Figure 2.13 shows, in the left panel, a sketch of the mechanical structure of one of the ALICE RPCs; while the right panel contains a sketch of the whole MID system. The RPCs are read out on both sides, by means of perpendicular copper strips (for a total of $\sim$ 22k readout channels[98]). Different strip pitches have been adopted, according to the expected occupancy, as explained in Reference [98], and pitches of 1, 2 and 4 cm have been adopted.

The RPCs are operated in the so-called *maxi-avalanche* or saturated avalanche mode, meaning that the total charge per hit is $\sim$ 100-150 pC, to be compared to the charge content of pure avalanche mode $\sim$ 30 pC, for a 2 mm single gas gap RPC[99]. The chosen gas mixture is composed by 89.7% R134a, 10% i-C_4H_{10} and 0.3% SF_6, and its properties will be discussed later.

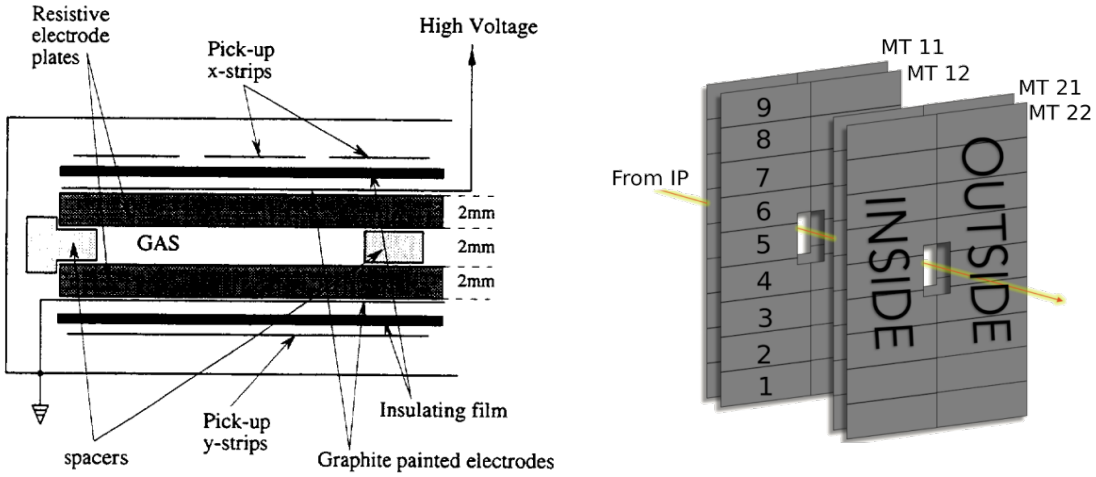

Figure 2.13: Left panel: scheme of the mechanical construction for one ALICE RPC, figure taken from [9]. Right panel: sketch of the ALICE MID layout (image: courtesy of Gabriele Fronzè)

The RPCs are flushed via 24 gas pipes, with each gas channel supplying 3 detectors in parallel. The gas mixture is recirculated with a re-circulation

fraction of 75%[100], meaning that only 25% of the total circulating gas is injected as fresh gas in the system. The rest is circulated through purifying cartridges to remove any impurity[101] that might be produced by the interaction between gas and ionizing particles. The total gas volume amounts to ~ 0.3 m^3 and a gas replacement rate of 0.5 volumes per hour is maintained. This translates into a total flow of ~ 150 l/h (and ~ 40 l/h of injected fresh gas).

2.3.2 The MID RPC gas mixture

Many studies have been carried out before the currently employed gas mixture was adopted. Initially, it was decided to operate the RPCs with a streamer mixture during heavy-ion collisions[102,103] and a saturated avalanche one during the pp data-taking periods[104]. This choice was dictated by the expected spatial resolution and trigger selectivity requirements. Indeed, the streamer mode exhibits a smaller cluster size that the avalanche, as shown, e.g., in Reference [104]. A possible explanation for this observation is that the pulse amplitude spectrum is narrower (around its mean value) than the avalanche one (which shows an exponential decrease), meaning that in the latter case a relatively low threshold has to be adopted in order not to lose the signals with lower amplitude. The drawback of this choice is that a large avalanche would induce a signal above threshold on several neighbouring strips, leading to a larger cluster size.

An issue to be faced was the maximum impinging particle rate that can be tolerated by an RPC working in streamer mode without significant efficiency loss. This value is reported to be ~ 100 Hz/cm^2[105]. The maximum expected hit rate in ALICE was ~ 50 Hz/cm^2 [103], which is tolerable but with a very small safety margin. To improve the rate capability of the ALICE RPCs, the adoption of low resistivity ($\simeq 3.5{\cdot}10^9$ $\Omega{\cdot}$cm) bakelite sheets to build the RPCs was pursued and the first results obtained with such low-resistivity bakelite are reported in Reference [102]. Furthermore, the number of integrated hits foreseen in the ion runs was on the order of 100 Mhits/cm^2 (for the whole lifetime of the detector and with a safety factor 2 included), so a mixture with a charge per hit of a few hundreds pC (such as a streamer mixture) was not expected to create excessive damages to the RPCs. For the pp operations, instead, less stringent spatial resolution constraints were expected but, at the same time, a greater exposure ($\sim$ 200 Mhits/cm^2/year) was foreseen. To slow down the aging induced by pp operation, a large-amplitude avalanche mixture, with a lower charge per hit

with respect to the streamer mode, was investigated.

An important factor that led to the choice of a maxi-avalanche, and not pure avalanche, gas mixture lies in the front-end electronics that were initially developed for the ALICE muon RPCs. Indeed, the foreseen front-end electronics were equipped with the ADULT (A DUal Threshold) chip[106], specifically developed for streamer mode operation. This front-end electronics was exploiting the fact that usually a streamer signal is preceded by a large-amplitude avalanche (as described in Section 2.1), which is a fast and precise signal (in terms of timing resolution). The ADULT chip was using the large-avalanche signal to get the time reference and the streamer signal (within a programmable time interval from the avalanche) to confirm the hit. In order to discriminate the two signals, two thresholds are needed (a lower one for the avalanche and a higher one for the streamer). With this technique, a similar time resolution was obtained with the avalanche and streamer mixtures. Even when both thresholds were set to the lowest achievable value (above noise), a pure avalanche mixture would not provide signals above this minimum threshold, hence the need to obtain very large avalanche signals.

After studying the detector response using cosmic muons and beam tests, their long-term operation had to be assessed as well. This was done by means of aging studies in which the detectors were exposed to a high ionizing particle flux to simulate their long-term operation in the experiments. Those tests were carried out at the CERN Gamma Irradiation facility[107], where a 0.5 TBq ^{137}Cs source could be used (in combination with a muon beam to test detector performance) to simulate a high radiation background to accelerate the RPC aging process and study their long-term behavior.

The results of the aging test with the streamer mixture (50.5% Ar, 41.3% R134a, 7.2% C_2H_{10} and 1% SF_6) are shown in Figure 2.14. The left panel shows the trend of the dark current and dark counting rate (quantities measured when the detector is not exposed to the GIF ^{137}Cs source), as a function of the integrated charge (integral of the current in time, assuming 500 pC/hit on average, 50 mC/cm^2 correspond to the above mentioned 100 Mhits/cm^2). An increase of the dark current is observed, while the dark counting rate remains stable around 0.4 Hz/cm^2. The right panel of Figure 2.14 shows instead the trend of the efficiency as a function of the integrated charge. A slight decrease over time can be observed, which was attributed to an increase in bakelite resistivity following the irradiation[103]. Nevertheless, at the end of the irradiation studies, the RPC efficiency is above 97%, still compatible with operation in ALICE.

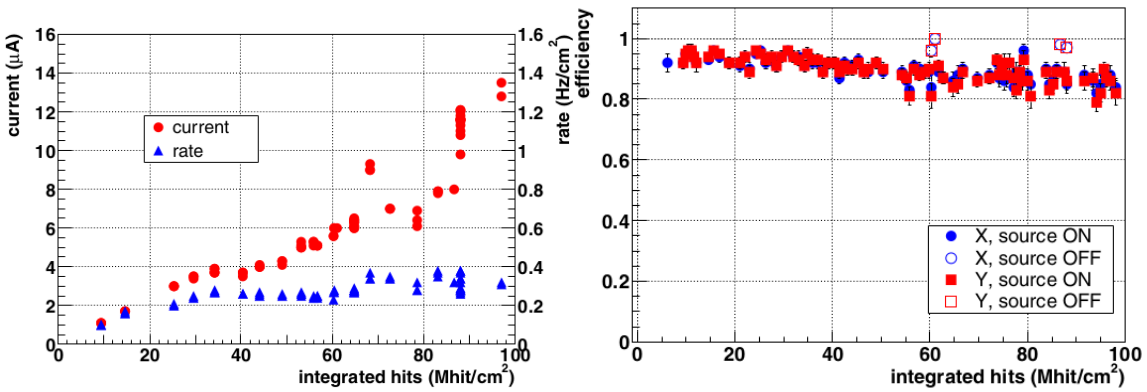

Figure 2.14: Left panel: trend of dark current/dark counting rate as a function of the integrated charge with streamer mixture during aging studies. Right panel: trend of efficiency with streamer mixture during aging studies. Figures taken from [103]

The results for the test with a saturated avalanche mixture are reported in Reference [104]. Initially, a mixture of 88% R134a, 10% C_4H_{10} and 2% SF_6 was tested (with an operating voltage $\sim$ 11000 V). The idea behind the high i-C_4H_{10} concentration is to operate the RPCs with a highly quenched gas mixture, in order to avoid streamer formation even for the high gas gain, needed to operate with the ADULT front-end electronics, which did not provide an amplification stage[104]. Acceptable values, in terms of efficiency, cluster size (slightly higher than with the streamer mixture but still acceptable for pp data taking), time resolution and charge per hit were reached with the prototype under test. Moreover, a lower impurity production with respect to the streamer mixture was observed. During aging studies, after the integration of 100 Mhits/cm^2, some current instabilities were noticed and were attributed to the high detector working voltage. It was then decided to lower the SF_6 content down to 0.3% (while increasing the R134a fraction) and to test the detector performance with this new mixture. Acceptable values of all the measured parameters were found, moreover the working voltage was lowered to about 10100 V and the average charge per hit was reduced to about 150 pC/hit. A new aging test was carried out with two RPC prototypes and the results of this campaign are shown in Figure 2.15. The left panel shows the trend of absorbed dark current/rate, and efficiency, as a function of the integrated charge. The dark current remains low and the efficiency stable throughout the whole irradiation period. The right panel shows instead the comparison of the efficiency curve, before and after the aging test: no voltage shift of the efficiency curve is observed.

The tests described above are a summary of the main steps followed by the ALICE RPC group in the search for a proper gas mixture for the operation in ALICE. The full details of the the process, as well as the full list of

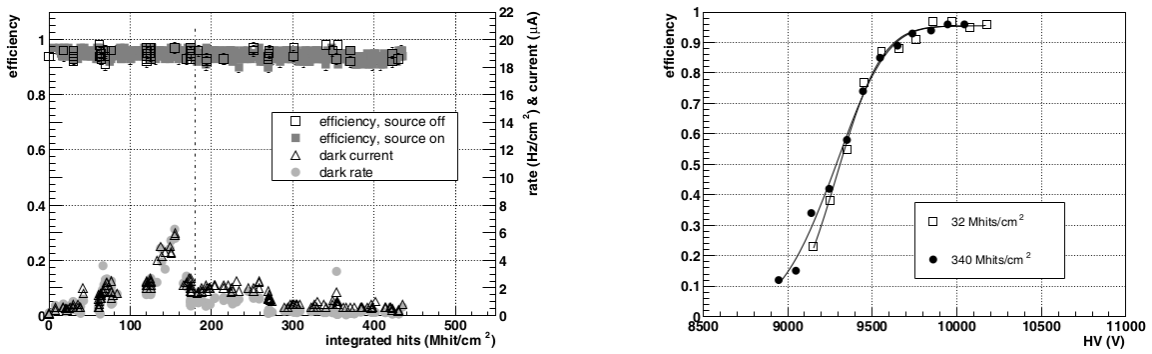

Figure 2.15: Left panel: trend of dark current/dark counting rate/efficiency as a function of the integrated charge with maxi-avalanche mixture during aging studies. Right panel: comparison of efficiency plateau at the start and at the end of the aging test. Figures taken from [104]

publications regarding the subject can be found in Reference [108]. In the end, following the very promising results obtained from the maxi-avalanche aging tests, it was decided to use the same maxi-avalanche mixture for all types of colliding systems (meaning for both pp and Pb-Pb collisions), also due to the measured charged-particle multiplicity of Pb-Pb collisions at the LHC[109], which turned out to be lower than the values (extrapolated from RHIC measurements) assumed during the detector design and R&D phase.

2.3.3 MID running conditions in RUN3 and RUN4

By the end of LHC RUN2, in 2018, some of the ALICE RPCs had integrated an amount of charge close to their certified lifetime of 50 mC/cm^2, as shown by Figure 2.16, where the integrated charge versus time for one of the MID RPC planes is shown. The figure reports values for the RPC which integrated the largest amount of charge ($\sim$ 30 mC/cm^2) and the average value ($\sim$ 12 mC/cm^2) by the end of RUN2.

To slow down the integrated charge accumulation and, at the same time, improve the detector rate capability, it was decided to upgrade the front-end electronics to a new model, called Front-End Rapid Integrated Circuit (FEERIC, extensively described in Reference [111] and in 4.3.4.3). This new front-end electronics allows one to discriminate signals with a much smaller charge content, allowing one to operate the RPCs at $\sim$ 1 kV lower voltages and reducing the mean charge per hit by a factor 3-4, improving the rate capability and slowing down aging. Figure 2.17 shows the comparison of the absorbed current at the working point with the old (ADULT) and new (FEERIC) front-end boards. The current reduction is evident and is shown for different values of FEERIC thresholds.

Table 2.1 shows the expected hit rate for the MID RPCs in pp and Pb-

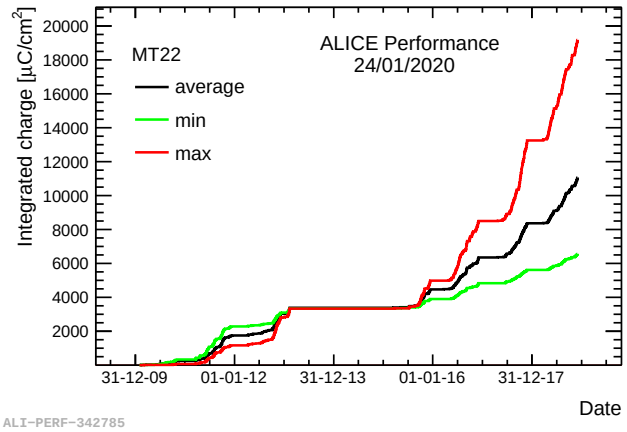

Figure 2.16: Trend in time for the accumulated charge by one ALICE MID RPC plane. The green and red curves refer to the RPC which integrated the least and the most charge while the black one represents the average. Figure taken from [110]

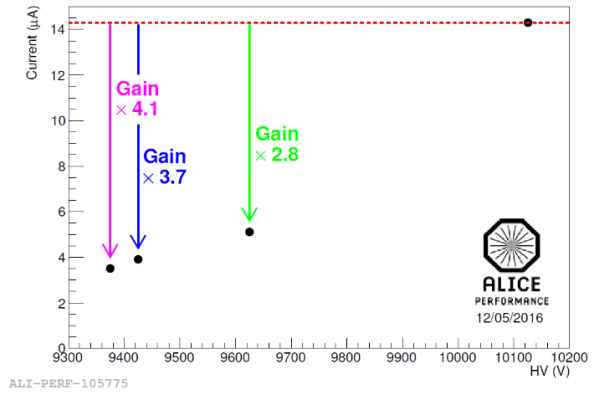

Figure 2.17: Comparison of the absorbed current at working point for an ALICE MID RPC if the signals are discriminated with the old (ADULT) and new (FEERIC) front-end electronics, for different FEERIC thresholds. A reduction in the absorbed current is observed due to the fact that the RPC is operated at much lower voltages. Figure taken from [112]

Pb collisions during RUN3 and RUN4[112]. The table reports the expected average rate, as well as rate for the most exposed RPC. The Pb-Pb estimates are for an interaction rate of 100 kHz, i.e., a safety factor of 2 is considered.

Table 2.2 reports an estimate of the integrated hits and integrated charge for RUN3 and RUN4. The calculations assume 1 month of Pb-Pb and 6 months of pp collisions per year and assume a 60% running time and the worst-case scenario (i.e. the maximum rate reported in Table 2.1) is assumed. Moreover, a charge per hit of $\sim$ 30 pC is assumed, according to Reference [111]. Another scenario, identified as RUN4 (ECO) is presented in the table and it contains the expected integrated charge in case the detectors will be operated with one of the eco-friendly alternatives discussed in Chapter 4. As it was said at the beginning of this chapter, the subject of this thesis is the search for an eco-friendly alternative to operate the RPCs of

pp Average	pp maximum	Pb-Pb average	Pb-Pb maximum
5 Hz/cm^2	13 Hz/cm^2	48 Hz/cm^2	90 Hz/cm^2

Table 2.1: Expected hit rate for the MID RPCs in pp and Pb-Pb collisions in RUN3 and RUN4. Table taken from [112]

the ALICE MID during RUN4, so this scenario is also presented in Table 2.2. The charge calculations are based on the results presented in 4.5.3, where it will be shown that the potential eco-friendly alternative gas mixtures have a charge per hit that is ∼1.6-1.7 times as high as the standard gas mixture, hence a charge per hit ∼ 50 pC is assumed in the calculations.

	Mhits pp	Charge pp	Mhits Pb-Pb	Charge Pb-Pb
RUN3	485 Mhits/cm^2	15 mC/cm^2	550 Mhits/cm^2	17 mC/cm^2
RUN4	485 Mhits/cm^2	15 mC/cm^2	550 Mhits/cm^2	17 mC/cm^2
RUN4 (ECO)	485 Mhits/cm^2	24 mC/cm^2	550 Mhits/cm^2	27 mC/cm^2

Table 2.2: Estimate of integrated hits and charge for the MID RPCs in RUN3 and RUN4, for the most exposed RPC and assuming a charge of ∼ 30 pC per hit. The possible scenario where an eco-friendly gas mixture is employed in RUN4 is also considered (see text for details)

2.4 A study of aging effects in the MID RPCs

This section shortly summarizes the studies performed by the author of this thesis shortly before, and partially in parallel, with the main thesis work presented in Chapters 4 and 5. The outcome of these studies is published in Reference [110].

By the end of RUN2, in 2018, possible signs of detector aging, under the form of an increase in the absorbed dark current, were observed in around 50% of the MID RPCs[100]. This is the only potential sign of aging shown by the system, since the trend of efficiency in time did not show any sign of degradation, as shown in the left panel of Figure 2.18. Shown there is the trend of the average RPC efficiency in one of the four detection planes (referred to as MT22) during RUN1 and RUN2. Similar trends have been observed for the other three detection planes. The figure reports two different trends, addressed to as bending and non-bending plane: the names refer to the strip plane orientation, with respect to the dipole magnetic field. The horizontal strips correspond to the bending direction, while the vertical ones to the non bending. The right panel of Figure 2.18 shows the trend of

the dark current for the RPCs in the same detection plane (MT22): the black line refers to the average dark current of all RPCs, the green one to the RPC which absorbs the minimum dark current and the red one to the one with the highest dark current. The efficiency shows a stable trend throughout the whole period shown (LHC RUN1 and 2), while the dark current shows the above mentioned increase, especially during RUN2 (2015-2018).

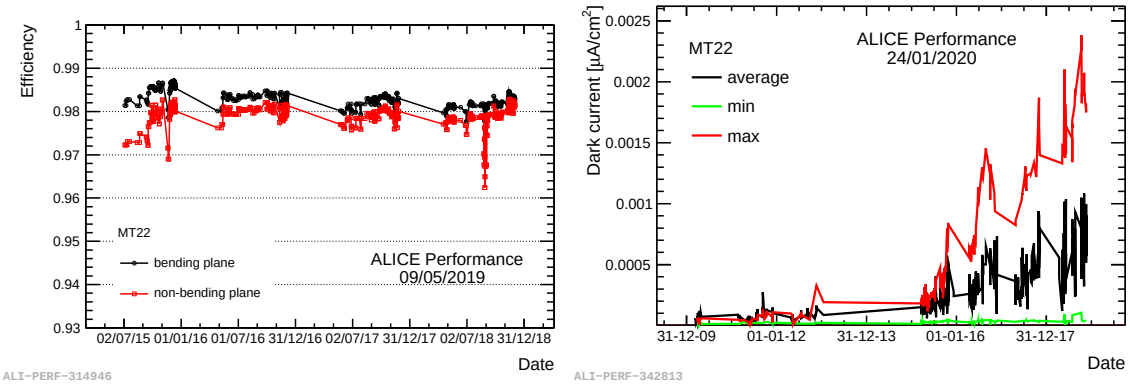

Figure 2.18: Left panel: trend of bending and non-bending plane efficiency for MT22. Right panel: trend of dark current for the RPCs in plane MT22. Figures taken from [110]

A possible explanation for the observed dark current increase could be the deposition of fluorinated compounds (mainly HF), on the inner surfaces of the detectors. These can be created by the interaction of F^- ions (produced by the breakage of the F-rich gases in the mixture by the radiation) with the water vapour present in the mixture[74]. These compounds can stick to the inner bakelite layers, creating a thin conductive layer, which could lead to an increase of the dark current. To test this hypothesis, a few RPCs that showed particularly high dark current were flushed with pure Ar and kept with the high voltage switched on for $\sim$ one month and the presence of pollutants in the output gas was monitored. It is well known, as reported in Reference [85], that when RPCs are flushed with pure Ar and the high voltage is switched on, a plasma is created inside the gap. If some impurities are deposited on the inner surfaces of the RPCs, the impinging ions and electrons from the plasma, might be able to mechanically detach those impurities and the gas flow might be able to remove them from the detector. By analyzing the output gas, one could observe the presence of those detached impurities. To carry out the gas analysis, a gas chromatograph (GC), a mass spectrometer (MS) and an Ion Selective Electrode (ISE) were connected to the output gas lines of the RPCs. The GC is used to separate the gas mixture in its constituents, while the MS (connected in series to the GC) is used to identify them. The ISE is specifically calibrated to detect F^- ions in

concentrations smaller than the GC-MS resolution.

Together with the study of possible impurities in the exiting gas, another goal of this test was to check whether the action of the Ar plasma could lead to the reduction of the absorbed dark current. This was measured and compared before and after the test. Around 20 RPCs were flushed with pure Ar while the others were left open to air. Out of the 20 flushed RPCs, the high voltage was switched on (and the Ar plasma created) only for two of them but the dark current was compared in all cases, in order have a full-spectrum (with Ar plasma, Ar without plasma and no treatment) comparison before and after the test. Figure 2.19 shows the experimental setup just described.

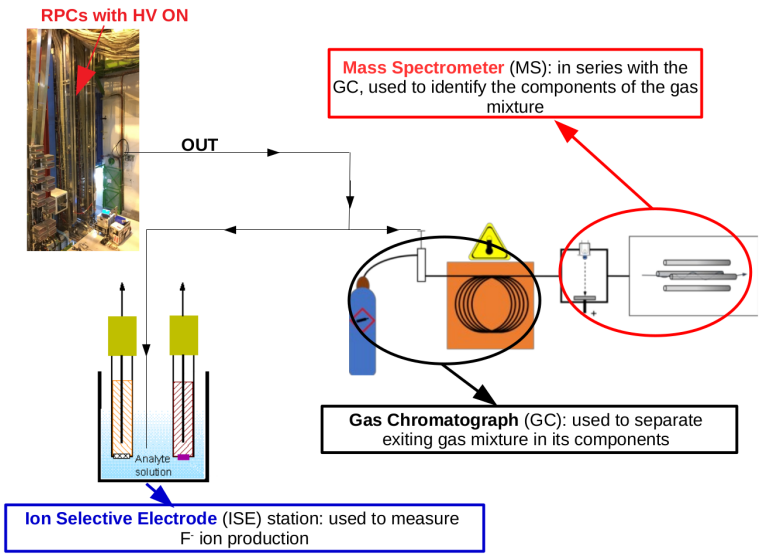

Figure 2.19: Scheme of the Ar plasma setup for impurities production measurement in the output gas. Figure taken from [110]

The outcome of the measurement was two-sided: on the one hand, the production of an impurity, identified as CO_2 thanks to the mass spectrometer, was observed with the GC when the RPCs were flushed with Ar and the high voltage was switched on. On the other hand, thanks to the ISE, the production of fluorinated compounds was observed when the high voltage was switched on. The first observation may be explained by considering the ionic current conduction model in linseed oil, hypothesized by Va'vra in [113]. This is supported by the fact that the measured CO_2 concentration in the output gas is directly proportional to the circulating current. The second observation can be linked to the detachment of fluorinated compounds from the inner surfaces of the RPCs thanks to the action of the Ar plasma. This hypothesis is supported by the fact that no fluorinated compounds were present if the high voltage was not switched on. Moreover, no F^- ions were observed in the input gas. Figure 2.20 shows the two res-

ults just described. The left panel shows the correlation between current and CO_2 concentration, while the right one shows the F^- ion production (expressed in ppm/h), as a function of the integrated charge during the Ar plasma test.

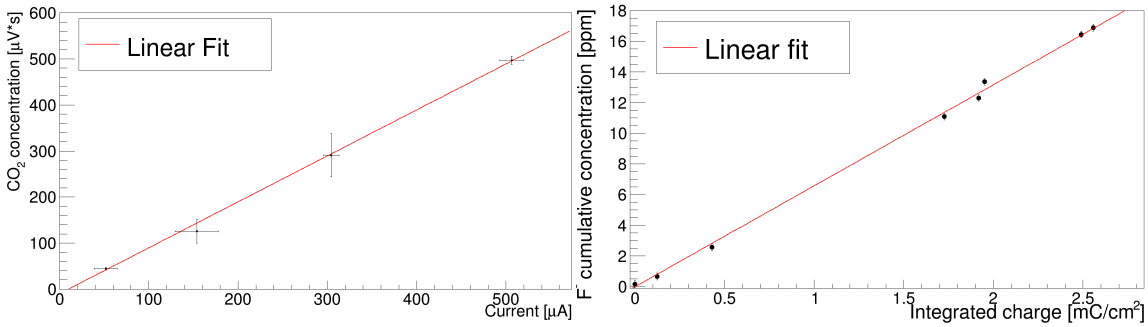

Figure 2.20: Left panel: trend of CO_2 concentration as a function of the current. Right panel: trend of F^- ions production as a function of the integrated charge during the Ar plasma test. In both cases the RPCs were flushed with Ar. Figures taken from [110]

The F^- ions production does not seem to decrease, meaning that, potentially, if one continues to maintain a plasma in the RPCs, more fluorinated impurities would be detached and removed by the gas flow; this could not be done due to time constraints. The dark current was compared to the values before the Ar plasma test and no significant reduction was measured for any chambers, neither for the two detectors where the plasma was created nor for the ones that were simply flushed with Ar. The observations regarding CO_2 and F^- ion production are indeed interesting and would deserve further studies, but it remains an open question to which extent they are related to the observed dark current increase.

Chapter 3

The search for an eco-friendly gas mixture for RPCs

This chapter is meant to provide an introduction to the main subject of this thesis, i.e., the search for an eco-friendly gas mixture for RPC detectors, and specifically for the RPCs of the ALICE muon identification system (MID). As already mentioned at the beginning of Chapter 2, the goal is to find an eco-friendly replacement for the gas mixture of these detectors by the start of the LHC RUN4 (foreseen in 2029). Section 3.1 describes why this subject is a hot topic for RPC communities (not only) at CERN. Section 3.2 provides a description of the current state of the art in the search for eco-friendly gas mixtures for RPC detectors; it contains a summary of recent studies carried out by the ALICE group in Turin, and also a brief overview of the work carried out by other groups. Section 3.3 introduces the ECOgas@GIF++ collaboration, since most of the work described in the following was carried in the context of said collaboration. The ECOgas@GIF++ was born as a joint effort among the LHC experiments and the CERN detector technologies group, to share knowledge and means in the search of eco-friendly gas mixtures for RPC detectors.

3.1 F-gases emissions at CERN

As discussed in Chapter 2, RPC detectors are usually operated with a gas mixture that contains a high fraction of fluorinated gases (F-gases), mainly *1,1,2,2-tetrafluoroethane* ($C_2H_2F_4$), also known as R134a or simply *freon*, and *sulfur hexafluoride* (SF_6). As mentioned in 2.2.4, such gases pose a serious environmental threat due to their negative impact on global warming. Indeed, new European Union regulations[94] have set the ambitious goal to reduce non-CO_2 emissions (including F-gases) by 80%, with respect to 1990 levels, by the year 2050. Different strategies have been adopted to move

in this direction but, without a doubt, the most efficient one is to impose a progressive phase-down of the F-gases production and placement on the market. Although research facilities are currently exempt from this type of regulation, the global phase-out of these gases has already caused an increase of their price and a reduced availability[114], making the search for more eco-friendly alternative a priority for a number of gaseous detectors, and in particular for RPCs.

In 2020, CERN has published its second environment report[115], providing a comprehensive description of the environmental impact of all the activities carried out in the laboratory. The section regarding F-gases emissions is divided into three scopes: scope one contains the direct emissions from the experiments (detectors and cooling systems), scope two reports the indirect emissions due to the generation of electricity, heating/cooling and, last, scope three comprises other indirect emissions, such as catering, commutes and official travels of personnel.

It is customary to quantify the emissions of any greenhouse gas using the *CO_2 equivalent*. This metric is based on the concept of Global Warming Potential (GWP, introduced in Section 2.2.4) and it can be calculated by multiplying the amount of gas expelled in the atmosphere (usually expressed in tonnes) by its GWP. Figure 3.1 shows the CERN CO_2 equivalent consumption as reported in the second environment report.

As it can be clearly seen in the right panel of Figure 3.1, RPCs (main subject of this thesis) are the detectors which contribute the most to these emissions, mainly due to leaks at the detector level. Some of the leaks cannot be repaired, due to physical inaccessibility of the RPCs inside the experiments. In absolute terms, the emission by CERN is comparable to the one by a medium-size industry. Despite this consideration, the reduction of F-gases consumption is advisable, to align to the new EU regulations. A few solutions have been explored for the short-term operation of the detection systems[117] and they mostly consist in a reduction of the amount of used gas but they don't foresee a complete abandonment of F-gases. One possibility is to optimize the current technology, for example by improving the gas re-circulation systems. The main concern with this approach is that re-circulation of the gas mixture requires a very efficient purification system, to filter out all the impurities that are created in the gas when it interacts with the radiation. This is not easy and, at the same time, one cannot recirculate 100% of the gas and a certain fraction of fresh gas will always be needed, for example to compensate leaks. Another approach is the one of gas recuperation, meaning that the gas mixture exiting from the

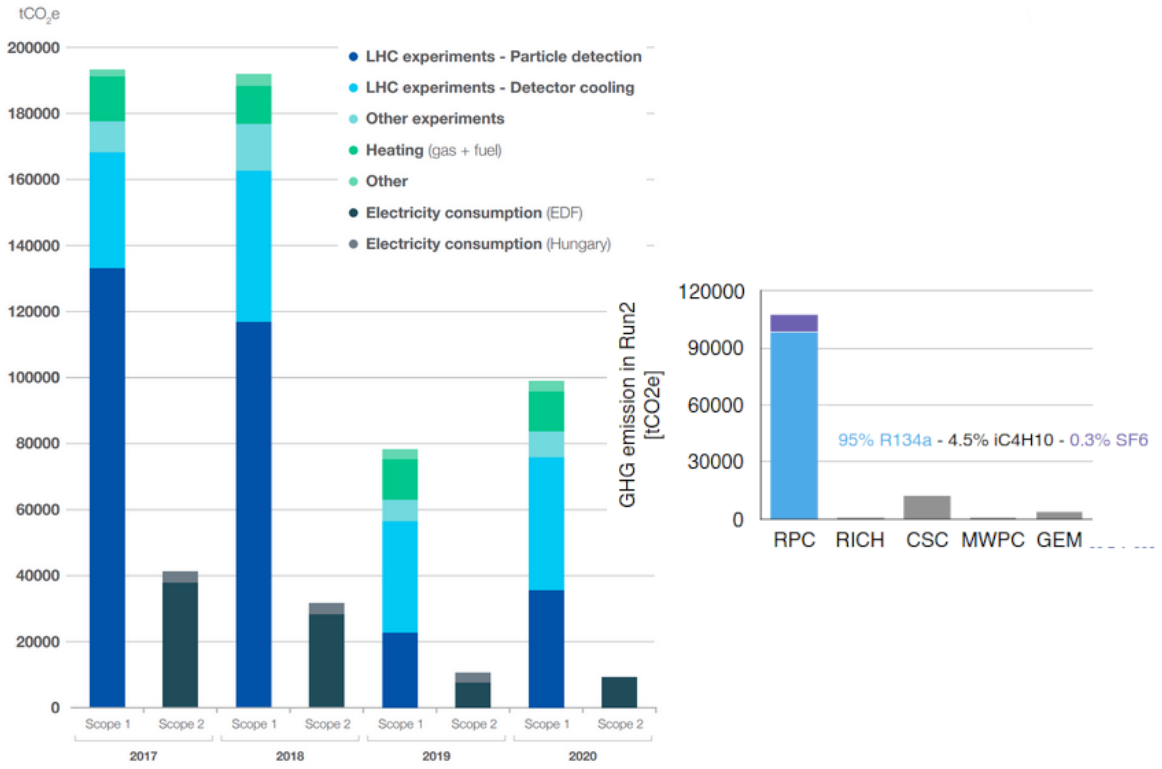

Figure 3.1: Left panel: CERN CO_2 equivalent gas consumption from scope one. Figure taken from [115]. Right panel: detailed emission levels from different detection system at CERN. Figure taken from [116]

detectors is recovered and its components are separated and reused. This solution is even harder than re-circulation and the yield is very low, making it costly and far from perfect, since the procedure to separate the individual components cannot be fully optimized due to the chemistry of the gases in the mixture[117]. These two solutions may yield acceptable results in the short-term but, as outlined, they are costly, not perfect, and could lead to issues in the detector operation (for example due to the presence of non-filtered pollutants in the recycled gas mixture). More fundamentally, they would still rely on the availability of F-gases on the market. A third, more radical approach is to find a new, more eco-friendly gas mixture, where at least R134a is replaced by a different gas, while preserving performance and long-term detector stability. This approach is discussed in detail in the next section.

3.2 State of the art

Many laboratory studies have started in the direction of finding an eco-friendly alternative for RPC detectors[118–120]. They focus on the replacement of the main contributor to the mixture GWP, that is R134a. Although some

more recent investigations have also addressed SF_6[121], the search for an alternative this crucial gas is still in a primordial stage and will not be discussed further in this thesis.

Possible candidates for the replacement of R134a have been identified in the family of the *hydrofluoroolefins* (or HFO) gases. These are chemically very similar to R134a but with a much lower GWP ($\sim$ 6, vs 1488 for R134a). Among those gases, the 2,3,3,3-tetrafluoropropene (HFO-1234yf) and 1,3,3,3-tetrafluoropropene (HFO-1234ze) are of particular interest, given their employment in the refrigeration industry, leading to widespread availability and relatively low cost. Between the two, HFO-1234ze was chosen, since the yf allotrope is reported to be mildly flammable (reason of concern for the experiment safety). Figure 3.2 shows the 3D chemical structure of the R134a (left) and HFO-1234ze (right). The grey circles represent the carbon atoms, the light green ones fluorine and the white ones hydrogen.

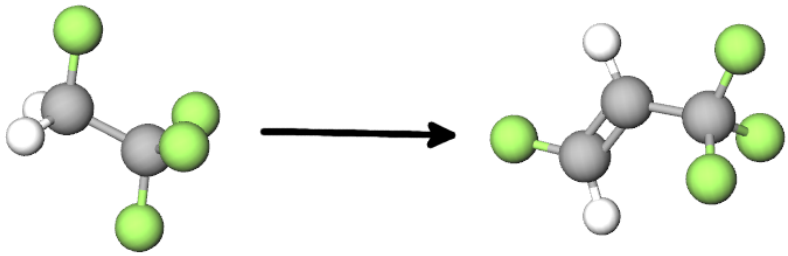

Figure 3.2: Left: R134a molecule ($C_2H_2F_4$). Right: HFO-1234ze molecule ($C_3H_2F_4$). The arrow symbolizes the transition from one molecule to the other

Some results of the studies of full replacement of R134a with HFO-based gas mixtures will be illustrated in the following. They are organized in two subsections: the first one describes the results obtained by the ALICE group, while in the second one studies from other groups (mainly from the ATLAS collaboration) will be summarized. The main difference between the ALICE studies and those of other groups is the i-C_4H_{10} content of the tested gas mixtures. Indeed, as previously shown in Section 2.3, the current ALICE gas mixture contains a higher i-C_4H_{10} fraction with respect to the gas mixture employed in ATLAS and CMS[122], and this feature was propagated to the choice of the first eco-friendly mixtures to be explored.

3.2.1 Preliminary studies on HFO-based gas mixtures

Ideally, one would take the standard gas mixture and fully replace the R134a with the HFO. Such a strategy was shown to be unfeasible, mainly because the HFO has a lower first Townsend coefficient, with respect to R134a[123],

hence the working voltage for a 2 mm gas gap detectors would be above 15 kV (against the current 9.5-10 kV). This would pose too strict requirements on the quality of the inner electrode surface, as even the slightest imperfection would become a source of noise counts and extra-current. Also, the currently employed high voltage infrastructure (cables, connectors and so on) was not designed to support such a high voltage. Hence, the working point has to be reduced. A possible solution would be to introduce in the mixture a gas that acts as place-holder, meaning that it does not actively take part in the charge multiplication process, but it has the effect of reducing the partial pressure of HFO in the mixture, thus reducing the detector working voltage[124].

3.2.1.1 Search for eco-friendly gas mixtures in ALICE

References [120] and [125] present the results of studies carried out in the framework of the ALICE experiment. In these works, the performance of an ALICE-like RPC prototype (50x50 cm^2 single gap RPC, with 2 mm thick bakelite electrodes and 2 mm gas gap), flushed with various HFO-based gas mixtures have been studied and compared with the ALICE standard gas mixture (89.7% $C_2H_2F_4$, 10% i-C_4H_{10} and 0.3% SF_6). In particular, the dilution of HFO with different atmospheric gases (such as O_2, N_2, Ar and CO_2) was studied, using a cosmic-ray telescope at the Turin INFN laboratory. The RPC response was studied using the new ALICE MID front-end electronics (FEERIC[111]), to compute the RPC efficiency and cluster size. The discrimination threshold was set to $\sim$ 130 fC, to be in line with the value used for tests carried out during the ALICE data taking between 2015 and 2018, aimed at validating the new front-end electronics[126]. At the same time, the readout strips were coupled to an oscilloscope, allowing the authors to also perform signal shape and streamer contamination studies. In these studies, all the signals with amplitude above 18 mV (over 50 Ω at the oscilloscope input) are classified as streamers.

Figure 3.3 shows the comparison of the efficiency and streamer contamination curves for the ALICE standard gas mixture and a mixture composed by pure HFO. When the ALICE standard gas mixture is used, the efficiency plateau is reached at $\sim$ 9.8 kV, and the corresponding streamer probability is $\sim$ 5% (black curve). For what concerns pure HFO, instead, the efficiency does not show any sign of growth up to 14 kV (meaning that the detector working point is at higher voltages).

The first step taken to lower the working point was to dilute the HFO

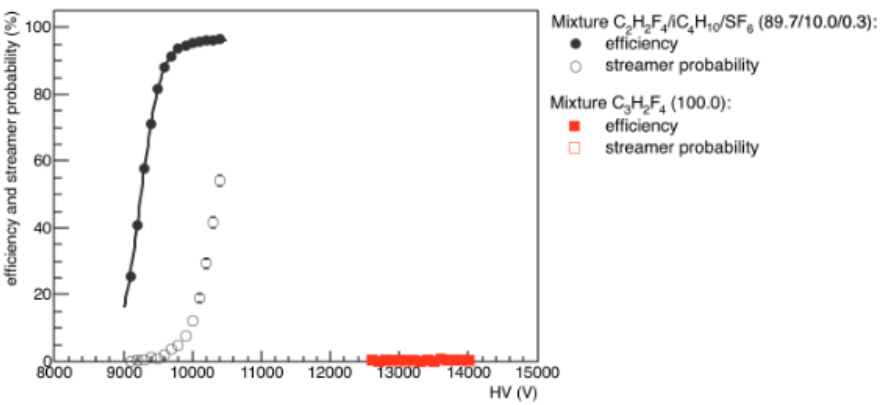

Figure 3.3: Efficiency and streamer contamination curves for the ALICE standard gas mixture (in black) and for pure HFO (in red). Figure taken from [125]

with some atmospheric gases. In particular, mixtures composed by 45% HFO, and remaining fraction by either O_2 or N_2 or Ar were tested. The efficiency and streamer contamination curves for these mixtures are shown in Figure 3.4, where the desired reduction of the working point can be clearly observed. In detail, the working point for the mixture containing 55% Ar (in red in Figure 3.4) is $\sim$ 200 V lower with respect to the ALICE standard gas mixture. For the mixtures containing O_2 and N_2 (in green and blue respectively) the working point is lower than pure HFO but it is, respectively, 1 kV and 1.5 kV higher with respect to the ALICE standard gas mixture. The bottom panel of Figure 3.4 shows the trend of the streamer fraction for the mixtures listed above: streamer suppression is bad for all the HFO-based mixtures. In detail, the streamer fraction at the working point is $\sim$ 80%, while it is $\sim$ %5% with the ALICE standard gas mixture.

Measurements of the prompt charge were also carried out and it was reported that, for the ALICE standard gas mixture, the average prompt charge (at the detector working point) is $\sim$ 2.6 pC. For the HFO-Ar and HFO-N_2 mixtures, the value increased up to $\sim$ 66 and $\sim$ 68 pC. It was reported to be lower for the O_2-diluted mixture, at a value of $\sim$ 36 pC. When the detector was operated with a high O_2 fraction, current instabilities were observed over a short time span (few hours). The high charge content, coupled with these instabilities, makes these gases not suitable for RPC operation, so the attention was shifted to another atmospheric gas, CO_2. Different concentrations of HFO and CO_2 have been tested and the results are shown in Figure 3.5.

In the top panel, the efficiency curves for three different mixtures are shown (ratio of 45/55, 50/50 and 55/45 HFO/CO_2). Two clear observations can be inferred by looking at those curves: first, the efficiency curve for

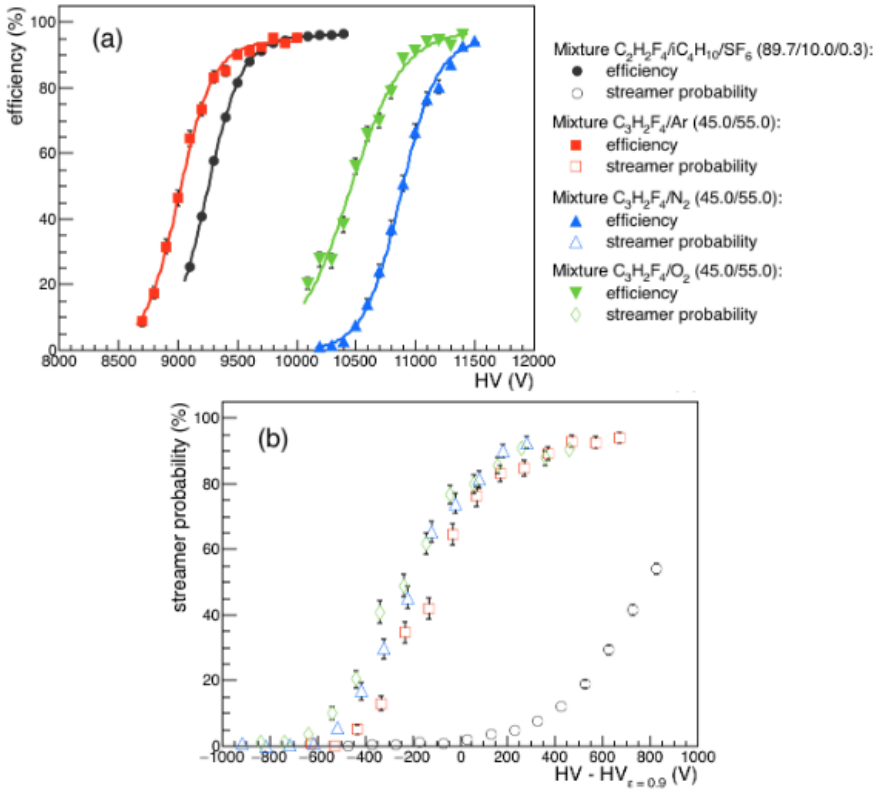

Figure 3.4: Top panel: Efficiency curves for gas mixtures containing 45% HFO and 55% O_2 or N_2 or Ar, and for the ALICE standard gas mixture. A 200 V decrease of the working point if Ar is used as place-holder is observed, while a 1-1.5 kV increase is seen if O_2 or N_2 are employed. Bottom panel: streamer contamination curves for the same mixtures described above. No significant difference among the mixtures but higher streamer fraction with respect to the ALICE standard gas mixture (in black) can be observed. Figure taken from [125]

the mixture with the lowest HFO concentration is shifted by 1 kV to higher voltages, with respect to the ALICE standard gas mixture; second, increasing the HFO concentration has the effect of shifting the working point to higher voltage, by roughly 1 kV every 10% added. From the bottom panel of Figure 3.5, it is possible to see that the same HFO addition has the effect of lowering the streamer contamination ($\sim$ 55% at working point if the mixture with 55% CO_2 is considered). The average prompt charge per hit, with this mixture, is $\sim$ 27 pC, still an order of magnitude higher than the with the standard gas mixture but much lower than the previously described mixtures. Also, no current instability was observed when CO_2 was employed. All these observations make CO_2 the most promising candidate as a place-holder gas. To improve the streamer suppression in the HFO-CO_2 gas mixtures, the addition of different fractions of i-C_4H_{10} and SF_6 has also been studied. It is well known (as reported in Section 2.2.4), that i-C_4H_{10} has a high photon-absorption cross section, so it acts as a quenching gas, absorbing the photons generated by atom de-excitation or ion-electron recombin-

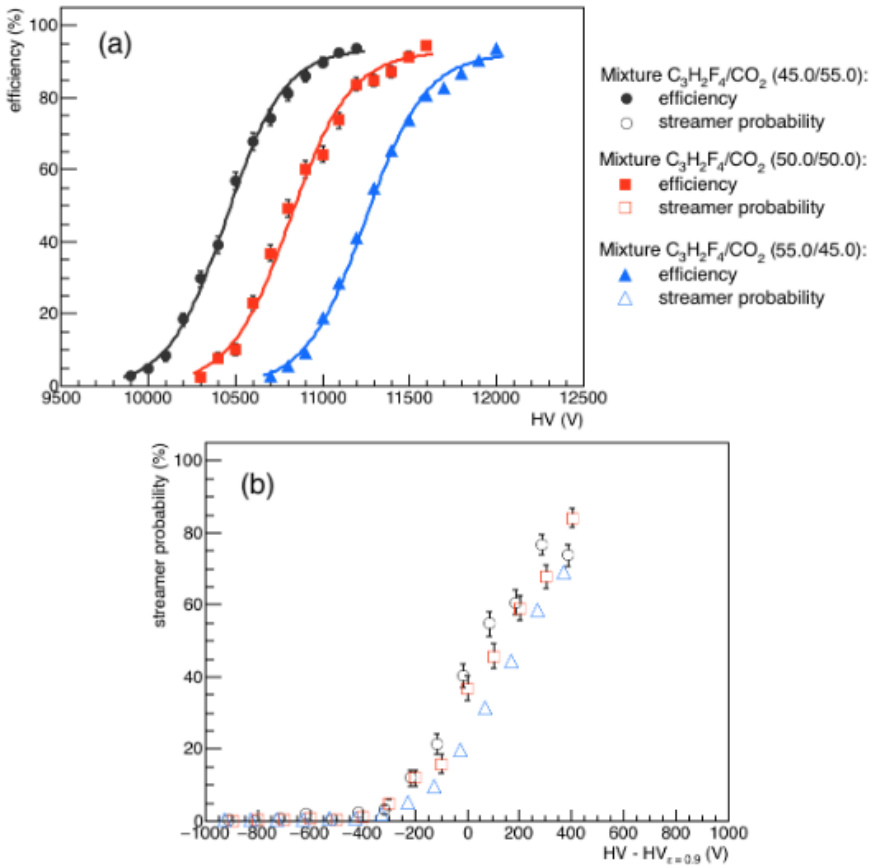

Figure 3.5: Top panel: efficiency curves for gas mixtures containing varying fractions of HFO and CO_2. An increase of the working point by roughly 1 kV every 10% of HFO added is observed. Bottom panel: streamer contamination curves for the same mixtures described above. An increase of the streamer suppression is observed if the HFO concentration is increased. The streamer suppression is still much lower than the one of the ALICE standard gas mixture. Figure taken from [125]

ations in the gas. SF_6, thanks to its high electron attachment coefficient, can absorb free electrons in the gas, reducing the avalanche size both in terms of charge (hence increasing streamer suppression) and spatial development.

The HFO concentration was kept at 45% and different fractions of i-C_4H_{10} and CO_2 were added to the mixture. The iso-butane concentration was varied from 0 to 30% and the effects of this process are shown in Figure 3.6. In terms of efficiency (top panel), no clear behavior emerges if the isobutane is in the range 0 - 10%, but going from 10 to 20%, produces a shift to higher voltages by $\sim$ 600 V in the efficiency plateau. The streamer contamination at the working point (shown in the bottom panel of the figure) decreases from 40% (if 0 or 5% isobutane is added to the mixture) to 20% if more than 10% isobutane is added to the mixture.

The role of SF_6 was studied as well, using a mixture of HFO and CO_2. The results of the addition of 1% SF_6 to a mixture of 50% each HFO and

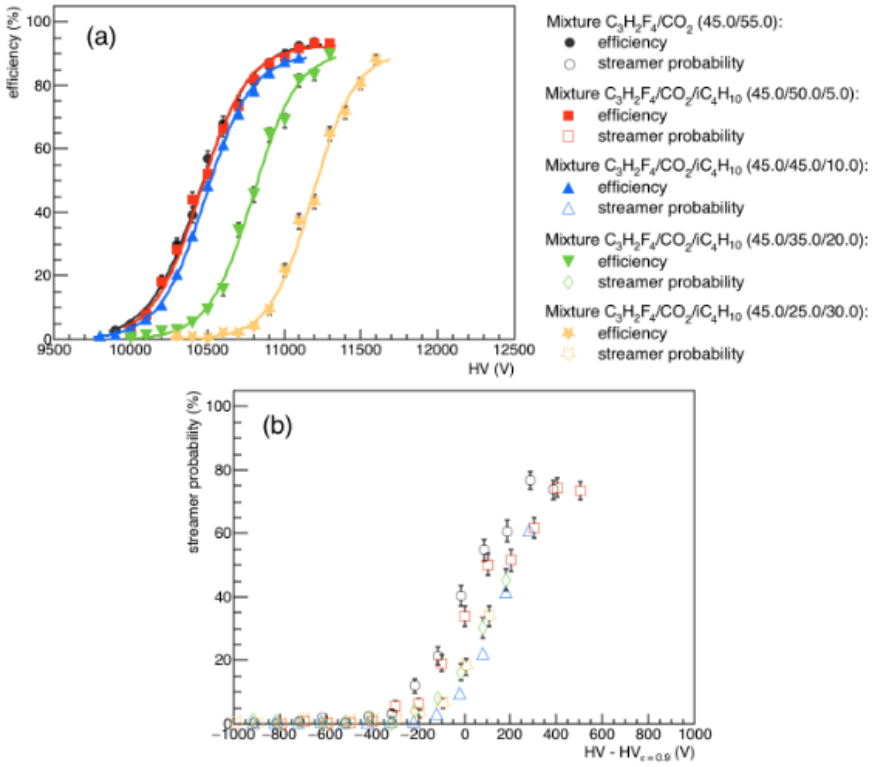

Figure 3.6: Top panel: efficiency curves for gas mixtures containing varying fractions of i-C_4H_{10} and CO_2 (HFO concentration is fixed to 45%). A shift of $\sim$ 600 V is observed if the isobutane fraction is increased from 10 to 20%. Bottom panel: streamer contamination curves for the same mixtures described above. An improved streamer suppression is observed if the isobutane concentration is increased. Figure taken from [125]

CO_2 are reported in Figure 3.7. This addition has the effect of shifting the efficiency plateau by 1 kV towards higher voltages and, at the same time, to reduce the streamer contamination down to 5% at the working point. Also, the average prompt charge per hit, at working point, is lowered to $\sim$ 4 pC (recall that for the ALICE standard gas mixture, this figure is $\sim$ 2.6 pC and for a mixture of 50% HFO and 50% CO_2 it is $\sim$ 33 pC). These figures are comparable to the performance of the ALICE standard gas mixture. The issue is that the working point is shifted by $\sim$ 2 kV to higher voltages and this is not advisable, due to the constraints posed by the current detector technology and high voltage infrastructure, as outlined in Section 3.1.

In summary, this study showed the response of a single gap RPC, operated with different HFO-based gas mixtures, containing different gases as place-holders. Among those, CO_2 was shown to be the most promising one, in terms of current stability and charge released in the gap. The addition of i-C_4H_{10} and SF_6 to the mixture also showed very encouraging results in terms of streamer suppression and released charge. Systematic studies in which the ratio between the four components of the mixture was varied

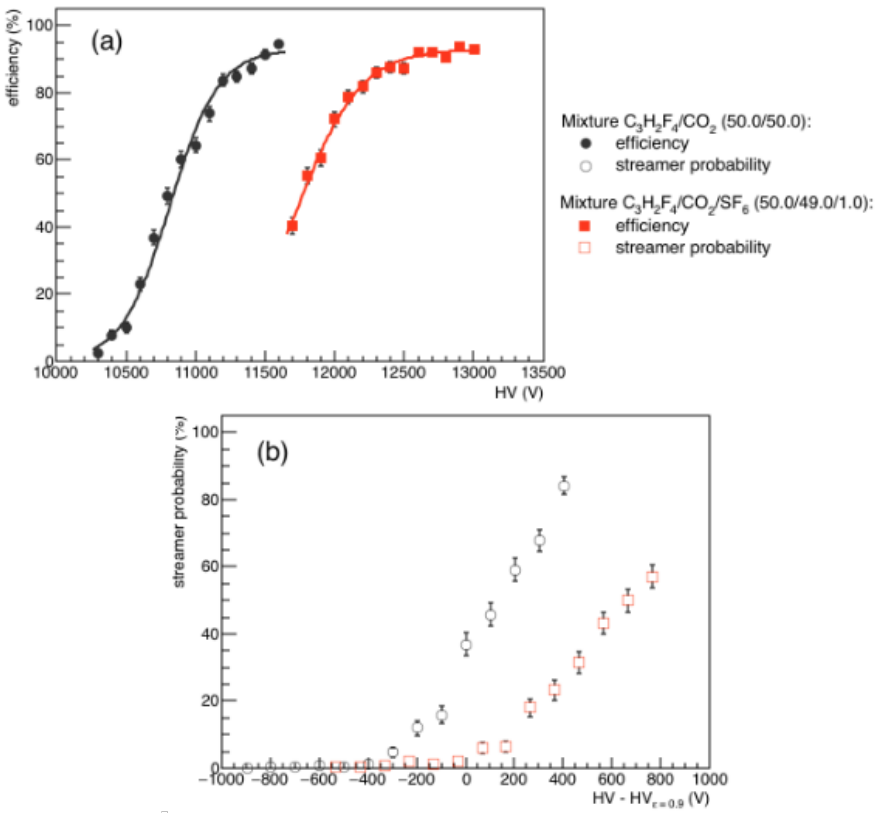

Figure 3.7: Top panel: Efficiency curves for a gas mixture based on HFO and CO_2, with and without SF_6. Adding 1% SF_6 shifts the working point by $\sim$ 1 kV towards higher voltages. Bottom panel: streamer contamination curves for the same mixtures described above. The SF_6 addition greatly lowers streamer contamination, down to $\sim$ 5% at working point. This is compatible with the ALICE standard gas mixture performance. The working point is almost 2 kV higher with respect to the standard gas mixture. Figure taken from [125]

two at the time can be found in Reference [120]. The two most promising gas mixtures that were pinpointed by these studies are composed as follows: 50% CO_2, 39.7% HFO, 10% i-C_4H_{10}, 0.3% SF_6 and 50% CO_2, 39% HFO, 10% i-C_4H_{10}, 1% SF_6. Their GWPs are respectively 72 and 232 (to be compared against the current 1400 of the ALICE standard gas mixture). The behavior of the RPC under test, when flushed with these two mixtures, is shown in Figure 3.8. One can see that for the mixture with lower SF_6 content, the working point is close to the one obtained for the ALICE standard gas mixture but the streamer probability (shown in the bottom panel of the figure) is much higher with respect to the standard gas mixture ($\sim$ 12% at HV-$HV_{\epsilon=0.9}$ of $\sim$ 200 V). The gas mixture with a higher SF_6 content, instead, shows a shift of the working point towards higher voltages but, at the same time, also a greater streamer suppression (lowering the streamer contamination to $\sim$ 6%). Similarly to the R134a-based gas mixtures, SF_6 seems to be playing a key role in streamer suppression in HFO-based gas mixtures, with

the addition of CO_2.

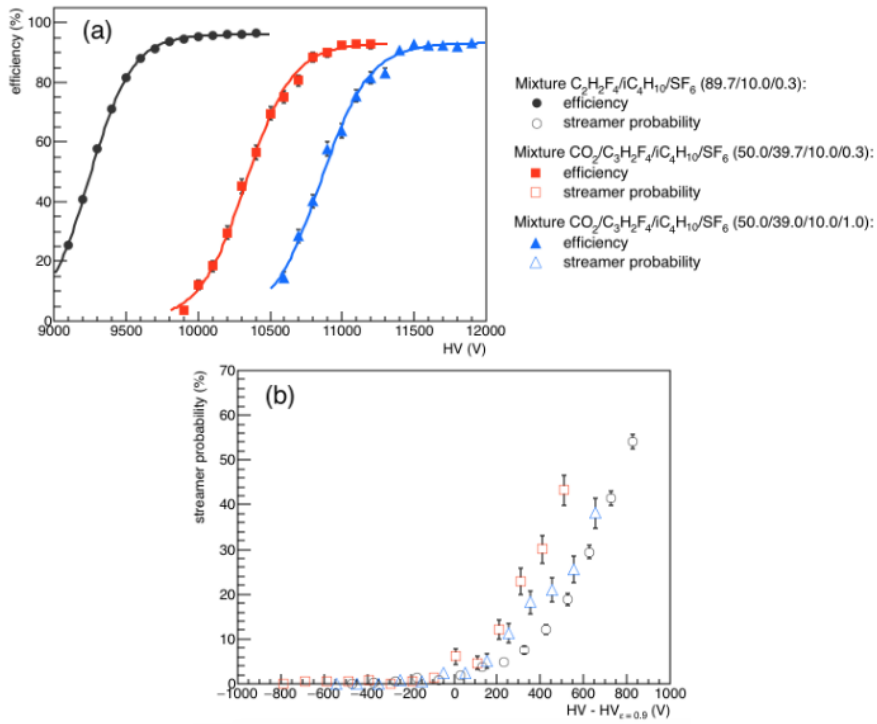

Figure 3.8: Top panel: efficiency curves for the two most promising HFO-based gas mixtures pinpointed by the ALICE group. With a lower SF_6 content the working point is closer to the one obtained with the ALICE standard gas mixture. Bottom panel: streamer contamination curves for the same mixtures described above. Increasing the SF_6 concentration to 1% decreases significantly the streamer contamination at working point, from $\sim$ 12 to $\sim$ 6%. This value is similar to the one obtained with the ALICE standard gas mixture. Figure taken from [120]

3.2.1.2 Search for eco-friendly gas mixtures in other groups

The results discussed in the previous section have shown how two promising HFO-based gas mixtures, with the addition of CO_2, have been found in the context of the ALICE collaboration. However, the i-C_4H_{10} concentration was kept at 10%. A mixture with a higher isobutane content (classified as flammable) can be employed in the ALICE experiment since all the 72 RPCs of the muon identification system can be easily accessed (unlike the ones in the other LHC experiments) and any gas leak can be repaired. For the other LHC experiments, such as ATLAS and CMS, the use of a flammable gas mixture is not advisable. The RPCs in those experiments are operated with a different gas mixture, composed as follows: 95.2% R134a, 4.5% i-C_4H_{10} and 0.3% SF_6[122]. The following section will report some of the preliminary results obtained using gas mixtures with a reduced isobutane content (5%). In particular, part of the studies performed by the ATLAS collaboration and reported in Reference [127] are summarized here.

In this work, a small ATLAS-like RPC prototype (57 x 10 cm^2, 2 mm gas gap and 1.8 mm thick bakelite electrodes) was tested using cosmic muons. The signal, without amplification, is read out on both sides of a single strip, using an oscilloscope. One of the two signals is acquired with the maximum scope sensibility, to optimize the avalanche studies, while the other is readout with a variable scale in the oscilloscope, to study the streamers (acquisition window: 200 ns in both cases). Furthermore, the ionic signal (which gives the best estimate of the total charge released in the detector) is also acquired, using a 10 kΩ resistor connected to the ground graphite electrode (acquisition window: 100 μs). The cosmic trigger is provided by the coincidence of four RPCs and a 1 mm-gap RPC is used as a confirmation signal for the efficiency measurements.

These studies report, together with efficiency measurements, three different charge values, defined as follows: avalanche charge (integral in the 10 ns window around the first peak that crosses the threshold), total prompt charge (integral in the last 180 ns interval, first 20 ns are used to estimate the RMS of the signal) and ionic charge (integral of the last 80 μs of the long acquisition window, the first 20 μs are used for noise calculation).

These studies have shown how, for the HFO-based gas mixtures, a great fraction of events are characterized by multi-avalanche signals, shown in the right panel of Figure 3.9 (next to an example of single avalanche signal). For this reason, the term *extra-charge* probability is introduced and used, rather than streamer probability or contamination.

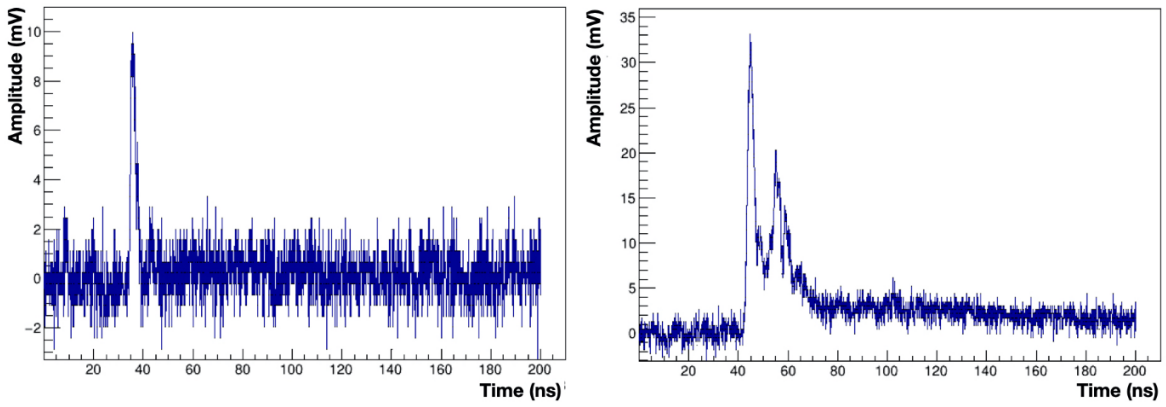

Figure 3.9: Left panel: example of single avalanche signal. Right panel: example of a multi-avalanche signal, identified as *extra-charge*. These signals also include the events usually classified as streamers. Figure taken from [127]

In the main study reported in [127], the i-C_4H_{10}/SF_6 fractions were kept constant at 5% and 1% respectively, while three different sets of HFO and CO_2 fractions were tested: 38%/56%, 33%/61% and 28%/66%. The i-C_4H_{10}

and SF_6 fractions were chosen following preliminary studies, also reported in [127]. These show that changing the isobutane concentration has the only effect of moving the detector working point, while it does not have any effect on the total charge delivered at working point and on the avalanche/extra-charge separation. Hence, the smallest possible isobutane fraction was preferred to grant the non-flammability of the gas mixture.

Figure 3.10 shows the results obtained with the three mixtures discussed above.

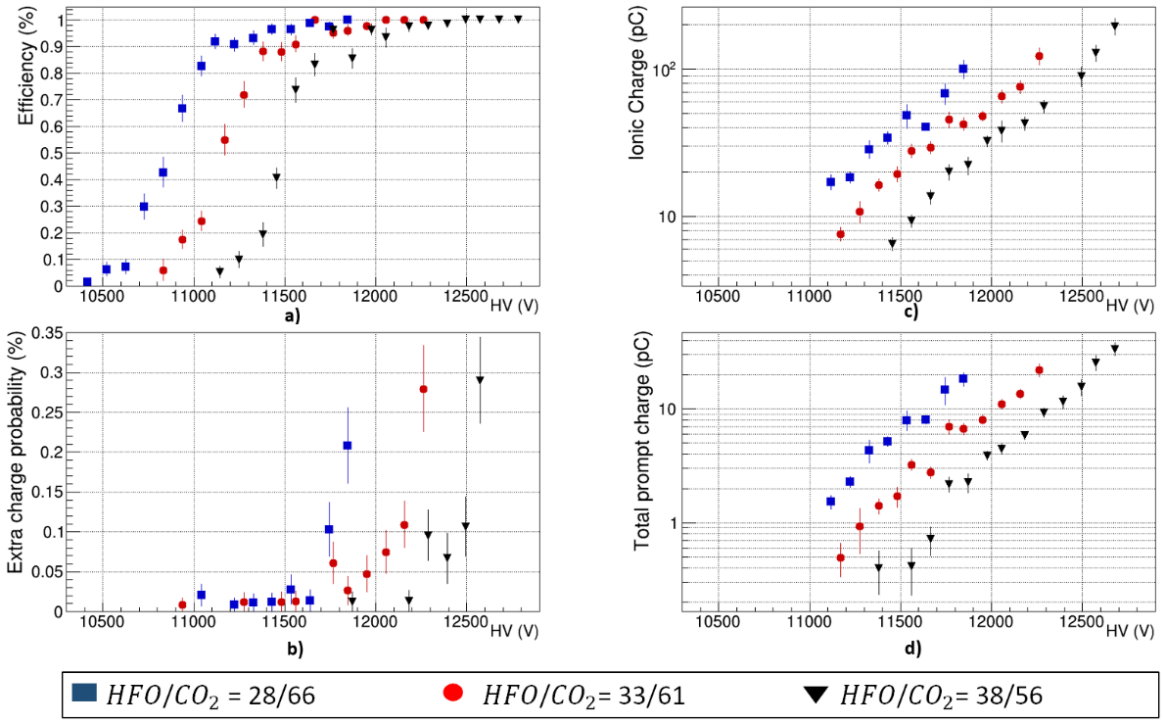

Figure 3.10: a) Efficiency curves for the three tested gas mixture; increasing the HFO concentration shifts the working point towards higher voltages (∼ 400 V every 5% HFO) **b)** Extra-charge probability as a function of high voltage; the extra-charge contamination is smaller for mixtures with higher HFO content **c)** Ionic charge as a function of the high voltage; the value at working point is greater for the gas mixture with higher HFO concentration **d)** Prompt charge as a function of the high voltage; the value at working point is compatible among the mixtures. Figure taken from [127]

.

Panel a) shows the efficiency curve for the three mixtures tested. As highlighted also in [125], the reduction of the HFO content lowers the detector working point (in this case by ∼ 400 V every 5%). Panel b) shows the extra-charge contamination and one can see that it becomes smaller for the mixtures with a greater HFO content, pointing to a larger separation between avalanche and extra-charge events in this mixture. The ionic charge, shown in panel c), seems to be larger for the mixture with higher HFO content (∼ 30 pC versus ∼ 20 pC for the other two) while the total

prompt charge for the three mixtures (shown in panel d), seems to be similar at working point (11.3, 11.7 and 12 kV for increasing HFO content respectively) and it is around $\sim$ 3 pC. These results have to be compared to the ones obtained with the standard ATLAS gas mixture, also reported in [127], which show a total avalanche charge and ionic charge, at the working point, of $\sim$ 2 and 15 pC respectively. The studies by the ATLAS group, just discussed above, have shown how HFO-based gas mixtures with lower isobutane content with respect to the ones described in References [120, 125] also yield promising results in terms of detector performance.

3.3 The way forward

The works described above showed how promising HFO-based gas mixtures, with the addition of CO_2, i-C_4H_{10} and SF_6, have been found and how RPCs operated with them have shown satisfactory results when exposed to cosmic rays. The next steps, in the search for eco-friendly gas mixtures, foresees the study of detector performance in more controlled environments, such as in beam tests. Indeed, a collimated charged-particles beam, with known direction and energy, provides a cleaner data taking environment, rather than the cosmic muons. Furthermore, it allows one to collect a high amount of signals in a shorter amount of time, increasing the available statistics for detailed studies, e.g, of the signal shape and amplitude. Together with this, one should also investigate the rate capability of the detectors, that is the study of the detector response when operated in a high background environment (as is the case in the LHC experiments). Moreover, the study of the long-term stability of the detectors, when operated with these new gas mixtures, has to be carried out. This can be done by means of an aging test, where the detectors are exposed to a higher particle flux than what they are expecting to face when operated in the experiments, allowing one to simulate many years of operation in a shorter time span and to monitor their stability.

This thesis presents, in Chapters 4 and 5, the results of the first beam and aging tests ever carried out on these new eco-friendly gas mixtures. Since this kind of studies is of interest for all the LHC experiments, members of the ALICE, ATLAS, CMS, LHCb collaborations and of the CERN detector technologies (EP-DT) group decided to launch a common R&D program, giving birth to the ECOgas@GIF++ collaboration. The idea behind this collaboration is to have a common experimental setup installed at the CERN Gamma Irradiation Facility (GIF++)[128], where both the beam tests and aging stud-

ies can be carried out. Each of the groups provided one or more prototype detectors, to be installed on the common setup, sharing the infrastructures for gas, high voltage, monitoring and data acquisition. In this approach, the cost (both in terms of manpower and money) is reduced and, last but not least, the exchange of knowledge, experience and ideas in a collaborative environment is facilitated.

Following the main findings of the preliminary works cited in this chapter, the strategy adopted by the collaboration is to fully replace the R134a with various combinations of HFO and CO_2 as placeholder gas. Different mixtures have been proposed and tested, both for what concerns their performance in beam tests and their aging properties. The results shown in this thesis will be focused mainly on the RPC of the ALICE group but a brief description of the other RPCs will be provided, and, when needed to complete the discussion, results obtained with other RPCs will be reported.

Chapter 4

Beam test studies at the CERN Gamma Irradiation Facility

This chapter contains the description of the beam tests that have been carried out with HFO-based gas mixtures at the CERN Gamma Irradiation Facility (GIF++) and it is organized as follows. Section 4.1 contains a brief introduction to the beam test and describes the different gas mixtures that have been tested. Section 4.2 describes the GIF++, focusing on its gamma source and muon beam. Section 4.3 contains a description of the experimental setup: the detectors employed, the services (gas, high voltage), the logic behind the trigger creation and, last, the data acquisition systems employed when the new ALICE MID front-end electronics (FEERIC) were used to discriminate the RPC signals, and when the readout strips were coupled directly to a digitizer, to perform signal shape and charge analyses. The rationale behind this choice is explained and also the complementary aims of these two operation modes are listed in the same section. Finally, the results of all the measurements are reported in Section 4.5, which features three subsections: 4.5.1 introduces the measured quantities and the corresponding data analysis strategy, describing mixtures with a lower working point with respect to the standard gas mixture, while 4.5.2 describes the results obtained with mixtures that exhibit a higher working point with respect to the standard gas mixture; a specific subsection (4.5.3) is devoted to the discussion of the mean charge per hit for all the mixtures under test. Finally, a comparison between all the mixtures tested is carried out in Section 4.6.

4.1 Beam test studies with eco-friendly gas mixtures

Section 3.2 showed how promising HFO-based gas mixtures for RPC detectors have been pinpointed by various laboratory studies with cosmic rays, and that it is now necessary to refine the knowledge on these mixtures by performing performance studies in more controlled environments, such as beam tests. With respect to cosmic ray studies, a beam test provides a series of advantages: precise timing, higher particle rate (reducing the data taking duration for a given statistical uncertainty), control over the particle direction and energy and overall a much cleaner data taking environment. When coupled with the GIF++ photon source, the beam test also allows one to study the detector performance under different levels of counting rate.

The beam test studies discussed in this chapter have been carried out in the context of the ECOgas@GIF++ collaboration and their aim was to fully characterize a series of eco-friendly gas mixtures in terms of detector response, by studying the efficiency, cluster size, average charge per hit, prompt charge, time resolution, and rate capability.

4.1.1 Gas mixtures tested

A total of 7 eco-friendly gas mixtures, based on HFO with the addition of CO_2 as place-holder, were tested. Table 4.1 reports the composition of the various mixtures studied, with an extra column, called *Readout*, which shows which data taking approach was used for a given mixture. The readout was performed either with the FEERIC front-end electronics, coupled with a TDC (4.3.4), or with a digitizer, directly coupled to the RPC strips (4.3.5). For some of the mixtures in the table both methods have been adopted. The value of GWP for each mixture is also reported in another column of the table.

The names of the mixtures have been chosen according to the order in which they have been tested. Different mixtures have different HFO and CO_2 fractions, while the fractions of i-C_4H_{10} and SF_6 were kept constant. This was done in order to study the possible interplay between HFO and CO_2, since they are the new gases in the mixture and their interaction is not yet fully understood. Notice also that the mixture called MIX5 corresponds to the mixture that will be referred to as "ECO2" in Chapter 5. A different naming convention has been adopted in beam and aging studies simply due to an internal decision of the collaboration.

Mixture	$C_2H_2F_4$ %	HFO %	CO_2 %	i-C_4H_{10} %	SF_6 %	GWP	Readout
STD	95.2	0	0	4.5	0.3	1488	TDC, Digitizer
MIX0	0	0	95	4	1	730	Digitizer
MIX1	0	10	85	4	1	640	Digitizer
MIX2	0	20	75	4	1	560	Digitizer
MIX3	0	25	69	5	1	529	TDC, Digitizer
MIX4	0	30	65	4	1	503	Digitizer
MIX5	0	35	60	4	1	482	TDC, Digitizer
MIX6	0	40	55	4	1	457	Digitizer

Table 4.1: Composition of the different mixtures tested in beam periods, together with their GWP and the readout method employed

According to the definition provided for example in [94]: *"The GWP of a mixture is calculated as a weighted average, derived from the sum of the weight fractions of the individual substances multiplied by their GWP, unless otherwise specified, including substances that are not fluorinated greenhouse gases".* Since the percentages reported in Table 4.1 are fractions of volume, and not weight, one has to perform the conversion before calculating the GWP. To do so, one should consider 1) The molecular weight of the gases (in g/mol) and their GWP, both reported in Table 4.2 and 2) Avogadro's law, stating that equal volumes of all gases at the same temperature and pressure contain equal numbers of particles.

Gas	Molecular weight [g/mol]	GWP
$C_2H_2F_4$	102.03	1430
i-C_4H_{10}	58.12	3
SF_6	146.06	22800
CO_2	44.01	1
HFO	114	6

Table 4.2: Molecular weight[129] and GWP[93] of the gases employed in the different RPC mixtures

With these information, one can calculate the, for example, the GWP of the STD gas mixture:

- Volume fractions: 1 l STD = 0.952 l $C_2H_2F_4$, 0.045 l i-C_4H_{10} and 0.003 l SF_6
- From Avogadro's law, 1 mol : 22.4 l = x mol ($C_2H_2F_4$) : 0.952 l (and same proportion for the other two gases with their fraction in l)

- Gas mixture composition in g: 4.34 g $C_2H_2F_4$, 0.12 g i-C_4H_{10} and 0.02 g SF_6
- Weight fractions: 96.88% $C_2H_2F_4$, 2.68% i-C_4H_{10} and 0.45% SF_6
- GWP of the mixture as weighted average of the GWP of each gas: (0.9688*1430) + (0.0268*3) + (0.0045*22800) $\sim$ 1488

With the same calculations, all the GWPs reported in Table 4.1 have been derived.

4.2 The CERN Gamma Irradiation Facility

This section contains a description of the CERN GIF++, where the beam tests described in this chapter, as well as the aging studies described in Chapter 5 have been carried out by the ECOgas@GIF++ collaboration have been carried out.

4.2.1 The GIF++ ^{137}Cs source

The GIF++ is an experimental facility located in the CERN North area. It is equipped with a 12.5 TBq ^{137}Cs source, which provides an intense 662 keV photon field, allowing the users to carry out aging tests, i.e., to operate the detectors in a high radiation environment and to simulate years of operation in a shorter time. At the same time, in dedicated periods of the year, the facility is served by a high intensity 100 GeV/c muon beam, obtained using protons coming from the SPS H4 beam line[130]. A big advantage of the facility is the possibility to combine the muon beam with the source, allowing one to also study the detector performance under irradiation (rate capability). As Figure 4.1 shows, there are two irradiation zones in the GIF++ bunker (name given to the irradiation area of the facility), usually referred to as upstream (to the right of the source) and downstream (to the left of the source), with respect to the direction of the muon beam. The red lines in the figure show the aperture of the irradiation cone ($\pm$ 37.5° with respect to the center line) and the vertical green lines are distance markers from the source. The irradiator is marked by a black circle in Figure 4.1

The irradiator is placed in an enclosed structure, with two windows for the two different irradiation zones, and the radiation can be attenuated independently in the two fields, thanks to a set of lead filters. A total of 24 possible attenuation (ABS) factors can be obtained, as shown in Figure 4.1, where 1 means irradiator fully opened (maximum irradiation) and 46415

means irradiator fully closed (minimum irradiation). The same absorption factors can be applied in both irradiation zones. Of course, the ^{137}Cs source can also be completely shielded, allowing one to enter the facility to work on the detectors. This special case will be addressed in the following as *source off*. Lastly, the irradiator is provided with an angular correction filter, transforming the irradiation field from the one of a point-like source dependence ($\propto 1/r^2$) to a flat distribution in a vertical plane perpendicular to the bunker walls.

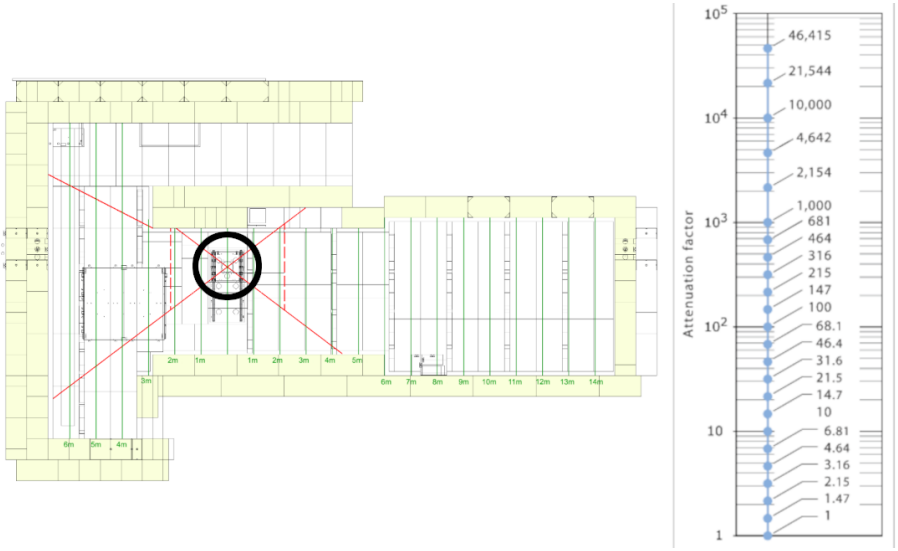

Figure 4.1: Left panel: layout of the GIF++ bunker. The red lines show the aperture of the irradiation cone, the green ones are distance markers from the source. The irradiator is circled in black. Right panel: nominal photon field attenuation values. Figures taken from [128]

The ECOgas@GIF++ collaboration has installed two different mechanical supports inside the irradiation zone, located in the upstream region, at roughly 3 and 6 m from the source (*trolley 3* and *trolley 1* respectively). The different distances have been chosen by keeping in mind the needs of the different experimental groups: the ALICE and SHiP detectors have been installed further away from the source, given the lower rate expected in the experiments (as explained in the last part of 2.3.2), while the ATLAS, CMS and EP-DT detectors are closer to the irradiator.

4.2.2 The muon beam at GIF++

The GIF++ is located in the CERN North Area, in the Prevessin site, on the H4 secondary SPS beam line[131]. The SPS proton beam is collided with several fixed targets (namely T2, T4, T6 and T10), to produce secondary beams containing electrons, hadrons and muons. Those beams are then sent to various secondary beam lines (among which the aforementioned

H4) and to the users located along them. A simple sketch of the targets and beam lines in the north area is shown in Figure 4.2.

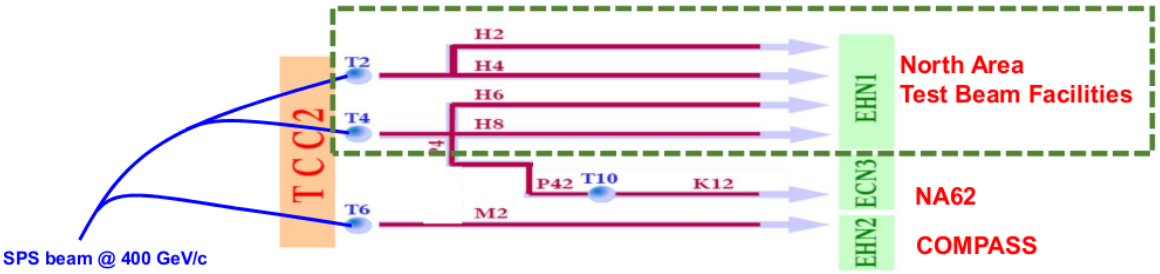

Figure 4.2: Sketch of the targets and secondary beam lines at the CERN north area. The GIF++ is located on the H4 beam line, downstream of the T2 target[132]

Several components for tuning and monitoring the beam parameters (intensity, composition and momentum) are located along each beam line: dipoles, quadrupoles and collimators are used to guide and shape the beam and to ensure proper particle momentum selection; absorbers are used to control the beam composition and intensity. Finally, beam monitoring detectors are inserted in various positions along the beam line, allowing one to have real time information on the beam quality and position. The settings of the components listed above are controlled by the north area beam physicists and they are negotiated with the physics coordinator of each experiment, in order to get the optimal configuration. In the case of the GIF++, the beam is composed by high energy muons with a momentum of ~ 150 GeV/c. The muon beam is not a continuous stream of particles, rather it is sent to the facility in bursts of ~ 5 s duration (so-called *spills*) with $\sim 10^4$ muons per spill. Figure 4.3 shows an example of what is known as *SPS cycle*, available on the SPS web page.

The SPS cycle provides real time information on the current SPS user. Note that GIF++ is not the only facility that is served by the SPS, as the north area also hosts a number of fixed target experiments, also relying on the SPS beam. Furthermore, the SPS is used as an LHC injector (see Chapter 1) and the LHC filling process is also part of the cycle. Figure 4.3 is divided into 3 sections: section 1 and 2 refer to the SPS serving the fixed target experiments while section 3 is related to the LHC filling process. The yellow curve represents the intensity of the circulating beam; the two increasing steps seen in sections 1 and 2 refer to the SPS filling procedure: the flat part corresponds to the SPS acceleration and the straight decreasing line represents the extraction from SPS and the sending to the different fixed targets, which are listed in the bottom part of the figure. The white curve represents the current in the SPS magnets, which increases during the accel-

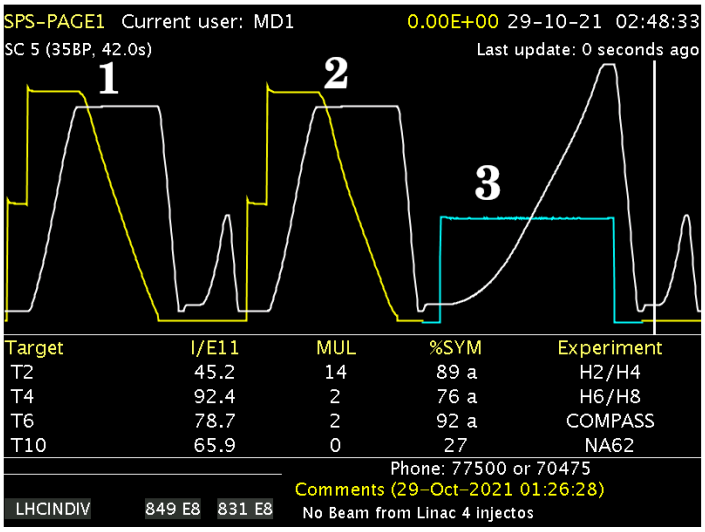

Figure 4.3: Example of SPS cycle. The yellow line represents the number of particles circulating, the white line gives information on the magnet status and the numbers at the bottom represent beam intensities on different fixed targets. The bottom right part contains messages for the users

eration phase and goes down after the extraction is completed and before the next injection. Finally, the blue line in section 3 is related to the LHC filling process. Note that the SPS constantly provides a logic signal (referred to as *spill signal* in the following) that is normally a logic 0 and it becomes 1 during a spill. This is a key aspect of the trigger setup, described in the following.

4.3 Experimental setup

This section contains a description of the data taking setup. It is divided into four subsections: 4.3.1 describes the experimental setup in terms of detector hardware and services (gas and high voltage systems); 4.3.3 describes the trigger logic, used to provide both a beam trigger and a way to measure the gamma-induced counting rate on the RPCs. Subsections 4.3.4 and 4.3.5 describe, respectively, the setup used when the front-end electronics are employed in combination with a TDC for data readout, and the one used for the readout with a CAEN digitizer.

4.3.1 Detectors and services

The experimental setup consists of two parts, one located outside the GIF++ bunker (gas and high voltage infrastructure) and the other one inside the bunker, hosting the detectors. The GIF++ team provides the users with the most commonly used gases, such as $C_2H_2F_4$, i-C_4H_{10}, Ar etc, through

a general distribution system. For more user-specific gases, such as HFO, each group has to use its own distribution system. In the case of the ECO-gas@GIF++ collaboration, a small HFO bottle, with a pressure regulator and a leak detection apparatus, has been installed in the gas distribution room, in the floor above the facility, highlighted in red in Figure 4.4. Due to the amount of gas used, and the total volume of all the detectors, a small HFO bottle usually lasts around 30 days, after which it has to be manually swapped for a new one.

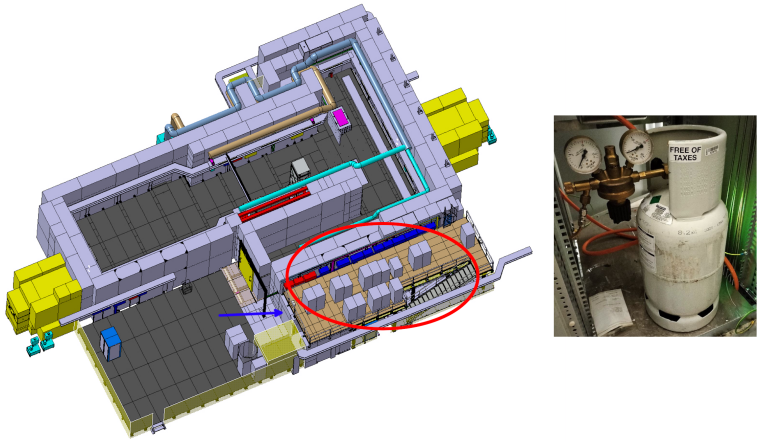

Figure 4.4: Left panel: 3D model of GIF++, the gas room is highlighted in red, while the service area is indicated by the blue arrow. The detectors are placed in the area inside the concrete shielding. Right panel: the HFO bottle located in the gas room

The HFO line, together with the ones coming from the main GIF++ supply, is sent to the gas distribution system. The latter is composed by different elements that will be described in the following.

The ECOgas@GIF++ system allows one to mix up to four gases; each line is equipped with a Mass Flow Controller (MFC) to set the desired flow. The output of the four MFCs is sent to a mixing unit, where the different gas mixture components are mixed up. The output line is then split into two lines, namely *wet* and *dry*. The former is sent to a humidifier module, where the gas is bubbled into distilled water and it picks up water vapor (this is needed to prevent the RPC bakelite electrodes from drying up by releasing water vapor to the gas, and the consequent alteration of their electrical and mechanical properties, see, e.g., Reference [83]), while the latter does not go through the humidifier. The two lines are then re-joined and the gas passes through a dew point sensor, which provides information on the relative humidity of the mixture. By adjusting the amount of gas flowing in the wet and dry lines (through two more MFCs), one can regulate the humidity content of the gas mixture. A valve to bypass the humidifier is also installed: by opening it, the gas will only flow through this line (since it has a lower

impedance with respect to the dry and wet) and the resulting gas mixture will be completely dry. A scheme of the system is reported in Figure 4.5.

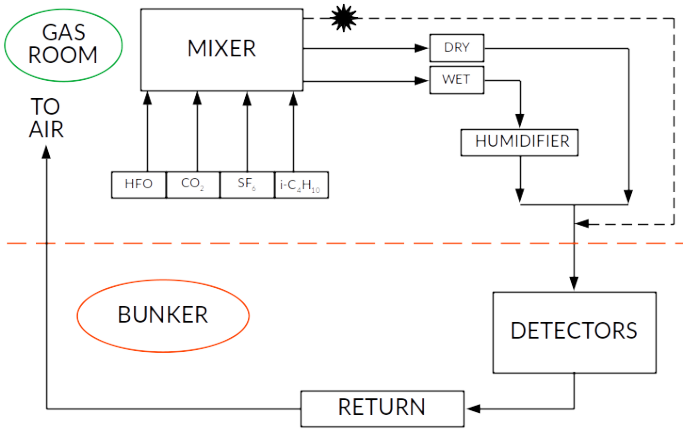

Figure 4.5: Scheme of the ECOgas@GIF++gas mixing and distribution system. The dashed line from the mixer to the detectors represents the humidifier by-pass line. The red dotted line is used to indicate the separation between the components of the setup located inside and outside of the irradiation area (*bunker*).

Once the gas has gone through the dew point sensor, it flows to the bunker, where it is split and sent, in parallel, to all the ECOgas@GIF++ detectors. This distribution is done on a patch panel located on trolley 3 (the one closer to the γ source), where the main pipe branches into different lines (one per detector). The gas flow in each RPC is set using a variable area rotameter, in series with the chamber. This technique is rather simple and it poses some limitations, the main issue being that the rotameter has originally been calibrated with a certain gas, now unknown, hence the flow measurement provided does not correspond to the real one. In order to solve this issue, a more precise flow cell has been installed at the input of each detector, to provide a reading of the input flow. This instrument cell was calibrated with air and, using the conversion factor provided by FLUIDAT[1], one can simply convert the measured flow into the actual one, thus solving the issue highlighted earlier.

All the return lines of the detectors are joined in a common return line, which is then brought back to the gas room and vented into atmosphere. Given the amount of detectors, their geometry and the number of desired volume changes per hour ($\sim$ 1 vol/h), the nominal gas flow is around 10 l/h.

The high voltage (HV) is provided by CAEN modules. These comprise a mainframe (CAEN SY1527) and two HV boards (one A1526P and one A1526N) that are plugged into the mainframe. The HV system is located

[1]FLUIDAT is a collection of routines to calculate physical properties of gases and liquids. This service is provided by Bronkhorst®

in the service area of the GIF++, outside the bunker beneath the gas room. The HV and signal cables have been pulled from the service area to inside the bunker; they run under a false floor and reach the detectors through openings. The low voltage supply to the front-end electronics is detector-specific, and so is the signal readout. In Table 4.3 the main characteristics of the detectors installed by the collaboration are listed.

Detector	Area [cm^2]	Gaps	Thickness [mm]	Strips	Readout
ALICE	2500	1	2	32	TDC/Digitizer
ATLAS	550	1	2/1.8	1	Digitizer
CMS GT	7000	2	2	128	TDC
CMS KODEL	1200	2	1.4	–	–
CMS RE11	4350	2	2	128	TDC
SHiP	7000	1	1.6	64	TDC
EP-DT RPC3	7000	1	2	–	–
EP-DT RPC6	7000	1	2	7	Digitizer
BARI-1p0	7000	1	1	64	TDC

Table 4.3: Features of the detectors of the ECOgas@GIF++ collaboration. The names in italics refer to legacy RPCs while the ones in bold are still under test at the time of writing.

The detectors with their name in italics are legacy RPCs, meaning that they have been installed at the beginning of the ECOgas@GIF++ studies (in 2019) and have later been replaced by new detectors, due to various reasons. The ones with the name in bold in the table are the ones that are still being tested at the time of writing this thesis. The final goal of each group in the collaboration is to find a gas mixture to operate the RPCs in a specific experiment, hence the detectors have to satisfy different requirements. For this reason, several different RPCs are being tested. The other obvious advantage of this setup, given the high number of detectors under test, is the possibility to disentangle detector-specific issues from general ones (related for example to the gas mixture employed).

Since the work in this thesis has been carried out in the context of the ALICE experiment, a more detailed description of this RPC will be given. It is a small (50x50 cm^2) ALICE-like prototype, meaning that it was built using scrap bakelite from the latest ALICE production, described in Reference [133]. It has a single 2 mm gas gap and the thickness of the bakelite is also 2 mm. It is equipped with two perpendicular readout planes, one per side, of 16 strips (with pitch $\sim$ 3 cm) each, thus providing 2D information for each hit. During the beam tests, as described in Chapter 4, the strips were either connected to the FEERIC front-end boards[111] (the currently employed

front-end in ALICE, as mentioned in Chapter 1) or to a CAEN digitizer, to perform signal shape and charge studies. In the digitizer readout mode, due to the limited number of input channels, only 7 vertical strips were read out. Figures 4.6 and 4.7 show two pictures of the ALICE RPC, hanging from the trolley inside the GIF++ bunker.

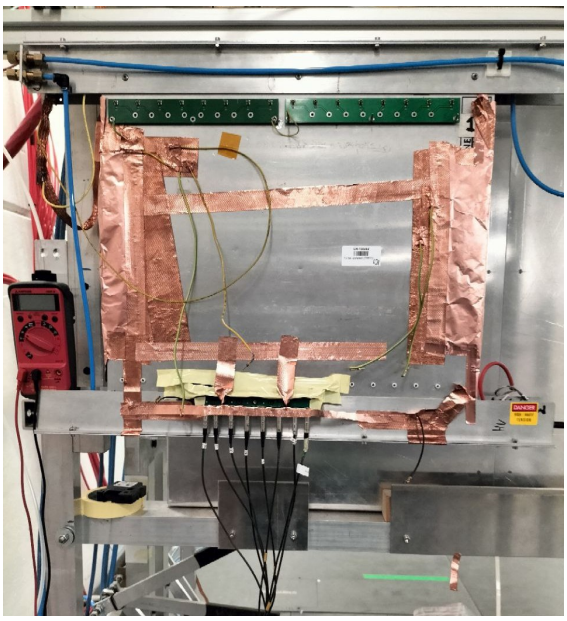

Figure 4.6: Front view of the ALICE RPC with digitizer connection

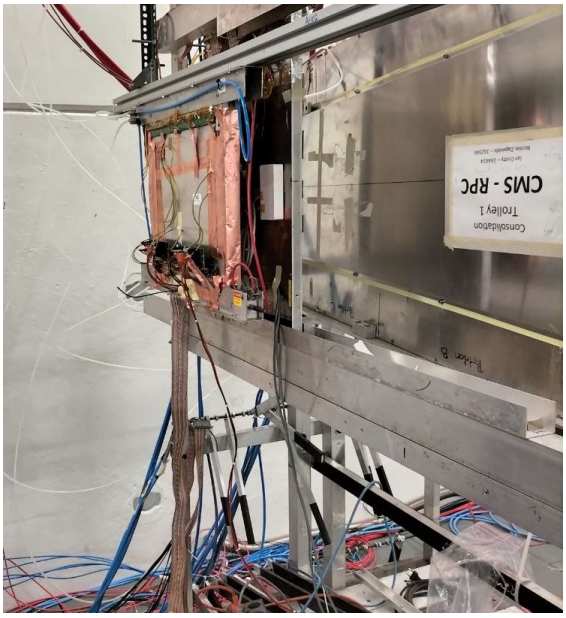

Figure 4.7: Side view of the ALICE RPC with FEERIC connections

4.3.2 Data acquisition setup

In order to carry out the data taking procedure, a software that was developed for the CMS RPC group has been readjusted for the needs of the ECOgas@GIF++ collaboration. It will be referred to as *webdcs*[134], since it acts as Detector Control System (DCS) and it has an online interface (web). Its role is to carry out the data acquisition (as it will be explained in 4.3.4 and 4.3.5) and also to configure and monitor the detector parameters.

The results in the following sections will be presented as a function of the effective high voltage (for the reasons discussed in Section 2.2.3) and one of the tasks of the webdcs is to apply a PT correction to the applied high voltage, according to Equation 4.1, discussed extensively in Reference [92]

$$HV_{app} = \beta \cdot HV_{eff} = \left((1-\alpha) + \alpha \cdot \frac{P}{P_0} \cdot \frac{T_0}{T}\right) \cdot HV_{eff} \tag{4.1}$$

where T_0 = 293.15 K and P_0 = 990 mbar are taken as reference values and α = 0.8. This formula implements the correction employed in CMS[92] (as

anticipated in Section 2.2.3), which is slightly different from the one used for the ALICE data-taking (reported in Reference [135] and based on Eq. 2.12). The webdcs grants a high level of flexibility, allowing the user to easily include or exclude a given detector from the data taking. It also provides basic data quality monitoring tools.

4.3.3 Trigger logic

As anticipated in 4.2.2, the peculiarity of GIF++ is the possibility to combine the muon beam with the ^{137}Cs source, in order to test the detector performance when exposed to an intense gamma flux. The trigger setup and logic is the same for the TDC and digitizer data acquisition setups. The muon beam trigger is based on scintillators, coupled with photomultipliers, due to their fast response and ease of use. Usually a beam trigger is provided by the coincidence of two or more scintillators and, due to the presence of the gamma background, the scintillators cannot be installed only inside the bunker, since the number of fake coincidences (and fake triggers) would be too high. For this reason, the GIF++ team has installed a pair of 30x40 cm^2 scintillators outside the bunker (referred to as outer scintillators) which can be put in coincidence with other, smaller, scintillators to provide a more defined trigger area. In the case of the ECOgas@GIF++ collaboration, it was decided to install two 10x40 cm^2 scintillators (referred to as inner scintillators) on the two trolleys (labelled 3 and 1, where the former is closer to the source and the latter is further away, see 4.2.1), perpendicular to one another, to create a reduced trigger area of $\sim$ 10x10 cm^2. Figure 4.8 shows a sketch of the GIF++ bunker, where the outer scintillators are represented by the red boxes and the internal ones by two blue boxes, drawn next to the trolleys (the black rectangles) for visualization purposes (in the setup they are attached to the trolleys' metal structure). The distance between the internal scintillators is $\sim$ 3.5 m while the distance between the external ones is $\sim$ 25 m.

The rate of photons impinging on the RPCs under test can not be measured using the RPCs themselves, since the photon conversion probability (which is on the order of 10^{-3}-10^{-2}) is not precisely known. Of course, knowing the source activity, the absorber configuration and the distance of the detector from the irradiator, one could estimate the gamma rate. This estimation, though, would not be precise enough since it does not take into account the presence of other materials between the source and the detectors and also because the real attenuation provided by the filters is not the

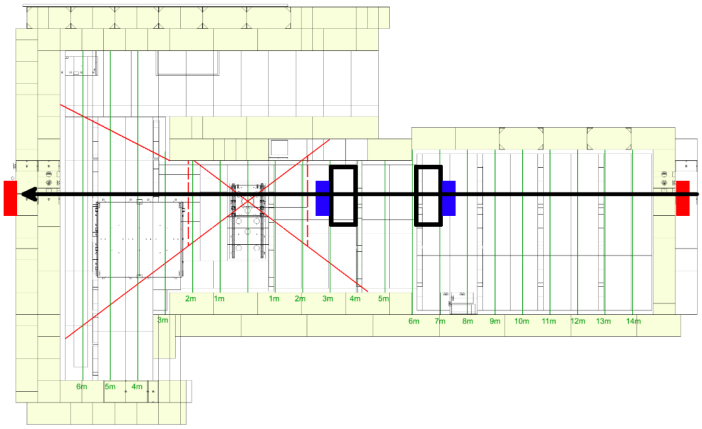

Figure 4.8: Layout of the GIF++ with highlighted the outer (red) and inner (green) scintillators used to provide the beam trigger in the beam tests. The two ECOgas trolleys (in black) are also visible in the sketch. The red crossed lines show the irradiation zone

same as the nominal absorption factors, mainly due to the presence of the source angular correction filter, as reported in Reference [128]. Hence, to quantify the level of gamma irradiation on the detectors, one can use the gamma-induced counts on the detectors under test. To do so, one can exploit the fact that the beam coming from the SPS is not a continuous stream of muons, but it is divided into trains of muons (spills, as explained in 4.2.2). Knowing this, one can sample the detector response in the periods between spills, when no muons are present, obtaining data for the gamma-induced counting rate.

4.3.4 TDC setup

The setup described here is used when the TDCs are used in combination with the ALICE FEERIC front-end electronics. The trigger logic is common for the two readout modes (TDC and digitizer).

4.3.4.1 Data acquisition setup

The beam test data acquisition is executed by the webdcs. A scheme of the setup is shown in Figure 4.9. It uses NIM modules[136] for the creation of the trigger and VME modules[137] for the data acquisition itself.

The coincidence of the discriminated signals from the external scintillators is provided by the GIF++ infrastructure while the one for the internal ones is built separately, to create a global coincidence of the four. This signal is used to provide the muon trigger. The trigger signal for the periodic sampling of the RPC signals outside of the muon spill (referred to as *random trigger* in the following) is provided by the V1718 CAEN VME bridge.

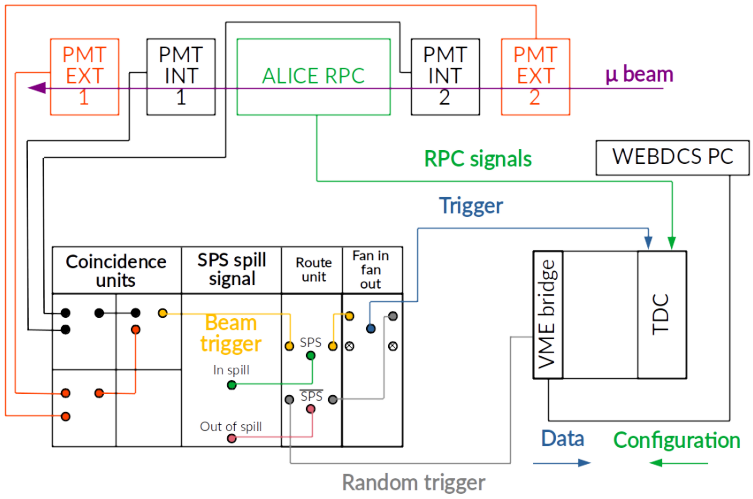

Figure 4.9: Logic scheme of the trigger setup employed in the beam test. NIM and VME modules are shown together and the most important components are highlighted. Refer to the text for a full explanation of the trigger logic

This module has two purposes: on the one hand, it provides the connection between the VME crate and the webdcs computer (via USB 2.0 cable), on the other hand, it generates (via one of its programmable outputs) a square wave with adjustable frequency, which is used as the random trigger.

One has to find a way to switch between the two trigger types, depending on the SPS status. This is possible thanks to a particular NIM module, called *route unit*, which is essentially a gated-output NIM module. As seen in Figure 4.9, the route unit has two inputs; the beam trigger is connected to one and the random trigger to the other. The output of these channels is gated, meaning that the input signal is propagated to the output only if the gate is open. The peculiarity of this module is that the two channels share the same gate and it is inverted between the two. In this way, if one of the gates is open, the other is closed and only one signal at a time can pass through. In the case of the GIF++ setup, the gates are connected to the SPS spill signal. If a spill is occurring, and the spill signal is a logic 1, then the gate for the beam trigger opens and that signal passes through, while the random trigger is blocked. If, on the other hand, a spill is not in progress, the opposite gate is opened and the random trigger signal can go through. In this way it is possible to automatically toggle between beam and random trigger.

The signals from the front-end electronics are readout by a CAEN TDC, model V1190. This is a multi-hit TDC, with 128 LVDS inputs and 100 ps resolution for every input channel. A total of three TDCs is used by the ECOgas@GIF++ collaboration and the trigger input is daisy-chained from

one TDC to the other. Before data taking can start, the TDC modules have to be configured; this procedure is carried out by the webdcs, hence the arrow named *configuration* in Figure 4.9. The VME bridge is also responsible for the data transfer from the TDC modules to the computer. The data acquisition code also takes care of applying the desired high voltage to the detectors, performing the PT correction and saving all the relevant parameters for each run.

4.3.4.2 TDC data format

For several of the studies reported in this chapter, the RPC response is measured as a function of the applied high voltage. On average (depending on the available time), 10 to 14 high voltage values are scanned. For each high voltage point, a number of beam and random triggers is set and two separate counters are increased, according to the type of trigger (this information is sent to the VME bridge, which communicates it to the PC), until both counters reach the predefined values. After that, the high voltage is changed to the next value and the process is repeated, until all points have been scanned. In case either of the two counters (beam or random) reaches the target before the other, events of that type are still collected until the counter reaches 200% of the set value, then that acquisition is stopped until the other counter reaches the target value.

The TDC stores the time of each hit, regardless of the trigger type, together with the channel number, into a hit buffer. When a trigger signal is detected, a trigger matching, with programmable time window, is performed by the TDC. In the GIF++ beam test the window width was set to 5000 ns. If a given hit lies inside the matching window, the data are transferred to a readout FIFO to be read out and saved by the data acquisition PC. In order to avoid overfilling the buffer, any data that does not receive a trigger within a matching window is automatically discarded.

For each HV point, three files in ROOT format are produced and they contain all the data necessary for the analysis. In the following, they will be referred to as the DIP, CAEN and DAQ files. The DIP file contains all the environmental (temperature, pressure etc) and source (on/off, absorption factor etc) parameters. The CAEN file contains information on the high voltage parameters; a measurement of the applied, effective and monitored high voltage and of the current is performed every two seconds and the data are stored in histograms. Finally, the DAQ file contains the detector response data, which is saved as a ROOT tree[138] with several branches, as

shown in Figure 4.10.

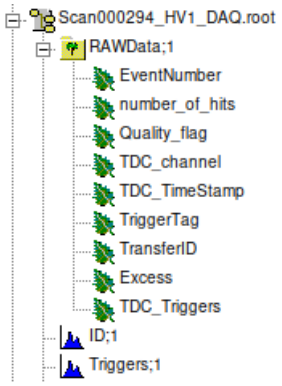

Figure 4.10: Screenshot of the DAQ file content. The *RAWData* tree contains the data coming from the detectors, together with other information for debugging purposes

The data in the tree branches are arranged per trigger and the type of data saved changes according to the data type. The branches *TDC_channel* and *TDC_TimeStamp* contain vectors with the TDC channels which were fired (the correspondence between TDC channel and RPC strip is known) and the timestamp of the hit, with respect to the trigger time. The branch *TriggerTag* contains an integer that is used to classify each trigger either as a muon or as gamma (0 if it is a muon, 1 if it is a gamma). All the other branches are used for debug purposes, especially the *Quality_flag* one, which contains information regarding possible errors that happened during the data transfer in a given trigger. Only data whose quality flag is good can be analyzed.

4.3.4.3 FEERIC front-end electronics

The setup just described is used when the RPC signals are discriminated with the new ALICE MID front-end electronics, FEERIC[111], that have been installed in ALICE before the start of the LHC RUN3 and have been commissioned in 2022[133]. A picture of one of the FEERIC cards used in the beam test is shown in Figures 4.11a (the front side) and 4.11b (the back side). Due to the pitch of the RPC under test in the beam periods, a total of 4 cards was employed, two for the 16 vertical strips (8 channel per card) and two for the 16 horizontal ones.

A brief description of the main features of the FEERIC boards is presented here. The main logical component of the electronics is the FEERIC chip, highlighted in blue in Figure 4.11a, which amplifies and discriminates the input signal and drives the LVDS circuit for the logic output signal generation. Note that, as already anticipated in Chapter 2, the main difference

with respect to the old Muon TRigger (former name of the Muon IDentifier) front-end electronics is the presence of an amplification stage at the input of each channel (trans-impedance amplifier), which allows one to operate the detectors at lower gain by reducing the effective signal amplitude threshold. Multiple FEERIC cards can be connected in series, allowing one to power them using a single power supply; furthermore, the threshold can be distributed across multiple boards using the I^2C protocol. FEERIC has the capability to discriminate both positive and negative signals, according to the strip plane to which it is connected. The required voltage to power-up the electronics is 4 V, and during the beam and ageing tests it was provided by means of a lab-bench power supply, installed directly on the trolley, inside the bunker. According to specifications, each board should draw around 150 mA of currents, so a total of 600 mA was expected; the measured current was around 620 mA.

Other components of the FEERIC board are highlighted in Figure 4.11a and are used to distribute the low voltage and the threshold across different boards. As part of the beam test preparation, a quick way to set the thresholds was developed. For this reason, a slightly more detailed description of the process is provided. To perform this operation, an Arduino Uno WiFi was used. This module is capable of establishing I^2C communication, through its dedicated SDA and SCL pins and the *Wire.h* library. The WiFi version of the Arduino was originally selected because it was meant to be installed inside of the GIF++ bunker and to be permanently connected to the front-end boards, in order to vary the threshold on-the-fly, without entering the bunker. Unfortunately, said solution could not be implemented, due to the appearance of noise in the electronics, induced by the Arduino module itself. For this reason, the WiFi approach was abandoned and, each time the thresholds needed to be set, the Arduino was connected to the front-end electronics, the threshold set and the Arduino disconnected. By design, the FEERIC cards memorize the applied threshold, as long as they have power, so this procedure had to be performed only a handful of times during the beam test.

In order to establish communication via I^2C, each FEERIC card needs to be assigned a unique address. This is done by means of DIP switches, highlighted in red in Figure 4.11a, which are also used to set the polarity of the signals expected to be discriminated by the board. The full Arduino code is reported and discussed in appendix A.1; it essentially opens the communication with one FEERIC board at a time, sets the threshold and moves on to the next board. The component that actually sets the threshold

on the FEERIC board is a LTC1669IMS8#PBF 10 bit Digital to Analog Converter (DAC) with peak-to-peak voltage (V_{pp}) of 3 V. The threshold values for each board, expressed in mV since they are applied at the output of the trans-impedance amplifier, are provided in the Arduino code. The values in mV are then converted to DAC counts (keeping in mind that $3V/2^{10} \simeq 2.93$ mV/DAC unit) and this value is either added or subtracted from the 1.5 V FEERIC internal baseline (translating to a maximum and minimum threshold values of ± 1.5 V). After the conversion, the value of threshold in DAC counts is written via I^2C. Lastly, once the code is run, one can check with a multimeter whether the expected threshold was applied, thanks to the presence of two contact points on the FEERIC cards. The results shown in this chapter were obtained with an applied threshold of ± 100 mV (value used so far in ALICE[133]), depending on the signal polarity. The conversion between threshold in mV (pulse height after amplification) and fC (charge before amplification) is not trivial, but [86] provides this conversion for some values: 88 mV corresponds to ∼ 142 fC and 117 mV to ∼ 189 fC, hence the 100 mV value is somewhere in between.

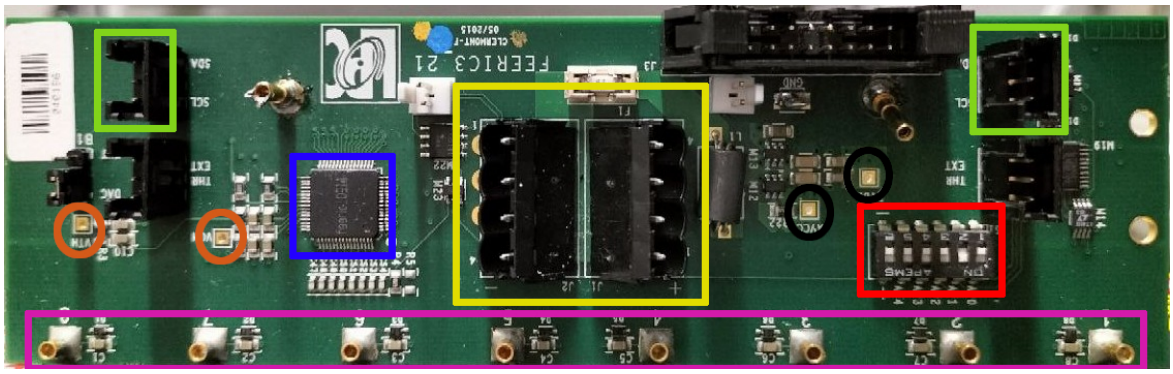

(a) Figure 4.11a Front view of the FEERIC front-end board. Highlighted in red are the DIP switches to select board ID and input signal polarity. The yellow connector is used to daisy-chain the low voltage, while the green one is used for the I^2C connections to set the threshold. The blue component is the FEERIC chip itself, responsible of signal discrimination and LVDS output generation. The orange contact points are used to check the threshold value while the black ones are to check the powering of the board

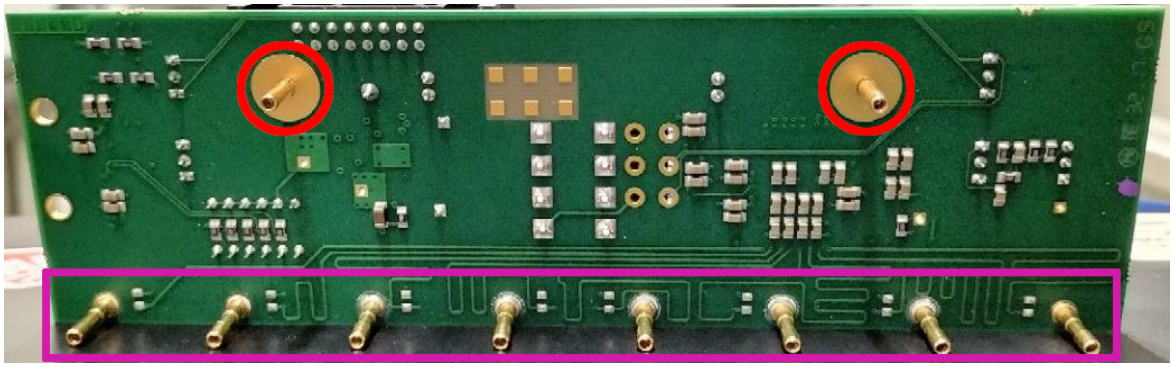

(b) Figure 4.11b Back view of the FEERIC front-end board. Circled in red are the ground pins while the pins highlighted in violet are used to couple the board to the RPC strips

4.3.5 Digitizer setup

For what concerns the experimental setup employed with the digitizer, the trigger logic does not change: the in-spill and out-of-spill signals are used to trigger on the muon beam and to measure the gamma rate. What changes is the readout method. Here, the strips are not connected to the FEERIC cards and are directly coupled to a V5742 CAEN digitizer. The data acquisition process is also managed by the webdcs. The digitizer has 16 input channels, with a 1 V peak-to-peak input and 12 bit resolution (LSB = 0.24 mV). It has three different sampling frequencies: 1, 2.5 and 5 Gs/s and, since signal digitization is performed via an array of switched capacitors (fixed amount), the number of samples per trigger is fixed to 1024. The different sampling frequencies of 1, 2.5 and 5 Gs/s correspond, respectively, to an acquisition window of 1024, 409 and 204 ns. Last, two trigger inputs are present, namely *TRIG IN* and *TR0*, the main difference is the reduced latency of the TR0 (also referred to as *fast trigger*) input, which makes it more suitable for precise timing measurement, since it can also be digitized.

Figure 4.12 shows how the cabling of the digitizer was carried out. First of all, it was decided to read out 7 strips of the RPC since the core of the muon beam is $\sim$ 10x10 cm^2 and the length covered by 7 strips is $\sim$ 7x3 cm (strip pitch) = 21 cm so the full beam should fit in 7x7 strips. Those cables are connected to the input of channels 1 through 7. The signal provided by the coincidence of the internal and external scintillators was connected to channel 0. This was done to allow the data acquisition code to classify an event either as a muon or as a gamma. Indeed, if a trigger is generated by a muon, the coincidence of the scintillators will provide a non-zero signal, that will be detected in channel 0. If, on the other hand, the trigger signal was generated by a gamma, no activity will be seen in channel 0. In this way, the data acquisition code can either increase the muon or the gamma counter (and the same information can be used in the data analysis).

Due to the length of the cables employed for the trigger signal propagation, the delay between the latter and the RPC signal was measured to be over 500 ns, so the only usable sampling frequency, that allows one to have both the trigger and the muon signal in the same window, is 1 Gs/s (recall that the number of samples is fixed to 1024, regardless of the sample frequency). Figure 4.13 shows an example of said delay. The left panel reports an example of a beam trigger during a spill (coincidence of four scintillators), while the right panel shows the signal from one of the RPC strips. The delay of more than 500 ns between the two is visible .

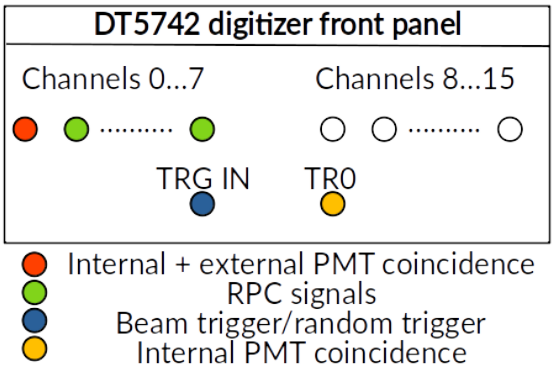

Figure 4.12: Scheme of digitizer cabling, allowing one to exploit both the TRIG IN and TR0 output and to distinguish between a muon and a gamma event

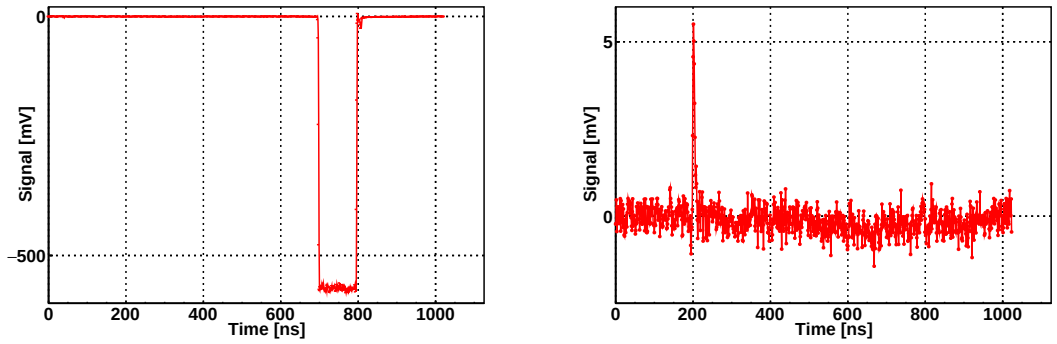

Figure 4.13: Left panel: trigger signal provided by four-fold coincidence of scintillators (as described in 4.3.4.1). Right panel: example of an RPC signal as seen by the digitizer. The delay of more than 500 ns is visible in this Figure

To provide the trigger signal to the digitizer, the same logic explained in 4.3.4.1 was used. During a spill, the coincidence of internal and external scintillators is used as trigger, while, when no spill is present, the random trigger is used. This alternating signal (between beam and random trigger) is sent to the TRIG IN input and it is normally used during the runs. Moreover, in order to improve the time resolution (and be able to use 5 Gs/s as sampling frequency), the coincidence of only the internal scintillators was connected to the fast TR0 input. In this case, the delay between the trigger and RPC signal is reduced to less than 100 ns, enabling one to work with 5 Gs/s. Special runs with this sampling frequency have been taken without gamma background, using the the TR0 input as a trigger, to carry out time resolution measurements. The connection was performed only once, since each channel can be enabled/disabled, and the trigger input selected, via software.

4.3.5.1 Digitizer data format

The same data taking strategy illustrated for the TDC data taking is carried out with the digitizer. For each high voltage value chosen, a number of beam and random triggers is set. According to the criteria highlighted in the 4.3.5, if a non-zero signal is present in channel 0, the amount of muon triggers is increased, otherwise, if no signal is present in channel 0, the gamma counter is. Once the desired amount of triggers is reached, the HV is changed to the new value. This process continues until all the HV values have been scanned. At the same time, the CAEN parameters (high voltage and current) are also saved.

The output from the digitizer is a set of text files, organized as follows: for each HV value, one file is created per strip (7 files in total), plus another one in case the TR0 input is digitized. When the digitizer is triggered, it samples the signal 1024 times and it returns, for each sample, the amplitude of the signal at the specific time, expressed in ADC readings. Each text file contains a list of numbers, corresponding to the aforementioned ADC values, interspersed with information on the event, i.e., trigger number, number of samples, sampling frequency and so on (8 lines every 1024 lines).

In order to improve the processing speed of these files, as soon as a run was completed, the text files were converted into ROOT files. Each file contains different trees (one per HV value), each branch of which corresponds to a digitizer channel and is filled with vectors. Each vector contains the ADC counts for a given trigger. Figure 4.14 shows an example of this tree structure.

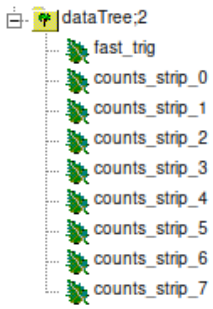

Figure 4.14: Screenshot of the ROOT file structure. The tree contains the data coming from the digitizer. Each branch corresponds to a digitizer input channel (branch ”fast_trig” contains the data from the TR0 input)

4.4 Data analysis procedure

4.4.1 TDC data analysis

The format of the data obtained when using the TDCs was briefly outlined in 4.3.4.2. The data is organized as follows: for all the high voltage values that were scanned, a ROOT file is created. Each file contains a tree with as many entries as the number of triggers set by the user for the specific HV point. Each entry corresponds to a trigger and it contains a list of all the TDC channels that were fired in the given trigger (also referred to as hits in the following) and the time of each signal. Each entry of the tree is classified either as a beam event, collected during the SPS spill, or as gamma/background event, collected outside of the SPS spill. The first step of the analysis consists in the creation of the so-called time profile, where the time of all the hits collected upon a trigger is displayed as a histogram. Recall that for every trigger (beam or random), a 5000 ns window is opened and all the hits that fall in this interval are collected. Ideally, upon a beam trigger, only signals that are generated by muons would be collected, while the random trigger would collect only signals from the photon background. This is not the case, since, under gamma irradiation, the photon background is always present and counts due to photons will appear also in a beam trigger acquisition window. Furthermore, even when the source is off, counts from intrinsic detector and/or electronic noise are present. Figure 4.15 shows two examples of time profiles which demonstrate the behavior just mentioned. The one on the left is taken with source off (no irradiation) and the one on the right is taken with ABS 1 (maximum irradiation), and both are taken at the same value (90%) of RPC efficiency.

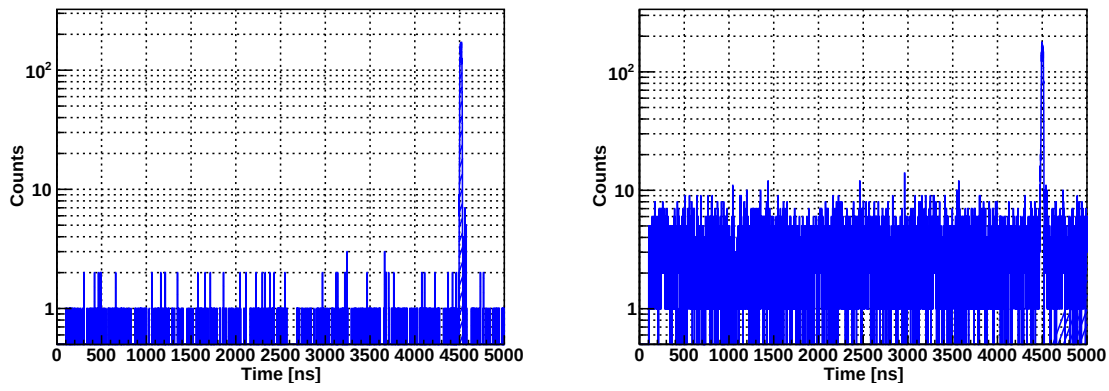

Figure 4.15: Left panel: RPC time profile with standard gas mixture and source off. Right panel: time profile with standard gas mixture and maximum irradiation. The data correspond to the same detection efficiency of 90%

The time profile is a superposition of all the hits recorded by the TDC for a given data-taking interval (usually, a step in the high-voltage scan). In both panels of Figure 4.15 one can observe a peak around 4500 ns. Since the time interval between the beam trigger and the RPC signal is constant (dominated by the RPC and scintillators jitter) the accumulation of signals represents the real muons. All the other counts, uniformly distributed in the acquisition window are not real muon signals (since they arrive at random times in the TDC) but they represent, as mentioned before, either intrinsic noise in the detector and/or in the electronics or gammas from the ^{137}Cs source in case the latter is on. Indeed, in the right panel of Figure 4.15 one can observe how the randomly distributed counts outside the muon interval increase, due to the gamma background.

Going back to the muon time profile, one would expect the width of the muon peak to be dominated by the jitter of the trigger and RPC signals ($\sim$ 2-3 ns) but, upon closer inspection, the width is found to be closer to $\sim$ 25-30 ns. This behavior can be explained by considering that the internal clock of the TDC (that determines the trigger sampling frequency) runs at 40 MHz (since the TDC was developed for LHC applications and 40 MHz corresponds to the LHC clock frequency), which means that the trigger is sampled every 25 ns and this creates a jitter that dominates over the one due to the detectors. This also makes precise timing measurements unfeasible, since the precise timing information on the trigger is not available. The solution to overcome this problem would be to send a copy of the trigger signal in one of the TDC input (the time resolution on the single hit is 100 ps) to have a precise trigger timing measurement. This solution was not adopted due to lack of available channels but it was overcome with the digitizer (as better explained in the next section).

In order to properly tag a signal as muon, a muon window has to be estimated. This is done by performing a Gaussian interpolation of the peak around 4500 ns. To take the contribution of the non-muon counts into account, a Gaussian with a constant offset is used. First the offset value is estimated by performing an interpolation of the time profile with an horizontal line in the interval 0-3000 ns (away from the muon window), then the peak is fitted with the Gaussian plus offset (using as initial value for the offset the one obtained from the previous fit). The muon window is then defined as the time interval in the $\pm$ 3σ range around the Gaussian mean. This means that, if the time of a given hit falls in this window, it is tagged as a muon. Figure 4.16 shows the RPC strip profile (only for muon triggers and with maximum background radiation) if all the events in the time pro-

file are considered (left panel) and if only the ones inside the muon window are considered (right panel). The hit profile shows clearly that the RPC was aligned with the core of the muon beam. The knowledge of the hit time allows one to isolate the muons, even in the presence of a high background radiation. Of course, the signal from a background photon can fall inside of the muon window; this effect is corrected for in the determination of the detector efficiency.

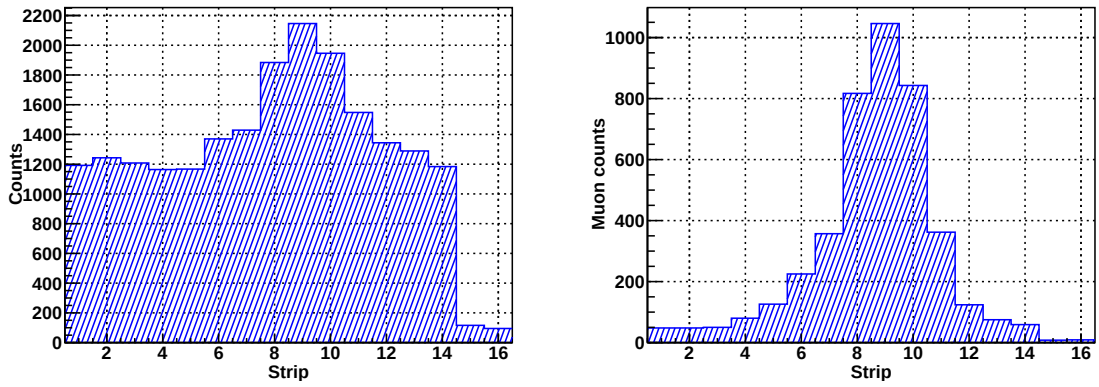

Figure 4.16: Standard gas mixture, RPC strip profile at maximum irradiation. Left panel: all hits in the muon acquisition window are plotted. Right panel: only hits in the muon window are plotted, beam profile more evident

If, for any given trigger, there is a hit inside the muon window calculated earlier, the RPC is considered efficient for the given trigger. Since the ALICE RPC is readout on two perpendicular strip planes, one can compute three different efficiency values, referred to as X plane, Y plane and 2D efficiency. The X and Y plane efficiencies are computed by looking only at the hits on the horizontal and vertical strip plane respectively, while the 2D efficiency requires at least a hit in both detection planes for the RPC to be considered efficient in a given event.

As said before, a gamma signal can happen at any time, even in the muon window. In case this happens, it could lead to an overestimation of the efficiency so it has to be taken into account. To estimate the gamma contribution to the muon efficiency, a *fake efficiency* (meaning efficiency for gamma detection) is calculated, based on the hit rate outside the muon window. The window chosen for the gamma rate measurement (gamma window) is the range 100-4350 ns. Once all the triggers for a given high voltage value have been analyzed, the 2D raw (without the subtraction of the gamma contribution) muon efficiency, and its error, are computed as:

$$\epsilon_{raw} = \frac{n_{hits}}{n_{trig}} \quad \text{and} \quad \sigma_{\epsilon_{raw}} = \sqrt{\frac{\epsilon_{raw}(1-\epsilon_{raw})}{n_{trig}}} \tag{4.2}$$

where n_{hits} represents the number of events with at least one hit in both detection planes inside the muon window and n_{trig} is the number of muon triggers. For what concerns the fake efficiency, the following is used:

$$\epsilon_{fake} = \frac{n_\gamma \tau_\mu}{n_{trig} \tau_\gamma} \quad \text{and} \quad \sigma_{\epsilon_{fake}} = \frac{\tau_\mu}{\tau_\gamma} \frac{1}{n_{trig}} \sqrt{\frac{n_\gamma (n_{trig} - n_\gamma)}{n_{trig}}} \tag{4.3}$$

where n_γ is the number of events with at least one hit in both detection planes in the gamma window, τ_γ is the duration of the gamma window and τ_μ is the duration of the muon window.

Finally, the corrected muon efficiency is estimated as:

$$\epsilon_{2D} = \frac{\epsilon_{raw} - \epsilon_{fake}}{1 - \epsilon_{fake}} \tag{4.4}$$

and the error is obtained by propagating the errors on the raw and fake efficiencies. The derivation of this formula is reported in appendix A.2. It was decided to report the values of 2D efficiency throughout the thesis since it reduces the contribution of spurious counts due to electronic noise.

Once the efficiency has been estimated for all the voltages in the run, its trend as a function of the high voltage is interpolated using a logistic function[74]:

$$\epsilon(HV) = \frac{\epsilon_{max}}{1 + e^{-\lambda(HV - HV_{50})}} \tag{4.5}$$

where the ϵ_{max} parameter represents the asymptotic maximum efficiency reached by the detector, λ is the steepness of the efficiency rise and HV_{50} represents the high voltage value where the efficiency reaches 50% of the maximum efficiency. Figure 4.17 shows the typical trend of an RPC efficiency curve, when operated with the standard gas mixture and without any gamma background. The efficiency is zero when the electric field is below the threshold for charge multiplication; once the multiplication region is reached the curve presents a steep rise, followed by what is typically referred to as a *plateau*, meaning that the efficiency value has reached its maximum value and is approximately constant as a function of the high voltage. The inflection point between the rise and the plateau is known as the *knee* of the efficiency curve. Typical values for the three parameters from the interpolation are listed in Figure 4.17. Since no irradiation is present, no correction for gamma contamination is applied in this particular case.

A key parameter for the RPC operation, that can be extracted from the interpolation with the logistic function, is the detector working point (WP),

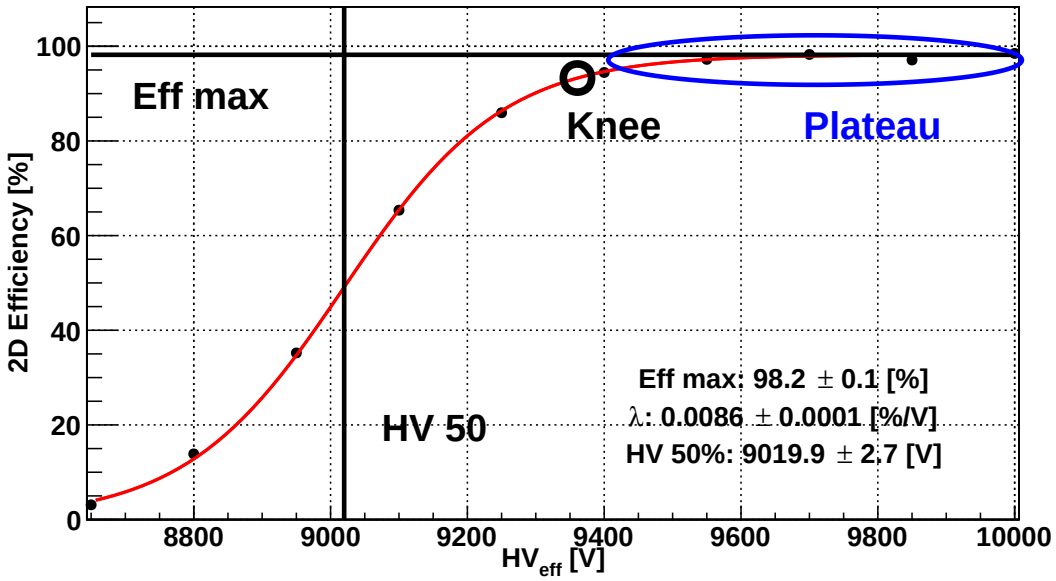

Figure 4.17: Example of an efficiency plateau, obtained with the standard gas mixture and without irradiation. Interpolation with the logistic function and the values of the fit parameters are reported in the figure

meaning the lowest value of high voltage such that, for small voltage variations, the efficiency remains unchanged. Usually the WP is defined as the voltage corresponding to the knee plus a fixed amount: in the following, unless otherwise specified, the WP is defined as in [122]:

$$WP = \frac{log(19)}{\lambda} + HV_{50} + 150V \tag{4.6}$$

where the term $\frac{log(19)}{\lambda} + HV_{50}$ comes from a mathematical definition of the knee as the voltage value where the efficiency reaches 95% of its maximum value (see A.4 for a derivation). The determination of the working point is of crucial importance to characterize a detector with a given gas mixture. As discussed in Chapter 3, the final goal of these studies is to find a mixture with compatible performance with respect to the standard gas mixture and with a not-too-high working point.

After the efficiency calculation, the clustering is carried out next, both for muon and for gamma events. The aim of the clustering procedure is to determine the cluster size (in terms of number of strips hit by a single particle) and the cluster multiplicity, meaning the number of clusters in any given trigger. The clustering algorithm implemented is described in detail in A.3 but the main idea is to check the strip number and time difference between hits in the same trigger window and, if adjacent strips are fired with a time separation less than 15 ns (the choice of this value is also explained in A.3), the hits are joined together in a cluster. The result of the clustering

procedure is a *cluster vector*, which contains a number of elements equal to the number of clusters, and each element represents the number of strips in each cluster. Two separate histograms, one for the cluster size and one for the multiplicity, are filled for each high voltage value. Once the analysis of a given HV is over, the mean and its error are extracted from the histograms and the trend of these quantities as a function of the high voltage is created. The value of cluster size is related to the transverse size of the avalanche inside the gas gap and is important for the detector spatial resolution, which is approximately given by cluster size · strip width / $\sqrt{12}$ (as explained in 2.2.2).

The last quantity that is calculated in the TDC data analysis is the gamma cluster rate, which is expressed in Hz/cm^2 and is an estimate of the background rate measured by the detector. Indeed, by analyzing the data that are taken outside of the muon spill, one can obtain information on the rate of photon-induced hits. In particular, one can create a strip profile in the same way as the one shown in Figure 4.16, but considering gamma events. The profile will be flat, since the photon background is uniformly distributed on the detector surface. An estimate of the background (expressed in Hz/cm^2) can be calculated by counting the number of gammas detected by the RPC and dividing this number by the total acquisition time and the active area of the detector. The total acquisition time can be calculated as $n_{gamma-triggers} \cdot 4900$ ns, where $n_{gamma-triggers}$ is the number of gamma triggers collected and 4900 ns is the duration of the acquisition window for each trigger (5000 ns minus the first 100 ns, which are excluded due to the presence of possible data corruption in the transfer). The number of gamma hits is calculated after the clustering procedure (because one photon could produce a response in more than one strip), as the total number of clusters. This value, divided by the total acquisition time and by the active area of the detector, provides the gamma cluster rate (or gamma hit rate), which is the best estimate of the background rate measured by the detector. In the case of the ALICE RPC, since the readout is carried out on the two sides of the RPC, one has two estimates of the photon rate, one for the vertical and one for the horizontal strips. Since the front-end threshold is the same, also the measured photon rate is very similar and for this reason, the average value between the two was chosen as the best estimate of gamma cluster rate. The maximum values of background rates at which the results presented in this chapter were obtained are about 200-300 Hz/cm^2, which are orders of magnitude lower than the nominal GIF++ background rate, reported in [128]. This is because the photon detection efficiency in RPC detectors is of the or-

der of the ‰, so the number of detected photons is much smaller than what is delivered by the source. Furthermore, other detectors. located between the ALICE RPC and the source, contribute to further absorb photons and reduce the intensity of the background on the detector.

The current absorbed by the detector is also measured throughout the data taking procedure. The value is sampled and saved every 2 seconds and it is inserted in a histogram, which is attached to the ROOT output file. Dividing the current density (in μA/cm^2) by the gamma cluster rate (in Hz/cm^2), provides an estimate of the total charge per hit, released in the gas gap. As explained in [139], the current density (ratio between measured current and detector area, I/A, after subtraction of the dark component) circulating in the detector when exposed to a photon flux, can be expressed as:

$$\frac{I}{A} =< Q > \cdot \frac{N_{\gamma-detected}}{A\Delta t} \tag{4.7}$$

where <Q> is the average charge per hit and $N_{\gamma-detected}$/(A Δt) is the gamma cluster rate. This information is very useful to compare the properties of different gas mixtures.

4.4.2 Digitizer data analysis

The same physical quantities cited above can also be measured using data from the digitizer, although one should expect differences due to the fact that the threshold set in the FEERIC cards cannot be easily reproduced when analyzing the digitizer response. Having access to the full waveform, more information can be extracted. Specifically, one can calculate the prompt charge of each signal, as reported in Reference [74], the time over threshold, the signal amplitude and, by using the fast trigger input (TR0, described in 4.3.5) one can also perform time resolution measurements. The disadvantage of using the digitizer is that the amount of data produced is much bigger, with respect to what is obtained when using the TDCs. Indeed, for each trigger 8 channels are readout (7 strips plus the trigger), for each channel 1024 samples are acquired and, on average, 12500 triggers are acquired (2500 beam triggers and 10000 random triggers for gammas) for each high voltage value. The typical size of the output files from a high voltage scan with the digitizer is around $\sim$ 10 GB in text format and around 2 GB in ROOT format. The developed analysis code had to be optimized to work with files of this size and it is able to fully analyze a typical scan in $\sim$ 1-2 minutes. The steps of the analysis are outlined in the following.

The starting point for the digitizer analysis is the sampled waveform for each signal, expressed as a vector of 1024 values (corresponding to 1024 samples), for each strip. Recall from 4.3.5 that the data in channel 0 of the digitizer contain the beam trigger signal (coincidence of the four scintillators), in order to distinguish between a beam event and a background one. Indeed, if the background trigger is present the beam trigger is absent and the content of channel 0 is a flat line. By checking the content of this channel, one is able to distinguish between a muon and a gamma event. This difference is shown in Figure 4.18 Each event is tagged accordingly, for further processing.

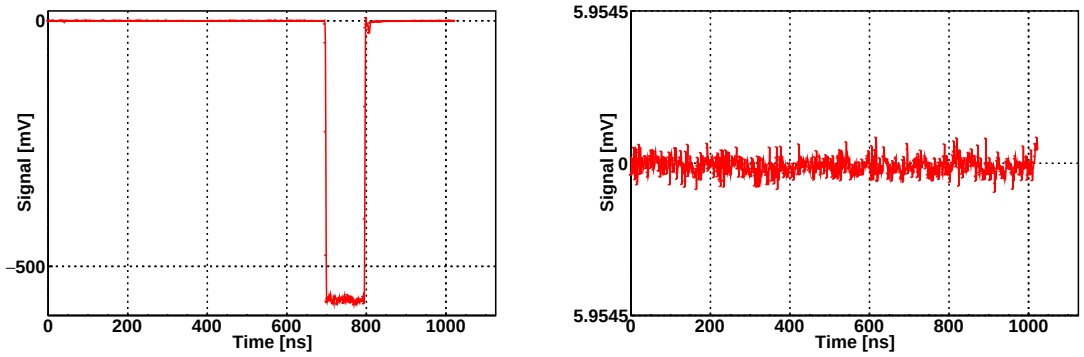

Figure 4.18: Difference between channel 0 response (beam trigger signal) for a muon event (left panel) and a gamma event (right panel). In the gamma event the trigger is absent and this allows one to distinguish between muon and gamma triggers

The values of each sample are expressed as ADC counts. The readings are affected by the internal baseline of the digitizer. In order to convert these values to mV, the average value of the signal oscillations (expressed in ADC counts) is calculated for each trigger in a window between samples 50 and 100, defined as the noise window. This value is then subtracted from each sample value. Once this is done, keeping in mind that the ADC has a resolution of 12 bits, and a V_{pp} = 1 V, the conversion to mV is performed by multiplying the ADC counts by $V_{pp}/2^{12}$. This part of the analysis is common, both for muons and for gammas. The treatment of a muon signal will be described in the following.

Once a signal is tagged as a muon (signal present in channel 0), the first step is to check if the RPC was efficient in the given event. The analysis cycles through the waveforms of the 7 strips and, if the signal in any strip is above a given threshold inside what is defined as the muon window, for at least two samples, the RPC is considered efficient. The threshold has been set to five times the RMS (expressed in mV) of the signal in the noise window, while the muon window has been set by checking manually (using

an oscilloscope) the distribution of the muon arrival time with respect to the trigger (in the case of 1 Gs/s this window is 100 ns wide, while for 5 Gs/s it is 30 ns). All the strips that satisfy the efficiency request are selected for further analysis. In particular, a custom-developed peak finding algorithm is used to locate the signal peaks, to calculate the prompt charge and the time over threshold.

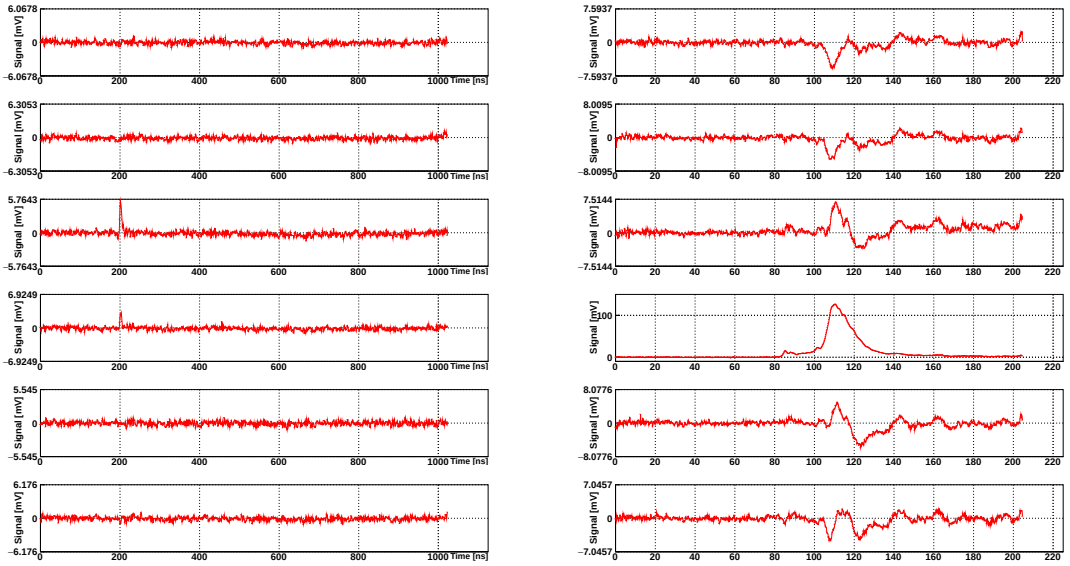

(a) Example of event where the RPC was efficient, with the standard gas mixture. Strips 2 and 3 are efficient in this case

(b) Example of event where the RPC was efficient, with the MIX0. The signals induced by the big signal on channel 4 can be seen. In this case, the algorithm (described later) would classify only strip 4 as efficient

Figure 4.19: Signal examples where the RPC is considered efficient. Standard gas mixture on the left and MIX0 (CO_2/HFO 95%/0% on the right)

Since, in the digitizer readout mode, the signals from the ALICE RPC are readout on the cathode, they are expected to have a positive polarity and almost all the signals collected with the standard gas mixture are characterized by the presence of a single peak with such polarity, so a basic peak detection algorithm is enough to characterize it. With the eco-friendly alternatives tested, the behavior of the RPC is different: the signals could be characterized by multiple peaks, have also negative peaks and, lastly, their amplitude could be much higher than the one of the standard gas mixture and this could lead to cross-talk, of either sign, between neighbouring strips. Due to these facts, a more advanced algorithm had to be developed, to take care of the variety of cases just listed. Figure 4.19 shows in the left panel, the response of the strips with the standard gas mixture. The right panel is an example of RPC response with one of the eco-friendly alternatives tested.

Precisely finding the start of a peak is important to improve the preci-

sion of the charge calculation. The peak finding algorithm is divided in two iterations: the first one runs on the waveform samples, starting from the first sample of the muon window. If a sample is above the threshold, a peak could be present; as Figure 4.20 shows, the first point above threshold does not coincide with the real start of the peak. The real starting point is shown in the figure with a black circle and, to determine it, the algorithm starts from the first point above threshold and it moves backwards by one sample. In each iteration a pair of neighbouring points (current sample and the one just before) is considered and the discrete derivative[2] is calculated between them. It is possible to see that, in the case of a positive peak, the sign of the discrete derivative is always greater than 0, up to the starting point. Indeed, considering the pair formed by the starting point and the point just before, the discrete derivative changes sign, hence one is able to determine the starting point of the peak (a similar observation can be made for negative peaks, changing only the expected sign of the derivative). If the search for a peak has started, the sample where the signal goes once again below the threshold is found, and a similar approach of discrete derivative is applied to find the real end of the peak. Together with the start and end of the peak, also its sign is saved (+1 if positive and -1 if negative). Furthermore, to calculate the time over threshold (time in which the signal is above threshold), the precise intersection between the signal and the threshold is found (this point is explained in detail in 4.5.1.3). At this stage, no requirement is imposed on the peak sign (it can be either positive or negative), the only request is that the peak has to be above threshold for at least 2 samples, for it to be considered a peak. Moreover, the strip must have at least one peak which starts inside of the muon window. If such a peak is not found, the strip is discarded from further analysis.

As described, the algorithm scans the whole waveform and detects all the peaks, independently of their polarity. It returns a list which contains, for each peak, the start/end sample number, the sign, and the start/end of time over threshold. If multiple peaks are found in a strip, the information is reported for all peaks. Subsequently, the second iteration of the algorithm executes a more refined peak search, which performs the separation between ”real” signals and cross talk, as well as the detection of multiple peaks in a given strip (pulses delayed with respect to the initial signal). This takes a different number of steps, according to the number of peaks found:

- If only one peak is found in the data, the above mentioned values are

[2]The term discrete derivative is a loosely used term to describe an analogue of derivative for a function whose domain is discrete

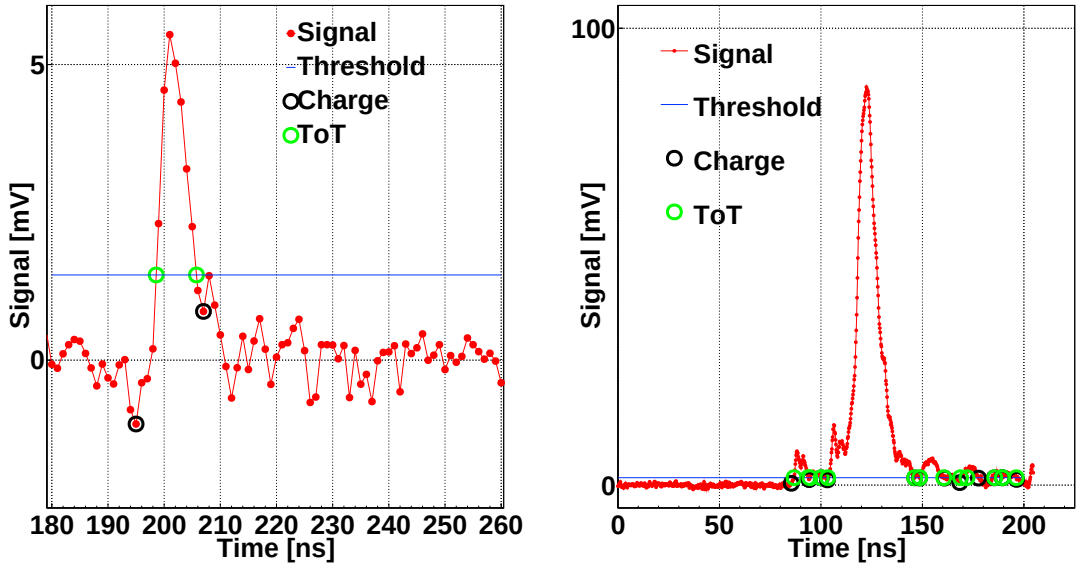

(a) Muon signal example, standard gas mixture

(b) Muon signal example, MIX0

Figure 4.20: Enlargement of muon signals obtained with the standard gas mixture (left) and with an eco-friendly alternative (right), at source off. Highlighted are the start and end of the charge integration interval (in black) while in green are the start and end of the ToT

returned

- If two peaks are found, a distinction in four cases is done, according to the sign of the peak. Let the sign of the peak be indicated by + for positive and - for negative.
  - Case: +/+ both peaks are considered real and charge and time over threshold is calculated as the sum of those quantities for the two peaks.
  - Case: +/- or -/+ the change of sign between the two peaks could be a sign of cross-talk, since it was observed that such a behavior is typical of those signals. Nonetheless, it was also observed that, especially in the case of very large signals (> 100 mV), the positive peak is often preceded by a small negative dip. To distinguish between these two cases, the absolute value of the ratio between the maximum and the minimum amplitude of the peaks is computed, since it was observed that in the case of cross-talk signals this value is close to 1. If it is greater than 1, then the signal is tagged as a real peak and the charge integration process and time over threshold calculation is carried out on the positive peak only. If, instead, the ratio is ≤ 1, the peaks are tagged as ripples (terms used to describe signals resulting from mutual induction) and discarded.

  - Case: -/- both peaks are discarded and the strip is not considered efficient since a positive peak is expected, in accordance to what was described earlier. This type of signals results, with certainty, from cross-talk.

- If more than two peaks are found the algorithm divides them in "super-peaks": it calculates the time difference between each peak and, as long as it this is ≤ 40 samples, the peaks are inserted in the same super-peak. When a super-peak is complete, either because the last peak in the vector is reached or because the distance between two peaks is > 40 samples, the absolute value of the ratio between maximum and minimum in the super-peak is calculated. As before, if this value is > 1, the peak is considered as a real one while, if it is ≤ 1, it is considered as a ripple and discarded. The prompt charge and time over threshold calculations are carried out only on the positive peaks, while negative peaks are discarded from the analysis.

Once the peaks have been identified and classified as real signals, or cross-talk, the prompt charge is calculated by integrating the positive peaks of the signal in the intervals found by the algorithm. The prompt charge is calculated on all the strips with a "good" peak and it is summed over all of them, in order to get the total prompt charge released in the gas. In order to obtain a charge value, the integral is divided by 50 Ω, i.e., the input impedance of the digitizer. The time over threshold is also computed, by summing the time ranges where the positive signal is above threshold, as provided by the peak-finding algorithm described above. For each high voltage point, a charge distribution is created and the classification of the signals as avalanches or streamers is done. As will be further discussed in 4.5.1.2, it was decided to tag as streamers all the signals with a prompt charge > 20 pC. The left panel of Figure 4.21 shows an example of efficiency curve, obtained with the digitizer, together with the average avalanche and streamer charge (the avalanche charge is extracted as the mean of the charge distribution in the interval 0-20 pC while the streamer charge is computed as the average of the charge distribution for charge > 20 pC). The muon cluster size and multiplicity are computed with the same algorithm as for the analysis of TDC data, described in A.3.

For what concerns the analysis of the photon signals, the same peak finding algorithm is applied. This time, peaks can be anywhere in the acquisition window, since the gamma background is uniform. Once all the peaks in a given trigger are found, the clustering is performed with the algorithm

described in A.3 and the cluster rate is calculated as the number of clusters, divided by the active area (strip area * number of strips (7)) and the total acquisition time (number of triggers * duration of an acquisition window). The cluster rate is used to estimate the background rate on the detector. The right panel of Figure 4.21 shows an example of cluster rate curve, as a function of the high voltage, for the standard gas mixture.

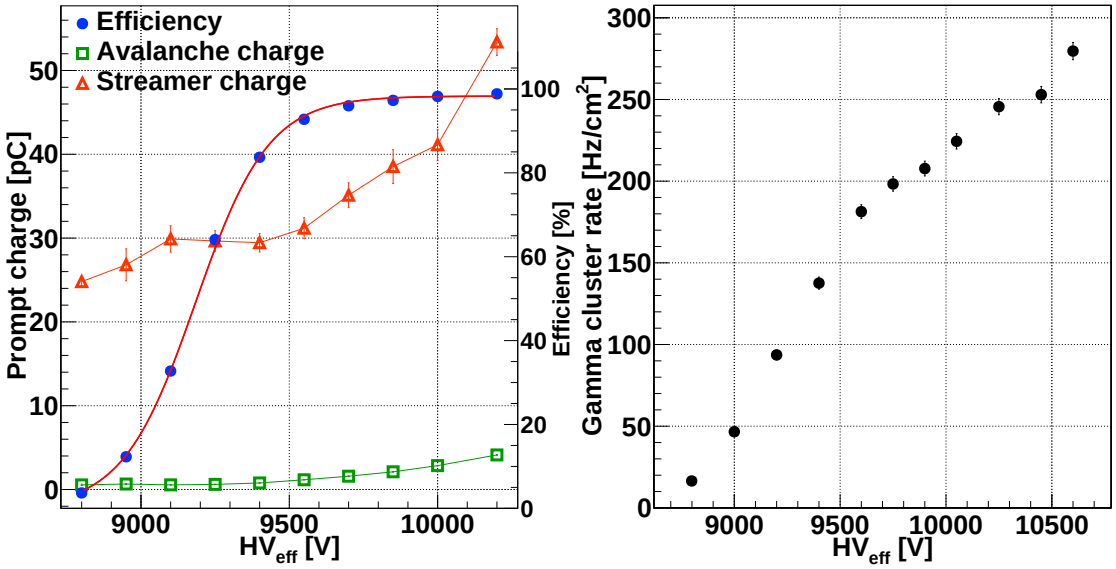

(a) Trend of efficiency, average avalanche and streamer charges, as a function of the high voltage, source off, standard gas mixture

(b) Cluster rate as a function of the high voltage, standard gas mixture, ABS 2.2

Figure 4.21: Example curves with key information extracted by the digitizer analysis. Efficiency, prompt charge and cluster rate. The efficiency curve was fitted with the logistic function of Equation 4.5, while the charge data points are connected with a straight line to guide the eye

4.5 Gas mixture characterization in the beam test

This section contains the results of the beam tests carried out at the GIF++ with the different HFO-based gas mixtures introduced listed in Table 4.1. They have been characterized in terms of detector response to the muon beam (efficiency, cluster size, prompt charge and streamer contamination) and also in terms of response to the photon background (currents, cluster rate and total charge per photon hit). Since several mixtures have been tested, the criterion used to divide the description of the results is based on the estimated working point: the first results discussed are for mixtures with a lower working point than the one calculated for the standard gas mixture (in 4.5.1), while the results for mixtures with a higher working point than the standard mixture will be presented later (in 4.5.2). Note that for

the mixtures with lower working point the data taking has been carried out only with the digitizer. For the mixtures with higher working point, the FEERIC front-end cards have been employed as well. Finally, a comparison among all the mixtures will be performed (in 4.6). Of course, the performance of each gas mixture will be compared to the standard, which is used as a baseline.

4.5.1 Mixtures with lower working point than the standard mixture

This section reports the performance of the ALICE RPC, when operated with three HFO-based gas mixtures with lower working point with respect to the standard gas mixture, namely (with reference to Table 4.1) MIX0, MIX1 and MIX2. These have a HFO content ranging from 0 to 20%. The HFO content has been increased in steps, to study specifically the interplay with the CO_2, since the concentration of the other gases was kept constant. The mixtures were first tested with source off, using the digitizer configuration with 5 Gs/s (200 ns acquisition window) in order to increase the resolution on the measurement. The coincidence of the internal scintillators was used as beam trigger, to reduce the delay between the RPC signal and the trigger (as explained in in 4.3.5).

The mixtures were then tested with the gamma irradiation, up to a hit rate of ~ 250 Hz/cm^2, this time using the 1 Gs/s sampling frequency, due to the delay between the (external and internal) scintillator trigger and the RPC signal (see 4.3.5). All the quantities described in the previous section have been studied under irradiation and they will be compared to the source-off behavior.

4.5.1.1 Source off and irradiation currents

The first parameter that is monitored is the current absorbed by the detector. When the RPCs are exposed to a flux of ionizing particles (such as the photons from the ^{137}Cs source in GIF++, or the muon beam) those will ionize the gas and will cause current to circulate in the detector. This quantity is strictly related to the total charge released inside the gas, indeed if a mixture contains gas(es) with a smaller quenching effect, the amount of released charge will be greater and the current will be higher. Of course, the higher the flux, the higher the current absorbed by the detector will be.

Figure 4.22 shows (in the left and right panel respectively) the results of the current measurements at the working point (with the standard gas

mixture) at source-off and under maximum irradiation (ABS 1, cluster rate $\sim$ 300 Hz/cm^2). The current distribution has two distinct populations: the main peak (at lower values of current) corresponds to the dark current (in the source-off case) or the gamma-induced current (under irradiation) while the other peak refers to the current measured during the muon spill (beam-induced current). The two populations appear because of how the current is measured: every two seconds the value monitored by the high voltage module is saved, independently of the status of the SPS (that is, the measurement can be taken either during or a spill or in between spills).

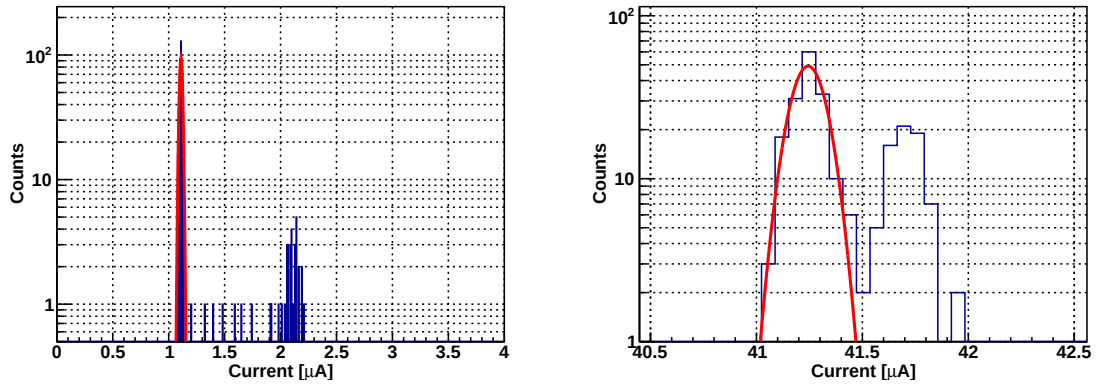

Figure 4.22: Left panel: distribution of measured current when no gamma irradiation is present. Right panel: distribution of measured current at maximum gamma irradiation. Both distributions are taken at the working point with the standard gas mixture

To isolate the gamma-induced (or dark) component of the current, for a given value of applied high voltage, a Gaussian fit is performed around the peak with the greatest amount of counts, which always corresponds to current values measured outside of the muon spill (a spill usually lasts $\sim$ 5 s while the inter-spill period is on the order of $\sim$ 20-30 s). Once the Gaussian interpolation is carried out, its average (with the error provided by the fit) is taken as an estimate of the photon-induced (or dark) current. In the following, all the current values reported correspond to the outcome of the above mentioned process. The gamma-induced current is important for the determination of the average charge per hit, as will be explained in 4.5.3.

Figure 4.23 shows, in the left panel, the current at source off, as a function of the effective high voltage for the mixtures mentioned above. The left panel shows the current values evaluated as the average of the distribution, without performing the subtraction of the beam-induced current. The right panel shows the contribution of the beam-induced to the total RPC current, as difference between the total current and the one obtained from the Gaussian interpolation explained earlier.

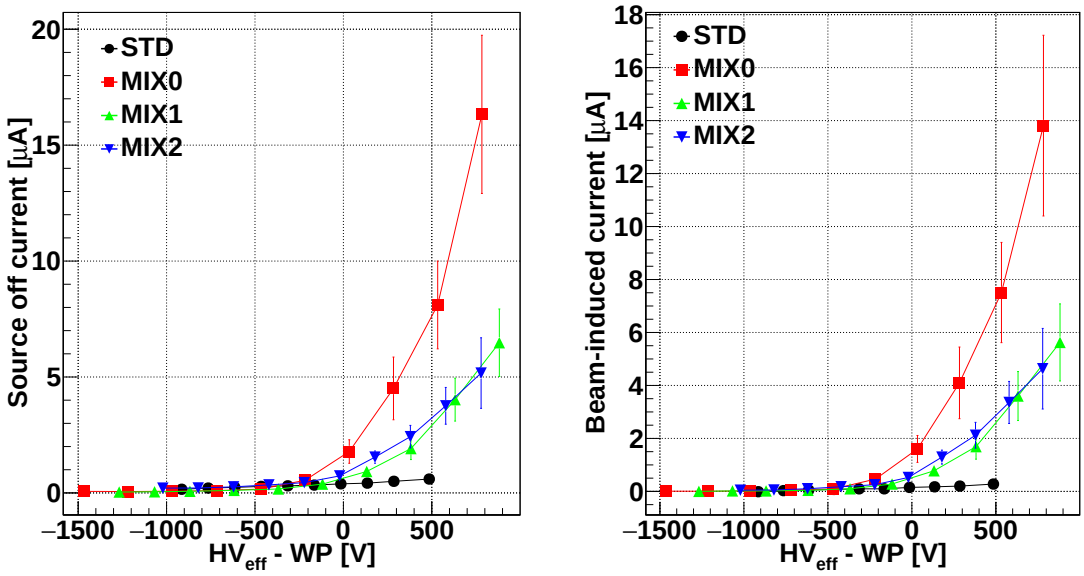

(a) Total absorbed current at source off

(b) Beam-induced current at source off

Figure 4.23: Total current and beam-induced component for three eco-friendly gas mixtures vs standard gas mixture. HFO/CO_2: 0/95 (MIX0), 10/85 (MIX1), 20/75 (MIX2) - source off

The charts in Figure 4.23 report on the x-axis the values of high voltage minus the working point. This choice allows one to compare the results of mixtures with far apart working points (changing the HFO/CO_2 ratio one obtains mixtures with working points that differ by 1-1.5 kV). The comparison between the curves for the eco-friendly alternatives and the standard gas mixture shows that the beam-induced current is always greater for the eco-friendly mixtures than for the standard mixture. Also, the current at a fixed voltage (minus working point) decreases as the HFO concentration increases. As anticipated at the beginning of this section, a higher current hints to a greater charge release in the gas, and this hypothesis will be confirmed by studying the prompt charge distribution.

Since the high voltage power supply was limited to a maximum current of 99 μA (also not to damage the detector), it was not possible to test all the mixtures up to the maximum irradiation, in particular the MIX0 (0% HFO) was tested only at source OFF, since the measured current was close to the power supply limit. Figure 4.24 shows the current (total and with subtraction of the beam-induced component) absorbed at the maximum common irradiation available for STD, MIX1 and MIX2. The relative beam-induced contribution to the total current is reduced, with respect to the source off case, and the correction becomes more and more negligible as the gamma background increases.

Figure 4.25 shows the trend of the current measured at working point (with the subtraction of the beam-induced component) as a function of the

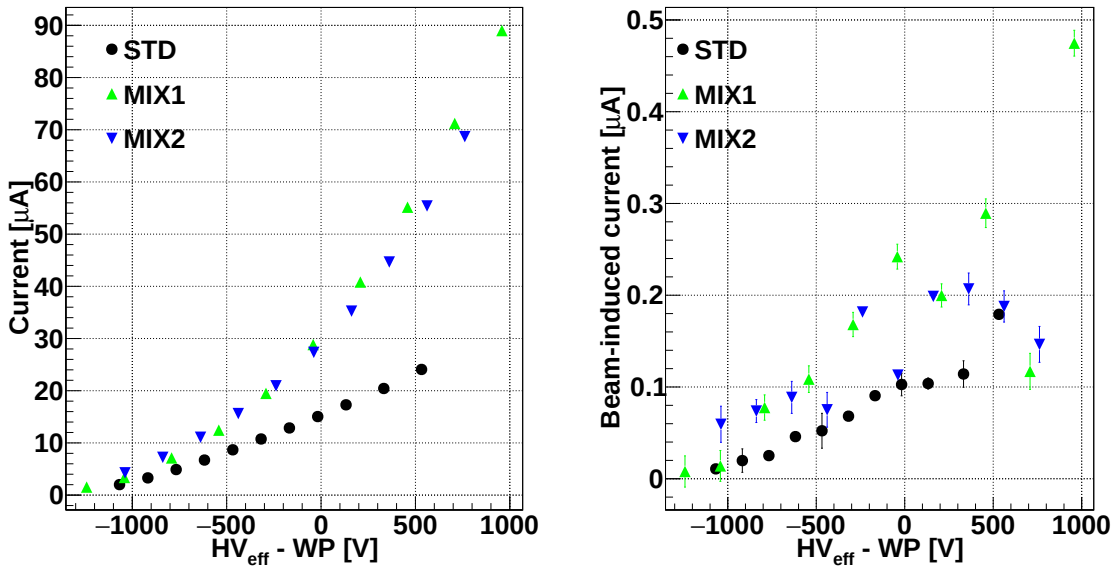

(a) Total absorbed current at ABS 4.6

(b) Beam-induced current at ABS 4.6

Figure 4.24: Total current and beam-induced component for three eco-friendly gas mixtures vs standard gas mixture. HFO/CO_2: 10/85 (MIX1), 20/75 (MIX2) - ABS 4.6

gamma cluster rate (measured at working point). The values of rate correspond to the same set of ABS values across all the mixtures tested: 22, 10, 6.9, 4.6 and 2.2 (from lowest to highest irradiation). Note that for MIX1, the maximum achieved rate corresponds to ABS 4.6 (and not 2.2) due to above mentioned current limit. The source-off value for each mixture is also reported in the chart.

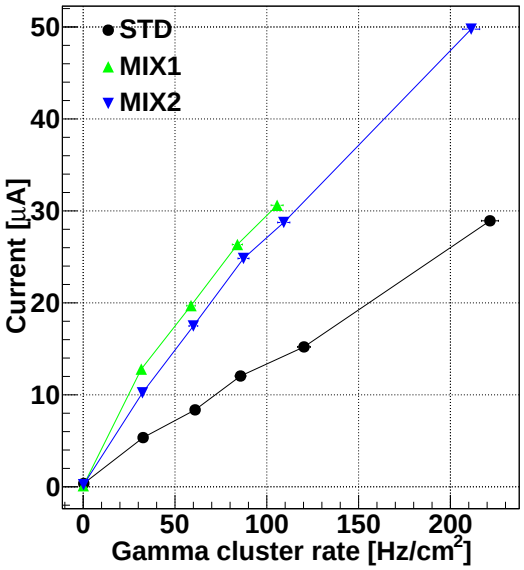

Figure 4.25: Current at working point as a function of the gamma cluster rate measured by the detector. HFO/CO_2: 10/85 (MIX1),20/75 (MIX2)

Figure 4.25 shows that the measured rate for a given ABS is similar for different mixtures, although variations can be observed; those could be at-

tributed to gas mixture-related effects, such as different gamma detection efficiency for different mixtures. The current absorbed by both eco-friendly alternatives is more than doubled (for a fixed value of gamma cluster rate), with respect to the standard gas mixture. This can be explained by considering that the HFO content in these mixtures is low and the quenching effect of the 1% SF_6 is not sufficient to reduce the charge per hit. Recall that, while MIX0 (0% HFO) could not be tested under irradiation due to too high currents, the addition of 10% HFO (in MIX1) already reduces the currents and enables one to work under gamma irradiation.

4.5.1.2 Source-off efficiency, streamer contamination, charge distribution and cluster size

As explained in 4.4.2, the RPC is considered efficient if the amplitude of the signal on at least one strip crosses the threshold, inside the muon window. The streamer fraction is defined as the fraction of signals whose total prompt charge is above 20 pC. Recall that the prompt charge is computed as the sum of the prompt charge of all the strips selected, within the muon time window, by the peak-finding algorithm described in 4.4.2. The streamer threshold of 20 pC was chosen by studying the charge spectrum obtained with the standard gas mixture at voltages higher than the working point, since it offers a clear avalanche/streamer separation[74], as can be seen in Figure 4.26. The spectrum shows two peaks: the one at lower charge values represents the avalanches, the one at higher charge values, the streamers. By performing an interpolation of the two peaks with two Landau functions, one finds that their intersection, which marks approximately the avalanche/streamer separation, is around $\sim$ 20 pC. Note also that the streamer contamination in the standard gas mixture is low, hence a run with 10000 muon triggers (vs the standard 2500) had to be taken in order to observe a statistically significant streamer peak.

It is interesting to look at the charge distribution for the mixtures discussed so far and compare them to the results obtained with the standard gas mixture. This comparison is shown in Figure 4.27 where the prompt charge spectra (at the detector working point) are reported. It was decided to use a logarithmic scale on the x-axis (with logarithmic bins as well) since the charge content spans from about 10^{-2} pC up to some 10^3 pC.

By comparing the prompt charge spectra, some difference with respect to the standard gas mixture (shown in black) can be pointed out. First of all, the streamer contamination is higher, with counts up to few hundred

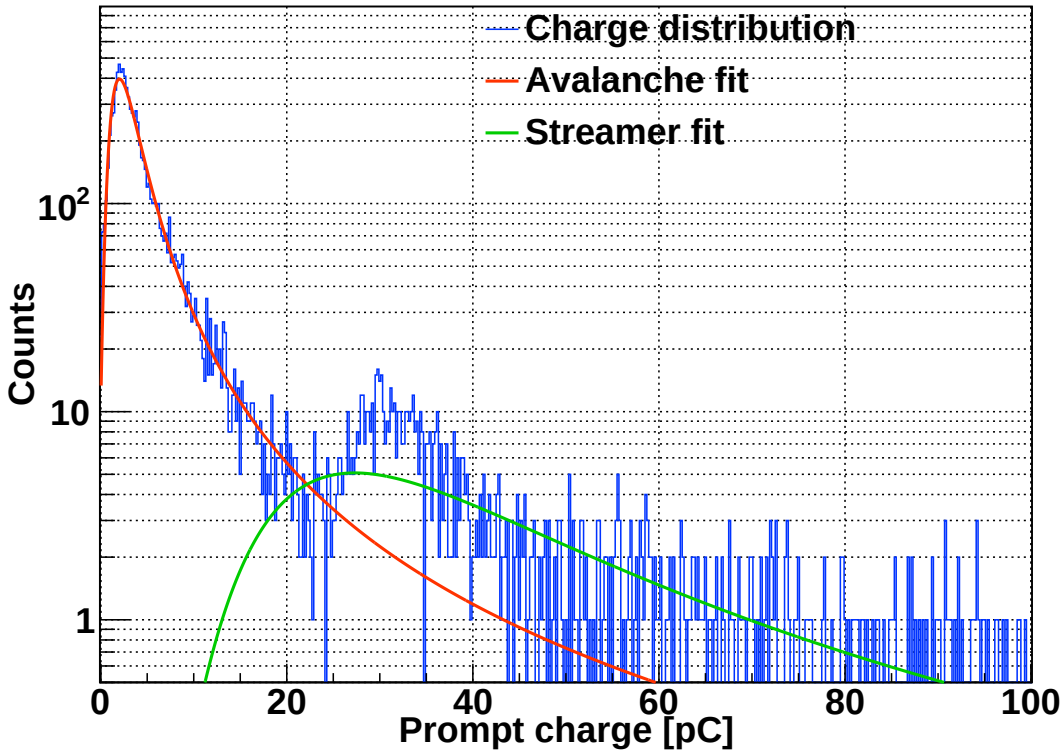

Figure 4.26: Prompt charge distribution for the standard gas mixture in the source off condition. The intersection of the two Landau interpolations is used as a discriminant for the avalanche/streamer classification

pC, especially in the mixture with lower HFO content. Moreover, the actual shape of the distribution is different with respect to the standard gas mixture, which shows a peak around 1 pC. The mixtures with lower HFO concentrations ($\leq$ 20%) shows a greater amount of events with a very low charge (< 0.5 pC) and the charge distribution is broader than the one obtained with the standard gas mixture. This observation can also be related, to the low number of primary (and secondary) ionization clusters in CO_2: if the impinging muon ionizes the gas in a space region close to the anode, the electron multiplication is negligible and only a tiny amount of charge is released in the gas. If, on the other hand, the charge multiplication process develops, the avalanche is not quenched sufficiently by the other gases in the mixture, hence the higher streamer contamination. This observation makes mixtures with a high CO_2 content not suitable to be employed in detectors with a thin gas gap. With the ALICE RPC (a 2 mm gas gap detector) an acceptable value of efficiency (see Fig. 4.28) is reached thanks to the thickness of the gas traversed by the particle, but at the cost of a large streamer contamination. The addition of HFO to the gas mixture has the effect of reducing the quantity of signals with small charge and, at the same time, shifting the first peak (avalanche peak) of the charge distribution to-

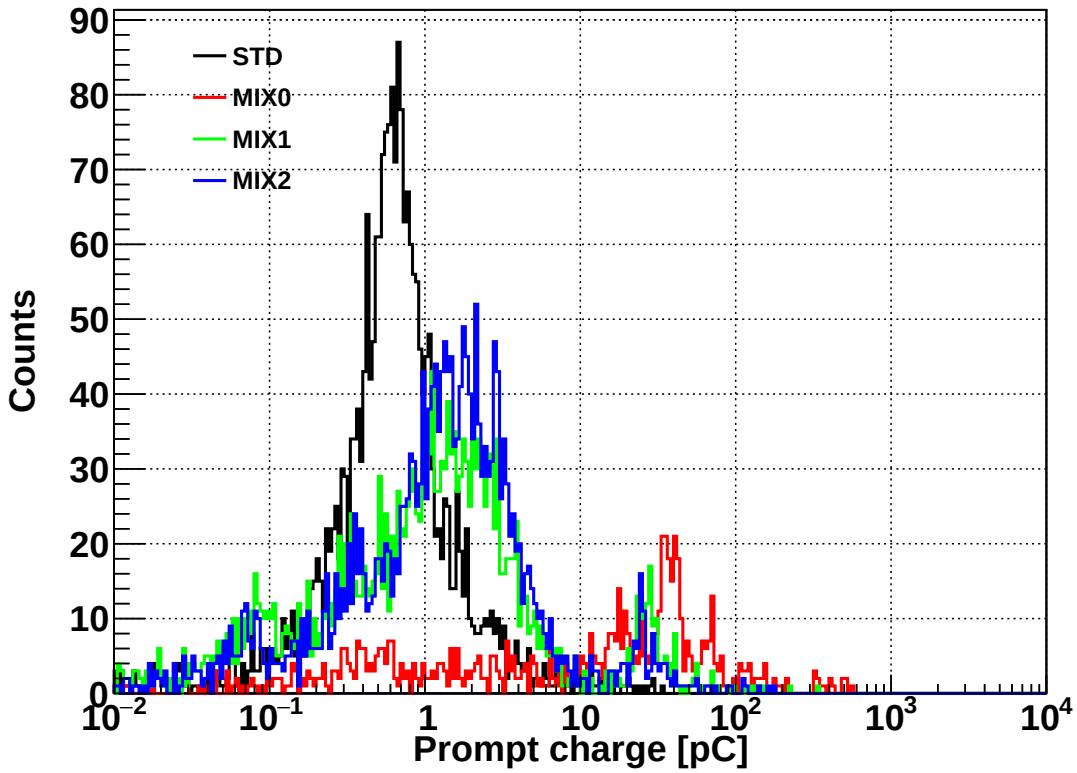

Figure 4.27: Source-off prompt charge distribution at the voltage closest to the working point for the three eco-friendly gases under test, compared to the standard gas mixture. A clear difference in streamer contamination and distribution shape can be observed. HFO/CO_2: 0/95 (MIX0), 10/85 (MIX1),20/75 (MIX2)

wards higher values; it also slightly reduces the population of the streamer region due to the improved quenching properties.

The RPC efficiency curve at source off is shown in the left panel of Figure 4.28, while the right panel contains the streamer probability. The addition of 10% HFO produces a shift of the working point by $\sim$ 1 kV, consistently with what reported in [125, 127]. The number of primary clusters produced by the CO_2 ionization is much smaller, due to its lower density of $\sim$ 1.84 mg/cm^3 [73] with respect to other gases, such as R134a (4.25 mg/cm^3 [140]) or HFO (4.82 mg/cm^3 [140]). This might explain why the maximum value of efficiency reached with MIX0 (which has the largest CO_2 content) is lower than with the other mixtures.

The right panel of Figure 4.28 shows the streamer probability with all the eco-friendly alternatives considered so far. The standard gas mixture exhibits a streamer probability of $\sim$ 2% at working point, while the same quantity is $\sim$ 42%, 21% and 7% for MIX0 (HFO/CO_2: 0/95), MIX1 (HFO/CO_2: 10/85) and MIX2 (HFO/CO_2: 20/75), respectively. Moreover, the standard gas mixture is characterized by a streamer contamination < 10% for voltages up to 500 V above the working point;. Neither MIX0 nor MIX1 exhibit this

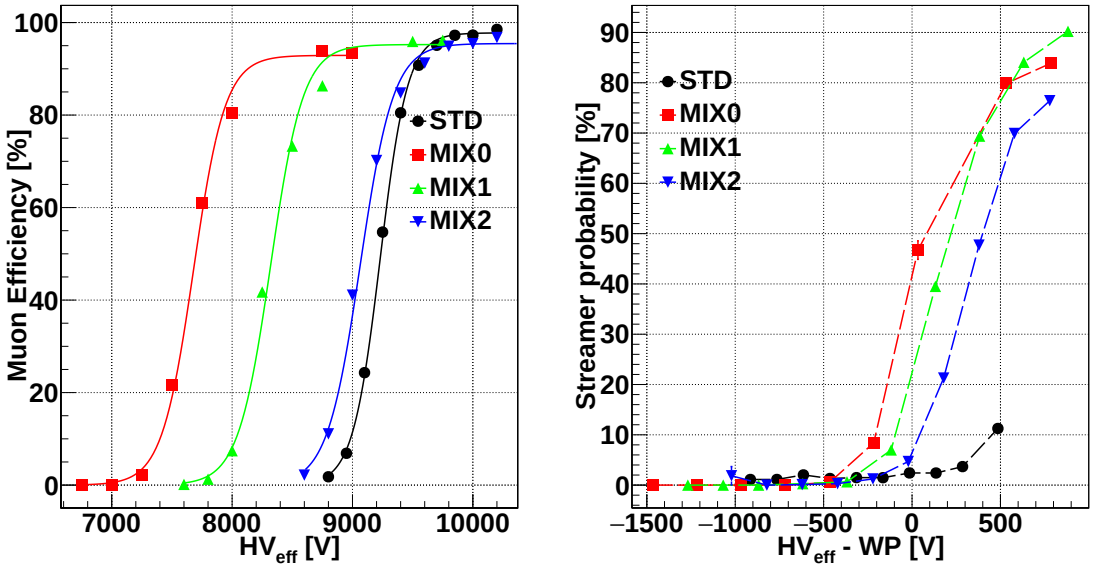

(a) Efficiency as a function of the effective high voltage

(b) Streamer probability as a function of effective high voltage minus detector working point

Figure 4.28: Efficiency and streamer probability curves at source off. HFO/CO_2: 0/95 (MIX0), 10/85 (MIX1), 20/75 (MIX2) - source off

property, showing a streamer contamination above 10% already at the working point. MIX2 is the only mixture for which the streamer probability is lower than 10% at working point, but, as soon as the voltage is increased, the streamer contamination increases rapidly.

Another parameter that has been measured is the muon cluster size. This, is defined as the number of adjacent strips that are fired in an event, within a fixed time window. The clustering algorithm is defined in A.3 and the fixed time window within which hits on adjacent strips are considered a cluster has been set to 15 ns. Indeed, a detailed study of the signal shapes has revealed that, especially for the mixtures with a low HFO content, a large fraction of the events is characterized by a signal amplitude of more than 200 mV (recall that the signals are picked up from the strips without any amplification). When such signals occur, they tend to induce some sort of signal on several readout strips, with very complicated patterns. Some examples are shown in 4.4.2. The cluster size is unambiguously defined only when some front-end electronics is used to discriminate signals, but even when the detector response is studied with the digitizer, it is interesting to compare the number of neighbouring strips that are ”lit up” by the muon signals. The signal-shape-based selection described in 4.4.2 was mainly developed to exclude ”ripple” signals from the prompt charge calculation but, to be consistent with this choice, it was decided to use the same criteria for the cluster size calculation. Note also that the pitch of the ALICE RPC strips

(∼ 3 cm) is relatively large, so tiny variations in the cluster size might be difficult to appreciate. The cluster size at source off for the three mixtures described in this section is reported in Figure 4.29, as a function of the high voltage minus working point.

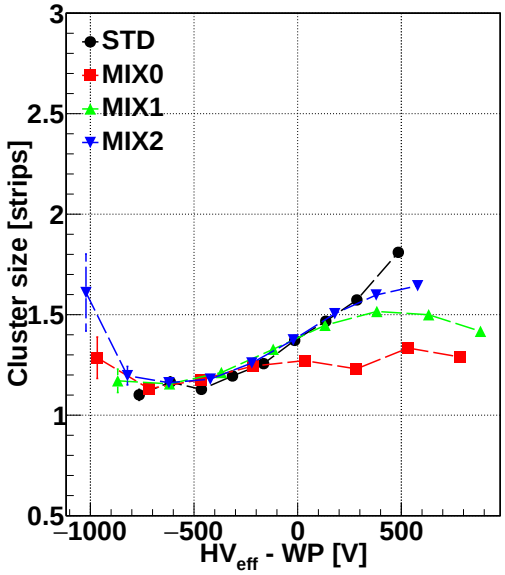

Figure 4.29: Muon cluster size as a function of the high voltage minus working point for the three mixtures described in this section. HFO/CO_2: 0/95, 10/85, 20/75 (MIX0, MIX1, MIX2) - source off

The cluster size values are similar across the different gas mixtures, although it seems that, for the eco-friendly alternatives, the cluster size tends to decrease for decreasing HFO content. This could be explained by the significant fraction of signals with small prompt charge (such as the one shown in panel c of Figure 4.33) in CO_2-rich mixtures. The cluster size values for the eco-friendly alternatives tend to saturate for voltages above the working point, while for the standard gas mixture such saturation is not observed in the explored voltage range. The results of a properly-defined cluster size will be reported for the mixtures studied with the front-end electronics, in 4.5.2.

4.5.1.3 Time resolution and time over threshold

By using the digitizer one can also compute the time resolution of the RPC, when operated with the different mixtures. Recall from 4.3.5 that the digitizer is equipped with a ”fast trigger” input, whose peculiarity is that its input can be digitized and used as a time reference for the other channels. If coupled with the 5 Gs/s sampling frequency (200 ps resolution on the single hit), this allows one to perform precise timing measurements. Recall from 4.3.5 that only the coincidence of the internal scintillators can be connected

to the fast trigger input. Hence, time resolution measurements have been performed only at source off, when the rejection of accidental coincidences (from photon hits) by the external scintillators is not required. For each event, the trigger signal is digitized through the fast trigger input of the digitizer, together with the response from all the RPC strips. The time of the RPC signal is defined as the time when the signal crosses the threshold, while the time of the trigger signal is defined as the time when it crosses 50% of its amplitude. The amplitude of the signal is calculated event-by-event by taking the difference between the minimum value of the signal (since the signal is in NIM logic) and its baseline (average of the sampled values in the interval 10-40 ns). In order to improve the estimation of the threshold crossing time, one can take the two samples closest to the threshold (one just before and one just after) and interpolate the two with a line. The intersection between this line and an ideal horizontal line, corresponding to the threshold, gives a more precise time measurement that can be used to compute the time resolution of the detector (see also [141]). This process is repeated for all the events at fixed value of high voltage and a histogram is filled with the difference between the trigger time and the RPC time. Finally a Gaussian fit is performed to the distribution and the standard deviation σ of the Gaussian provides an upper limit to the RPC time resolution (since it is also affected by the jitter of the trigger scintillators and photomultipliers). It can happen, especially for the mixtures with a low HFO content, that a strip responds with a signal with multiple peaks (as explained in 4.4.2): in order to deal with this, only events with a single peak are taken into account for the timing measurements. Moreover, if more than one strip is fired in a given trigger, the time of each strip is considered in the calculation, as long as it is characterized by a single peak. The left panel of Figure 4.30 shows the procedure to determine the precise time of the trigger signal while the right panel shows the distribution of the time difference between the RPC and trigger signals, for the standard gas mixture at the detector working point. It also displays the value of the σ from the Gaussian fit of the peak.

The time resolution values, measured with this method, are reported in the left panel of Figure 4.31 as a function of the high voltage minus the working point. The error on the measurements is defined as the error on the parameter resulting from the Gaussian fit. The data points at lower voltages have a bigger error due to the smaller number of efficient events, used to compute the time resolution. The results are similar for the different gas mixtures (although, it seems, slightly better for the eco-friendly alternatives than for the standard). The dependence on high voltage is small at voltages

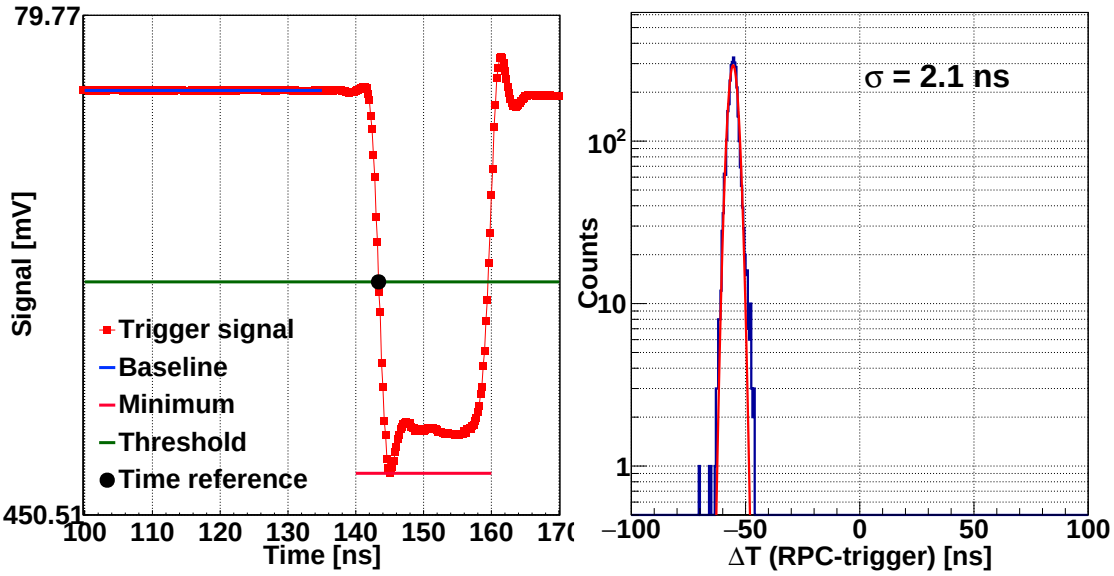

Figure 4.30: Left panel: enlargement of fast trigger signal and time estimation with the technique shown in [141]. The signal in red is the trigger. The lines called *baseline*, *minimum* and *threshold* represent the baseline oscillations, the minimum of the signal and the threshold, defined as the 50% of the signal amplitude respectively. Right panel: distribution of time difference distribution between RPC and trigger signals for the standard gas mixture at working point - source off

around the working point.

A complementary observation can be made by looking at the distribution of the time over threshold (ToT) of the same signals: recall that for the time resolution measurements, only signals with a single peak are considered. For the same signals, the time over threshold is defined as the total time interval in which the signal is above threshold. The ToT distributions shown in the right panel of Figure 4.31 illustrate the different behavior of the mixtures: the mean value of ToT for the standard gas mixture is ~ 7 ns, with no count exceeding the 15 ns mark. The other mixtures show some different features: first of all, the region where the ToT is < 1 ns becomes more populated (due to the low-charge events shown in 4.5.1.2); second, the mean value of the distributions is increased, with counts up to values that correspond to the whole acquisition window. This is not desirable in LHC applications, where the RPCs must provide correct bunch crossing identification down to 25 ns[142]. It appears that this effect becomes less severe as the HFO concentration increases in the mixture.

Last, by studying the correlation between time over threshold and signal charge, one can discover another feature of the low-HFO gas mixtures, i.e., the presence of events with a modest charge content (< 20 pC) but with a high value of ToT. These events are characterized by a small amplitude in terms of mV (~ 10 mV) but they tend to remain over threshold for a long

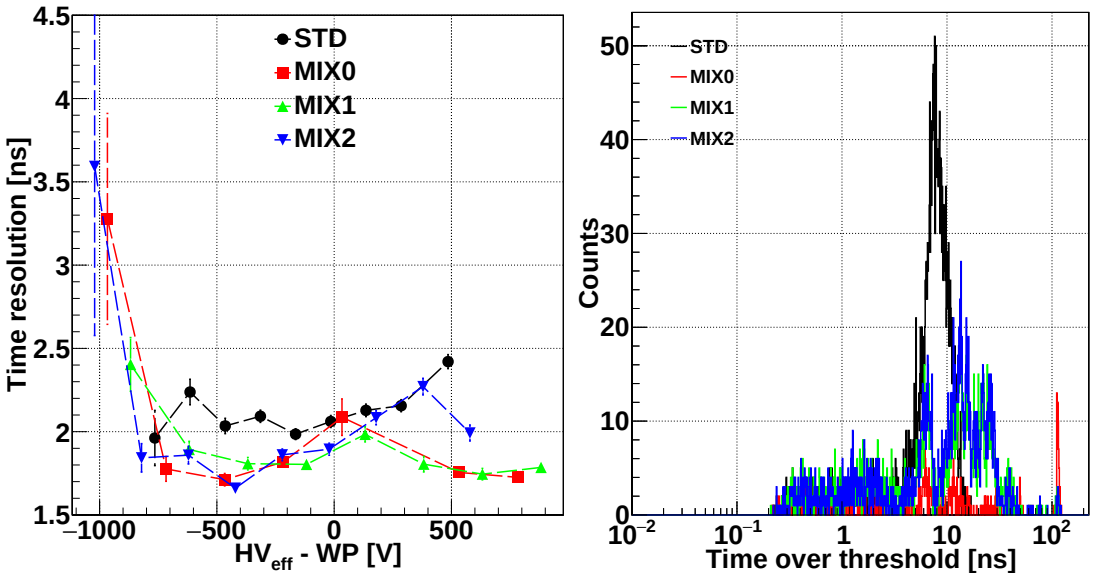

(a) Time resolution of the RPC (upper limit) as a function of the high voltage minus working point

(b) Time over threshold distribution measured at the detector working point for the mixtures discussed thus far

Figure 4.31: Left panel: time resolution trend as a function of the high voltage minus working point. Right panel: time over threshold distributions at working point for the mixtures tested. HFO/CO_2: 0/95,10/85,20/75 (MIX0, MIX1, MIX2) - source off

time (> 40 ns). This type of events is not found with the standard gas mixture. Indeed, in this case, a higher time over threshold always corresponds to a higher prompt charge. This correlation is shown, at the working point, for the different gas mixtures, in Figure 4.32. The events at very high charge and TOT values represent the streamers. The events close to 0 pC and small ToT are instead those that contribute to the small charge values observed in 4.27.

The chart in Figure 4.32 contains the information on all the events characterized by a single peak signal on the strip. The maximum ToT reported is close to 120 ns because the start of the muon window is set at 80 ns and the total acquisition window is 200 ns long. Together with the spectrum, three examples of signals are shown in Figure 4.33. The signal in the top left has a ToT $\sim$ 50 ns and a prompt charge of $\sim$ 3.2 pC, due to the presence of a long tail with low amplitude. The one in the top right is a signal with a ToT of $\sim$ 16 ns and a prompt charge $\sim$ 33 pC, due to its high amplitude of more than 200 mV (note that for the standard gas mixture, a signal with the same ToT would correspond to a much lower value of prompt charge, $\sim$ 5-6 pC). Last, in the bottom panel, an example of a short and low-charge-content event is reported: the ToT is $\sim$ 2 ns and the integrated charge is $\sim$ 0.06 pC. The blue horizontal line in all the charts represents the threshold value. All these signals were obtained with the mixture without HFO (MIX0). By looking

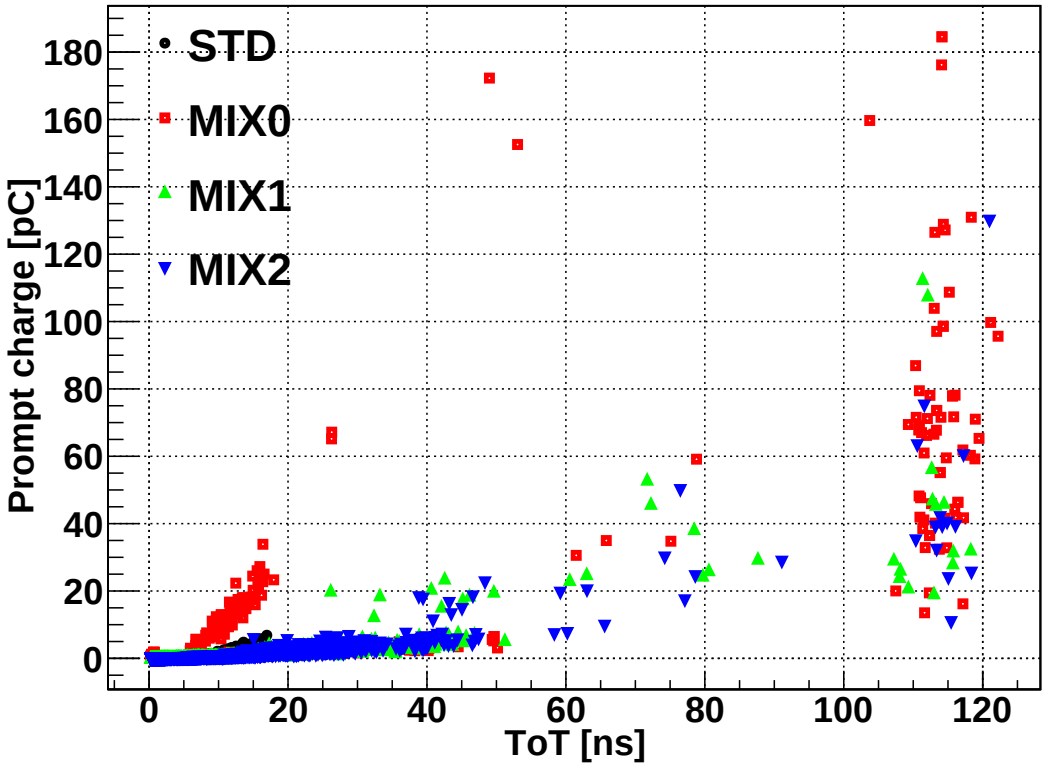

Figure 4.32: Correlation between prompt charge and time over threshold for the different mixtures tested. Results shown at working point and no irradiation. Different event populations can be distinguished: low charge and low ToT, more present in the eco-friendly gases rather than the standard gas mixture. Events with high ToT but relatively small charge and events with a short ToT and relatively high charge are a feature specific to the eco-friendly alternatives. HFO/CO_2: 0/95,10/85,20/75 (MIX0,1,2)

at Figure 4.32 one can see that adding 10% HFO to the mixture the component of signals with small ToT (between 5 and 20 ns) and high charge (> 10pC) tend to disappear, and the correlation between prompt charge and ToT tends to flatten.

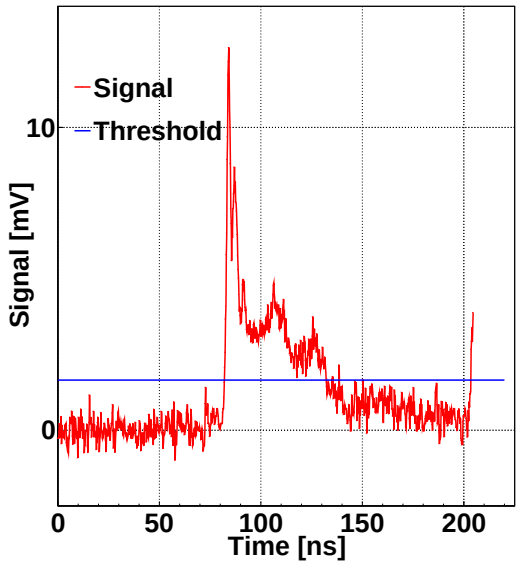

(a) Signal with long ToT but small charge (50 ns/3.16 pC)

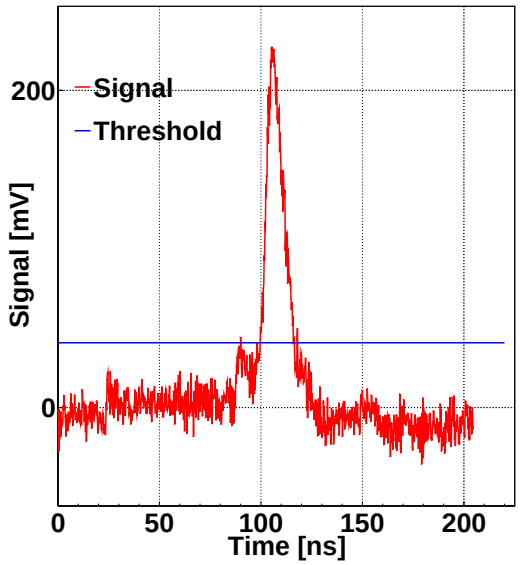

(b) Signal with short ToT but high charge (16 ns/33 pC)

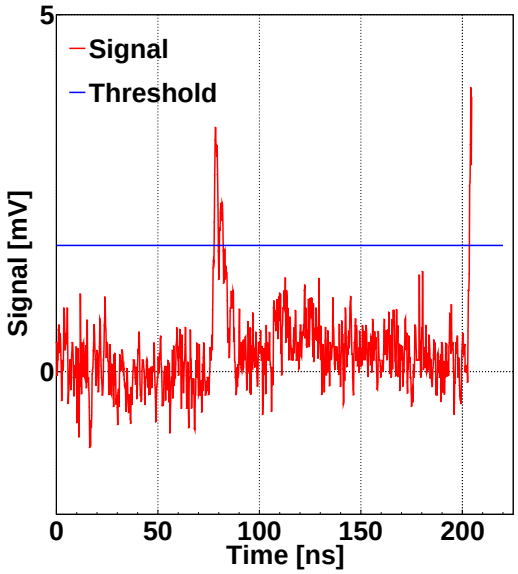

(c) Signal with short ToT and small charge (2 ns/0.06 pC)

Figure 4.33: Example of signal shapes with peculiar characteristics in terms of ToT and prompt charge

4.5.1.4 Results under irradiation

This section discusses the behavior of the ALICE RPC when operated with the mixtures described above and exposed to the gamma flux of the GIF++ ^{137}Cs source. As stated before, the RPCs have been exposed to a gamma hit rate up to $\sim$ 250 Hz/cm^2 and, as mentioned in 2.3.3, this background rate is about 2.5 times higher than the maximum expected value in ALICE (already including a safety factor of 2) during the LHC RUN3 and RUN4[112].

Nevertheless, it is useful to study the response of the detectors at such high rates to find the upper limit of the rate capability granted by the mixtures.

When the detectors are exposed to the gamma flux, the circulating current increases correspondingly, as shown in Figure 4.25. The current flows through the gas and, to complete the circuit, it passes through the bakelite electrodes that enclose the gas gap. This current generates a voltage drop across the bakelite electrodes and this, in terms, reduces the actual high voltage that is applied to the gas, i.e., the one available for the charge multiplication process. This is shown in Figure 4.34, where a sketch of a RPC detector is presented, together with a high voltage generator, connected to the RPC. The power supply provides the voltage *HV*, which is then split into the voltage drop across the gas, HV_{gas} and the drop on the bakelite electrodes, indicated as R^*I since the bakelite behaves as an Ohmic resistor (R is the resistance and I is the circulating current), hence the drop is proportional to the current and the bakelite resistance.

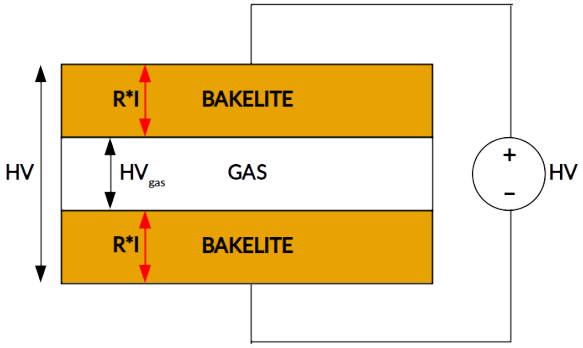

Figure 4.34: Sketch of the RPC connection to the high voltage module with explicitly indicated the voltage drop across the bakelite electrodes, due to the current circulating in the detector

The reduction of the actual voltage applied to the gas (due to the drop on the bakelite electrodes) causes a decrease in the detector gain (as reported in Section 2.2) for a given value of applied high voltage, which, if not negligible, translates into a shift of the efficiency plateau towards higher voltages. The shift is more pronounced if the absorbed current increases (for example if the irradiation is increased). The shift of the efficiency plateau can be observed in the left panel of Figure 4.35, where the efficiency curves (as a function of the high voltage) for different background rates are reported, together with the curve corresponding to the no irradiation condition (in black). In the same figure, the curves of the streamer probability for the different irradiation conditions are also reported. The efficiency curves have been fitted using the logistic function introduced in 4.4.1 while the lines in the streamer probability curves have been added for visual aid.

By looking at those curves, it appears that also the streamer contamination decreases for increasing irradiation.

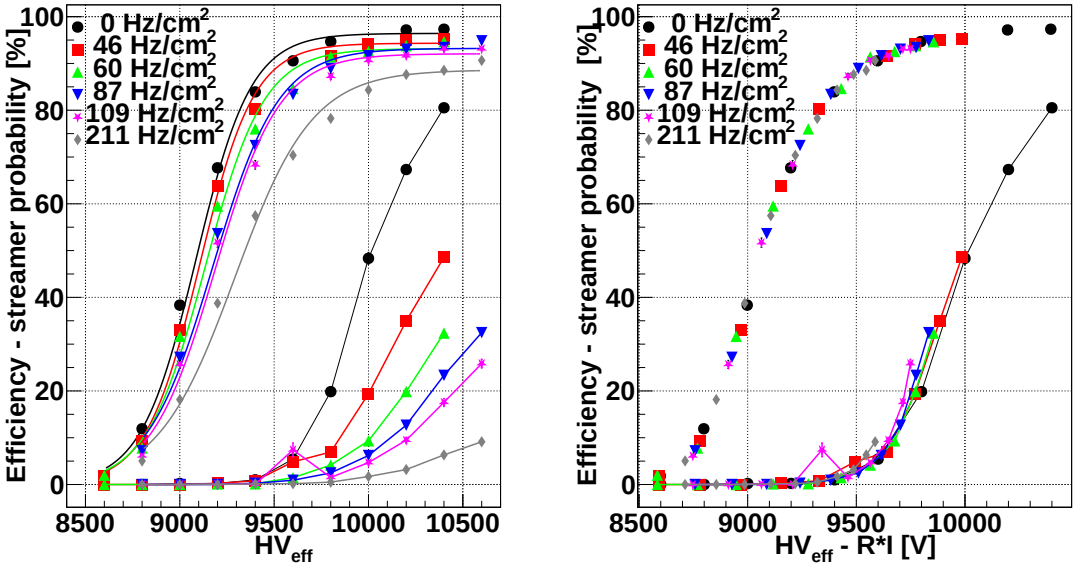

(a) Efficiency and streamer probability curves as a function of the effective high voltage for MIX2. The shift of the efficiency plateau towards higher values is shown together with the apparent decrease of the streamer probability

(b) Efficiency and streamer probability curves as a function of HV_{gas} for MIX2. The curves tend to superimpose with one another in this case

Figure 4.35: Effect of showing efficiency and streamer probability curves under irradiation as a function of the effective high voltage (left panel) and HV_{gas} (right panel).

Since the voltage drop on the bakelite is proportional to its resistance and the current flowing through the detector, by measuring both quantities, the real voltage across the gas (HV_{gas} in the following) can in principle be determined as the difference between the applied high voltage (HV in the following) and the term R*I (that is, HV_{gas} = HV - R*I). If no other "parasitic" voltage drops are present, then, by plotting the efficiency as a function of HV_{gas}, the observed shift between the curves should disappear. The values of the absorbed current are saved by default during a run and periodic resistivity measurements, performed with the Ar method described in Section 2.2, are performed to monitor the evolution of this quantity in time. The measurement closest to the beam test was carried out one month before and it provided a resistance value of R = $1.24 \cdot 10^7$ Ω. The right panel of Figure 4.35 shows the trend of efficiency and streamer probability for MIX2 as a function of HV - R*I (with the value of R just mentioned). One can see that the efficiency curves are superimposed with one another, and the same holds for the streamer probability curves. Beside the superposition of the curves, the comparison of the two panels in Figure 4.35 reveals another feature: especially for higher rates, it appears that the efficiency curves reach

a plateau (at lower and lower values of efficiency as the rate increases), if they are plotted against the effective high voltage, while this behavior is not reproduced if the efficiency is shown as a function of HV_{gas}. This can be explained by considering the voltage drop across the bakelite planes: even if the effective high voltage is increased, the drop on the bakelite increases as well and, effectively, the increase of HV_{gas} is much smaller than that of HV, and the increase of efficiency is consequently also small. This gives the visual impression of the curve reaching a plateau, due to the "wrong" scale on the x axis. If one then observes the trend as a function of HV_{gas} (shown in the right panel of Figure 4.35), it is possible to see that the points that appeared to be in the plateau in the left panel of Figure 4.35, are actually still in the rising portion of the efficiency curve. The same can be inferred for the streamer probability: the reason why it appears to be decreasing, for increasing irradiation, is because the actual voltage applied to the gas is lower than what is provided by the high voltage module, hence the gas gain is lower and the charge multiplication process leads to smaller released charge in the gas gap.

The efficiency curves under irradiation for STD and MIX1 are reported in Figures 4.36 and 4.37.

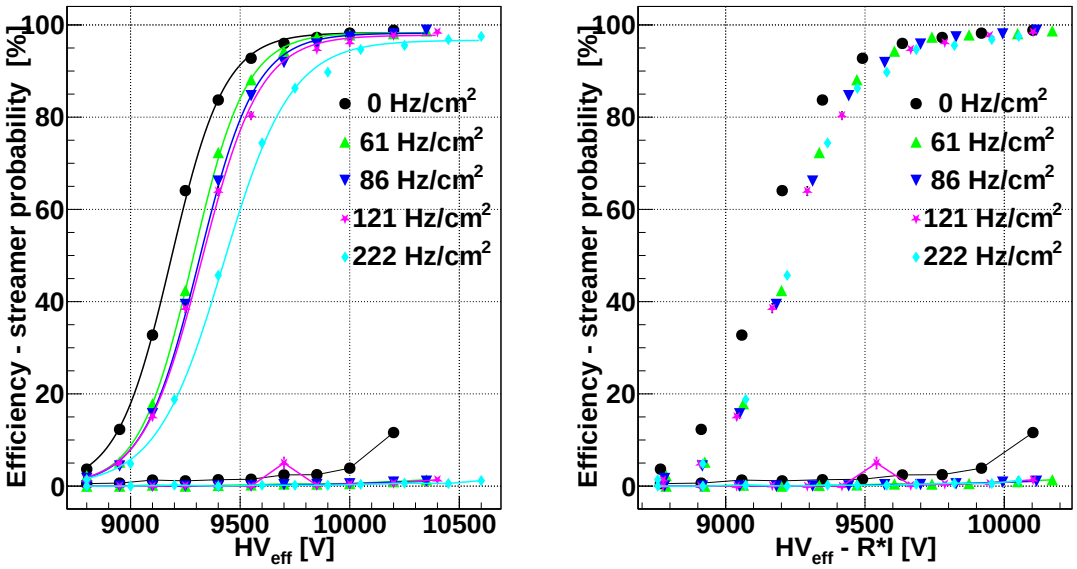

(a) STD efficiency - streamer probability curves as a function of HV_{eff}

(b) STD efficiency - streamer probability curves as a function of HV_{gas}

Figure 4.36: STD gas mixture

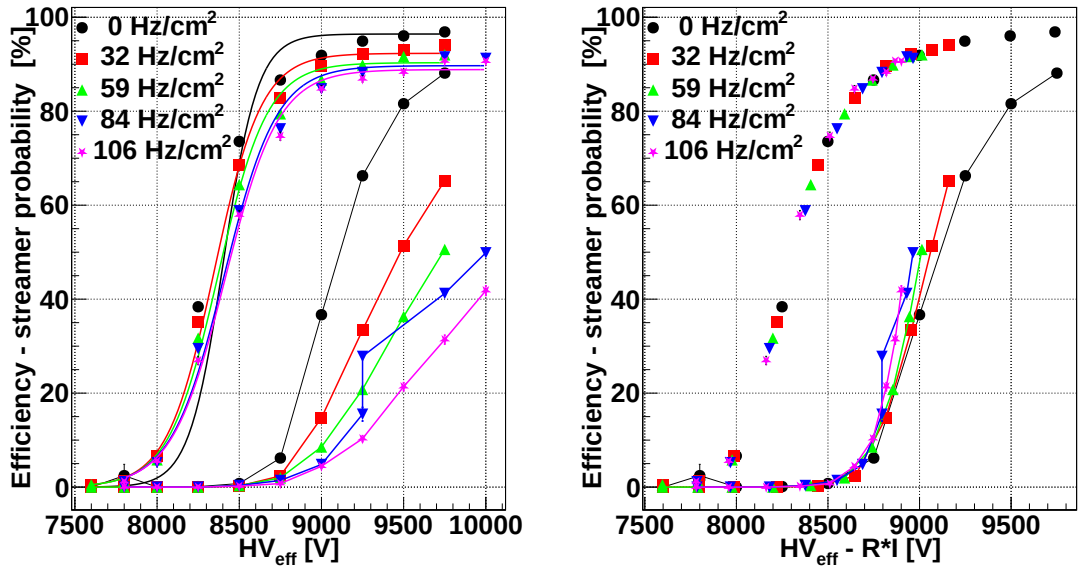

(a) MIX1 efficiency - streamer probability curves as a function of HV_{eff}

(b) MIX1 efficiency - streamer probability curves as a function of HV_{gas}

Figure 4.37: MIX1 gas mixture

To visualize the behavior of all the mixtures as a function of the gamma-induced counting rate at a glance, another format to show the results will be adopted in the following. The data presented in this new way is reported in Figure 4.38, where only the values of efficiency and streamer probability at working point are shown as a function of the measured gamma rate. Since the efficiency curves are shifted towards higher voltages, the value of working point is itself shifted and has been re-calculated under each irradiation condition. Figure 4.38, also reports the value of the efficiency at the working point of the source-off condition. Of course, due to the shift of the efficiency curves discussed above, the efficiency drop at the source off working point is greater than what is measured if the working point is re-calculated for each irradiation condition. It is interesting to monitor this efficiency reduction since in a real-life scenario one might not be able to easily change the applied high voltage according to the particle rate. With this idea in mind, the choice of the source off working point represents the worst case scenario and it is interesting to study it.

Table 4.4 reports the results shown in the chart of Figure 4.38, together with the values of working point estimated from the logistic function interpolation. It is important to monitor both the shift of working point with increasing irradiation, as well as the efficiency drop with respect to the source-off condition. For the standard gas mixture, the efficiency drop at the (re-determined) working point is $\sim$ 2.5 pp (percentage points), from source off to maximum irradiation; while for both MIX1 and MIX2 this value is $\sim$ 8 pp.

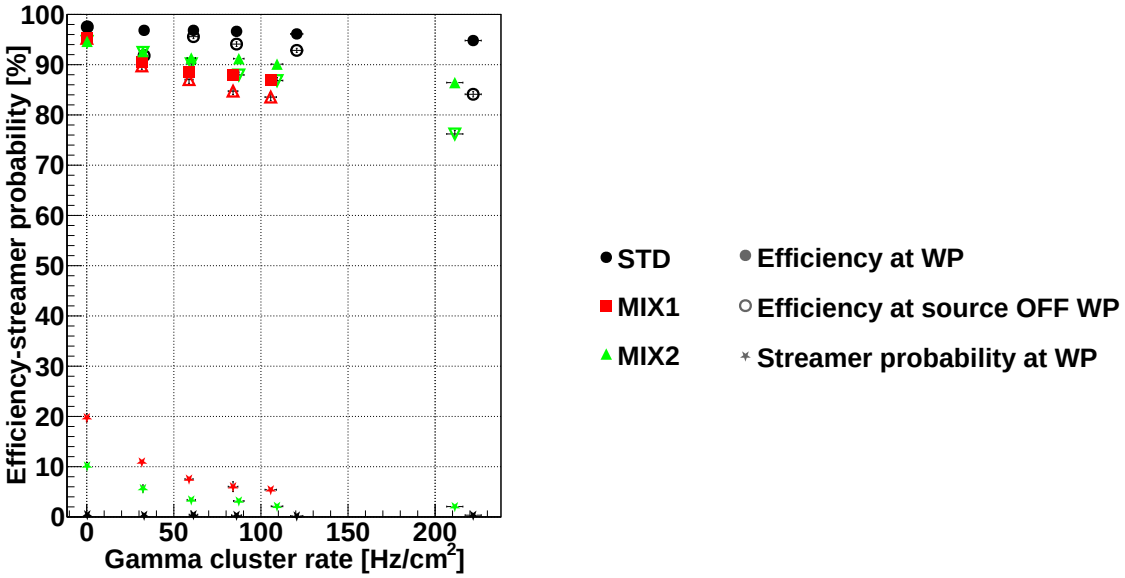

Figure 4.38: Efficiency and streamer probability computed at working point and source-off working point as a function of the gamma rate on the detector for the different mixtures. HFO/CO_2: 10/85,20/75 (MIX1, MIX2). The source-off condition is also reported in the chart

As reported in 2.3.3, the most exposed RPCs in ALICE, during the LHC RUN3 and RUN4, will have to sustain a hit rate of $\sim$ 100 Hz/cm^2 (already including a safety factor of 2). The efficiency drop (at the re-calculated working point) is $\sim$ 1.2/1.3 pp for the standard gas mixture while it is $\sim$ 7 pp for MIX1 and $\sim$ 5 pp for MIX2. The source-off efficiency value at working point is slightly lower for the HFO-based gas mixtures, with respect to the standard gas mixture, due to the high CO_2 content, which translates to lower number of primary/secondary ionization clusters and reduced detection efficiency. The working point shift is similar across all mixtures but due to the higher currents circulating with the eco-friendly gases (which leads to a greater voltage drop across the bakelite), the maximum efficiency reached under irradiation appears to be much lower, with respect to the standard gas mixture. All in all, the performance of the ALICE RPC with the first three eco-friendly alternatives is worse than with the standard gas mixture, especially in light of the streamer contamination and of the efficiency drop for a background rate of $\sim$ 100 Hz/cm^2. Hence, none of them can be considered as a strong candidate for operation in ALICE. However, the results obtained show that the performance of the detector is improving as the HFO content is increased. Following this observation, it was decided to further increase the HFO content to observe whether the RPC response would improve further. The results from these mixtures are reported in the following section.

The muon cluster size was also measured under gamma irradiation. Since

Mix	$WP_{off}[V]$	Rate [$\frac{Hz}{cm^2}$]	$\epsilon_{WP_{off}}$	WP [V]	ϵ_{WP} [%]	Str prob[%]
STD	9716	0.3	97.5	9716	97.5	0.44
		33	91.8	9890	96.9	0.3
		61	95.6	9793	96.9	0.5
		86	94.2	9843	96.8	0.3
		121	92.8	9868	96.1	0.2
		222	84.1	10027	94.8	0.3
MIX1	8861	0.09	95.2	8861	95.2	20
		34	89.8	8923	90.7	11
		62	87	8962	88.6	8
		83	84.7	9028	87.8	6
		110	83.6	9042	87.1	5
MIX2	9666	0.03	94.7	9666	94.7	10
		36	92.5	9678	92.6	6
		65	90.2	9742	91.4	4
		95	87.9	9838	91.2	4
		115	86.6	9838	90.1	2
		230	76.2	10048	86.4	2

Table 4.4: Summary table of working point at source off (WP_{off}), re-calculated working point (WP), efficiency and streamer probability (at the re-calculated WP) at different counting rates for the mixtures discussed so far. HFO/CO_2: 10/85,20/75 (MIX1, MIX2)

the real voltage applied to the gas is reduced, due to the drop measured on the bakelite electrodes, the gas amplification is also reduced. This leads to a reduction of the avalanche spatial size in the gap and to a smaller cluster size for increasing irradiation. The trend of the cluster size measured at working point (re-calculated for each irradiation condition), as a function of the background rate, is reported in Figure 4.39.

The slight decreasing trend observed may be ascribed to the reduction of the actual high voltage applied to the gas for increasing irradiation.

4.5.2 Mixtures with higher working point than the standard mixture

This subsection reports the results obtained with mixtures that have a higher working point, with respect to the standard gas mixture. They will be addressed to as MIX3, MIX4, MIX5 and MIX6, with CO_2/HFO ratio 69/25, 65/30, 60/35 and 55/40 respectively. The results are organized in a similar fashion as 4.5.1, starting with the absorbed current, with and without irradiation, moving then to the performance with no irradiation (efficiency, time resolution, charge) and, last, to the performance under irradiation. The last

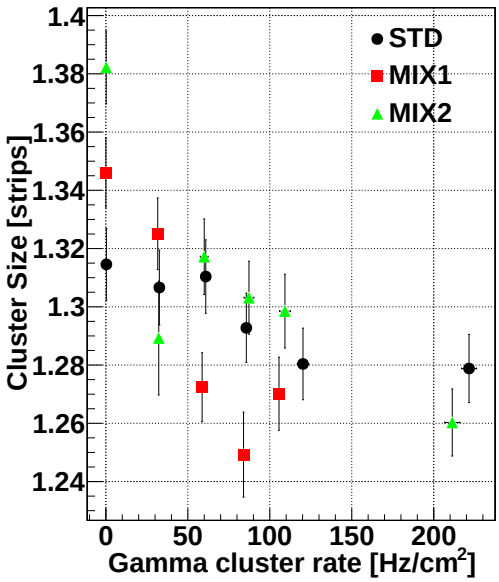

Figure 4.39: Trend of the cluster size measured at working point (re-calculated for each irradiation condition), as a function of the measured gamma cluster rate for the gas mixtures tested HFO/CO_2: 10/85,20/75 (MIX1, MIX2). The observed decreasing trend can be explained by considering the decrease of the real high voltage applied to the gas

part of this section contains a summary of the results, comparing all the mixtures described in this as well as in the previous subsection.

In addition to the results obtained with the digitizer, this section discusses also the performance of the ALICE RPC when the ALICE front-end electronics is used to discriminate the signals, and TDC modules were used to acquire them. It will be indicated whether a given result is obtained with the digitizer or with the front-end electronics.

4.5.2.1 Source-off and irradiation currents

As in 4.5.1, the first results shown here concern the current absorbed by the detector at source off, with the different gas mixtures under test. The effect of the beam-induced current was also studied. The left panel of Figure 4.40 reports the trend of the total current as a function of the high voltage minus the working point, while the right panel shows the beam-induced component of the current. Recall that the beam induced current is subtracted by performing a Gaussian fit to the main peak of the measured current distribution, for a given high voltage value (see 4.5.1.1 for a detailed description of the procedure).

The effect of the higher HFO content can be observed as a reduction of the beam-induced component of the current, with respect to the mixtures discussed in 4.5.1 and shown in Figure 4.23. The absorbed current at working point is, however, almost doubled with respect to the standard gas

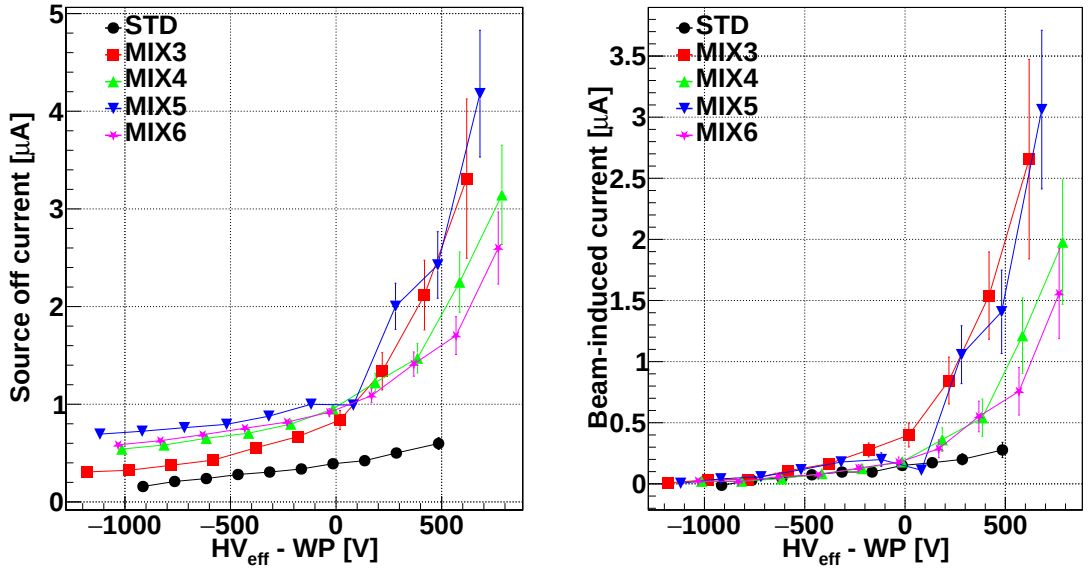

(a) Total absorbed current at source off

(b) Beam-induced component of current absorbed at source off

Figure 4.40: Total current and beam-induced component for four eco-friendly gas mixtures compared to the standard gas mixture. HFO/CO_2: 25/69,30/65,35/60,40/55 (MIX3, MIX4, MIX5, MIX6) - source off

mixture.

The current measured at the detector working point (with the subtraction of the beam-induced component), under irradiation, is shown in Figure 4.41 as a function of the measured gamma rate. Also in the case of these mixtures, the relative importance of the beam-induced component, tends to become less significant as the background increases. The maximum value of rate corresponds to ABS 2.2 for all mixtures.

The absorbed current seems to be compatible among the different mixtures tested, which suggests that the average charge per gamma hit at working point is similar for all the HFO-based gas mixtures. The current is $\sim$ 1.6/1.7 times higher with respect to the standard gas mixture (for the same irradiation condition).

4.5.2.2 Source-off efficiency, streamer contamination, charge distribution and cluster size

As it was done earlier for MIX0, MIX1 and MIX2, the efficiency response with source off will be discussed here, together with the streamer contamination results. The same algorithms discussed in 4.4.2 have been applied to the data obtained with these other mixtures. The addition, with respect to the previous section, is that the detector performance with two of the mixtures discussed here (MIX3 and 5), in terms of efficiency and cluster

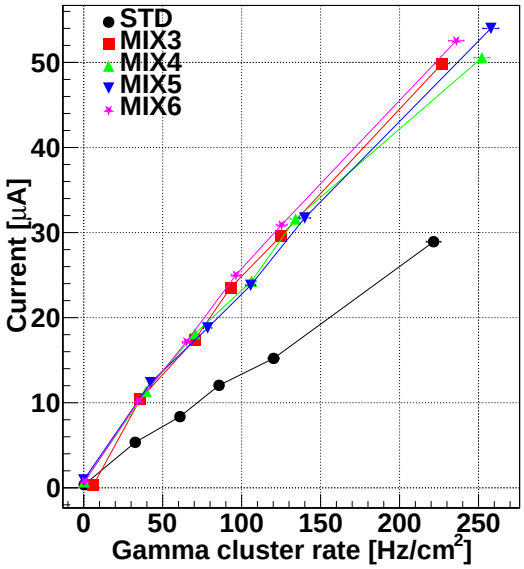

Figure 4.41: Current at working point as a function of the gamma rate measured by the detector. HFO/CO_2: 25/69,30/65,35/60,40/55 (MIX3, MIX4, MIX5, MIX6)

size, has been studied also using the ALICE front-end electronics (FEERIC), and the results will also be shown and discussed. For this purpose, was decided to set the same FEERIC thresholds that are currently being used in the ALICE detector[133], which correspond to ± 100 mV, after amplification. According to [86], this value roughly corresponds to a threshold in charge, before amplification, of ∼ 170 fC. The thresholds were set using the Arduino code, discussed in 4.3.4.3 and were monitored during the data taking period.

Figure 4.42 shows, in the left panel, the efficiency curves for all the mixtures under test, obtained with the digitizer, while the right panel shows the trend of the streamer probability, as a function of the high voltage minus the working point.

If the HFO concentration increases, the efficiency curves tend to shift towards higher voltages. The shift of roughly 1 kV every 10% more HFO, already shown in 4.5.1.2, can be also observed here. Moreover, since the density of the gas mixture (hence the number of primary ionization clusters, as reported in Section 2.2) is gradually increased (as the HFO concentration increases), the maximum value of efficiency tends to become compatible with the one obtained with the standard gas mixture.

For what concerns the streamer probability, the chart in the right panel of Figure 4.42 shows that it tends to decrease as the HFO concentration increases. The streamer probability at the working point is close to that of the standard gas mixture for all the mixtures shown in the chart, and it is around 5%. This is a promising result, since streamers are significantly

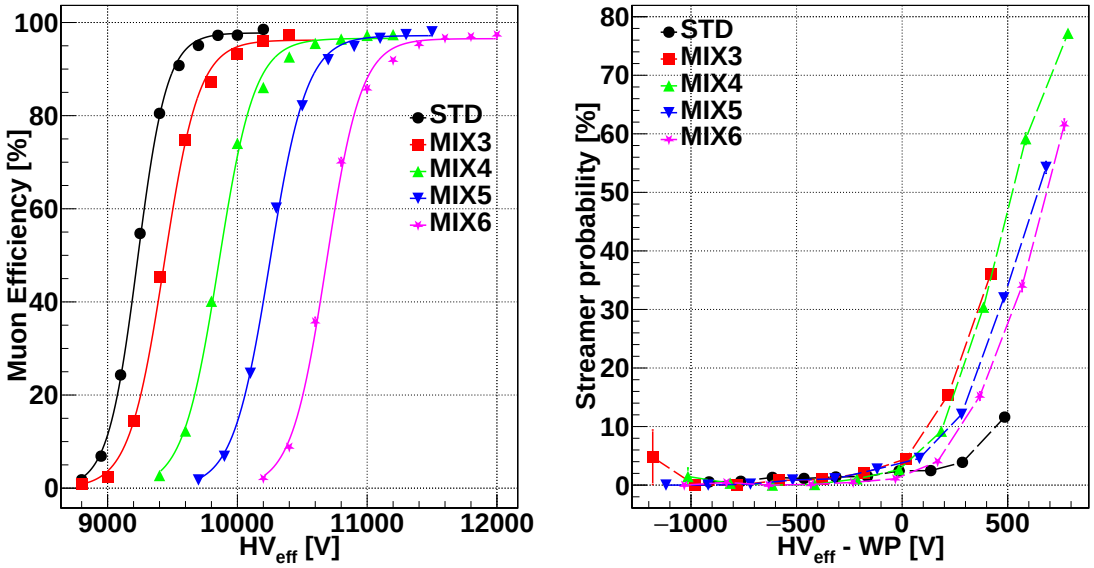

(a) Efficiency curves vs effective high voltage

(b) Streamer probability as a function of effective high voltage minus detector working point

Figure 4.42: Efficiency and streamer probability curves at source off. HFO/CO_2: 25/69,30/65,35/60,40/55 (MIX3, MIX4, MIX5, MIX6)

more suppressed than in the mixtures shown in 4.5.1. The main issue to be pointed out is that the high voltage range where the streamer probability remains under 10% is only around 150 V for MIX6 and it is even lower for the others. The drawback of MIX6 is that it is the one with highest source-off working point ($\sim$ 1.5 kV higher than the standard gas mixture) and (similarly to the other gas mixtures described here) the absorbed current is $\sim$ 1.6 times that for the standard gas mixture under the same irradiation and for the same efficiency.

The efficiency as a function of effective voltage at source off, obtained using the front-end electronics, for the standard gas mixture, MIX3, and MIX5 is shown in Figure 4.43. The algorithm to compute the efficiency is reported in 4.4.1: recall that the ALICE RPC is readout on two perpendicular strip planes and the so-called 2D efficiency is reported. This is computed by requesting that at least one hit in both strip planes is present upon a muon trigger. If one compares the working point obtained with the digitizer and the front-end electronics, the latter is found to be 100-150 V lower, with respect to the former. This is due to the fact that the threshold set in the digitizer analysis (5 times the baseline RMS as measured in the noise window) is somehow arbitrary, and turns out to be higher than the 100 mV used with the front-end boards. Moreover, the stricter event selection criteria applied when processing the data from the digitizer (such as the minimum duration above threshold imposed) might also contribute to the higher working point

values observed.

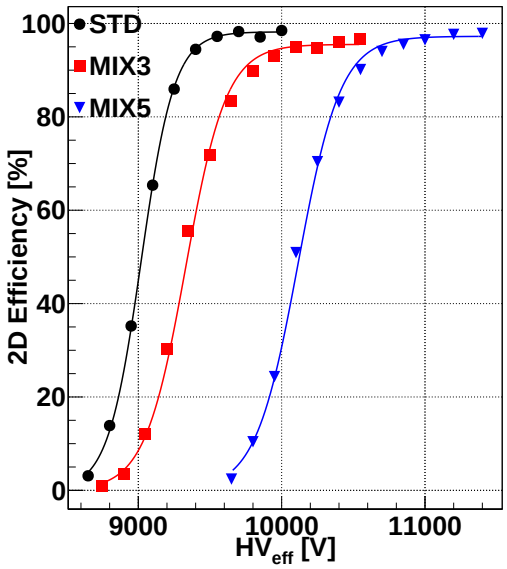

Figure 4.43: Efficiency curves obtained without irradiation, using the new ALICE front-end electronics. HFO/CO_2: 25/69,35/60 (MIX3, MIX5)

The efficiency curves have been fitted using the same logistic function as with the digitizer and the working point has also been estimated in the same way. The streamer probability at the FEERIC working point, interpolated from the curves obtained with the digitizer analysis and shown in the right panel of Figure 4.42, is $\sim$ 3% to 4% but, as previously stated, it tends to grow quite rapidly for small voltage increases (differently from the standard gas mixture).

The comparison between the prompt charge distributions at the voltage closest to the working point (in the source-off condition) for the HFO-based gas mixtures and the standard one is discussed next. The prompt charge distributions have been obtained using the digitizer and are shown in Figure 4.44. The left panel displays the results for the standard gas mixture, compared to MIX4 and MIX6, while the right panel shows the standard gas mixture, MIX3, and MIX5.

A few comments can be made, by comparing these spectra with the ones shown in Figure 4.27 that referred to mixtures with a lower HFO content. First of all, the number of counts at very low charge is reduced, making the charge spectrum more similar to the one obtained with the standard gas mixture. The avalanche peak becomes more and more pronounced as the HFO concentration increases and the population of the streamer regions decreases. Moreover, the width of the avalanche peak is reduced and, for MIX6, the peak is almost superimposed with the one of the standard gas mixture. The actual value around which the distributions are peaked is

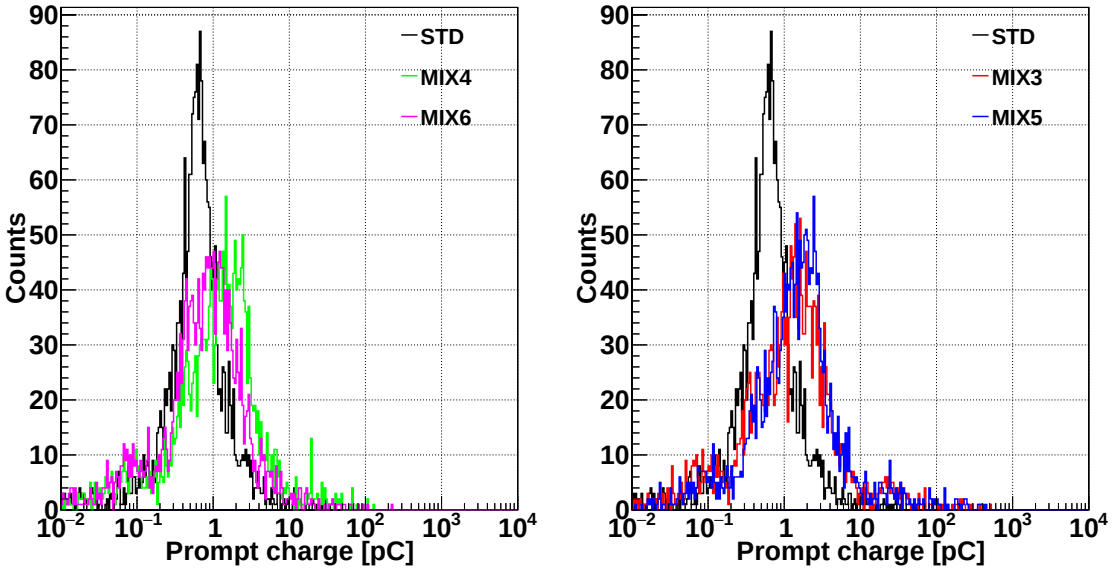

(a) Source-off prompt charge distribution for standard, MIX4 and MIX6

(b) Source-off prompt charge distribution for standard, MIX3 and MIX5

Figure 4.44: Source-off prompt charge distribution for the mixtures under test. HFO/CO_2: 25/69,30/65,35/60,40/55 (MIX3, MIX4, MIX5, MIX6)

greater than the standard gas mixture for all the mixtures, but it moves towards the value of the standard if a greater HFO fraction is added to the mixture. These observations seem to point in the direction that adding more HFO makes the RPC operation closer to the behaviour with the standard gas mixture. Although, as already stated before, this increases significantly the detector working point.

The other quantity that was studied both with the digitizer and the front-end electronics is the mean cluster size. The results of this measurement (at source off) are reported in Figure 4.45. The left panel shows the results obtained with the digitizer, while the right one is for FEERIC. Since in the latter case the RPC is readout on both planes, the average cluster size of the horizontal and vertical strips is reported. The results for both readout systems are reported as a function of the high voltage minus the working point and, although they refer to the same mixtures, it is possible to observe a difference in their behavior. For the digitizer the cluster size does not increase above 2 strips, while the one obtained from the front-end electronics, reaches up to 4/5 strips.

The different behavior can be explained by looking at the signal shapes obtained with the eco-friendly alternatives, specifically referring to what was said in 4.5.1.4, where it was shown that, especially for the mixtures with lower HFO content, some signals due to cross-talk between strips are present. The peak-finding algorithm eliminates this kind of events while

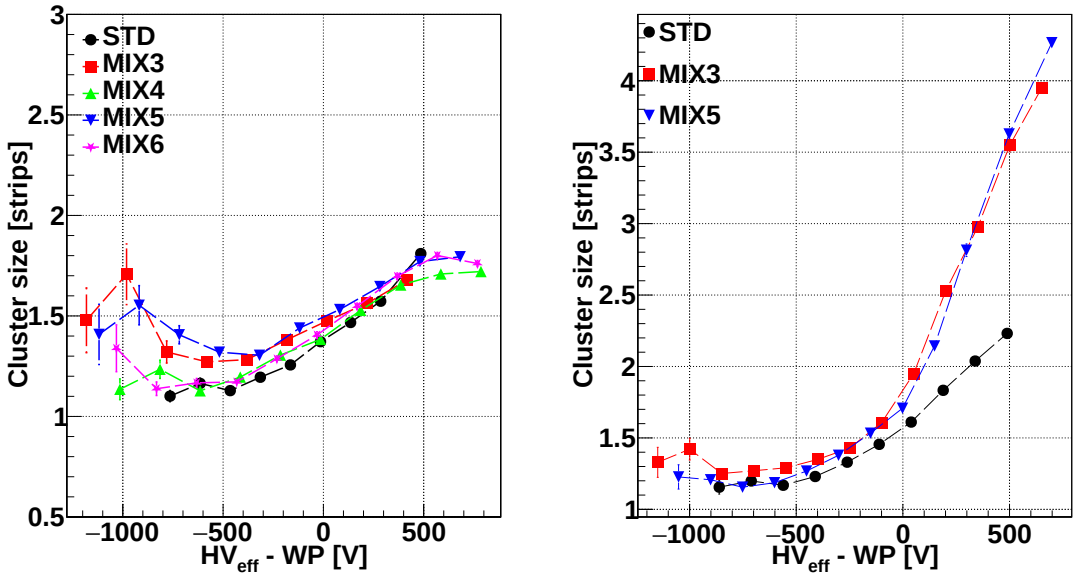

(a) Mean cluster size obtained from the digitizer data**(b)** Mean cluster size obtained from the FEERIC data

Figure 4.45: Trend of the mean cluster size as a function of the high voltage minus the working point for all the mixtures tested. HFO/CO_2: 25/69,30/65,35/60,40/55 (MIX3, MIX4, MIX5, MIX6) - source off

the front-end electronics accepts at least some of them, leading to an increase of the mean cluster size. The different sensitivity to ripple signals is probably the cause for the saturation at high voltage values, which is observed with the digitizer and not with FEERIC. While the digitizer studies are useful to understand the detector response, the results obtained with the front-end electronics are the ones that will matter, once a decision on which gas mixture to be employed in ALICE has to be taken, since the RPC signals are to be discriminated by FEERIC. To conclude, the cluster size at working point is similar for all the mixtures tested, although at higher voltages the increase with HV is faster with the eco-friendly gas mixtures than with the standard one, according to the results obtained with the front-end electronics. Moreover, no definite hierarchy among mixtures with different HFO content seems to emerge (note however that, given the relatively large strip pitch of ~ 3 cm, it may not be possible to appreciate small differences between mixtures).

4.5.2.3 Time resolution and time over threshold

The (upper limit to) the time resolution of the RPC, operated with the gas mixtures described in this section, has been determined as discussed in 4.5.1.3 and the results of this measurement are shown in Figure 4.46.

The results confirm what was already shown in Figure 4.31, which showed that the time resolution at working point for the eco-friendly gas mixtures is

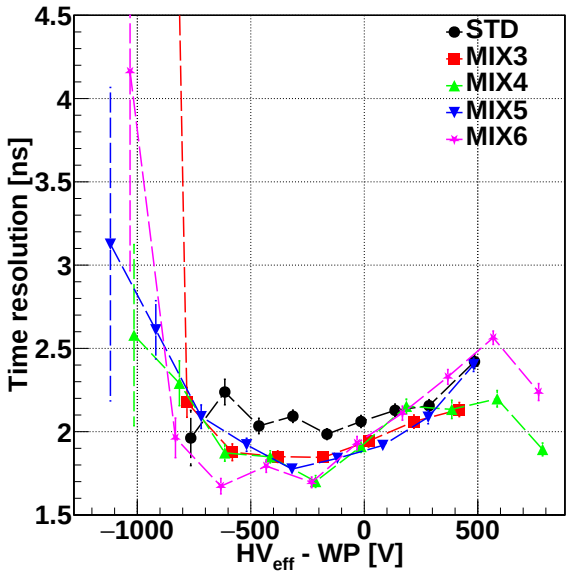

Figure 4.46: Time resolution as a function of HV at source off for the gas mixtures tested. HFO/CO_2: 25/69,30/65,35/60,40/55 (MIX3, MIX4, MIX5, MIX6)

the same or even slightly improved with respect to the standard gas mixture. One can conclude that the time resolution is not degraded by the presence of HFO and CO_2 in the gas mixture.

The time over threshold (ToT) distribution at the working point has also been studied and the results are reported in Figure 4.47. They have been split again in two panels, one for MIX4-6 and one for MIX3-5.

By looking at the ToT distributions one notices that, opposite to what happens in the case of the standard gas mixture, two peaks are present. The one peaked around 3-4 ns represents the avalanche signals, including those with very low charge, such as the one shown in panel c of Figure 4.33, which are still present although in reduced fraction. The second peak, around 10 ns, contains mostly signals with a modest charge content (as the event shown in panel a of Figure 4.33), as well as the streamers. This type of signals is shown in panels a and b of Figure 4.33. This region is also populated by avalanches, with a longer duration than in the standard gas mixture. The region above 30 ns contains the pure streamer signals and it seems to becomes less populated as the HFO content in the gas mixture increases. Contrary to the standard gas mixture, where a clear separation between avalanche and streamer signals is found, all the HFO-based gas mixtures show a more gradual transition between the two modes of operation, through events such as the ones shown in panels a and c of Figure 4.33.

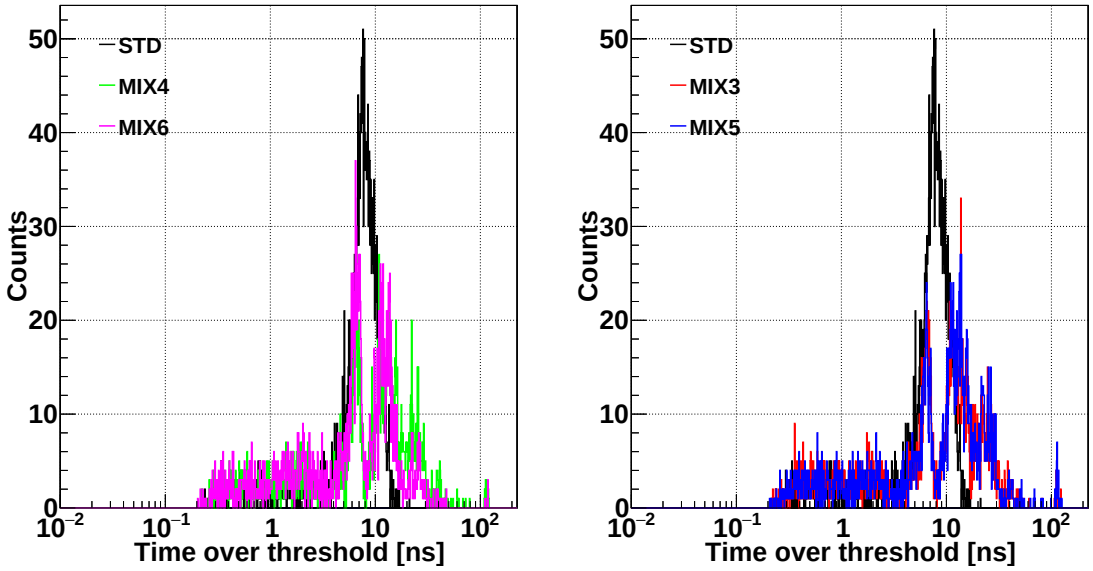

(a) Time over threshold distribution for standard, MIX4 and MIX6

(b) Time over threshold distribution for standard, MIX3 and MIX5

Figure 4.47: Source-off time over threshold distribution for the mixtures under test. HFO/CO_2: 25/69,30/65,35/60,40/55 (MIX3,4,5,6) - source off

4.5.2.4 Results under irradiation

This section contains the description of the detector performance under irradiation. The RPC response was studied both with the digitizer and the front-end electronics; the results of both measurements will be discussed in the following. When the front-end electronics were used, more absorption factors have been tested. In particular, data were taken at the maximum possible irradiation value available at GIF++, which corresponds to a measured rate of $\sim$ 300 Hz/cm^2 (ABS 1), while with the digitizer the available data with maximum irradiation are for to ABS 2.2. Figures 4.48 to 4.51 show, in the left panel, the efficiency (obtained with digitizer readout) and streamer probability curves for the mixtures discussed in this section as a function of the effective high voltage, for different irradiation conditions. The right panel shows the curves as a function of HV_{gas} (as defined in 4.5.1.4). The corresponding results for the standard mixture were presented earlier, in Figure 4.36.

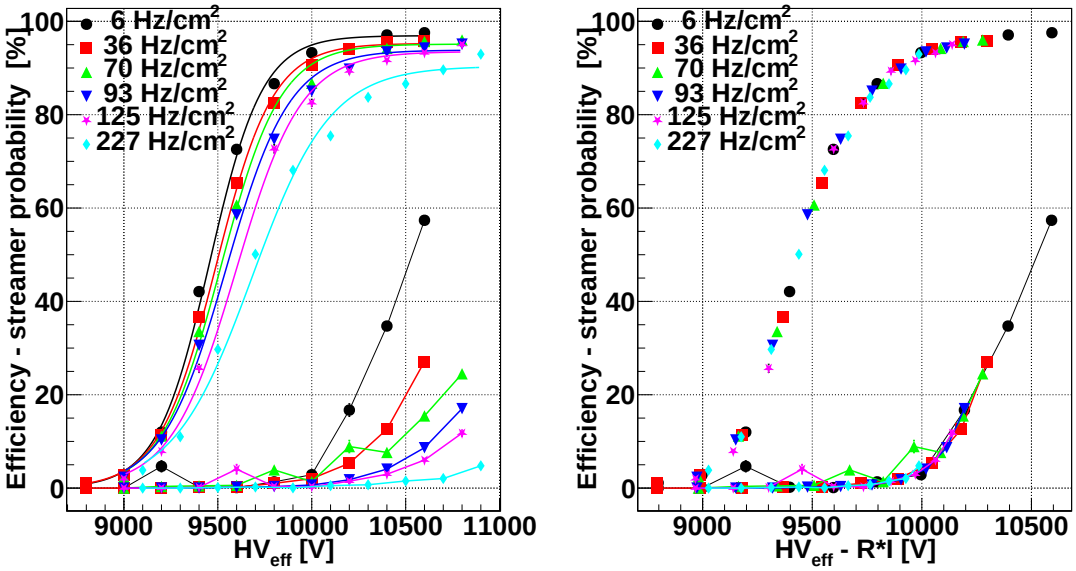

(a) MIX3 efficiency - streamer probability curves as a function of HV_{eff}

(b) MIX3 efficiency - streamer probability curves as a function of HV_{gas}

Figure 4.48: MIX3 gas mixture

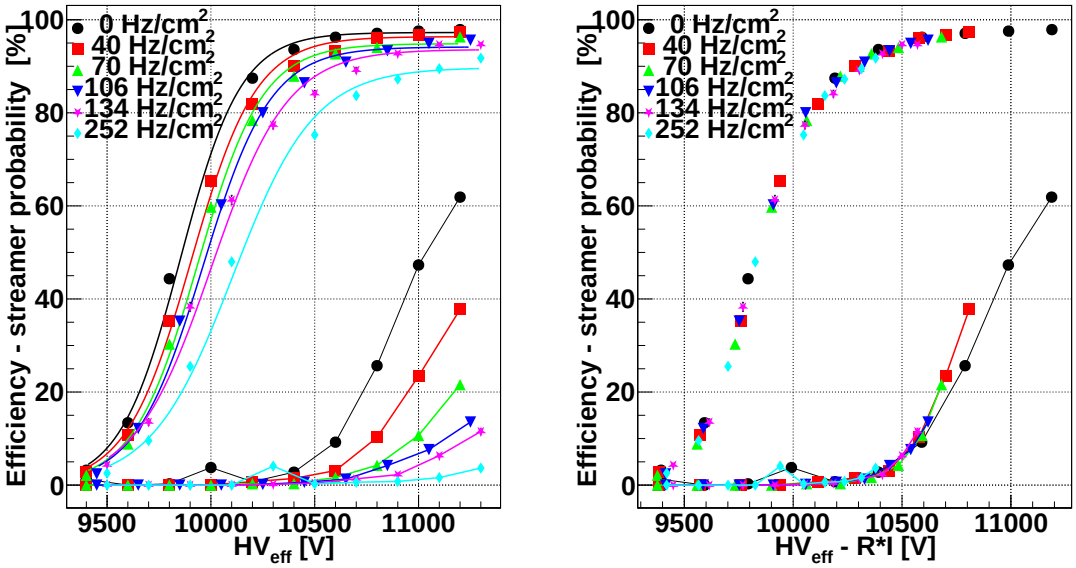

(a) MIX4 efficiency - streamer probability curves as a function of HV_{eff}

(b) MIX4 efficiency - streamer probability curves as a function of HV_{gas}

Figure 4.49: MIX4 gas mixture

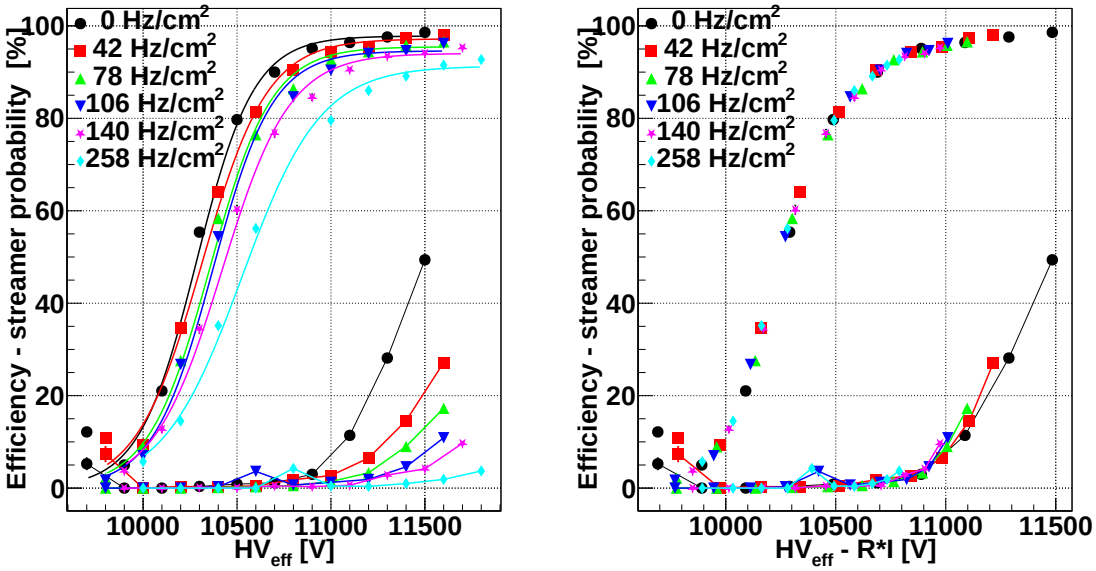

(a) MIX5 efficiency - streamer probability curves as a function of HV_{eff}

(b) MIX5 efficiency - streamer probability curves as a function of HV_{gas}

Figure 4.50: MIX5 gas mixture

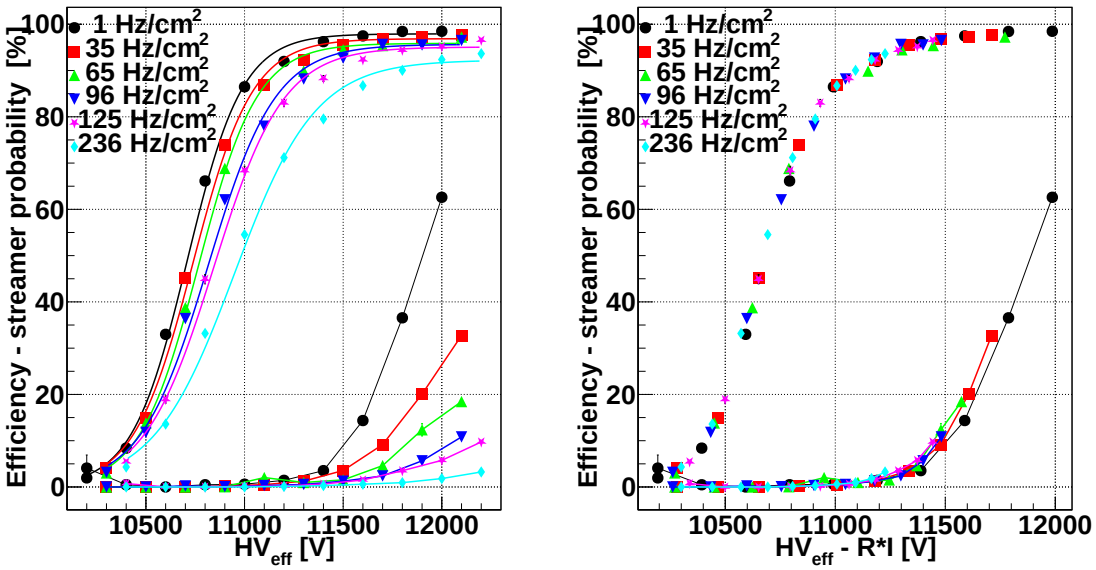

(a) MIX6 efficiency - streamer probability curves as a function of HV_{eff}

(b) MIX6 efficiency - streamer probability curves as a function of HV_{gas}

Figure 4.51: MIX6 gas mixture

Figure 4.52 shows, in the left panel, the efficiency measured (with digitizer readout) at the working point (estimated at each background rate), and at the source-off working point, as well as the streamer probability at working point. The right panel presents the same quantities (except for the streamer probability) as obtained with FEERIC.

The efficiency values at source off are compatible with one another, although the standard gas mixtures show the highest efficiency by 1-2 pp

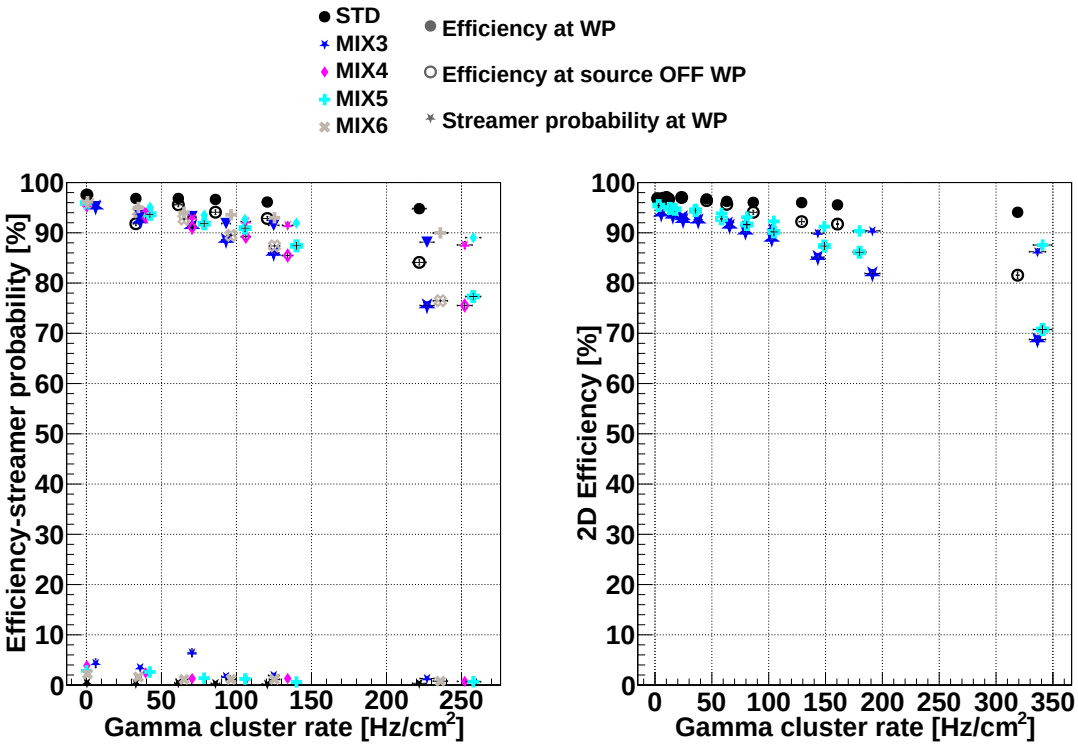

Figure 4.52: Efficiency and streamer probability values at working point and efficiency at source off working point for different gamma rates and for the different mixtures. Left panel, results with the digitizer. Right panel, results with the front-end electronics. HFO/CO_2: 25/69,30/65,35/60,40/55 (MIX3, MIX4, MIX5, MIX6)

(percentage points) with respect to all other mixtures, as can be seen in both panels of Figure 4.52. The efficiency drop, for the same irradiation conditions, is slightly greater in the case of the digitizer, due to the higher threshold employed, with respect to the one used with front-end electronics. The efficiency drop at the highest achieved irradiation is similar among all the mixtures tested and it is around 6-7 pp, if the working point at a given background value is considered. It becomes greater if the source-off working point is taken as a reference but it is similar to what was reported for MIX1 and MIX2 in 4.5.1.4. The streamer probability for the eco-friendly alternatives is slightly higher than for the standard, but it is reduced with respect to MIX1 and MIX2. It appears that the increased HFO content does not have a significant effect on the maximum efficiency obtained under irradiation, but it has the effect of reducing the streamer contamination and also the number of events with very small charge (< 0.5 pC), making the mixtures with more HFO more suitable for RPC operation. Moreover, the reduced number of small-charge events may make these mixtures more appropriate for the use in thinner-gap RPCs (for example the new 1 mm prototypes employed in the ATLAS upgrade, discussed in [139]).

The shift of the efficiency curves towards higher voltages discussed in 4.5.1.4 and it is also observed when analyzing the data from the front-end electronics, this time up to the maximum possible irradiation (ABS 1). Subtracting the expected voltage drop, due to the circulating current, from the applied HV has also been tried. The resistance of the detector was measured in Ar, close in time to the beam test performed with FEERIC readout, and found to be R = $1.25 \cdot 10^7$ Ω. The results for the efficiency are shown for the standard gas mixture in Figure 4.53 and for MIX5 and MIX3 in figures 4.54 and 4.55. The efficiency curves as a function of HV_{gas} for the standard gas mixture tend to superimpose for all irradiation values. For the HFO-based alternatives, this holds for irradiation up to ABS 2.2 (as already shown for digitizer data), while for the maximum background condition (ABS 1), the efficiency trend deviates from the other curves.

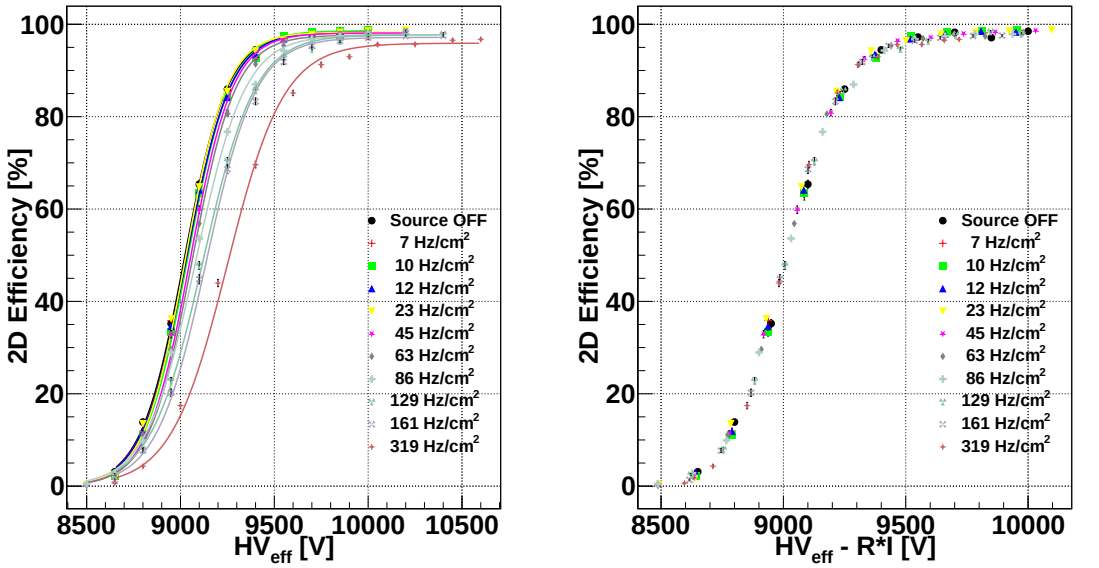

(a) STD efficiency curves as a function of HV_{eff} **(b)** STD efficiency curves as a function of HV_{gas}

Figure 4.53: STD gas mixture - FEERIC

This can be explained in two ways: the first hypothesis is that the efficiency values reported have been overestimated, for example because the gamma contribution was underestimated; the second is that the the voltage drop on the bakelite electrodes has been overestimated and the estimated efficiency curve shift is greater than the real one, which would explain the non-perfect alignment. The first hypothesis can be, in principle, discarded, since the non-perfect alignment of the efficiency curves is not observed with the standard gas mixture, but only with MIX3 and 5. Since the algorithm used to analyze the data is the same, a possible bias should be present with all the mixtures. So it should be safe to assume that this is not the explan-

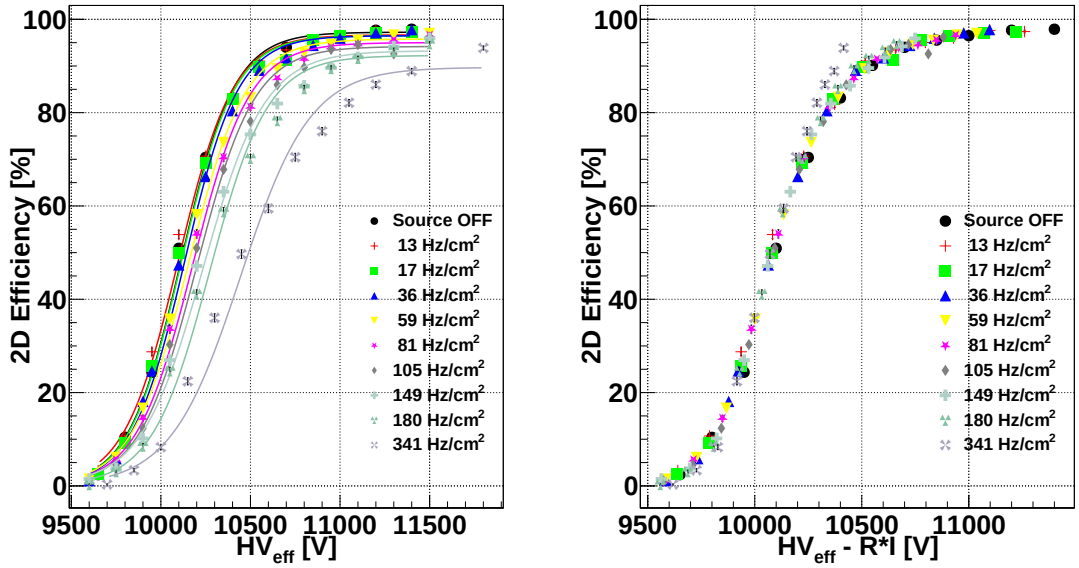

(a) Efficiency curves under irradiation for MIX5. High voltage not corrected for drop on bakelite, data from the front-end electronics

(b) Efficiency curves under irradiation for MIX5. High voltage corrected for drop on bakelite, data from the front-end electronics

Figure 4.54: MIX5 (HFO/CO_2 35/60) gas mixture - FEERIC

ation for the observed effect. The second hypothesis would imply a resistance decrease at very high gamma flux, which would lead to a smaller voltage drop on the bakelite for a given current. This hypothesis cannot be discarded and it is quite difficult to confirm with the available data since one should be able to measure the resistance of the bakelite under irradiation but this is not doable with the current set-up.

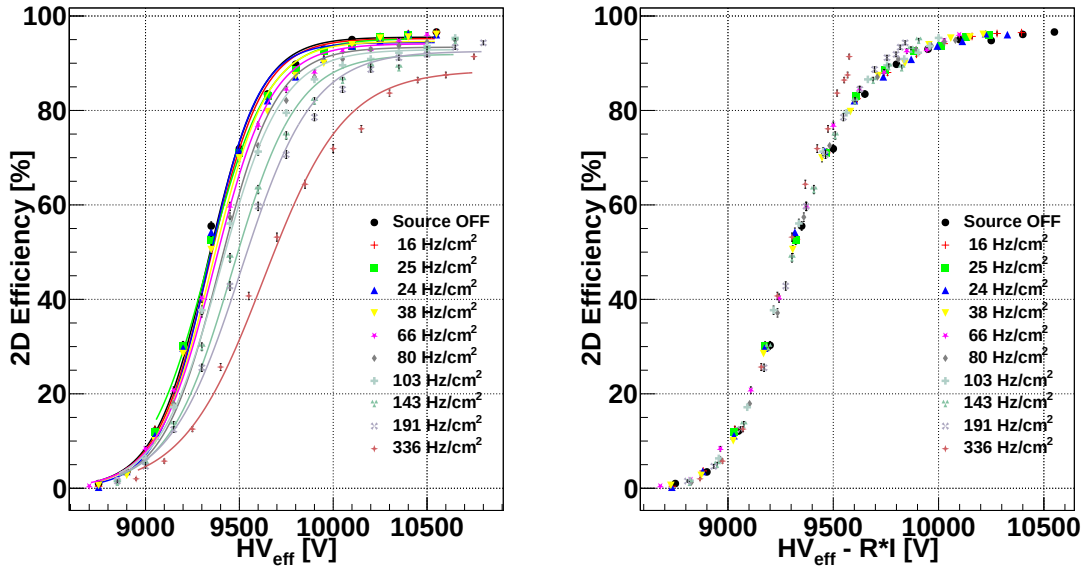

(a) MIX3 efficiency curves as a function of HV_{eff}

(b) MIX3 efficiency curves as a function of HV_{gas}

Figure 4.55: MIX3 (HFO/CO_2 25/69) gas mixture - FEERIC

Figure 4.56 shows the results from the SHiP RPC (1.6 mm single gas gap) of the ECOgas@GIF++ collaboration. It is interesting to compare the performance of this detector to the ALICE RPC since the SHiP chamber also uses the FEERIC front-end electronics and a TDC for readout. The figure shows the trend of efficiency and absorbed current as a function of the effective high voltage, for three irradiation conditions and for the same mixtures that have been tested with the ALICE RPC equipped with FEERIC (STD, MIX3 and MIX5). The addition of 10% HFO from MIX3 to MIX5 causes a smaller shift of the efficiency plateau with respect to the ALICE RPC ($\sim$ 0.8 kV vs $\sim$ 1 kV). This effect is expected due to the thinner gas gap of the SHiP RPC. A slightly larger increase in the absorbed current with respect to the standard gas mixture (a factor $\gtrsim$ 2, was 1.5-1.6 for the ALICE RPC) is observed.

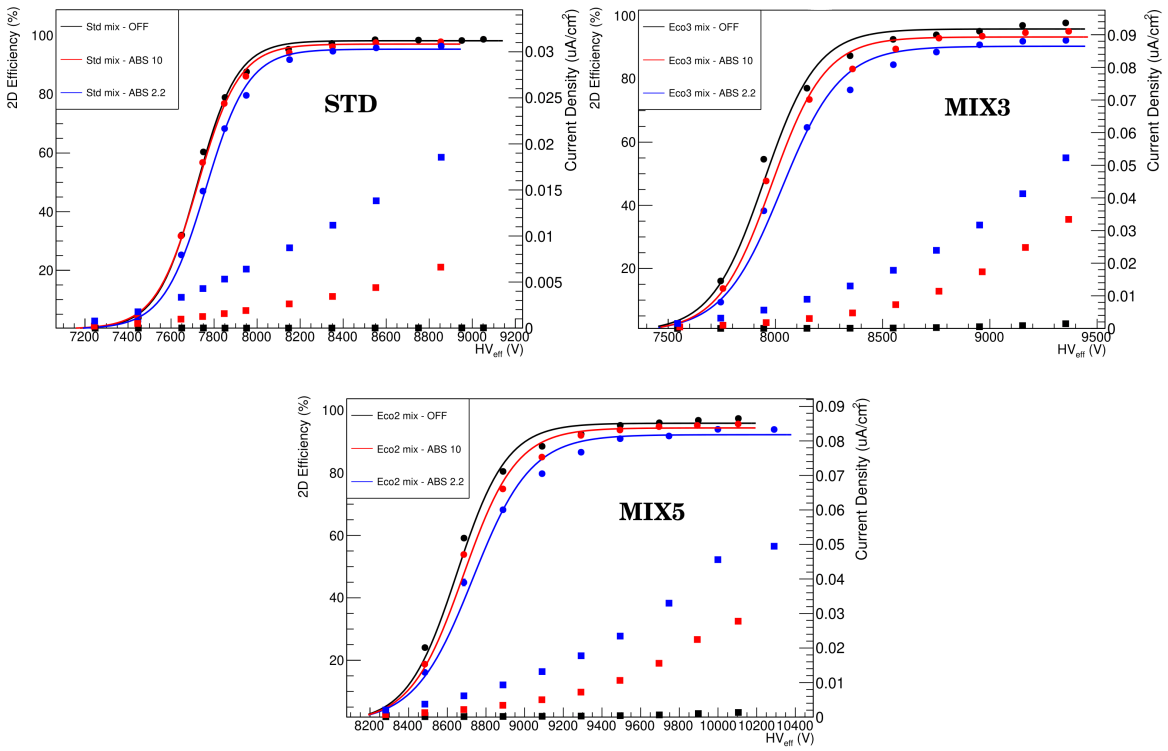

Figure 4.56: Efficiency and absorbed current under irradiation for the SHiP RPC (1.6 mm single gasp gap detector with FEERIC readout) when operated with the same mixtures that were tested with FEERIC and the ALICE RPC. Figure taken from [143]

The last quantity that was measured under irradiation is the mean cluster size. Figure 4.57 shows the trend of this quantity, calculated at working point (re-calculated for the different irradiation conditions), as a function of the measured gamma rate, for all the mixtures tested. The left panel refers to the digitizer data, while the right one to the data from the front-end electronics.

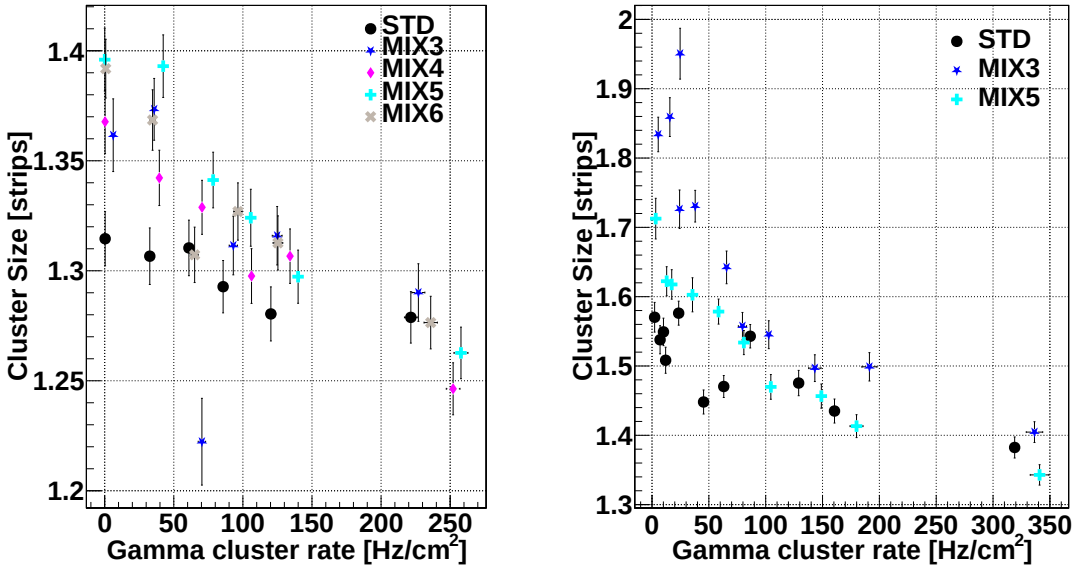

(a) Mean cluster size at working point (re-calculated for the different irradiation conditions) for different irradiation conditions, data from the digitizer

(b) Mean cluster size at working point (re-calculated for the different irradiation conditions) for different irradiation conditions, data from the front-end electronics

Figure 4.57: Mean cluster size as a function of the measured gamma rate

The same decreasing trend already highlighted in 4.5.1.4 can be observed also in this case. It can be explained by considering that the actual voltage applied to the gas is reduced by the factor R*I mentioned above. The values obtained with the front-end electronics are slightly higher, with respect to the digitizer ones, due to what was discussed in 4.5.1.4, regarding the signal shapes and the cross-talk between strips. What can be inferred is that the mean cluster size is compatible across all the mixtures tested. It is possible that, if strips with a smaller pitch were used, some minor difference between the mixtures would have been spotted.

4.5.3 Mean charge per hit

Every time the charge was addressed, thus far, it was always referred to as prompt charge. This is because a typical charge signal from an RPC is composed by two component[74]: a faster one, due to the collection of the avalanche electrons and a slower one, induced by the movement of the positive ions. To have a better estimate of the total charge released in the gas, one should acquire the signal due to the ion collection but, since the ion collection time is order of magnitudes longer than for electrons, one would need to have a dedicated set-up and an acquisition window in the order of tens of μs, while the longest window of the digitizer is 1 μs. To collect the signal from the positive ions, one should use a setup like the one described

in [127] and already commented on in 3.2.1.2. In that case, the ionic signal is readout on a 10 kΩ resistor connected to the ground graphite electrode and the acquisition window lasts 100 μs. In the lack of such a setup, one can only estimate the average total charge in the gap, by considering that, under irradiation, the absorbed current is proportional to the number of photons detected by the RPC (note that photon detection in RPCs comes almost exclusively from conversion of the photons in the bakelite [144]), as explained in Equation 4.7 and, according to it, one expects to measure a linear dependence of the current on the gamma cluster rate. Figure 4.58 shows the current density (current per unit surface, in μA/cm^2) at the working point, as a function of the gamma cluster rate (in Hz/cm^2) estimated at working point, for all the mixtures. Note that, by considering the current density, effectively one takes Equation 4.7 and divides all of its terms by the detector area. Note also that, at source off, a non-zero current and rate are measured. These are both due to intrinsic detector noise (plus, possibly, a Ohmic component for the current and a contribution by the electronics noise for the rate) and not to the photons. If the data shown in Figure 4.58 is fitted with a straight line, according to Equation 4.7, the angular coefficient of the fit represents the average charge per hit, for the given mixture, neglecting the above mentioned contribute at source off. The left panel of Figure 4.58 shows the current density for the mixtures tested with the digitizer, while the right panel shows the same data obtained with the front-end electronics. More values of rate are present in the latter, since more absorption factors have been employed, on the contrary, in the former case, only 5 attenuators have been used but more mixtures have been tested.

The angular coefficient is extracted from all the fits and the average charge per hit is found. This value is reported in Figure 4.59 for all tested mixtures. The left panel reports the results obtained with the digitizer while the right one the results using the front-end electronics. For a given mixture, the results obtained with the digitizer and the front-end electronics are slightly different: this is because the cluster rate measurement is threshold-dependent and, as already stated earlier, there is no correspondence between the threshold applied in the digitizer analysis and the 100 mV set on the front-end electronics. The values reported in these charts have to be taken as an estimate of this quantity, and are useful to compare different mixtures, while a more rigorous measurement has to be carried out using a technique similar to what described in [127]. What can be understood by the trends reported in Figure 4.59, is the relative change of the charge, in the sense that the total charge per hit is $\sim$ 1.6-1.7 times greater for all the eco-friendly

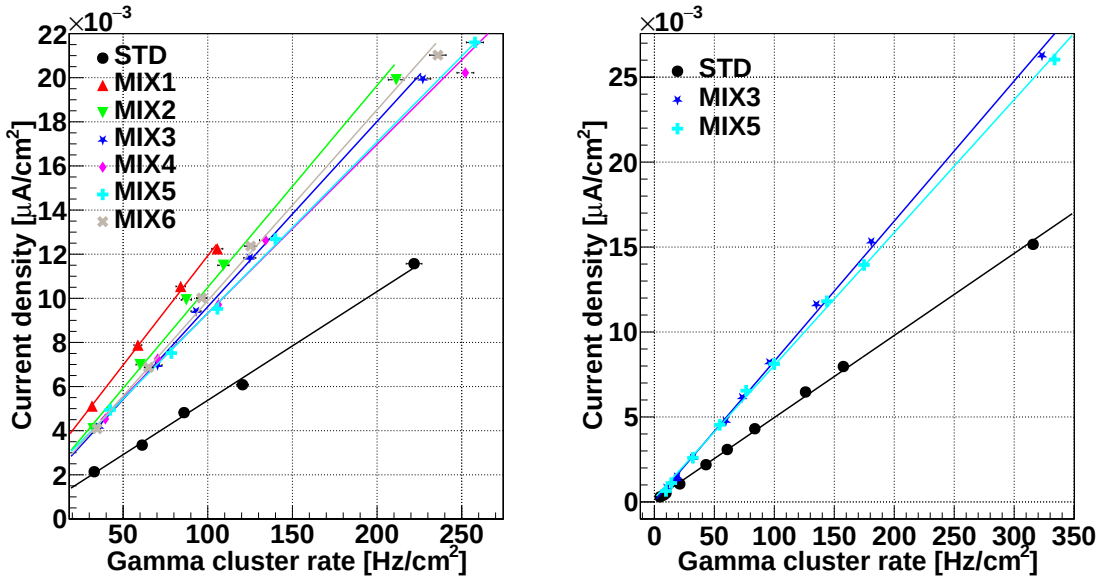

(a) Current density as a function of the cluster rate, with linear interpolation - data from the digitizer

(b) Current density as a function of the cluster rate, with linear interpolation - data from the front-end electronics

Figure 4.58: Current density vs cluster rate trends. Cluster rate measured with the digitizer and the front end electronics. The source off values have been subtracted in both cases

alternatives, with respect to the standard gas mixture.

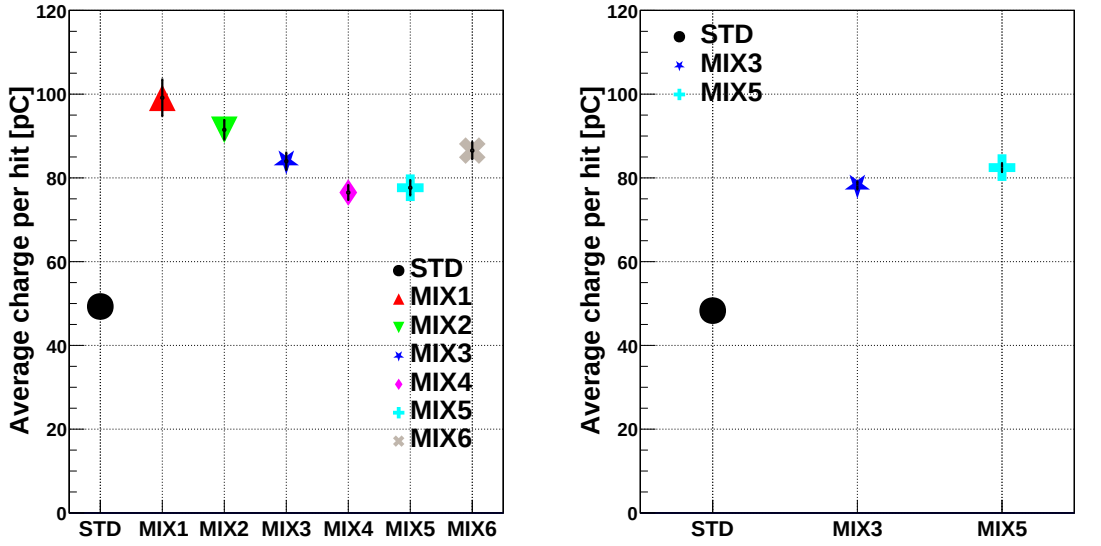

(a) Average charge per hit calculated with data from the digitizer

(b) Average charge per hit calculated with data from the front-end electronics

Figure 4.59: Average charge per hit obtained with the digitizer and the front-end electronics

4.6 Summary of beam-test studies

Seven HFO-based gas mixtures, with varying content of HFO and CO_2 have been tested in the framework of the ECOgas@GIF++ collaboration at the Gamma Irradiation Facility and their performance was compared to the standard, R134a-based, gas mixture. The main goal of this test was to fully characterize the detector response when operated with these new gas mixtures. The HFO content was gradually increased, from 0 up to 40%, while the CO_2 concentration was lowered from 95 down to 55% and the interplay between these two gases was studied. The detector was exposed to the gamma flux from the ^{137}Cs GIF++ source and its performance under irradiation was also studied. The data were collected using both a digitizer readout, for a more R&D oriented study, and with the new ALICE front-end electronics, to obtain more realistic results for future operation in the muon identification system in ALICE.

The main feature of these mixtures is that the absorbed current at working point, for the same background value, is $\sim$ 1.6/1.7 times as high, with respect to the standard gas mixture, and the same observation holds for the total charge released in the gas (obtained as the ratio of the current density over the gamma hit rate). This can be explained by considering that the quenching effect of the HFO is reduced, with respect to that of R134a.

The study of the efficiency with no irradiation showed that mixtures with a higher CO_2 content tend to reach slightly lower efficiency values, with respect to the standard gas mixture, mainly because of the reduced number of primary and secondary ionization clusters, due to the high CO_2 concentration in the mixtures. The efficiency curves tend to shift by $\sim$ 1 kV, for every 10% HFO added to the mixture. For the mixtures under test, the working point moves from 8 kV to 11.2 kV, as the HFO concentration increases.

Increasing the HFO content also leads to a reduction of the streamer contamination, making it almost comparable to the standard gas mixture, if 20-25% HFO is used. This is a promising result but the downside is that, if the applied high voltage is raised by some 100 V above the working point, the streamer contamination grows faster then in the case of the standard gas mixture.

The study of the prompt charge distribution and correlation with the time over threshold (ToT) revealed that the CO_2 addition to the mixture leads to the presence of signals with a modest charge content (< 20 pC) and a long ToT (> 50 ns), which are not present in the case of the standard gas

mixture. However this effect seems to be quite mitigated by the addition of HFO to the mixture.

The time resolution and cluster size are not significantly affected by the presence of the CO_2 and HFO. The cluster size is slightly higher for the HFO-based gas mixture, while the time resolution appears to be slightly improved, with respect to the standard gas mixture.

For what concerns the performance under irradiation, the standard gas mixture shows an efficiency drop of 2 percentage points (pp) between the source off and maximum irradiation case, while all the eco-friendly gas mixtures show a decrease of around 8 pp, if the HFO content is above 20% (both for what concerns the digitizer and the front-end results). When using the front-end electronics, the efficiency drop for a background rate of ~ 100 Hz/cm^2 (the hit rate expected on the most exposed RPC during LHC RUN3 and RUN4 [112]) with the standard gas mixture is negligible while for MIX3 and 5 is ~ 3 pp each. If the results of the digitizer are analyzed, a drop of $\sim$ 3-4 pp is observed for MIX3-6 and ~ 1 pp for the standard gas mixture. If the HFO percentage is lower, a greater degradation is observed. The RPC efficiency degradation with the gamma background rate is well described, with the exception of the highest background value, by a simple model that takes into account the voltage drop across the gas gap due to the circulating current and the resistivity of the bakelite electrodes.

In summary, acceptable performance have been achieved for background rates up to what is expected in the ALICE experiment during the upcoming LHC runs. The main concerns are the higher absorbed current and charge per hit of HFO-based mixtures, and the relatively high working point for mixtures with large HFO content, which seem to provide the best streamer suppression. These could lead to issues in the long-term operation of the RPCs with these new mixtures. For this reason a long-term irradiation campaign was started by the ECOgas@GIF++ collaboration, which is the subject of Chapter 5. Tables 4.5 and 4.6 contain a summary of all the parameters that have been obtained in the beam tests, using the digitizer. Table 4.7 shows the results obtained when the FEERIC cards were used.

Mixture	WP [V]	Rate [$\frac{Hz}{cm^2}$]	I [μA]	ϵ @ WP [%]	$WP_{off}[V]$	ϵ @ WP_{off} [%]	Muon CS @ WP [strips]	Str. prob @ WP [%]
STD	9717	0.3	0.4	97.52	9717	97.52	1.31	0.45
	9900	33	5.3	96.83		91.80	1.31	0.33
	9793	61	8.4	96.83		95.58	1.31	0.46
	9843	86	12.0	96.63		94.10	1.29	0.33
	9868	121	15.2	96.12		92.85	1.28	0.20
	10027	222	28.9	94.80		84.11	1.28	0.35
MIX1	8861	0.4	0.1	95.24	8861	95.24	1.35	19.76
	8923	32	12.8	90.63		89.75	1.33	10.94
	8962	59	19.7	88.61		87.03	1.27	7.54
	9028	84	26.3	87.88		84.73	1.25	6.02
	9042	106	30.6	87.04		83.55	1.27	5.42
MIX2	9666	0.03	0.2	94.64	9666	94.64	1.38	10.16
	9678	32	10.2	92.61		92.45	1.29	5.66
	9743	60	17.5	91.33		90.19	1.32	3.39
	9838	87	24.8	91.19		87.96	1.30	3.18
	9838	109	28.7	90.11		86.84	1.30	2.12
	10048	211	49.8	86.43		76.22	1.26	2.06
MIX3	10021	6	0.3	95.20	10021	95.20	1.36	4.35
	10088	36	10.4	93.43		92.45	1.37	3.48
	10134	70	17.4	93.22		91.31	1.22	6.44
	10192	93	23.5	91.84		88.56	1.31	1.74
	10260	125	29.6	91.48		85.99	1.32	1.92
	10446	227	49.9	88.13		75.53	1.29	1.31

Table 4.5: Summary of the results obtained with the digitizer - 1

Mixture	WP [V]	Rate [$\frac{Hz}{cm^2}$]	I [μA]	ϵ @ WP [%]	$WP_{off}[V]$	ϵ @ WP_{off} [%]	Muon CS @ WP [strips]	Str. prob @ WP [%]
STD	9717	0.3	0.4	97.52	9717	97.52	1.31	0.45
	9900	33	5.3	96.83		91.80	1.31	0.33
	9793	61	8.4	96.83		95.58	1.31	0.46
	9843	86	12.0	96.63		94.10	1.29	0.33
	9868	121	15.2	96.12		92.85	1.28	0.20
	10027	222	28.9	94.80		84.11	1.28	0.35
MIX4	10434	0.4	0.7	95.46	10434	95.46	1.37	3.86
	10515	40	11.3	94.46		93.20	1.34	2.40
	10546	70	18.1	92.99		91.08	1.33	1.28
	10592	106	24.3	92.23		89.22	1.30	1.08
	10692	134	31.6	91.49		85.48	1.31	1.31
	10834	252	50.6	87.58		75.53	1.25	0.73
MIX5	10884	0.5	0.9	95.91	10884	95.91	1.40	2.84
	10975	42	12.4	95.09		93.68	1.39	2.60
	10989	78	18.8	93.51		91.80	1.34	1.38
	10991	106	23.8	92.69		90.93	1.32	1.21
	11100	140	31.7	91.95		87.41	1.30	0.62
	11293	258	54.0	89.03		77.31	1.26	0.66
MIX6	11273	1.1	0.8	96.18	11273	96.18	1.39	2.20
	11330	35	10.2	95.04		94.21	1.37	1.61
	11356	65	17.2	94.06		92.75	1.31	1.13
	11469	96	25.0	93.59		89.50	1.33	1.14
	11514	125	30.9	92.99		87.40	1.31	1.14
	11704	236	52.6	89.98		76.48	1.28	0.77

Table 4.6: Summary of the results obtained with the digitizer - 2

Mixture	WP [V]	Rate [$\frac{Hz}{cm^2}$]	I [μA]	ϵ @ WP [%]	$WP_{off}[V]$	ϵ @ WP_{off} [%]	Muon CS @ WP [strips]
STD	9511	2	1.1	96.81	9511	96.81	1.57
	9529	10	2.1	97.19		96.96	1.55
	9528	12	2.4	96.88		96.66	1.51
	9504	23	3.7	96.95		97.03	1.58
	9537	45	6.6	96.75		96.40	1.45
	9553	63	8.8	96.25		95.66	1.47
	9619	86	11.9	96.05		94.08	1.54
	9678	129	17.4	96.01		92.22	1.48
	9677	161	21.1	95.56		91.73	1.44
	9842	319	39.1	94.09		81.56	1.38
MIX3	9899	5	2.1	93.80	9899	93.80	1.83
	9955	25	5.5	93.29		92.51	1.95
	9875	24	5.7	92.82		93.08	1.73
	9936	38	8.6	92.89		92.41	1.73
	9964	66	14.1	92.33		91.39	1.64
	9989	80	17.7	91.61		90.21	1.56
	10028	103	22.9	90.99		88.79	1.55
	10121	143	31.8	89.94		85.16	1.50
	10222	191	41.5	90.39		81.91	1.50
	10416	336	69.9	86.23		68.78	1.40
MIX5	10702	3	1.7	95.42	10702	95.42	1.71
	10700	17	4.5	94.66		94.68	1.62
	10723	36	8.3	94.67		94.40	1.60
	10775	59	13.2	93.85		92.77	1.58
	10795	81	18.3	93.11		91.64	1.53
	10824	105	22.2	92.27		90.18	1.47
	10894	149	31.7	91.23		87.37	1.46
	10900	180	37.0	90.36		86.13	1.41
	11169	341	68.1	87.57		70.76	1.34

Table 4.7: Summary of the results obtained with the FEERIC cards

Chapter 5

Aging studies

This chapter is dedicated to the description of the long-term stability (aging) studies in the context of the search for an eco-friendly gas mixture for RPC detectors. Section 5.1 reports the general methodology employed in the aging studies (5.1.1), together with a description of the mixtures that have been tested (5.1.2) and some generalities on the RPC monitoring system (5.1.3). Moreover, a characterization of the irradiator, in term of instant dose rate is also reported in 5.1.4. The results obtained so far are described in Section 5.2, with a focus on the ALICE detector. Three gas mixtures have been tested and the results are presented following a by-mixture arrangement.

5.1 General description of aging studies

The following section contains a general description of the aging studies carried out by the ECOgas@GIF++ collaboration: first, a description of the methodology adopted is presented, then the different gas mixtures that have been tested are listed. Lastly, an overview of the monitoring system is provided.

5.1.1 Methodology

The aging test is being carried out at the GIF++ (described in detail in 4.2.1), using the RPCs listed in Table 4.3. The aim of this kind of studies is mainly to assess the stability of detector current (since, for the moment, other parameters are not monitored), when operated over a long period of time, using the new eco-friendly gas mixtures. This is the next step, following the preliminary studies reported in Section 3.2 and the characterization described in Chapter 4, towards a full understanding of the promising alternatives found to replace the greenhouse gases employed in the standard RPC gas

mixtures. Indeed, one has to prove that RPCs can be operated with an eco-friendly mixture for a prolonged period of time, without showing any loss of performance or stability. An important parameter that can be introduced to numerically quantify what long-term means, is the so-called *integrated charge*. This quantity is measured in C/cm^2 (to quote an example, these values have been calculated for the ALICE MID RPCs in RUN3 and RUN4 and are reported in Table 2.2) and is defined as the integral in time of the current flowing through the detector, divided by its area.

Thanks to the set-up at GIF++ (described in Section 4.2), an accelerated aging test can be carried out. Accelerated means that one can expose the RPCs to a higher particle flux than what they would be exposed to in normal conditions, hence producing a higher current and integrating a greater amount of charge in a shorter time span. As an example, the stability of the RPCs currently employed in the ALICE muon trigger/identification system has been validated up to an integrated charge of 50 mC/cm^2, as was discussed in Section 2.3. This value corresponds to the projected amount of integrated charge for the first 10 years of operations at the LHC[104] and it was integrated during a time span of roughly 12 months. For reference, after the first two LHC physics runs, the most exposed RPCs have reached an integrated charge of $\sim$ 30 mC/cm^2 and have not yet shown any degradation in terms of efficiency[110]. The aging test described in Section 2.3 was carried out at the old GIF at CERN, while the studies with eco-friendly gas mixtures are being carried out at the GIF++, a new and updated version of the old facility. The main difference between the two is the activity of the ^{137}Cs irradiation source. In the former it was $\sim$ 0.5 TBq, while in the latter it is 12.5 TBq. This translates into an even faster acceleration of the charge accumulation process.

5.1.2 Gas mixtures tested

A total of three gas mixtures have been tested by the collaboration. First of all, the standard gas mixture employed by ATLAS and CMS[74] was tested (referred to as STD in the following), to provide a baseline result to which the eco-friendly gas mixtures can be compared (as done for the beam test studies described in Chapter 4). This mixture is composed by 95.2% $C_2H_2F_4$, 4.5% i-C_4H_{10} and 0.3% SF_6. It has a lower isobutane content with respect to the one employed in ALICE, which, precisely because of this higher i-C_4H_{10} fraction, is considered flammable and cannot be used at GIF++ for safety reasons.

As previously described in Section 3.3, the strategy adopted by the collaboration is to test HFO-based gas mixtures, with the addition of CO_2 as a place-holder gas to lower the detector working point. Two eco-friendly options have been tested, named *ECO1* and *ECO2*. The choice of mixtures has been agreed by the collaboration: ECO1 has been proposed due to its similarity with some of the mixtures tested by the CMS and ATLAS groups (as reported in [118, 127]). This mixture is not among the ones tested with the muon beam, and described in Chapter 4 since, as it will be shown in 5.2.2.1 the results obtained with it are not promising. ECO2 has been proposed as an alternative and it has been fully characterized with the muon beam. As already anticipated in 4.1.1, the latter was addressed to as "MIX5" when the beam test results were described but a different name has been adopted by the collaboration for aging studies. ECO1 is composed as follows: 45% HFO, 50% CO_2, 4% i-C_4H_{10} and 1% SF_6, while ECO2 (MIX5) has the same percentages of i-C_4H_{10} and SF_6, the HFO content reduced to 35% and the CO_2 content increased to 60%. Table 5.1 summarizes the mixtures just described, together with a column containing an estimate of their GWP.

Mixture	$C_2H_2F_4$ %	HFO %	CO_2 %	i-C_4H_{10} %	SF_6 %	GWP
STD	95.2	0	0	4.5	0.3	1488
ECO1	0	45	50	4	1	437
ECO2 = MIX5	0	35	60	4	1	482

Table 5.1: Composition of the different mixtures tested in aging studies

The GWP of each mixture has been calculated with the same procedure highlighted in 4.1.1. Mixture ECO1 was never mentioned in Chapter 4 since it has not been studied with the muon beam.

5.1.3 RPC monitoring system

During aging studies, several parameters have to be closely monitored. For example, the environmental temperature and pressure, the gas mixture composition, the relative humidity of the gas, the applied high voltage and the absorbed current. These values are gathered from a plethora of different sources and are all saved to a common database. The already mentioned webdcs (4.3.2) is used to carry out all the operation related to detector control and data logging; recall that this piece of software was specifically developed by the CMS collaboration and was adapted to the needs of the ECOgas@GIF++ collaboration. Moreover, a *Grafana*[145] web page has specifically

been developed to visualize the information saved into the database at a glance, to spot any obvious issue (for example, wrong mixture, unwanted source status and so on) without the need to download the data and write a specific piece of code to view them. Of course, one can still download all the data and perform more in-depth studies on them.

The webdcs is used to configure and monitor the detector parameters and to handle data-taking; among other tasks, it takes care of performing the pressure and temperature (PT) correction, according to Equation 4.1, to the applied HV, to maintain a stable effective high voltage (see Section 2.2.3) throughout the aging process (see also 5.1.1).

The webdcs grants a high level of flexibility, allowing the user to easily include or exclude a given detector from the data taking. It also provides basic data quality monitoring tools. Beside allowing one to view trends of selected quantities over a given time period, the Grafana web page can be set in up in such a way that configurable alarms can be inserted, in order to get an e-mail notification when some quantities are outside a predefined safety range. The webdcs and Grafana systems are also able to communicate with each other; for example, if the flow of a certain gas is too low, resulting in the wrong mixture sent to the detectors, Grafana can send a kill command to the webdcs, which would stop any ongoing data taking and bring the detectors to a safe state.

5.1.4 Dose rate measurement

Since the detectors are placed at different distances from the source (as reported in 4.3.1), and in order to compare the results obtained with the various RPCs, a detector-independent measurement of the dose rate at the positions of the two trolleys, for different absorption factors, was carried out using a Mirion RDS-31ITX dosimeter. The results of this measurement are reported in Figure 5.1.

The different dose values reported for the same (upstream) ABS value correspond to different values of the downstream ABS value. This is because another goal of the measurement was to test whether a change in downstream filter would significantly affect the measured rate upstream. As it can be seen from the figure, this is not the case, except for very large absorption factors (low radiation level). In order to compare the behavior of detectors that are installed on different trolleys, the following pairs of absorption factors can be used, which roughly correspond to the same instant dose rates for the two trolleys: ABS 10 and 69 (corresponding roughly

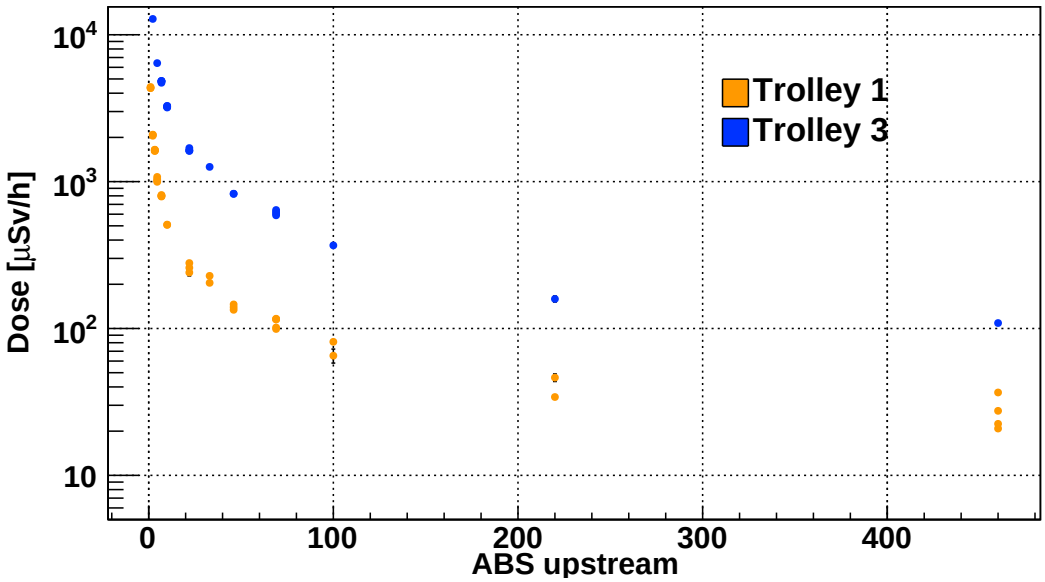

Figure 5.1: Measured instant dose rate as a function of the attenuation factors on the two trolleys of the collaboration

to 500 μSv/h) and 2.2 and 22 (roughly 2000 μSv/h). The first value of each pair is for the RPCs on trolley 1 (6 m from the source), the second for those on trolley 3 (3 m from the source). Together with these, the source-OFF condition is also taken as a baseline for the no-irradiation condition.

5.2 Results from aging studies

The three mixtures have been tested in the following order: STD (to validate the stability of the system), ECO1, and ECO2 (hence the names given to the mixtures). The data taking method has always been organized in the same way, so it will be shortly described here. The chosen mixture is flushed in the detectors, with roughly a 1 vol/h replacement rate in the ALICE RPC. After around 10/15 volume changes, the detectors are switched ON at the chosen working point and the detector control system is in charge of applying the temperature and pressure correction to grant the stability of the applied high voltage. The RPCs are exposed to the gamma irradiation coming from the ^{137}Cs source and the absorbed current (irradiation current) is monitored over time. The absorption factor chosen for the source is decided in collaboration with the other GIF++ users and it has been usually set to 2.2 or 4.6.

Once a week, during the source-OFF (source fully shielded) day, a full high voltage scan is carried out and the current is measured (this will be referred to as I(HV) scan in the following). In this case the current will

be addressed to as *dark*, meaning that it is the current absorbed without irradiation. The stability of both currents (dark and under irradiation) is monitored over time, since the increase of any of the two could be a sign of potential aging of the detectors.

By monitoring the current absorbed by the detector, one can also calculate the integrated charge, which serves as a quantitative estimate of the aging progression.

The following subsections are dedicated to a more extensive discussion of the results for each gas mixture tested. All the quantities shown in the upcoming charts are reported as a function of the integrated charge, since they show data that have been taken over long periods of time and not necessarily continuously. The integrated charge calculation is not as simple as taking the irradiation current and integrating it over time. For example, if a given detector was to have a high Ohmic component in the dark current (see 2), this would still be present even under irradiation and, since this current does not correspond to charge released in the gas gap, if not subtracted it would lead to an over-estimation of the integrated charge. Hence, the following precautions have been taken in all the calculations:

- Irradiation currents and applied high voltage are saved every 30 seconds together with the measurement timestamp.
- Since a source off I(HV) curve is taken weekly, any irradiation period has a reference source-off scan that can be used to estimate the Ohmic part of the current for the specific period. This is done by performing a linear interpolation of the curve from 0 to 5000 V (well below the multiplication threshold) and extrapolating the current to the working point. The extrapolated current is then subtracted from the measured current to obtain the so-called physics current, i.e., current due to charge liberation and multiplication processes occurring in the gas resulting from ionizing particles or intrinsic detector noise.
- The source status (on or off) is also saved to provide an estimate of the total time under irradiation, during the aging studies.

Figure 5.2 shows an example of a I(HV) source-off scan for the EP-DT detector. The red line is the linear interpolation mentioned above, while the vertical one marks the detector working point. The y coordinate of the intersection point between these lines is the Ohmic part of the dark current at working point. The values reported on the vertical axis are current density (measured in $\mu A/cm^2$), so that detectors with different areas can be

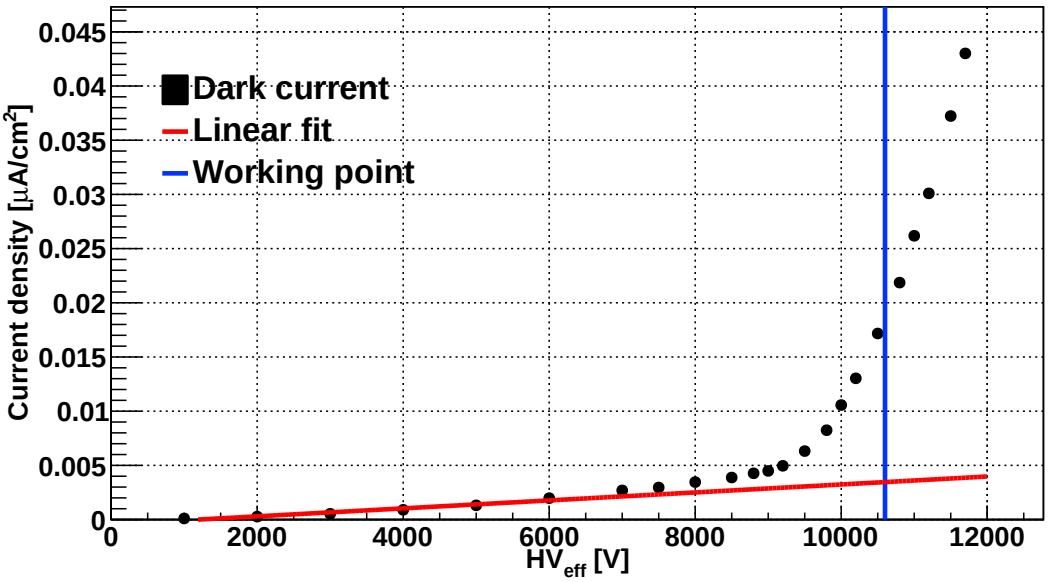

Figure 5.2: I(HV) source OFF scan for EPDT detector, illustrating the Ohmic component estimation procedure. The linear interpolation is used to estimate the Ohmic part of the current. The vertical blue line marks the detector working point

immediately compared. The estimated Ohmic part of the current is subtracted from the irradiation current and the results of this operation is shown, for the EPDT detector and for an arbitrary time period, in Figure 5.3. The figure shows the current under irradiation as a function of time; the blue curve is the total current absorbed by the RPC, while the red one shows the effect of the subtraction of the Ohmic component.

In Figure 5.3, the source conditions have not been taken into account. For completeness, the effect of completely shielding the source is shown in Figure 5.4. One can see that towards the end of the period shown, the current drops and, by checking the status of the source (shown in green in Figure 5.4) one can see that in correspondence of the current drop, the irradiation was stopped (status = 0 represents the source-off condition). The black vertical line represents the start of a period with source on, while the red one corresponds to when the source is fully shielded. In this example, the source was switched off only once but, especially for longer irradiation periods, it can happen that multiple periods with source off are found.

Figures 5.3 and 5.4 refer to an arbitrary stability run and to the EP-DT detector. The figures shown in the following present the results, obtained applying the procedure just discussed, for the ALICE RPC. Sometimes, for completeness and to support some of the arguments raised, results from other RPCs of the collaboration will be shown.

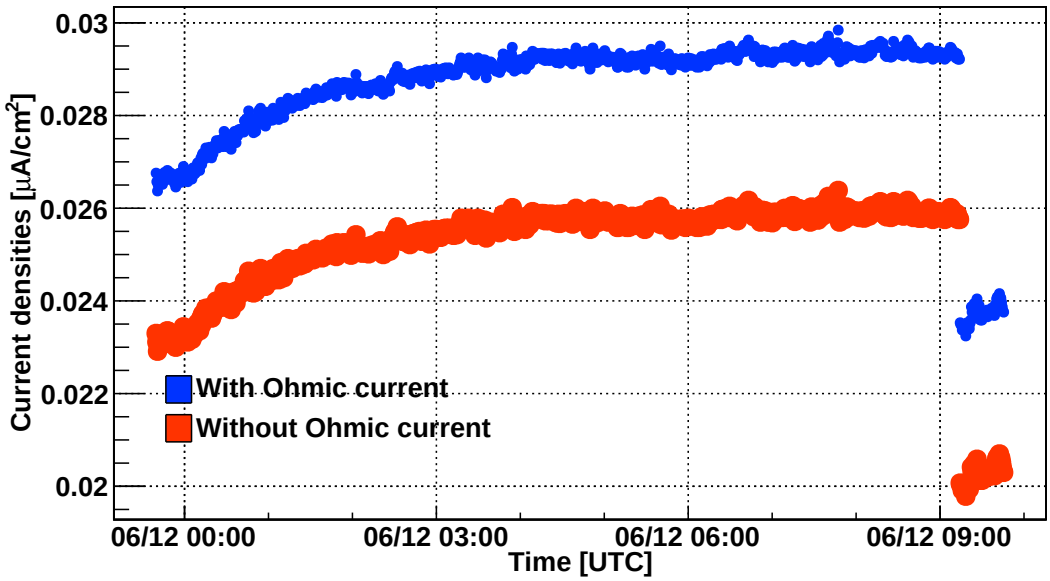

Figure 5.3: Trend of the current absorbed under irradiation by the EP-DT detector, showing the effect of the Ohmic component subtraction (the blue curve shows the current with the Ohmic component included, while it is subtracted in the red one)

5.2.1 STD gas mixture

The standard gas mixture has been used at the LHC for many years already: its performance and stability over time are well known, hence the aim of this test was to validate the data taking method and study the stability of the monitoring system. Since many parameters have to be monitored during this kind of studies, a dedicated database has been created to store all the values. This structure is populated and queried by the detector control system. The data are stored as a function of time and some of the most important values are: current, applied and effective high voltage, source status and value of absorption factor, ambient temperature and atmospheric pressure. The last two parameters are used to perform the pressure and temperature correction of the applied high voltage; the user sets a value for the effective voltage, and the PT correction varies the applied high voltage in such a way as to maintain a constant effective voltage, according to Equation 4.1. Furthermore, each time a new run is started, an ID gets attached to it, together with the start (and, eventually, the end) timestamp, in order to keep track of the chronological order in the data taking. Other important parameters, such as the gas flow, its relative humidity and gas composition, are saved into a separate database which is not directly managed by the detector control system.

The aim of this irradiation test with the standard gas mixture was also to test two more features of the system: 1) the software gas kill, meaning

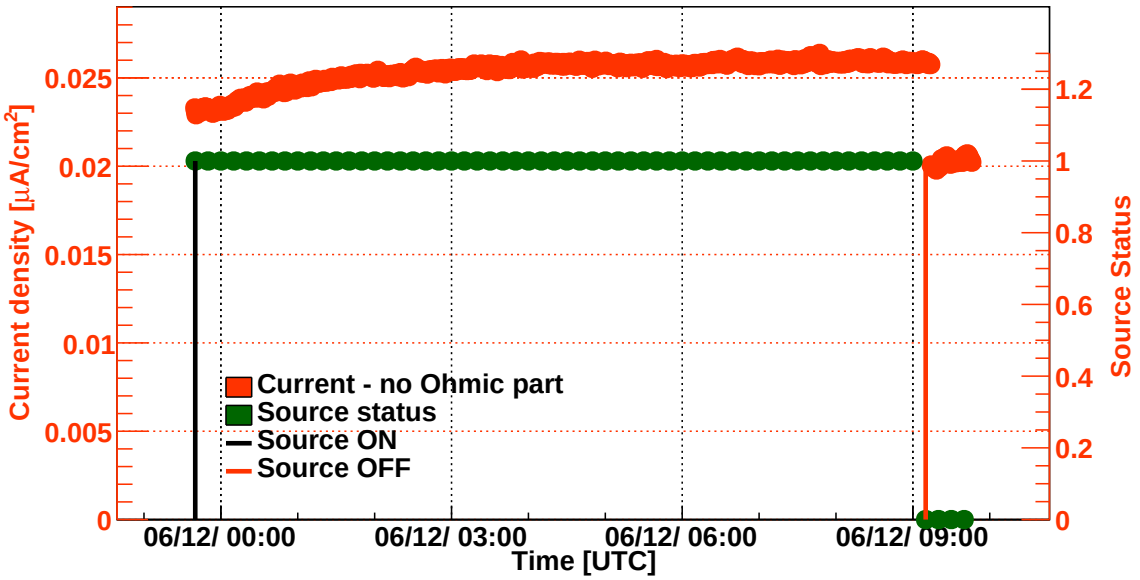

Figure 5.4: The effect of completely shielding the ^{137}Cs source during an irradiation period is a reduction of the absorbed current - example for the EP-DT detector

that, if the concentration of a given gas is different from the nominal one by more than a given tolerance, or if the flow of any gas is stopped, a software command is issued, the high voltage is switched off and the data acquisition is halted 2) a safety feature to reduce the high voltage applied to the detectors if the absorption factor goes below a given value, resulting in too high irradiation. This is done in order to protect the detectors from an excessive prolonged exposure to radiation.

5.2.1.1 Stability results

Figure 5.5 shows the results of the irradiation studies with the STD mixture. It reports, as a function of the integrated charge, the trend of effective high voltage and monitored current, with and without the Ohmic component of the dark current; since the Ohmic part is negligible, the two curves are almost superimposed.

In two occasions, at around 2 and 3 mC/cm^2, circled in red in the chart, it is possible to observe how the voltage is reduced to the standby value by the safety mechanism explained earlier because the absorption factor was lower than the threshold (recall that the lower the absorption factor, the higher the irradiation). The PT correction also works properly, as shown by the constant trend of the effective high voltage, and all the parameters are correctly saved in all the databases. Finally, it can also be seen that there are some integrated charge ranges where, despite the high voltage being constant, the current is higher or lower. This is due to the fact that

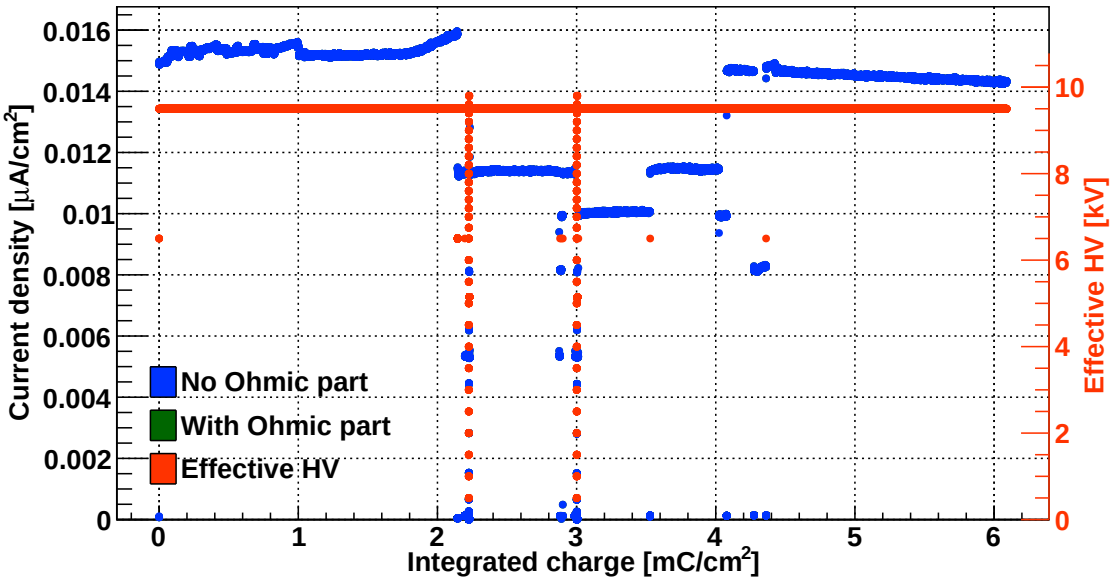

Figure 5.5: Effective high voltage and current density as a function of the integrated charge for the ALICE RPC - STD gas mixture. Red circles show the safety mechanism to lower the high voltage if the absorption factor goes below a given threshold (curves with and without Ohmic part are superimposed since the Ohmic component is close to 0)

the absorption factor was not kept constant over time.

5.2.1.2 STD gas mixture summary

The studies with the standard gas mixture only lasted around 7 days, most of which were with source ON. A total of 6 mC/cm^2 was integrated and the stability of the system was proven. A gas stop was simulated, by switching OFF one of the input valves and the system behaved as expected: the run was stopped, the high voltage was set to 0 V and an e-mail was sent to all the members of the collaboration, informing about the gas kill.

Figure 5.6 shows the trend of the integrated charge as a function of time. The horizontal portions represent periods of time in which the detector was off.

5.2.2 ECO1 gas mixture

The ECO1 gas mixture is composed as follows: 45% HFO, 50 % CO_2, 4% i-C_4H_{10} and 1% SF_6. It is the first eco-friendly gas mixture that has been tested by the collaboration. Once again, the i-C_4H_{10} content is lower, with respect to the ALICE standard gas mixture and to the eco friendly ones tested in [125], due to the flammability issues mentioned in 5.1.2. The working point for the 2 mm gaps has been set to 11.6 kV. Since these studies have been carried out in the initial stages of the collaboration effort, no beam test

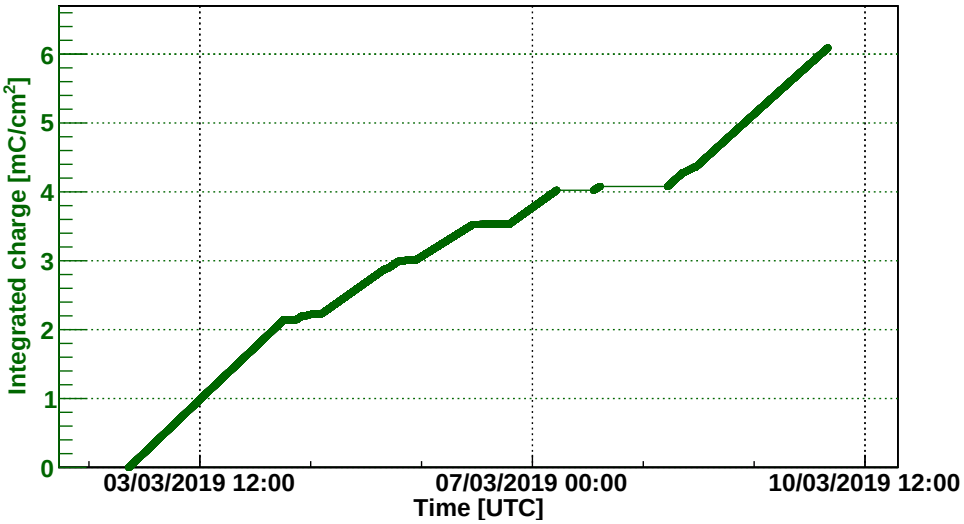

Figure 5.6: Trend in time of the integrated charge with the STD gas mixture for the ALICE detector. The horizontal portions of the chart represent periods of time when the detector was off

to fine tune the detector working point under irradiation had been carried out. For this reason, it was decided to operate the detectors at this value of effective high voltage after analyzing the I(HV) response of the RPCs when operated with the ECO1 gas mixture, under irradiation. Figure 5.7 reports two I(HV) scans taken with absorption factor 22: the blue one is taken with the standard gas mixture, the red one with ECO1.

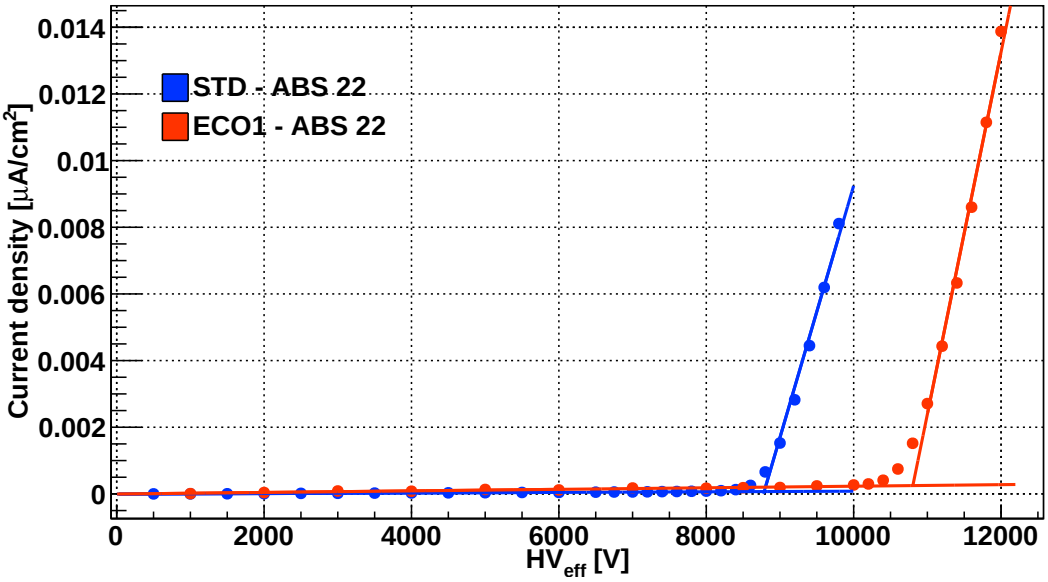

Figure 5.7: I(HV) scans with ABS 22, for the ALICE RPC, with the STD and ECO1 gas mixtures. A linear interpolation is used to estimate the turn-on point. A shift of $\sim$ 2 kV increase for ECO1, with respect to STD, is observed

In the figure, together with the aforementioned I(HV) curves, also four straight lines are present (two for each mixture). The purpose of these lines is to estimate the, so-called, turn-on voltage of the RPC, that is, the point

where the current becomes dominated by charge multiplication processes rather than by Ohmic conduction. This quantity was estimated as a preliminary information on the behavior of the detectors. This is done by performing two linear regressions, one to the Ohmic and one to the multiplication parts of the I(HV) curve, and by finding their intersection. The results of this process for the ALICE RPC are summarized in Table 5.2. The last line of the table reports also the difference Δ in turn-on voltage between ECO1 and STD gas mixtures. A difference of $\sim$ 2 kV is observed and, considering that the working point with the standard gas mixture is around 9.6 kV for the 2 mm gas gap, it was decided to operate the detectors at the above-mentioned voltage of 11.6 kV.

Mixture	Turn-on voltage [V]
STD	8785 ±82
ECO1	10803 ±92
Δ(ECO1-STD)	2018 ±122

Table 5.2: Turn-on voltage for the ALICE RPC

5.2.2.1 Results under irradiation

Following the above-described preliminary results, the irradiation campaign was carried out. As previously stated, the absorption factor was not constant throughout the whole period, mainly due to requests by other GIF++ users. Nonetheless, some interesting observations could be made. First of all, Figure 5.8 shows the trend of the absorbed current (with and without Ohmic part of the dark current, subtracted as discussed in 5.1.1) and effective high voltage of the ALICE RPC during the aging studies, as a function of the integrated charge. The effective high voltage is constant, except for a small period in the range 4-5 mC/cm^2, where a few I(HV) scans with source ON have been taken, hence the variation of HV_{eff}. The variation in absorbed current, observed throughout the whole irradiation period shown in Figure 5.8 is due to the different absorption factors set by the other users, so it is expected. What is non expected, though, is the fact that, after the integration of $\sim$ 5 mC/cm^2, the difference between the current with and without the Ohmic part starts to become more and more relevant. This is a sign that the Ohmic part of the dark current is steadily increasing. This behavior could be a sign of very early detector aging, that could be linked to the gas mixture, since this effect is observed on all the detectors of the

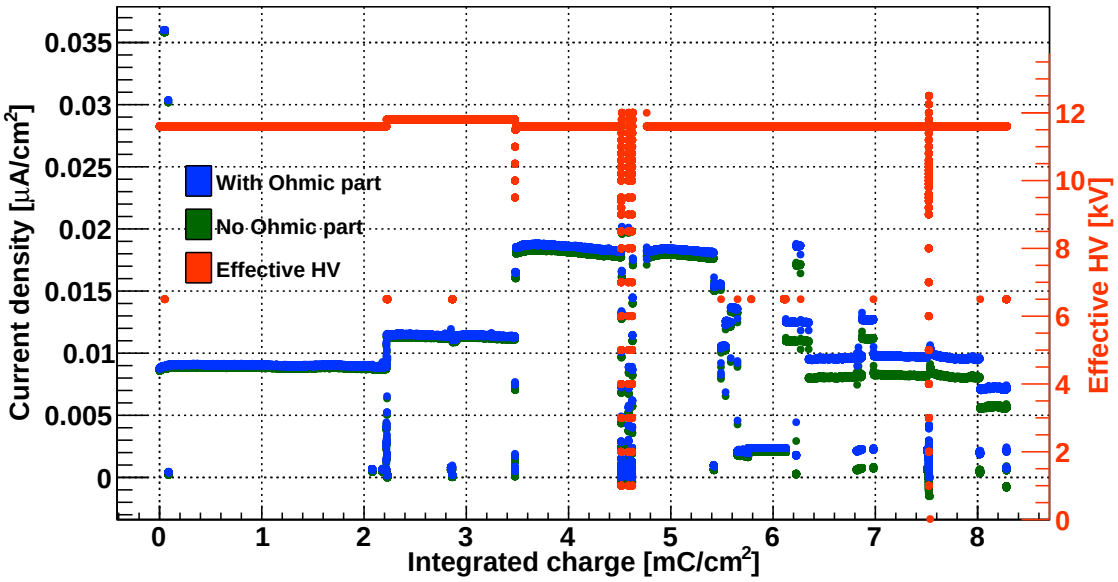

Figure 5.8: Effective high voltage and current density as a function of the integrated charge for the ALICE RPC - ECO1 gas mixture

collaboration[146].

5.2.2.2 Dark current investigation

Figure 5.9 shows the value of the dark current, both Ohmic and non-Ohmic, at the detector working point, as a function of the integrated charge. One can clearly observe the increase mentioned in the previous section. Indeed the dark current jumps from $\sim 0.0006\ \mu A/cm^2$ to $\sim 0.0022\ \mu A/cm^2$ between 5 mC/cm^2 and 8 mC/cm^2.

The hypothesis was made that this observation be related to the formation and/or deposition of impurities (produced by the interaction of the gamma radiation with the gas) along the spacers or the external frame, which would act as conductive channels. An attempt to recover the original conditions of the detectors was carried out. Indeed, it was decided to keep the RPCs for some time at a reduced voltage (so-called standby mode). In this way, the contribution of the gammas from the ^{137}Cs source is negligible (no charge multiplication and no further aging) but, nonetheless, the possibly present impurities could be burnt off and removed by the gas flow. During this period the absorbed current was also monitored, but no clear behavior emerges for the ALICE detector. This procedure did not prove successful for the ALICE RPC and both the Ohmic and non-Ohmic parts of the dark current of the detector did not seem to decrease. On the other hand, for other detectors of the collaboration this procedure proved somewhat successful and a reduction of the Ohmic part and/or of the total dark

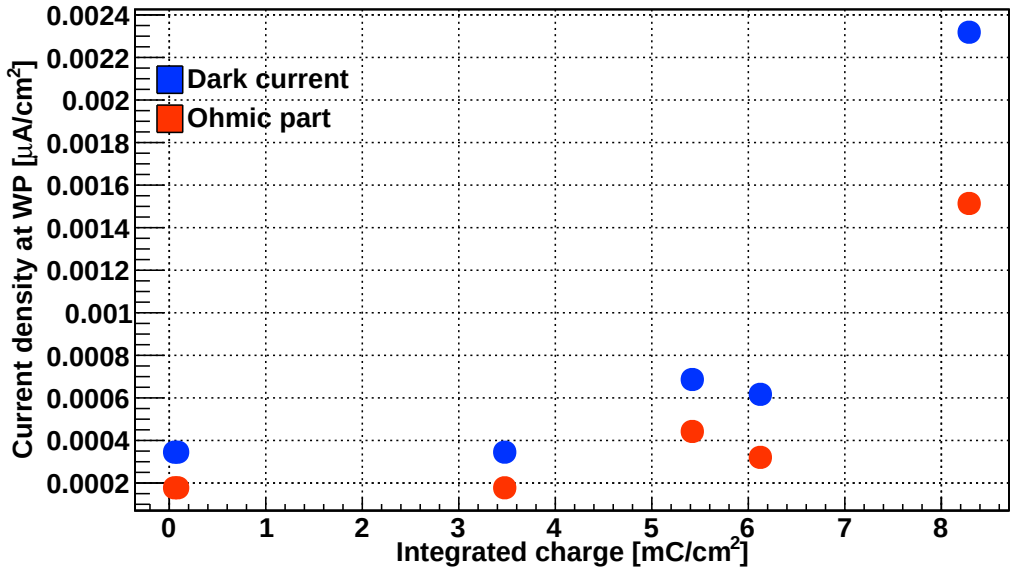

Figure 5.9: Dark current and its Ohmic part measured at detector working point for the first part of the aging studies - ALICE RPC - ECO1 gas mixture, with a clearly visible increase around the last points of the chart.

current was observed (see 5.2.2.4). Of course this kind of behavior, where a relaxation period is needed to operate properly, is not compatible with operation at the LHC. It is worth mentioning that for some detectors, such as the CMS-GT RPC, only the total dark current seemed to increase, while the Ohmic part was approximately stable over time, pointing to a different origin of the extra current. And indeed, for the CMS-GT RPC this effect was somewhat reverted by keeping the detectors in standby mode for a prolonged period of time.

5.2.2.3 Second irradiation attempt

Even though the preliminary results outlined above were not promising, it was decided to continue the studies with the ECO1 mixture, to better understand whether or not the dark current increase observed is linked to the gas mixture. Hence, after the irradiation at standby voltage, the detectors were exposed once again to the radiation at the nominal working point. The results of the full irradiation test are reported in Figure 5.10, where the first part of the chart (up to ~8 mC/cm^2) was already shown in Figure 5.8 and the second portion refers to the second irradiation attempt.

For integrated charge above 8 mC/cm^2, the difference between the current absorbed with and without the Ohmic part becomes more and more significant. This is once again a sign that the dark current (and especially the Ohmic part of it) of the ALICE RPC is greatly increasing over time. Also,

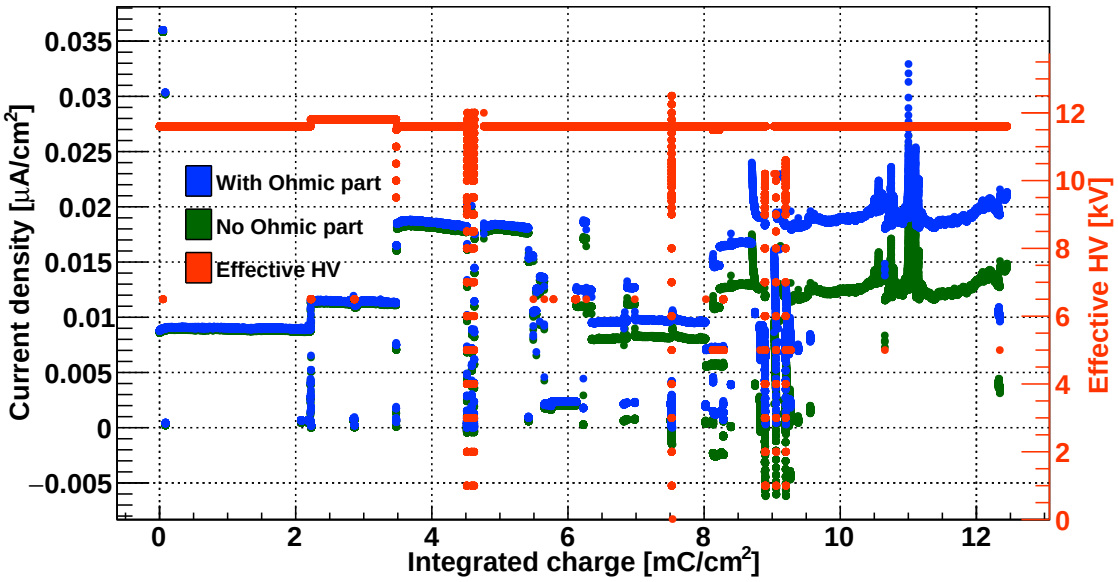

Figure 5.10: Effective high voltage and current densities as a function of the integrated charge for the ALICE RPC - ECO1 gas mixture, full irradiation campaign

a non stable trend can be seen for the current under irradiation. These could be signs of detector aging, and, since this effect was observed for all the detectors, it was decided to interrupt the studies with ECO1 and to move to a new gas mixture.

Figure 5.11 shows the values of the dark current, both Ohmic and non-Ohmic, at working point, for the whole irradiation period. The above-mentioned increase is here clearly visible. In this figure, the values of dark current measured during the standby period are not reported.

The Ohmic part of the dark current is very close to the total dark current. Moreover, the non-Ohmic component of the total dark current is increasing too, hinting to the presence of non-Ohmic effects as well.

Finally, note that in the first and the last irradiation period (from o to 2 and 10 to 12 mC/cm^2 respectively), the absorption factor was the same (ABS 22) but in the second period the absorbed current is much higher with respect to the first. This is explained by the increase in absorbed dark current alone. Indeed if one was to subtract the whole dark current (and not simply its Ohmic part) from the total absorbed current under irradiation, one would find that the gamma-induced current had not increased much (from ~ 0.01 to ~ 0.012 μA/cm^2). All things considered, this is the only promising result obtained with ECO1.

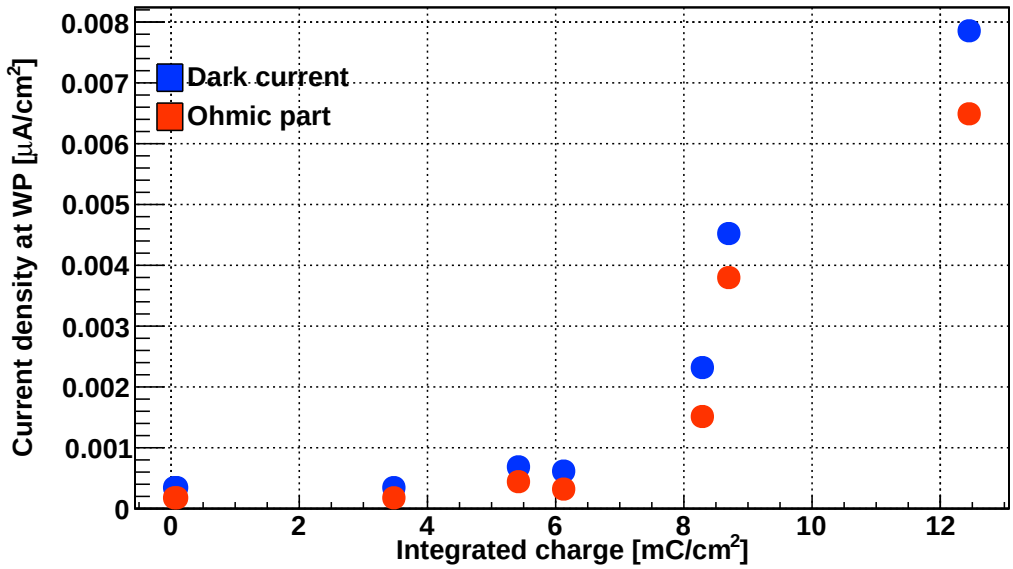

Figure 5.11: Dark current and its Ohmic part measured at detector working point for the whole aging with ECO1 gas mixture - ALICE RPC. The increase of the Ohmic component discussed in the text is clearly visible

5.2.2.4 ECO1 summary

Summarizing the results obtained with ECO1: the duration of the whole study was around 44 days, 17 of which with the detectors exposed to irradiation at working point. In this time frame, the ALICE detector integrated a total of $\sim$ 12.3 mC/cm^2, meaning around 0.7 mC/cm^2 per 24 hours of irradiation. The trend of the integrated charge in time is reported in Figure 5.12, where the horizontal sections represent time intervals in which the detector was off and no further charge was integrated.

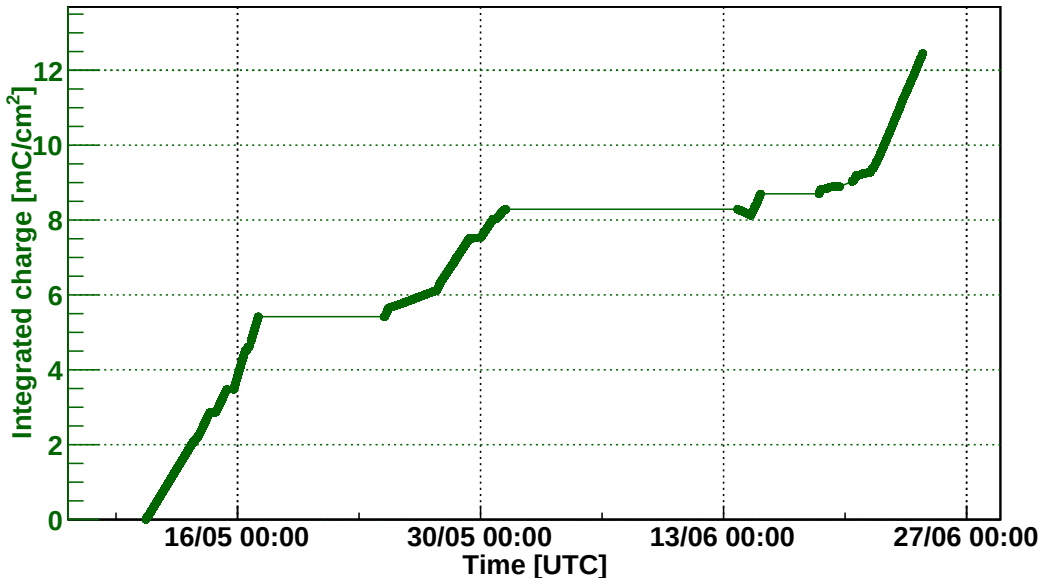

Figure 5.12: Trend in time of the integrated charge with the ECO1 gas mixture for the ALICE detector. The horizontal portions of the chart represent periods of time when no charge was integrated

Figure 5.13 shows the trend of the dark current (total with blue markers and Ohmic in with red markers), as a function of the integrated charge, for two other detectors of the ECOgas@GIF++ collaboration: CMS-GT top gap (2 mm double gap RPC) in the left panel and CMS-KODEL bottom gap (1.4 mm double gap RPC) in the right panel. The dark current increase pointed out in 5.2.2.3 for the ALICE RPC is also visible for the two above-mentioned detectors. For the CMS-GT top, the increase is only in the total dark current, while its Ohmic part is stable. For the CMS-KODEL bottom gap, instead, a slight decrease in the dark current (for an integrated charge between 5 and 6 mC/cm^2) shows the dark current decrease (especially in the Ohmic part) after the prolonged standby period mentioned in 5.2.2.1.

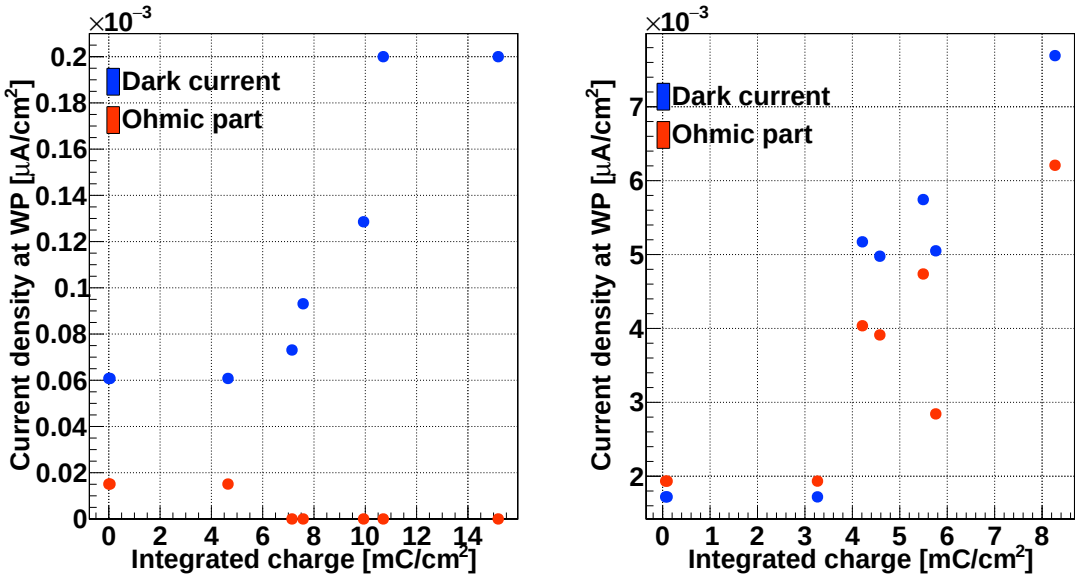

(a) CMS-GT top gap **(b)** CMS-KODEL bottom gap

Figure 5.13: Total and Ohmic dark current absorbed by two detectors of the ECOgas@GIF++ collaboration during the irradiation campaign with ECO1

Since, at the time that the ECO1 studies took place, the RPCs were not equipped with any front-end electronics, it was not possible to correlate the increase of dark current with a possible increase of detector dark counting rate (counts when the RPC is not exposed to any irradiation) or to highlight possible hot-spots in the RPC, that is to locate any point of the inner surface where the intrinsic detector noise rate is much higher than the in the rest of the detector.

5.2.3 ECO2 (MIX5) gas mixture

ECO2, labelled as MIX5 in Chapter 4, is the second eco-friendly mixture that was aging-tested. The difference with respect to ECO1 is a lower HFO concentration (35%) and a higher CO_2 fraction (60%), while i-C_4H_{10} and SF_6 are still at 4% and 1% respectively. The idea behind the CO_2 percentage increase is related to the fact that the HFO molecules seem to be more prone to breakage under irradiation than the $C_2H_2F_4$ ones[146] and, for this reason, mixtures containing HFO might produce a greater quantity of pollutants with respect to the R134a-based ones. Furthermore, it is known[125] that for every 10% HFO added to the mixture, the working point moves by about 1 kV to higher values. Following this reasoning, by reducing the HFO concentration, one might lower impurity production and, at the same time, be able to operate the detector at a lower voltage, which is expected to reduce the intrinsic noise from surface imperfections.

The ECO2 gas mixture was tested during a beam time period (as described in 4.5.2), so the behavior of the detector was known, in terms of efficiency and rate capability. The default value of absorption factor in GIF++ is 2.2. As a first step, the effective high voltage of the ALICE RPC was set to a value of 10.6 kV, which corresponds to the source-off knee and the counting rate of the detector with ABS 2.2 at this voltage corresponds to $\sim$ 160 Hz/cm^2. These observations could not be done with ECO1, since no beam test had been carried out before starting the irradiation. For this reason, for ECO1, the difference in turn-on point of Figure 5.7 was used.

5.2.3.1 Stability results

In order to carry out the studies with the ECO2 gas mixture, the ALICE RPC had to be replaced with a new one, because, following the aging test with ECO1 and during further irradiation studies with the standard gas mixture, the dark current had started to grow at much faster pace than usual. This specific issue was not observed in the other detectors, hence it has been attributed to a detector-specific problem, not related to the gas mixture. After closer inspection, it was found that the cause of this uncontrolled increase was a faulty high voltage connector. The replacement of the connector would have been more demanding than simply changing the detector. The new RPC is the one that was used for all the beam tests described in Chapter 4, which was tested with cosmic muons in Turin and whose performance was found to be fully satisfactory.

The irradiation campaign was started with all the detectors of the collaboration, and the same procedure as with ECO1 was followed. The high voltage is switched ON to the value discussed above (10.6 kV) and the stability of the absorbed current is monitored over time. Weekly I(HV) source off scans are performed to keep track of the dark current and its Ohmic component.

Figure 5.14 shows the stability of the absorbed current of the SHiP/LHCb RPC (1.6 mm single gas gap detector), as reported in Reference [143].

The high voltage and currents are shown as a function of the elapsed time from the start of the irradiation test and a good stability of the current is observed. The total amount of integrated charge for the period shown in the chart is $\sim$ 18 mC/cm^2. Similar results have been obtained also by other detectors. Also the dark current (both Ohmic and non-Ohmi) exhibited a stable behavior over time. This is a promising result, and much different than the one obtained with the ECO1 mixture.

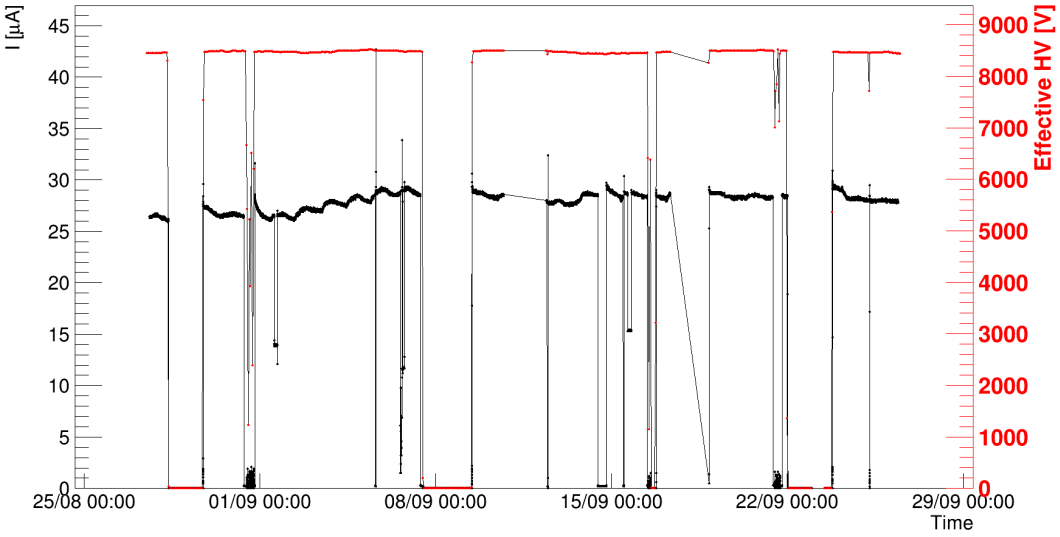

Figure 5.14: Trend of effective high voltage and absorbed current by the SHiP/LHCb RPC under irradiation with ECO2. The quantities are shown as a function of time and the total integrated charge in the period shown corresponds to $\sim$ 18 mC/cm^2. Figure taken from [143]

For what concerns the ALICE RPC, instead, the detector behaved as expected during the beam test and also in the beginning of the aging studies with ECO2. After the integration of $\sim$ 5 mC/cm^2 the current under irradiation (and also the dark current) started to drift over time. This effect was only observed for the ALICE detector, hence an investigation campaign was launched, to try and understand whether the issue is purely detector-related or it is still somehow connected to the gas mixture. The investigation is detailed in the following section. Note that the ALICE RPC is the only one in the ECOgas@GIF++ collaboration to have a double linseed oil coating on the inner surfaces of the bakelite (as discussed in Section 2.3) and this could interact differently with the gas mixture.

5.2.3.2 Current increase in ALICE

The steady increase of the absorbed current, anticipated in 5.2.3.1, is shown in Figure 5.15. The absorbed current was stable up to $\sim$ 5 mC/cm^2, but it then started to drift, almost doubling over the course of one week.

By analyzing a few I(HV) scans taken with source off, one can also see that the dark current absorbed by the detector was increasing over time. The increase is not so large for the Ohmic part but more clearly visible in the non-Ohmic component of the dark current. Figure 5.16 shows different I(HV) curves taken at source OFF, each of them corresponding to a given integrated charge value. The vertical line in the chart represents the effective high voltage maintained under irradiation (10.6 kV) and one can see how

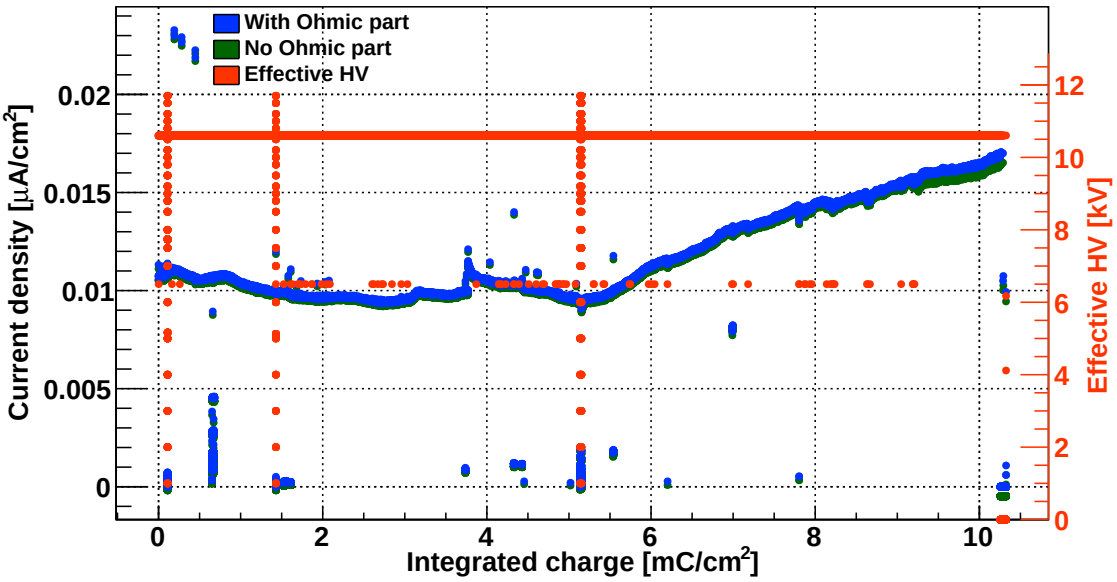

Figure 5.15: Trend of effective high voltage and absorbed current by the ALICE RPC under irradiation with ECO2. Values shown refer to source ON condition

the dark current greatly increased, especially in correspondence of the last I(HV) scan.

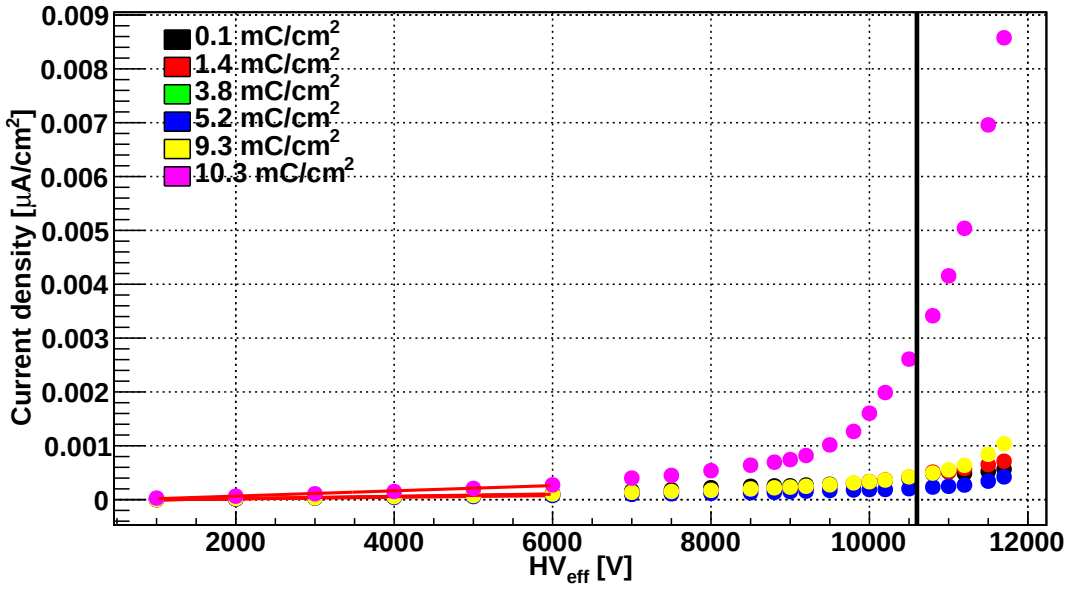

Figure 5.16: I(HV) scans with source OFF for different values of integrated charge with the ECO2 gas mixture. Increase of the dark current in the last scan clearly visible

The dark current increase itself does not justify the increase shown in Figure 5.15. Indeed, the dark current has increased from 0.0005 to 0.0028 μA/cm^2 while the current under irradiation has moved from 0.0093 to 0.0169 μA/cm^2. This means that whatever is causing the increase, is doing so for both dark and non-dark current but at a difference pace for the two.

The irradiation campaign with ECO2 continued normally for all the other

detectors, since they did not show any sign of current increase. Only the ALICE RPC was kept with the high voltage off and gas still flushing, to avoid damaging the detector further without having understood the cause of the observed current increase. In a first phase of the investigation on the observed current increase, the detector was switched on from time to time, to take periodic I(HV) scans at source off to monitor the evolution of the dark current. The results of those scans are reported in Figure 5.17. Each of them has a run number and timestamp attached (run numbers are chronological, meaning that a run with greater run number was taken later). Runs 272 and 382 are from before the current increase, while the others are taken after the detector was excluded from the irradiation studies. It is possible to notice how, by simply flushing the RPC in standard conditions, the dark current slowly decreases. This is particularly evident for runs from number 401 onward. After about four months of flushing with chamber off (except for the I(HV) source-off scans mentioned), the dark current is almost the same as before the current increase.

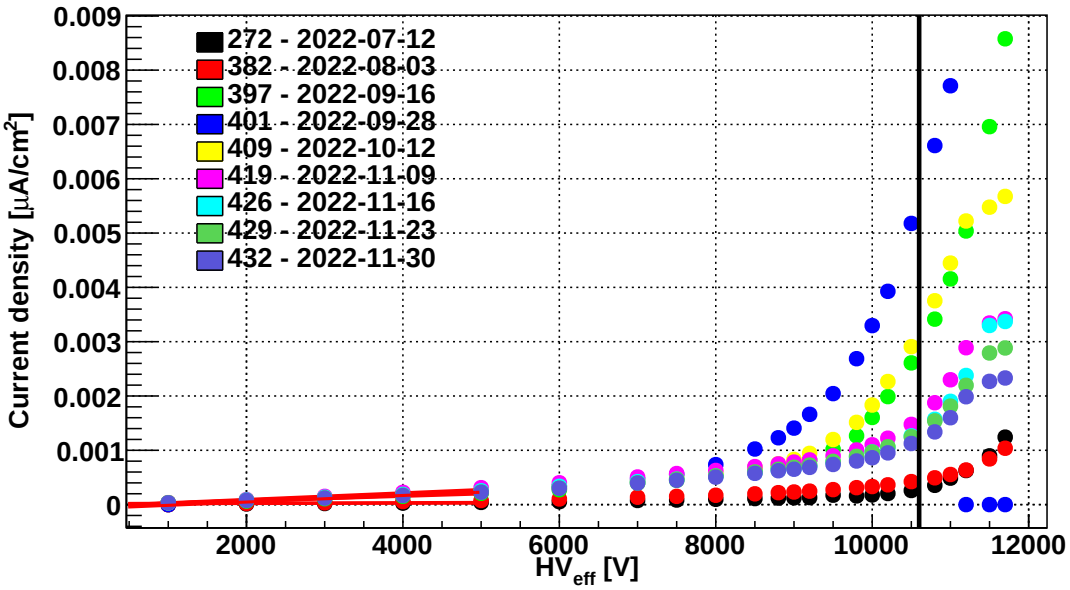

Figure 5.17: Different I(HV) scans at source OFF. Each scan is taken at a different time, over the span of three months. The vertical line represents the voltage value chosen for the irradiation with ECO2

This is an interesting observation, since it means that whatever is causing the current increase is most likely reversible.

The steps taken in the investigation are described in the following. The studies started from the problems that most commonly can affect RPC detectors, such as bad insulation of the high voltage electrode and/or issues with the high voltage connector. Those tests, carried out as soon as the current increase was noticed, have proven unsuccessful (no evident reason for

the increase was found), so the possibility that the gas mixture relative humidity was producing the observed current increase was investigated, i.e, an attempt to correlate the current increase with the gas mixture relative humidity was carried out. In parallel, a possible correlation between the detector dark current and dark counting rate was also investigated.

Search for current leaks

As the current increase was noticed, it was decided to perform some tests to exclude an hardware issue related to the HV cable/connector. Swapping the cable and changing the channel of the HV power supply did not seem to improve the situation. Replacing the HV connector on the RPC side did not change the behavior of the detector either.

Another explanation for the observed current increase could be a defective insulation between the RPC high-voltage electrode and ground, creating a conductive path for the current to *leak* through the mechanical frame of the RPC towards ground, without flowing through the gas gap. Figure 5.18 shows in detail how the ALICE RPC is connected to the high voltage module. In particular, the HV cable employed is coaxial, meaning that a single cable is used to connect the detector to the HV module. The core of the cable is what supplies the high voltage, while the externally woven copper shield is used for the ground (return line). The two are separated by means of a dielectric insulator and they are both inserted into an outer plastic shell. The connection of the cable to the detector is performed through two thin graphite coatings on the outer part of the bakelite electrodes. The electrodes are electrically isolated from the mechanical frames by a mylar sheet. If, for any reason, such insulation starts to deteriorate, some current may leak from HV to ground through the mechanical frame. The damage to the insulation could be worsening over time, possibly explaining the systematic current increase observed.

It is worth mentioning now that all the values of currents that have been shown so far are measured directly from the CAEN HV mainframe. If the detector is working properly, all the current measured by the module should be flowing through the gas gap. If this is not the case, part of the current could be flowing through other parts of the detector. In case of bad insulation, as explained earlier, it could be flowing through the mechanical frame to ground. Another possibility is that the current is flowing around the plastic spacers that are used to maintain the distance between the bakelite electrodes (see 2); as mentioned earlier, this could be due to deposition of

impurities around them, leading to the creation of conductive paths inside the gas gap.

Since the CAEN HV module provides only a reading of the total current (flowing from high voltage to ground), it is not possible to disentangle the different components of the currents. By connecting an amperometer in series with the return line (from the gas gap to ground), as shown in Figure 5.18 by the circle with an "A", one can measure only the current that is flowing through the gas gap. If the current measured by the amperometer is much lower than the value provided by the CAEN HV module, it is a good indication that some current is leaking, without going through the gas gap. Note that the hypothesis that current is flowing around the plastic spacers can not be tested with this strategy.

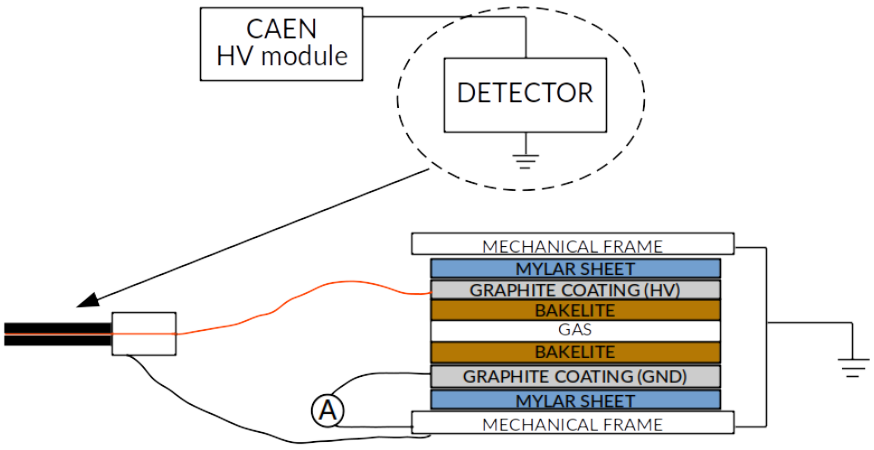

Figure 5.18: Sketch of the RPC connection to the coaxial high voltage cable (not to scale). The object labelled with "A" is the amperometer

The measurement has been carried out for different values of applied voltage and the results are shown in Table 5.3. Note that the measurements have been carried out without irradiation and after the replacement of the high voltage connector. To give some context to the measurements, it is useful to provide some numerical values of the dark current values. Before the current increase, the dark current at 10.6 kV effective high voltage was $\sim$ 0.00032 μA/cm^2 while after the current increase it was $\sim$ 0.0054 μA/cm^2, i.e., an increase by $\sim$ 16 times has been observed. The idea behind the measurement of current leak is to verify whether any discrepancy is present between the values provided by the HV module and the amperometer and to check if this discrepancy is compatible with the observed current increase. If this is the case, one can then assume that the increased current is not circulating in the gas gap but it is rather flowing through a parasitic path.

By comparing the data reported in the table, a discrepancy of $\sim$ 0.0004

μA/cm^2 can be observed for the highest HV values. There can be multiple explanations for this difference, ranging from low precision of the amperometer to the presence of a small current leak, and it is not possible to pinpoint the exact cause. Nonetheless, this difference is much smaller than the observed current increase (~ 0.005 μA/cm^2), so it is safe to state that a current leak cannot explain the observed current increase.

HV [V]	$\mathbf{I}_{CAEN}$ **[μA/cm^2]**	$\mathbf{I}_{AMP}$ **[μA/cm^2]**
0	0	8E-05
1000	2.8E-05	0.00012
3000	0.00018	0.0002
5000	0.000356	0.00032
6000	0.000464	0.0004
7000	0.0006	0.00048
7500	0.000672	0.00052
8000	0.000812	0.00064
8500	0.00102	0.0008
9000	0.00132	0.00104
9500	0.0018	0.00148
9750	0.002324	0.002
10000	0.002844	0.00256
10250	0.003252	0.0028

Table 5.3: Current measured by the CAEN HV module and by the amperometer for different values of applied voltage. The difference between the HV module and amperometer reading is ~ 0.0004 μA/cm^2 at most while the current increase is 0.0051 μA/cm^2, meaning that a current leak cannot explain the increase

The role of humidity

Once verified that no evident leakage issue is the cause of the current increase, the attention was shifted to another key component, the gas mixture humidity. As previously shown (in 4.3.1), the gas mixture is bubbled through water, to retain a certain amount of water vapor, in order to humidify the bakelite surfaces and keep their resistivity constant. One has to be very careful not to insert too much water vapor into the RPC, otherwise the resistivity of the bakelite could decrease and, as a consequence, the absorbed current increase. This was the case of the ALICE RPCs, which, when installed in the ALICE cavern, were flushed with a gas mixture that had a relative humidity content of 40% and, when switched on for the first time, had a similar behavior as the one shown earlier, where the absorbed current was constantly drifting over time. The humidity was lowered to 37% and

the current increase ceased and the original values were recovered[147].

In order to test if the same problem might be happening to the RPC under test at GIF++, the value of the gas mixture relative humidity was monitored, using the dew point sensor mentioned in 4.3.1 was carried out. One can compute an estimate of relative humidity value using a converter, such as the one provided by this website [1] if the dew point and the temperature of where humidification occurs are known. A dew point of 4°C, at a temperature of 20°C (typical temperature at the humidifier location) corresponds roughly to 40% relative humidity.

The gas mixture dew point was reduced and monitored throughout the test. This was divided into two phases: first, the detector was kept with the high voltage off, while flushing it with a reduced humidity content gas mixture; periodic I(HV) scans with source off were taken to check whether the reduced humidity had any effect on the dark current. In the second phase, the high voltage was switched on and the detector was kept under irradiation, with a reduced humidity gas mixture flowing. This time both the dark current and the current under irradiation were monitored and the effect of the reduced humidity on both was studied.

In order to test the effect of humidity, the dew point of the gas mixture was changed from the usual 4°C to around 0.5°C, 2.5°C, 4°C and back to 0.5°C. The different values have been set to understand if the detector behaves differently with changing dew point values. The trend of the gas mixture dew point (measured at the mixer level) is reported in Figure 5.19, for the whole duration of the test period.

The reason why the dew point value hovers around the set value is because the temperature where the gas mixture is humidified is not constant over time and a manual adjustment of the dew point is needed.

Initially the RPC was left flushing and the dew point of the gas mixture was lowered from 4°C down to $\sim$ 0.5°C ($\sim$ 42% down to 35% relative humidity), with the high voltage switched off and periodic source off I(HV) scans were taken, to check whether or not the reduced humidity content had any effect on the dark current. The results of these scans are reported in Figure 5.20. A scan taken before the current increase (the curve with black markers) is shown for reference; the other curves represent data taken with $\sim$ 0.5°C dew point. They span a period of around 4 days and it is possible to observe that the current seems to be slowly decreasing, although never reaching values comparable to before the increase. This behavior is similar to what was reported earlier, that simply by keeping the high voltage off

[1] https://www.calculator.net/dew-point-calculator.html

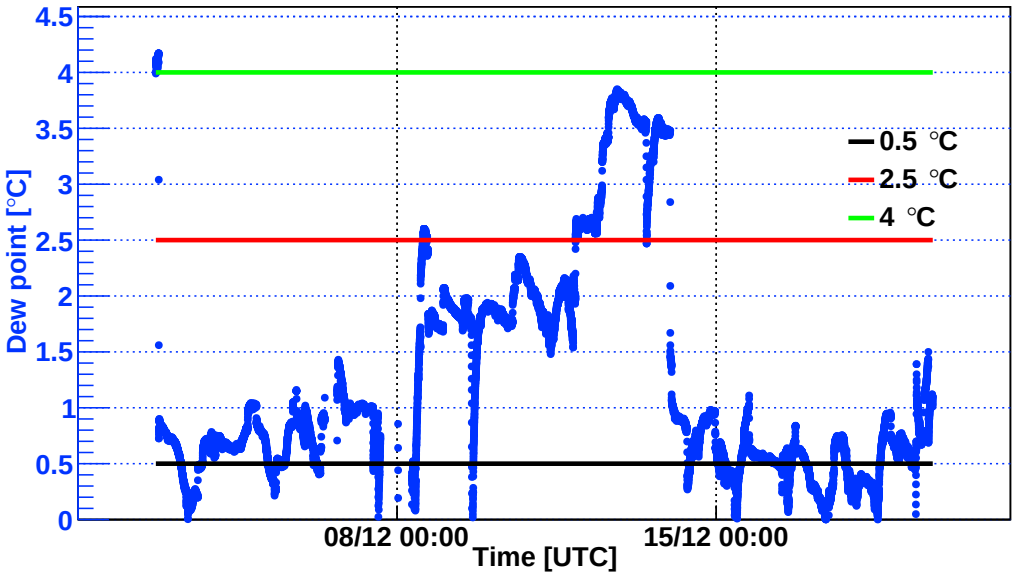

Figure 5.19: Gas mixture dew point measured at mixer level with the dew point sensor during the whole test period

and flushing the detector, the dark current decreases, so one can not unambiguously conclude that there is an effect of the humidity.

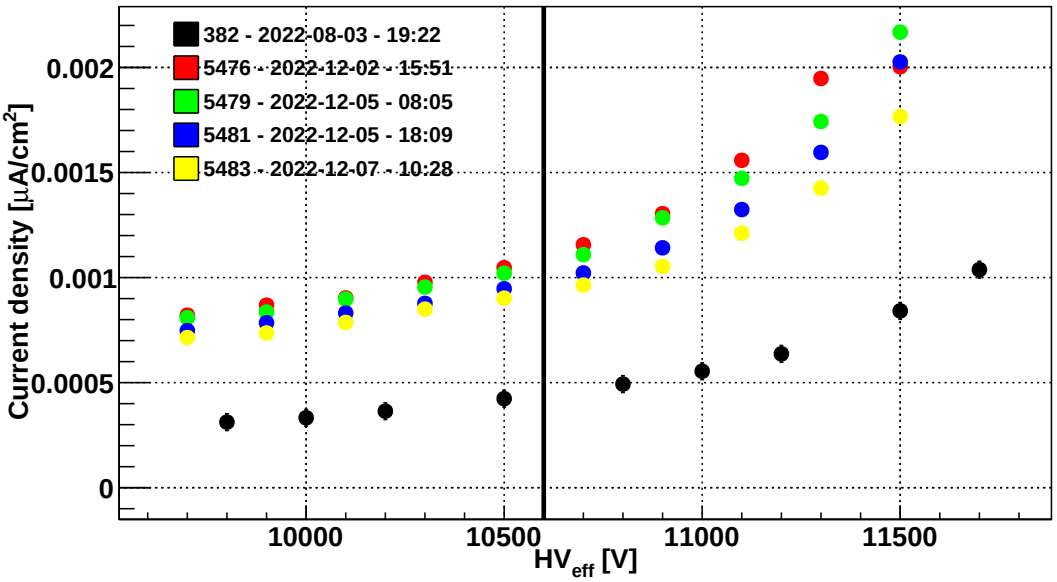

Figure 5.20: I(HV) source off scans taken with lower humidity (dew point set to 0.5°C). The scan in black was taken before the current increase

The high voltage of the RPC was switched on at the irradiation value of 10.6 kV and the detector was kept under irradiation for some time and the absorbed current under irradiation was monitored (recall that the first sign of current increase was observed as increase of current absorbed under irradiation). Together with the current under irradiation, also the dark current (without irradiation) was measured periodically to check for any variation

due to the radiation. The behavior of both currents is described in the following. Figure 5.21 reports (in the top panel), the status (on or off) of the source together with the value of absorption factor, while the bottom panel contains the trend of current and dew point, for the duration of the reduced humidity studies. Note that the applied voltage has been kept at 10.6 kV for the whole duration of these studies, except for the source-off scans.

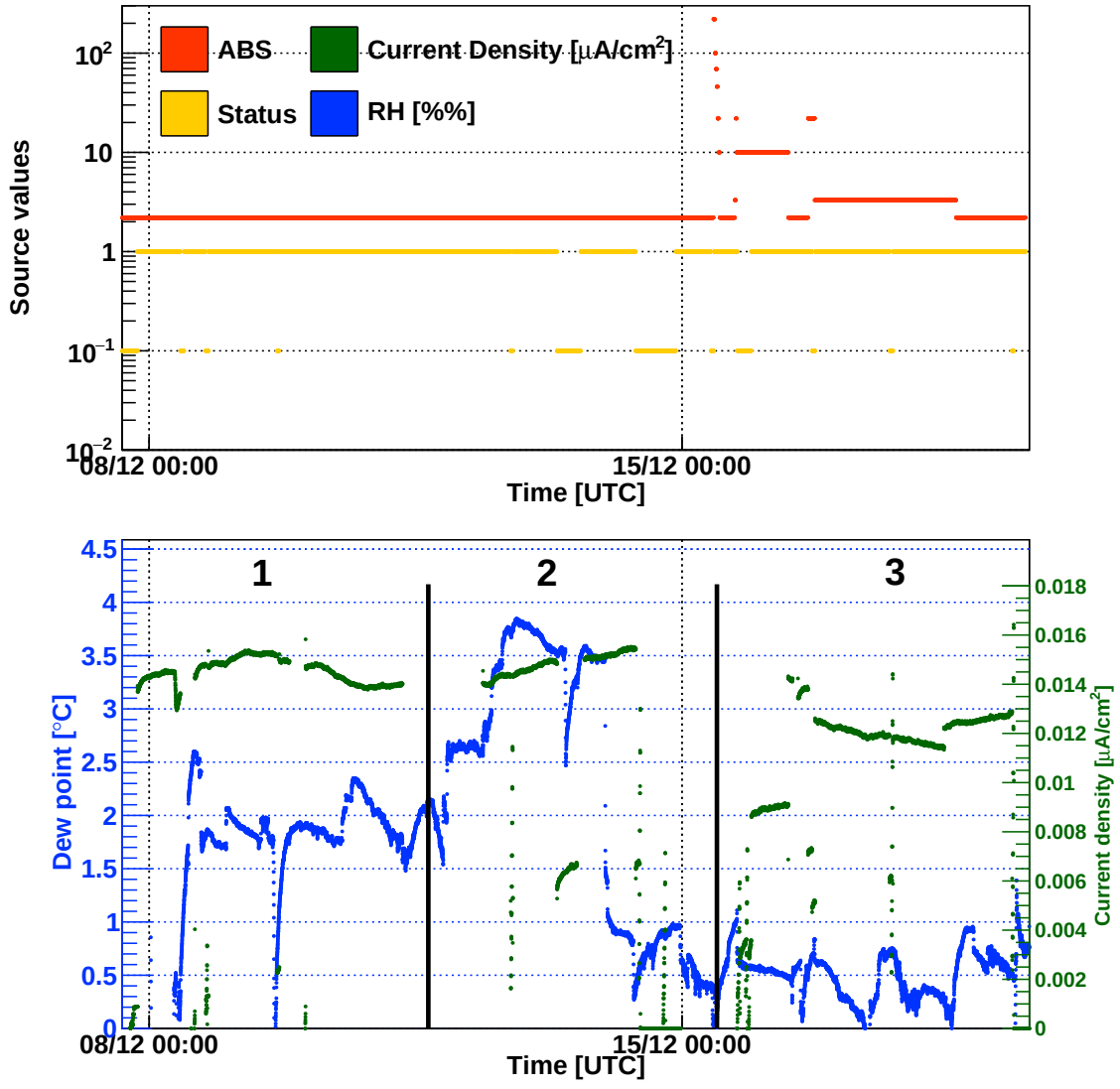

Figure 5.21: Trend of gas mixture dew point (in blue) and absorbed current (in green), at fixed value of high voltage. The three periods identified by numbers are associated to different values of dew point

In the regions marked with the number 1 and 2, the absorption factor was kept at 2.2 for the whole time and the dew point varied from to 2.5 to 4°C. No clear correlation appears between the absorbed current and the dew point of the gas mixture. In region 3, the value of ABS was changed quite

frequently due to requests by other users and this explains the current variations observed. No striking correlation appears between the current and dew point but one can observe a slight current decrease when comparing the current for ABS 2.2 in regions 1-2 with that in region 3 for the same ABS value. However, the effect is small, so it seems unlikely that the humidity content be responsible for the sudden current increase observed with ECO2 for the ALICE RPC.

Dark current and dark rate vs irradiation time

The current under irradiation does not show a clear correlation with the different values of gas mixture relative humidity that have been tested. The periodic I(HV) scans that have been carried out throughout the irradiation show, instead, a clear increasing trend of the absorbed dark current. All the runs taken are summarized in Table 5.4, together with a short remark regarding the conditions in which each measurement was carried out.

Run number	Comments	Dew point [°C]
5483	Baseline reference run	0.9
5486	HV on under irradiation for 118 hours since the start of the test - ABS 2.2	2.5
5487	HV on under irradiation for 159 hours since the start of the test - ABS 2.2	0.5
5488	HV off for 8 hours since scan 5487	0.9
5489	HV off for 32 hours since scan 5487	0.5
5490	HV on without irradiation for 2 hours since scan 5489	0.5
5494	HV on under irradiation for 48 hours since scan 5490 - ABS 3.3	0.5
5496	HV on under irradiation for 36 hours since scan 5494 - ABS 2.2	0.5

Table 5.4: Summary of high-voltage scans taken with reduced humidity content, with information on the status of each run

Figure 5.22 reports the I(HV) trend for the different scans taken at source off, throughout the irradiation period. One can clearly see that the dark current tends to increase for increasing irradiation time: going from run 5483 to 5487 the RPC was kept with the high voltage switched on under irradiation and the dark current at the irradiation high voltage (10.6 kV) increases from ~ 0.001 μA/cm^2 to ~ 0.006 μA/cm^2. However, it was observed that

keeping the high voltage off for some time, as it was done from run 5487 to 5489 (high voltage was off for $\sim$ 8 hours), has the effect of reducing the dark current from $\sim$ 0.006 μA/cm^2 to $\sim$ 0.002 μA/cm^2, hinting to a possible reversibility of the dark current increase just discussed.

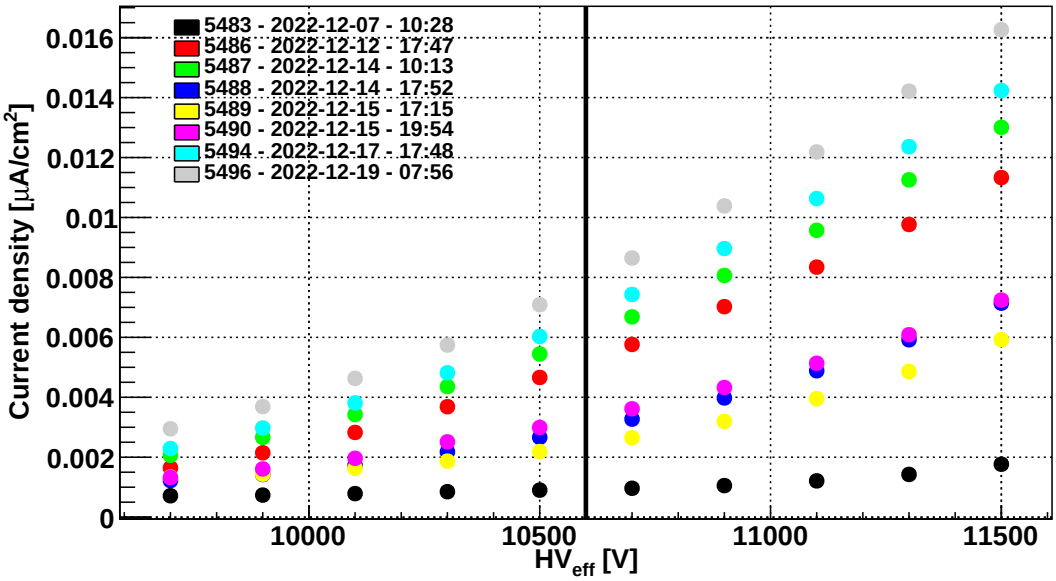

Figure 5.22: I(HV) scans with source off, taken throughout the low humidity test. Refer to Table 5.4 for the details of each scan

Another interesting observation is that also switching on the high voltage, without exposing the RPC to any irradiation (as is the case between runs 5489 and 5490), leads to a dark current increase, possibly indicating that this effect is not strictly related to the presence of irradiation. Moreover, a possible correlation between dark current increase and time spent with the high voltage switched off can be observed. Indeed, two periods when the high voltage was off can be identified: before run 5483 and between runs 5488 and 5489. The difference between the two is that, in the former case, the RPC was off for a few months, while in the latter only for $\sim$ 40 hours. If one compares the dark current increase between runs 5483-5487 (first portion of the irradiation with lower humidity) and runs 5489-5496 (second portion of the irradiation with lower humidity), the increase in the former is $\sim$ 0.005 μA/cm^2 while in the latter it is $\sim$ 0.006 μA/cm^2. Keeping in mind that the time under irradiation in the first case is 168 hours while in the second it is 86 hours, one can see that the current increment per unit time is greater in the second case (RPC had only been off for a couple of days before irradiation) than in the first case (RPC had been off for months before irradiation).

Together with the current measurements, it was also decided to measure

the dark counting rate of the detector, that is the counting rate of the RPC when no irradiation is present, to test whether the increase in absorbed current is related to an increase in dark rate. More specifically, the idea is to look for hot-spots, that is spots on the bakelite surface where the dark counts are much higher than the neighboring points. To carry out this measurement, the FEERIC front-end electronics were installed on the detector and a dark rate measurement was carried out periodically, in parallel with the measurement of dark current and for the same set of I(HV) scans. The data for the dark rate measurements have been collected using the random trigger described in 4.3.3, to sample the RPC response periodically and measure its noise counting rate. Recall that all the measurements are taken without irradiation, hence all the counts in the RPC are either from detector or electronics noise. Since the idea is to correlate the current increase with an increase in dark counts (hence detector noise), one has to disentangle these from the electronics noise. To do this, an offline auto-trigger algorithm has been developed. The idea behind it is to exploit the 2D readout of the ALICE RPC. Indeed, by checking whether a hit on a given strip plane is coupled with a hit on the perpendicular strip plane, within a short time window ($\sim$ 50 ns), one can greatly reduce the contamination of the electronics noise in the counts. This is the idea behind the algorithm: for each hit on the y-strips (vertical ones), go through all the hits on the x-strips (horizontal); if any of those hits happened within 50 ns from the y hit under consideration, then a 2D noise map is filled in correspondence of the intersection of the two strips. An example of such a measurement is reported in Figure 5.23.

The noise maps for all the runs are reported in Figure 5.24. Since for all measurements the number of triggers and the length of the acquisition window (20000 triggers with a duration of 5000 ns each) is the same, they can be directly compared with each other, without further normalization. The maps show the results at the irradiation high voltage (10.6 kV). Table 5.4 reports the conditions under which each run was taken. One can see that after roughly 160 hours of irradiation, three hot spots tend to appear (marked with a red circle in the left panel of Figure 5.24b). Furthermore, in run 5486, (right panel of Figure 5.24a), the counts in the top right corner of the RPC are globally much higher than the rest and this is due to a front-end board which was affected by high noise levels (the same happens in run 5489). Those counts are picked up as a signals by the auto-trigger algorithm since their noise frequency is $\sim$ 10 MHz, corresponding to a signal roughly every 100 ns due to how the output stage of the front-end boards is built[111].

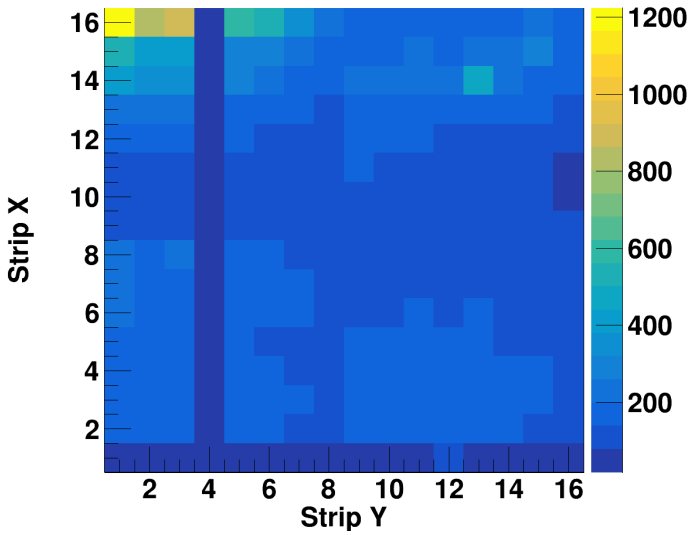

Figure 5.23: Example of 2D noise map of the ALICE RPC. The x axis represents the vertical strip number (horizontal coordinate), the y axis the horizontal strip number (vertical coordinate). The width of a strip is $\sim$ 3 cm

Between runs 5487 and 5488 (left and right panels of Figure 5.24b), the RPC was kept with the high voltage off for 8 hours and one can see that the previously mentioned hot-spots tend to disappear. This effect is even more visible after 24 more hours with the high voltage off, in run 5489 (left panel of Figure 5.24c).

The last aspect to be verified is whether the hot-spots are related to the presence of the irradiation or simply to the high voltage. To test this, the high voltage was switched on for some time without irradiation. The result, shown in run 5490, is that the same hot-spots tend to reappear, hinting to the fact that they are not (or not only) related to the action of the gammas on the detector.

The tests just described show that the dark current of the ALICE RPC is strictly correlated with a localized increase of intrinsic noise in a few spots, which tends to grow in time once the high voltage is switched on. The observed increase seems to be somewhat reversible by letting the detector *cool down* with the high voltage switched off. Of course this is not an expected behavior for the detector. The outcome of this test is not sufficient to prove that the problems are related to the detector only. Specifically, the highlighted hot-spots could respond in different ways to different mixtures. For this reason, before replacing the RPC, one should repeat the same measurements using the standard gas mixture. In case the results with the standard mixture are similar to the ones shown earlier, one could confirm that the issue is detector specific, and not related to the gas mixture. This is a planned activity for 2023. It could not be done in time for the writing of this thesis

since the gas mixture is shared with the other RPCs of the ECOgas@GIF++ collaboration, which, given the promising results obtained with ECO2 for all but the ALICE detector, gave priority to continuing the aging tests with such a mixture.

Once all the ”non-destructive” tests on the ALICE RPC have been carried out, one could also perform a microscopic analysis of the inner surfaces, in correspondence of the highlighted hot-spots to better understand their origin. This kind of tests imply removing the glue around the gas gap, making it unusable, hence they have to be performed as a last resource, when no more information can be extracted with other studies.

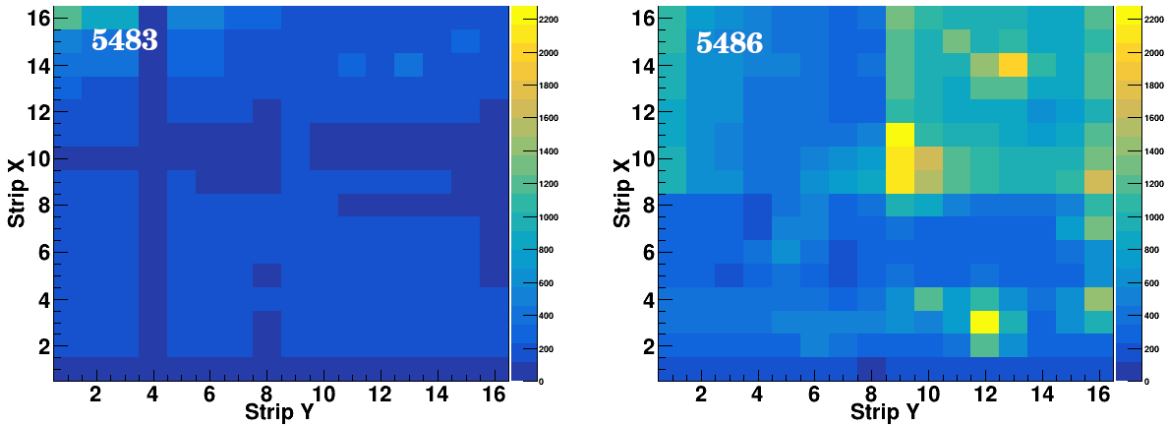

(a) Left panel: run 5483. Right panel: run 5486. RPC was kept with the high voltage on under irradiation. Time elapsed between the two runs: ∼ 118 hours. Appearance of hot-spots (circled in red) following irradiation

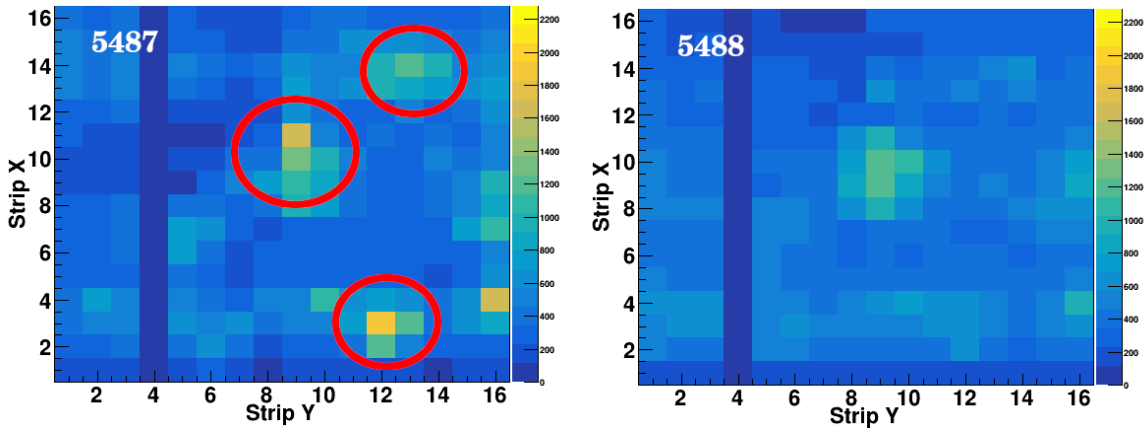

(b) Left panel: run 5487. Right panel: run 5488. Run 5487 was taken ∼ 40 hours after run 5486. Hot-spots are still visible. Between run 5487 and 5488, the high voltage was kept off for ∼ 8 hours, the hot-spots start to cool down

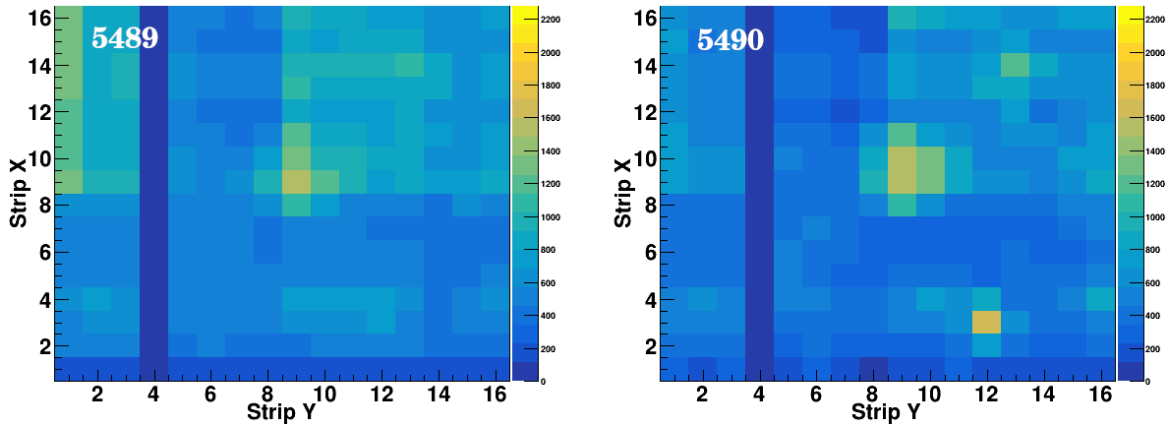

(c) Left panel: run 5489. Right panel: run 5490. Run 5489 was taken after further ∼ 24 hours with high voltage off, the hot-spots cool down even more. Between runs 5489 and 5490, the high voltage was kept on without irradiation for ∼ 2 hours, an increase in dark counting rate is visible

Figure 5.24: 2D noise maps taken at different times during the studies. The appearance of hot-spots after the high voltage is switched on for some time is clear. Also the disappearance after the HV is off can be seen. Refer to the text for further details about the conditions of each run

5.3 Summary of aging studies

This chapter outlined why aging studies are necessary in the framework of the search for new eco-friendly gas mixtures for RPC detectors. It also explained the methodology applied by the ECOgas@GIF++ collaboration and it described some of the results obtained thus far. In particular the results obtained with three mixtures, namely standard, ECO1 (45% HFO and 50% CO_2), and ECO2 (35% HFO and 60% CO_2) have been illustrated in detail. The standard gas mixture has been used as a reference, to test the data taking stability and all the safety mechanisms, such as the gas kill and the automatic lowering of the applied voltage in case of too low attenuation. ECO1 was the first mixture tested and it was discarded due to an increase of absorbed dark current (both Ohmic and non-Ohmic) in all the detectors of the collaboration. ECO2 is currently being tested and, so far, all the detectors but the ALICE one (which showed an increase of absorbed current under irradiation), have shown stable performance over time. For the ALICE RPC, an in-depth campaign to study this increase was carried out. It was found that the current increase is strongly correlated with the appearance of localised hot-spots when the high voltage is switched on for some time (even if no gamma irradiation is present). This is most probably due to the presence of defects on the inner surface of the bakelite, which points to a detector-specific issue. The test will be repeated in 2023, after the detector is flushed for some time with the high voltage kept off, to confirm the observed cool-down effect. Also, as anticipated earlier, the same tests will be repeated with the standard gas mixture. Depending on the results, this test may either provide the final confirmation that the issue is detector-specific and validate the stability of ECO2 also for ALICE, or prompt a deeper investigation of the interaction of the ECO2 mixture with the double-oiled bakelite electrode surface.

Chapter 6

Summary and outlook

The work presented in this thesis consists of two main investigations: on the one hand, a small ALICE-like RPC prototype has been used to characterize different HFO-based gas mixtures using a muon beam, also exploiting the photon flux provided by the CERN Gamma Irradiation Facility to study the detector rate capability. On the other hand, the same RPC prototype has been used to study the stability of its response (in terms of absorbed current) when operated, under irradiation, for long periods of time with HFO-based gas mixtures.

Both activities are inserted in the context of the ECOgas@GIF++ collaboration, formed by members of the four LHC experiments and of the CERN gas group to join forces in the search for an eco-friendly alternative to the currently employed RPC gas mixture.

The main results obtained with the beam tests are summarized in the following:

- Seven different HFO-based gas mixtures, with CO_2 addition, have been tested during beam periods at the CERN GIF++. The HFO concentration has been increased in steps, from 0% up to 40% and the CO_2 has been decreased accordingly, while keeping that of i-C_4H_{10} and SF_6 fixed. The aim of this study was to try and understand the possible interplay between HFO and CO_2.

- The RPC signals have been read out both using a digitizer, to perform signal shape and prompt charge analyses, and using the ALICE front-end electronics (FEERIC) to study the detector response in an ALICE-like readout scenario. The results obtained with the two methods can not be directly compared, due to different thresholds, but they lead to very similar overall conclusions.

- Beam-test results have shown that mixtures with higher CO_2 concen-

tration reach a lower efficiency (few percentage point) with respect to the standard (R134a-based) gas mixture and also show a higher streamer contamination

- Increasing the HFO concentration shifts the detector working point upwards by $\sim$ 1 kV for every 10% HFO added but, at the same time, it reduces the streamer contamination to values that are less than 10% and close to the ones of the standard gas mixture. The downside is that the contamination seems to grow rapidly with the high voltage, and the voltage range (above working point) where the streamer contamination is below 10% is significantly shorter than with the standard gas mixture

- Time resolution and cluster size values are very similar to those obtained with the standard gas mixture

- A shift of the efficiency curves towards higher voltages is observed for increasing irradiation. Such a shift is found to correspond, except for very high rates ($\sim$ 300 Hz/cm^2), to the expected voltage drop across the gas gap, induced by the gamma-induced circulating current and the electrode resistivity

- Results under gamma irradiation show an efficiency drop by 2 percentage points for the standard gas mixture, at the maximum irradiation reached with all gas mixtures ($\sim$ 250 Hz/cm^2), while all the eco-friendly alternatives show a drop by up to $\sim$ 8 percentage points; if the HFO concentration is greater than 20%, the efficiency degradation is slightly mitigated. The efficiency drop for a gamma-induced counting rate of $\sim$ 100 Hz/cm^2 (maximum expected rate on the MID RPCs in RUN3 and RUN4) is $\sim$ 3-4 pp for all the eco-friendly alternatives and $\sim$ 1 pp for the standard gas mixture.

- In general, the current absorbed under irradiation is found to be about 1.6 times higher than for the standard gas mixture, for all the eco-friendly alternatives tested. The average charge per hit has been estimated as the slope of the linear interpolation of the current density trend as a function of the average background hit rate and found to be $\sim$ 50 pC for the standard gas mixture and $\sim$ 80 to 100 pC for the eco-friendly mixtures

- The mixture containing 35% HFO, 60% CO_2, 4% i-C_4H_{10} and 1% SF_6 exhibited the best compromise between performance (in terms of effi-

ciency, prompt charge and streamer contamination) and working point shift

Long-term irradiation studies of RPCs operated with HFO-based gas mixtures have been carried out at the GIF++ as well, exploiting the gamma irradiation provided by the ^{137}Cs source. The detectors are exposed to the radiation and are switched on at a fixed voltage. The stability of the absorbed current is studied over time. Two HFO-based gas mixtures have been tested and the results are summarized in the following:

- The stability of the monitoring system (high voltage correction, data logging and stability of the data acquisition) has been tested using the standard gas mixture. Around 6 mC/cm^2 were integrated by the ALICE RPC, with stable performance.
- The first eco-friendly alternative tested was composed by: 45% HFO, 50% CO_2, 4% i-C_4H_{10} and 1% SF_6.
  - Detector characterization with this mixture was not carried out with the muon beam since the beam test campaigns had not started yet.
  - A total of $\sim$ 12 mC/cm^2 was integrated by the ALICE detector
  - An increase in the absorbed dark current (both Ohmic and non-Ohmic) was observed, for the ALICE detector as well as for all other detectors of the ECOgas@GIF++ collaboration
  - Due to the above-mentioned general current increase, the mixture was considered unstable and no further tests were carried out
- The second eco-friendly alternative tested was composed by: 35% HFO, 60% CO_2, 4% i-C_4H_{10} and 1% SF_6
  - This mixture was tested with the muon beam and the working point was calculated to be $\sim$ 1 kV above the standard gas mixture. The voltage of the detectors was initially set at the source off knee to study their stability at this voltage
  - For most detectors of the collaboration, the current (both dark and under irradiation) showed a satisfactory stability in time after the accumulation of $\sim$ 55 mC/cm^2. However, after the integration of $\sim$ 6 mC/cm^{2}the ALICE detector showed a sudden and sharp current increase with no apparent correlation to external parameters

(environmental or gas mixture-related). This behavior was closely studied and a correlation of the current increase with the appearance of hot-spots (regions where the noise counting rate is higher than the rest of the detector) has been found. This is encouraging as it points to an issue specific to the tested prototype rather than the gas mixture. Further tests are foreseen to confirm this hypothesis.

Currently the aging campaign is ongoing with the other detectors and the absorbed current (both irradiation and dark) appears to be stable . The installation of a new mechanical support for the RPCs is foreseen and this will allow for the installation of four scintillators (coupled with photomultipliers) that will provide a cosmic-ray trigger, allowing the collaboration to continuously monitor the detector efficiency throughout the aging campaign. Moreover, further beam test campaigns are planned for the future and they will be used to perform more detailed studies of the detector response, after the integration of a growing amount of integrated charge.

Appendix A

A few details from the beam tests

A.1 Threshold setting code with Arduino

```
#include <Wire.h>  //I2C Arduino library

#define CLOCK_FREQUENCY 50000 //FEERIC I2C clock frequency
#define DAC_ADDRESS 0x21 //I2C address of the DAC
#define BOARD_NUM 4 //Number of FEERIC cards
#define BASE_COUNTS 513 //1.5 V baseline in DAC counts

int boardAddress[BOARD_NUM] = {0,1,2,3}; //Board address
float thr[BOARD_NUM] = {96.0,100.0,-105.0,-102.0}; //Threshold values (mV)
int thrCounts[BOARD_NUM] ={0,0,0,0}; //For threshold values in DAC counts
uint16_t finalThr[BOARD_NUM] = {0,0,0,0}; //For threshold values after baseline subtraction/addition
byte LSB[BOARD_NUM] = {0,0,0,0}; //Default way to send threshold to the DAC
byte MSB[BOARD_NUM] = {0,0,0,0};

float mVperCount = 2.93; //mV per DAC count
void setup() {

  Wire.begin(); //Start I2C pins
  Wire.setClock(CLOCK_FREQUENCY); //Set clock frequency
  byte error; //Result of communication attempt

  for (int i = 0; i < BOARD_NUM; i++) {
    //Convert thr to DAC counts
    thrCounts[i] = abs(thr[i])/mVperCount;

    //Sum it or subtract it to the 513 baseline
    if (thr[i] >= 0) finalThr[i] = BASE_COUNTS + thrCounts[i]; //positive thr
    if (thr[i] < 0) finalThr[i] = BASE_COUNTS - thrCounts[i]; //negative thr

    //Calculate LSB and MSB to send to the DAC
    LSB[i] = (finalThr[i] & 0x00FF);
    MSB[i] = ((finalThr[i] & 0xFF00) >> 8);

    //Begin transmission with the board
    Wire.beginTransmission(boardAddress[i]); //Open communications with FEERIC board
    Wire.write(00000001); //Enable DAC
    error = Wire.endTransmission(); //Get result
    //If result is 0 -> good communication established
    if (error == 0) Serial.println("Com with board started");

    //Communicayte with the DAC
    Wire.beginTransmission(DAC_ADDRESS);
    Wire.write(00000000); //Send command
    Wire.write(LSB[i]); //Write LSB
    Wire.write(MSB[i]); //Write MSB

    error = Wire.endTransmission();
    if (error == 0) Serial.println("Data written to DAC");

```

```
50          Wire.beginTransmission(boardAddress[i]); //Begin transmission with the board
51          Wire.write(00000000); //Disable DAC
52          Wire.endTransmission();
53        }
54        Wire.end(); //End I2C transmission
55      }
```

A.2 Gamma contamination in muon efficiency estimation

The formula reported in 4.4.1, used to keep track of the gamma contamination in muon efficiency calculation is here justified. We start from the assumption that the events for which the RPC has given a signal are given by a combination of muons and photons. One can write:

$$N_{RPC} = N_{trig}[\epsilon_{real} + (1 - \epsilon_{real})(1 - e^{-<N_\gamma>})] \tag{A.1}$$

Where N_{RPC} is the total number of counts see by the RPC, N_{trig} is the number of muon triggers, ϵ_{real} is the "real" muon efficiency and the expression $1 - e^{-<N_\gamma>}$ is the probability to have at least one photon in the muon window, calculated as one minus the probability to have no photons in the muon window (given that $< N_\gamma >$ is the average number of photons in the muon window), assuming that the photon number distribution follows a Poisson distribution. In equation A.1 the result of the multiplication $N_{trig} \cdot \epsilon_{real}$ gives the number of signals tagged as muons, that are actually produced by muons, while the term $N_{trig} \cdot (1 - \epsilon_{real})(1 - e^{-<N_\gamma>})$ gives the number of signals tagged as muons but that are actually generated by photons.

With some algebra, equation A.1 becomes:

$$\frac{N_{RPC}}{N_{trig}} = \epsilon_{raw} = 1 - e^{-<N_\gamma>} + e^{-<N_\gamma>}\epsilon_{real} \tag{A.2}$$

and solving for ϵ_{real} gives:

$$\epsilon_{real} = \frac{\epsilon_{raw} + e^{-<N_\gamma>} - 1}{e^{-<N_\gamma>}} \tag{A.3}$$

Considering that $e^{-<N_\gamma>}$ is the probability to have no photons in the muon window, and remembering how the fake efficiency was defined in 4.4.1, one can see that $e^{-<N_\gamma>} = 1 - \epsilon_{fake}$ and that $e^{-<N_\gamma>} - 1 = -\epsilon_{fake}$ so

equation A.3 can be re-written as:

$$\epsilon_{real} = \frac{\epsilon_{raw} - \epsilon_{fake}}{1 - \epsilon_{fake}} \tag{A.4}$$

which is exactly the formula reported in 4.4.1. As explained there, the uncertainty on this measurement is estimated by propagating the errors on all the terms in the equation.

A.3 Clustering algorithm

The clustering algorithm has been developed from scratch and it exploits the fact that, together with the information on the strip that gave a signal, also the time of the hit is known, so a double condition (on strip proximity and time difference between the hits) is imposed. In particular, for two signals to be in the same cluster (clustering conditions), the strip difference must be equal to one and the time difference must be less than 15 ns, as explained in 4.4.1. The clustering algorithm returns a vector of clusters, meaning that each element of the vector represents a separate cluster and its value the number of strips in a given cluster.

The algorithm is the same for muon and photon triggers clustering and it works as follows: for each trigger, all the hits (fired strips) are coupled with their respective time and these pairs are ordered by increasing strip number. An example of hit-time pairs before ordering could be the following:

(2,100);(3,50);(4,55);(2,55);(1,110)

and the result of he ordering procedure would be the following:

(1,110);(2,55);(2,100);(3,50);(4,55)

Once this is done, an iterative algorithm runs over all the values in the following way:

- Take the first pair of hit-time (1,100) and compare it to all the others
- Check if the clustering conditions are satisfied, then 1) if they are not satisfied it means the first hit is ”alone” and so the cluster vector is filled with a ”1” and the alone element is deleted from the starting vector 2) if the clustering conditions are satisfied, the two elements are part of a cluster and are inserted in a temporary support vector, and a variable that keeps track of whether a pair is created or not, is set to true. Lastly, the two elements in the cluster are deleted from the original vector

- If a cluster is not created, the algorithm restarts from the first element and it goes through all the hit-time pairs until a cluster is created (if not, a series of 1 is pushed to the vector, meaning that a series of isolated hits is present)
- If a cluster is created, the algorithm checks if any of the cluster element satisfies the clustering condition with all the remaining vector element. If one element is found to satisfy the clustering condition, it is added to the cluster and deleted from the original vector. The algorithm keeps on comparing the residual elements of the original vector to all the ones in the cluster. If no element satisfies the conditions, it means that the cluster is complete and the number of strips in the cluster is pushed back to the cluster vector
- The clustering procedure continues until there are no more elements left in the original vector and the cluster vector is filled up
- Once the clusters vector is returned, the cluster size histogram is filled with its content, and the cluster multiplicity histogram is filled with its size

Usually, for a muon event, it is quite rare to have more than one cluster, for this reason this complicated algorithm was developed to estimate the cluster size of photon events, since multiple photons can produce a signal in the same acquisition window. In the example case taken above, the result of the clustering would be the following vector:

$$\text{clusters} = \{2,3\}$$

because the hits (1,100) and (2,200) would be paired in a cluster and the other three in another cluster. The cluster size histogram would be filled twice, in the bins 2 and 3 and the cluster multiplicity algorithm would be filled once, in the bin 2, since the size of the clusters vector is 2.

The reason why 15 ns was chosen as clustering time can be explained by looking at the chart in Figure A.1, where the evolution of the cluster size and multiplicity is shown as a function of the clustering time: this variable was varied from 0 to 40 ns and the trend of the cluster size can be explained as follows: if the clustering time is 0, the average cluster size per event is always equal to 1, because no cluster is created, since the clustering time is too small. On the contrary, the cluster multiplicity is maximum. If the clustering time is increased, the cluster size slowly rises and the cluster

multiplicity correspondingly decreases. This is true for values up to $\sim$ 7 ns, after that the trend seems to flatten and no variation of either quantity is observed. Since this study was not carried out systematically for all the runs taken, it was decided to set the clustering time at 15 ns (higher value than the 7 ns which grants stability) in order to be sure that the clustering results would be similar across the different runs taken.

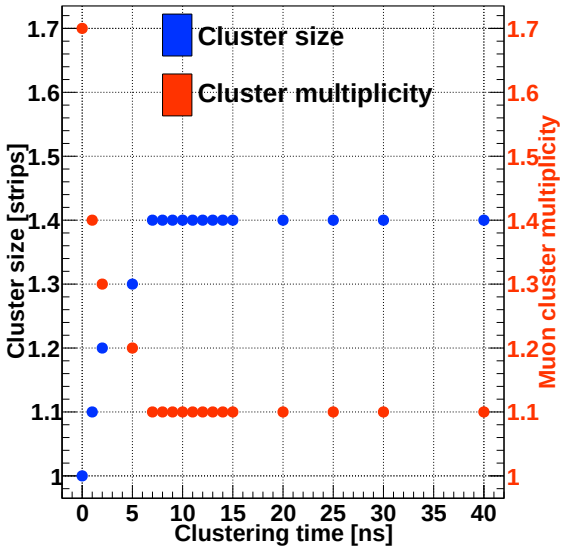

Figure A.1: Trend of the muon cluster size and multiplicity as a function of the clustering time. A stable trend of these quantities is observed if the clustering time is greater than 7 ns

Note that similar observations can be inferred for the photons, and the same clustering algorithm is employed in that case.

A.4 Knee derivation

Starting from the mathematical definition of knee, as the point where the efficiency reaches 95% of the maximum efficiency, one can write that:

$$\epsilon = 0.95 \cdot \epsilon_{max} = \frac{\epsilon_{max}}{1 + e^{-\lambda(HV_{knee} - HV_{50})}} \tag{A.5}$$

and from here one can solve to find the value of HV_{knee}, which corresponds to the knee point of the curve. With some calculations one finds

that:

$$\begin{aligned} 1 + e^{-\lambda(HV_{knee} - HV_{50})} &= \frac{1}{0.95} \\ \Rightarrow e^{-\lambda(HV_{knee} - HV_{50})} &= \frac{1}{19} \\ \Rightarrow HV_{knee} &= \frac{log(19)}{\lambda} + HV_{50} \end{aligned} \tag{A.6}$$

Which is the value that was anticipated in 4.4.1.

References

1 L. Evans and P. Bryant:
'LHC Machine',
Journal of Instrumentation **3**, S08001 (2008).

2 R. R. Bruce et al.:
'Studies for an LHC Pilot Run with Oxygen Beams',
in Proc. IPAC'21, International Particle Accelerator Conference 12, https://doi.org/10.18429/JACoW-IPAC2021-MOPAB005 (2021), pp. 53–56.

3 M. Schaumann et al.:
'First Xenon-Xenon Collisions in the LHC',
MOPMF039 (2018).

4 *LEP design report*,
https://cds.cern.ch/record/102083 (CERN, Geneva, 1984).

5 J. P. Blewett:
'200-GeV Intersecting Storage Accelerators',
eConf **C710920**, edited by M. H. Blewett and N. Vogt-Nilsen, http://cds.cern.ch/record/1068131, 501 (1971).

6 L. Rossi:
'The LHC Superconducting Magnets',
http://cds.cern.ch/record/630341 (2003).

7 D. Boussard and T. P. R. Linnecar:
The LHC Superconducting RF System,
tech. rep., https://cds.cern.ch/record/410377 (Geneva, 1999).

8 ATLAS collaboration:
ATLAS: Detector and physics performance technical design report. Volume 1,
Technical design report. ATLAS, http://cds.cern.ch/record/391177" (CERN, Geneva, 1999).

9 *ALICE: Technical proposal for a Large Ion collider Experiment at the CERN LHC*,
LHC technical proposal. ALICE, https://cds.cern.ch/record/293391 (CERN, Geneva, 1995).

10 CMS collaboration:
CMS Physics: Technical Design Report Volume 1: Detector Performance and Software,
Technical design report. CMS, http://cds.cern.ch/record/922757 (CERN, Geneva, 2006).

11 LHCb collaboration:
LHCb reoptimized detector design and performance: Technical Design Report,
Technical design report. LHCb, http://cds.cern.ch/record/630827 (CERN, Geneva, 2003).

12 T. Kramer:
'LHC Beam Dump System: Analysis of beam commissioning, performance and the consequences of abnormal operation',
Presented 05 Oct 2011, PhD thesis (Technische Universität Gratz, Institut für Hochspannungstechnik und Systemmanagment, 2011).

13 M. Vretenar:
Linac4 design report,
Vol. 6, CERN Yellow Reports: Monographs, https://cds.cern.ch/record/2736208 (CERN, Geneva, 2020).

14 K. H. Reich:
'The CERN Proton Synchrotron Booster',
IEEE Trans. Nucl. Sci. **16**, 959–961 (1969).

15 P. H. Standley:
'The CPS improvement programme',
https://cds.cern.ch/record/298664 (1966).

16 P. Collier, B. Goddard, R. Jung et al.:
The SPS as Injector for LHC: Conceptual Design,
tech. rep., https://cds.cern.ch/record/322782 (Geneva, 1997).

17 G. Bellodi:
'Source and LINAC3 studies',
in Injector MD Days 2017 (2017), pp. 113–116.

18 M. Chanel:
'LEIR: The low energy ion ring at CERN',
Nucl. Instrum. Methods Phys. Res., A **532**, 137–143 (2004).

19 S. Sourav, H. satz and B. Sinha:
The Physics of the Quark-Gluon Plasma,
Lecture Notes in Physics, https://link.springer.com/book/10.1007/978-3-642-02286-9 (Springer, Heidelberg, 2010).

20 ALICE Collaboration:
'ALICE upgrades during the LHC Long Shutdown 2',
10.48550/ARXIV.2302.01238 (2023).

21 H. Bartosik and G. Rumolo:
Performance of the LHC injector chain after the upgrade and potential development,
https://arxiv.org/abs/2203.09202, 2022.

22 ALICE collaboration:
Technical Design Report for the Upgrade of the Online-Offline Computing System,
tech. rep., https://cds.cern.ch/record/2011297 (2015).

23 R. Gupta:
Introduction to Lattice QCD,
https://arxiv.org/abs/hep-lat/9807028, 1998.

24 P. Skands:
'Introduction to QCD',
in Searching for new physics at small and large scales (2013).

25 R. Planeta:
'Physics of heavy ion collisions',
International Journal of Modern Physics E **15**, 10.1142/S0218301306004569 (2012).

26 K. Johnson:
'The M.I.T. Bag Model',
Acta Phys. Polon. B **6**, https://inspirehep.net/literature/2861, 865 (1975).

27 H. Appelshäuser:
Heavy-Ion Physics,
https://indico.cern.ch/event/999261/contributions/4393045/attachments/2286283/3886273/HASCO2021.pdf, 2021.

28 A. K. Chaudhuri:
'The glauber model',
in *A short course on relativistic heavy ion collisions*, 2053-2563 (IOP Publishing, 2014), 3-1 to 3–19.

29 P. Braun-Munzinger and B. Dönigus:
'Loosely-bound objects produced in nuclear collisions at the LHC',
Nuclear Physics A **987**, 10.1016/j.nuclphysa.2019.02.006 (2019).

30 J. D. Bjorken:
'Highly relativistic nucleus-nucleus collisions: The central rapidity region',
Phys. Rev. D **27**, 140–151 (1983).

31 B. Sumit, R. Chatterjee, B. K. Nandi, T. K. Nayak et al.:
'Temperature and Multiplicity Fluctuations as a New Tool of Characterization for Heavy Ion Collisions at LHC Energy',
in *Springer proceedings in physics* (Springer International Publishing, 2015), pp. 189–194.

32 E. Iancu:
'QCD in heavy ion collisions',
2011 European School of High-Energy Physics, ESHEP 2011 - Proceedings, https://cds.cern.ch/record/1445976/files/197-266%20Inacu.pdf (2012).

33 S. Voloshin and Y. Zhang:
'Flow study in relativistic nuclear collisions by fourier expansion of azimuthal particle distributions',
Zeitschrift für Physik C Particles and Fields **70**, 665–671 (1996).

34 S. Acharya et al. (ALICE collaboration):
'Anisotropic flow of identified particles in Pb-Pb collisions at $\sqrt{s_{NN}}$ = 5.02 TeV',
Journal of High Energy Physics **2018**, 10.1007/jhep09(2018)006 (2018).

35 S. Acharya et al. (ALICE collaboration):
'J/Ψ Elliptic Flow in Pb-Pb Collisions at $\sqrt{s_{NN}}$ = 5.02 TeV',
Phys. Rev. Lett. **119**, 242301 (2017).

36 S. Acharya et al. (ALICE collaboration):
'Anisotropic flow in Xe–Xe collisions at $\sqrt{s_{NN}}$ = 5.44 TeV',
Physics Letters B **784**, 82–95 (2018).

37 J. Adam et al. (ALICE collaboration):
'Enhanced production of multi-strange hadrons in high-multiplicity proton–proton collisions',
Nature Physics **13**, 535–539 (2017).

38 V. K. Tiwari and C. P. Singh:
'Strangeness enhancement: A potential signature for QGP phase',
Phys. Lett. B **411**, 225–229 (1997).

39 B. Abelev et al. (ALICE collaboration):
'Multi-strange baryon production in pp collisions at $\sqrt{s}$ = 7 TeV with ALICE',
Physics Letters B **712**, 309–318 (2012).

40 J. Adam et al. (ALICE collaboration):
'Measurement of pion, kaon and proton production in proton-proton collisions at $\sqrt{s}$ = 7 TeV',
The European Physical Journal C **75**, 226 (2015).

41 B. Abelev et al. (ALICE collaboration):
'Multi-strange baryon production at mid-rapidity in Pb–Pb collisions at $\sqrt{s_{NN}}$ = 2.76 TeV',
Physics Letters B **728**, 216–227 (2014).

42 J. Adam et al. (ALICE collaboration):
'Multi-strange baryon production in p-Pb collisions at $\sqrt{s_{NN}}$ = 5.02 TeV',
Physics Letters B **758**, 389–401 (2016).

43 K. Aamodt et al. (ALICE collaboration):
'Production of pions, kaons and protons in pp collisions at $\sqrt{s}$ = 900 GeV with ALICE at the LHC',
The European Physical Journal C **71**, 1655 (2011).

44 D. Kharzeev and M. Nardi:
'Hadron production in nuclear collisions at RHIC and high-density QCD',
Physics Letters B **507**, 121–128 (2001).

45 R. Pasechnik and M. Šumbera:
'Phenomenological Review on Quark–Gluon Plasma: Concepts vs. Observations',
Universe **3**, 7 (2017).

46 H. Hahn, E. Forsyth, H. Foelsche et al.:
'The RHIC design overview',
Nuclear Instruments and Methods in Physics Research Section A: Accelerators, Spectrometers, Detectors and Associated Equipment **499**, 245–263 (2003).

47 J. Adams et al. (STAR Collaboration):
'Transverse-Momentum and Collision-Energy Dependence of High-p_T Hadron Suppression in Au-Au Collisions at Ultrarelativistic Energies',
Phys. Rev. Lett. **91**, 6 (2003).

48 S. S. Adler et al. (PHENIX Collaboration):
'High-p_T charged hadron suppression inAu-Au collisions at $\sqrt{s_{NN}}$ = 200 GeV',
Phys. Rev. C **69**, 20 (2004).

49 K. Aamodt et al. (ALICE collaboration):
'Suppression of charged particle production at large transverse momentum in central Pb–Pb collisions at $\sqrt{s_{NN}}$ = 2.76 TeV',
Physics Letters B **696**, 30–39 (2011).

50 S. Acharya et al. (ALICE collaboration):
'Transverse momentum spectra and nuclear modification factors of charged particles in pp, p-Pb and Pb-Pb collisions at the LHC',
Journal of High Energy Physics **2018**, 13 (2018).

51 J. W. Cronin, H. J. Frisch, M. J. Shochet et al.:
'Production of hadrons at large transverse momentum at 200, 300, and 400 gev',
Phys. Rev. D **11**, 3105–3123 (1975).

52 J. Adams et al. (STAR collaboration):
'Experimental and theoretical challenges in the search for the quark-gluon plasma: The STAR Collaboration's critical assessment of the evidence from RHIC collisions',
Nuclear Physics A **757**, 102–183 (2005).

53 S. Acharya et al. (ALICE collaboration):
'Direct observation of the dead-cone effect in quantum chromodynamics',
Nature **605**, 440–446 (2022).

54 S. Acharya et al. (ALICE collaboration):
'Measurement of D^0, D^+, D^{*+} and D_s^+ production in Pb-Pb collisions at $\sqrt{S_{NN}}$ = 5.02 TeV',
Journal of High Energy Physics **2018**, 10.1007/jhep10(2018)174 (2018).

55 T. Matsui and H. Satz:
'J/ψ Suppression by Quark-Gluon Plasma Formation',
Phys. Lett. B **178**, 416–422 (1986).

56 P. Faccioli and C. Lourenço:
'The fate of quarkonia in heavy-ion collisions at LHC energies: a unified description of the sequential suppression patterns',
The European Physical Journal C **78**, 731 (2018).

57 J. Adam et al. (ALICE collaboration):
'J/Ψ suppression at forward rapidity in Pb–Pb collisions at $\sqrt{s_{NN}}$=5.02 TeV',
Physics Letters B **766**, 212–224 (2017).

58 S. Acharya et al. (ALICE collaboration):
'Υ suppression at forward rapidity in Pb–Pb collisions at $\sqrt{s_{NN}}$=5.02TeV',
Physics Letters B **790**, 89–101 (2019).

59 J. Adam et al. (ALICE collaboration):
'Measurement of an Excess in the Yield of J/Ψ at very low p_t in Pb-Pb Collisions at $\sqrt{s_{NN}}$ = 2.76 TeV',
Phys. Rev. Lett. **116**, 222301 (2016).

60 J. Adam et al. (ALICE collaboration):
'Differential studies of inclusive J/Ψ and Ψ(2S) production at forward rapidity in Pb-Pb collisions at $\sqrt{s_{NN}}$=2.76 TeV',
Journal of High Energy Physics **2016**, 179 (2016).

61 A. Adare et al. (PHENIX Collaboration):
'J/Ψ suppression at forward rapidity in Au-Au collisions at $\sqrt{s_{NN}}$ = 200 GeV',
Phys. Rev. C **84**, 054912 (2011).

62 X. Du and R. Rapp:
'Sequential regeneration of charmonia in heavy-ion collisions',
Nuclear Physics A **943**, 147–158 (2015).

63 A. Andronic, P. Braun-Munzinger, K. Redlich and J. Stachel:
'Statistical hadronization of heavy quarks in ultra-relativistic nucleus–nucleus collisions',
Nuclear Physics A **789**, 334–356 (2007).

64 ALICE collaboration:
Technical Design Report for the Upgrade of the ALICE Inner Tracking System,
tech. rep., CERN-LHCC-2013-024, ALICE-TDR-017 (2014).

65 ALICE collaboration:
Upgrade of the ALICE Time Projection Chamber,
tech. rep., https://cds.cern.ch/record/1622286 (Geneva, 2013).

66 ALICE collaboration:
Upgrade of the ALICE Readout & Trigger System,
tech. rep., https://cds.cern.ch/record/1603472 (Geneva, 2013).

67 ALICE collaboration:
The forward muon spectrometer of ALICE: addendum to the technical proposal for a Large Ion Collider experiment at the CERN LHC,
tech. rep., https://cds.cern.ch/record/314011 (Geneva, 1996).

68 S. Acharya et al. (ALICE collaboration):
'Energy dependence of forward-rapidity J/Ψ and Ψ(2S) production in pp collisions at the LHC',
The European Physical Journal C **77**, 392 (2017).

69 ALICE Collaboration:
'Multiplicity dependence of Υ production at forward rapidity in pp collisions at $\sqrt{s}$ = 13 TeV',
10.48550/ARXIV.2209.04241 (2022).

70 ALICE collaboration:
Technical Design Report for the Muon Forward Tracker,
tech. rep., https://cds.cern.ch/record/1981898 (Geneva, 2015).

71 C. Finck et al. (ALICE collaboration):
'The Muon Spectrometer of the ALICE',
Journal of Physics: Conference Series **50**, 397 (2006).

72 B. Abelev et al. (ALICE collaboration):
Upgrade of the ALICE Experiment: Letter of Intent,
tech. rep. (CERN, Geneva, 2014).

73 F. Sauli:
Gaseous Radiation Detectors: Fundamentals and Applications,
Cambridge Monographs on Particle Physics, Nuclear Physics and Cosmology, https://www.cambridge.org/core/books/gaseous-radiation-detectors/742D8E89DC5EFE1BE285978833E5A860 (Cambridge University Press, 2014).

74 M. Abbrescia, V. Peskov and P. Fonte:
Resistive Gaseous Detectors, Designs, performance and perspectives,
https://onlinelibrary.wiley.com/doi/book/10.1002/9783527698691 (Wiley-VCH, 2018).

75 H. Raether:
Electron Avalanches and Breakdown in Gases,
Butterworths advanced physics series,: Monographs on ionization and electrical discharges in gases, https://books.google.fr/books?id=DPC1wgEACAAJ (Butterworths, 1964).

76 M. I. Daion and G. A. Leksin:
'Spark detectors for charged particles',
Soviet Physics Uspekhi **6**, 428 (1963).

77 G. Charpak, R. Bouclier and T. Bressani:
'The use of multiwire proportional counters to select and localize charged particles',
Nuclear Instruments and Methods **62**, 262–268 (1968).

78 R. Santonico and R. Cardarelli:
'Development of resistive plate counters',
Nuclear Instruments and Methods in Physics Research **187**, 377–380 (1981).

79 E. Britannica:
Bakelite, chemical compound,
https://www.britannica.com/science/Bakelite, 2023.

80 S. Biswas, S. Bhattacharya, S. Bose et al.:
'Performances of linseed oil-free bakelite RPC prototypes with cosmic ray muons',
Nuclear Instruments and Methods in Physics Research A **602**, 749–753 (2009).

81 V. Cardarelli R. Makeev and R. Santonico:
'Avalanche and streamer mode operation of resistive plate chambers',
Nuclear Instruments and Methods in Physics Research Section A: Accelerators, Spectrometers, Detectors and Associated Equipment **382**, 470–474 (1996).

82 R. Cardarelli, A. Di Ciaccio and R. Santonico:
'Performance of a resistive plate chamber operating with pure CF_3Br',
Nuclear Instruments and Methods in Physics Research Section A: Accelerators, Spectrometers, Detectors and Associated Equipment **333**, 399–403 (1993).

83 R. Arnaldi, A. Baldit, V. Barret et al.:
'Influence of temperature and humidity on bakelite resistivity',
Nuclear Instruments and Methods in Physics Research Section A: Accelerators, Spectrometers, Detectors and Associated Equipment **456**, Proceedings of the 5th Int. Workshop on Resistive Plate Chambers and Related Detectors, 140–142 (2000).

84 G. D. Alkhazov:
'Statistics of electron avalanches and ultimate resolution of proportional counters',
Nuclear Instruments and Methods **89**, 155–165 (1970).

85 G. Aielli, P. Camarri, R. Cardarelli et al.:
'Fluoride production in RPCs operated with F-compound gases',
Nuclear Physics B - Proceedings Supplements **158**, Proceedings of the 8th International Workshop on Resistive Plate Chambers and Related Detectors, 143–148 (2006).

86 ALICE collaboration:
FEERIC: Front-End Electronics for the Resistive Plate Chambers of the ALICE Muon IDentifier - Production Readiness Review (PRR),
https://twiki.cern.ch/twiki/pub/ALICE/MIDFEERIC/PRR-FEERIC.pdf, 2016.

87 W. Riegler:
'Time response functions and avalanche fluctuations in resistive plate chambers',
Nuclear Instruments and Methods in Physics Research Section A: Accelerators, Spectrometers, Detectors and Associated Equipment **602**, 377–390 (2009).

88 E. Cerron Zeballos, I. Crotty, D. Hatzifotiadou et al.:
'A new type of resistive plate chamber: The multigap RPC',
Nuclear Instruments and Methods in Physics Research Section A: Accelerators, Spectrometers, Detectors and Associated Equipment **374**, 132–135 (1996).

89 F. Carnesecchi (ALICE collaboration):
'Performance of the alice time-of-flight detector at the lhc',
Journal of Instrumentation **14**, C06023 (2019).

90 G. Aielli, R. Cardarelli, L. Di Stante et al.:
'The RPC space resolution with the charge centroid method',
Journal of Instrumentation **9**, C09030 (2014).

91 P. Baesso, D. Cussans, C. Thomay, J. Velthuis et al.:
'Toward a rpc-based muon tomography system for cargo containers.',
Journal of Instrumentation **9**, C10041 (2014).

92 M. Abbrescia et al. (CMS collaboration):
'Operation, performance and upgrade of the CMS Resistive Plate Chamber system at LHC',
Nuclear Instruments and Methods in Physics Research Section A: Accelerators, Spectrometers, Detectors and Associated Equipment **732**, Vienna Conference on Instrumentation 2013, 195–198 (2013).

93 Intergovernmental Panel on Climate Change:
IPCC fourth assessment report,
https://www.ipcc.ch/assessment-report/ar4/, 2007.

94 Council of European Union:
Council regulation (EU) no 517/2014,
https://eur-lex.europa.eu/legal-content/IT/ALL/?uri=CELEX%3A32014R0517, 2014.

95 R. Arnaldi, E. Chiavassa, A. Colla et al.:
'Aging tests and chemical analysis of Resistive Plate Chambers for the trigger of the ALICE dimuon arm',
Nuclear Instruments and Methods in Physics Research Section A: Accelerators, Spectrometers, Detectors and Associated Equipment **533**, Proceedings of the Seventh International Workshop on Resistive Plate Chambers and Related Detectors, 112–115 (2004).

96 A. Gelmi, A. Fagot, M. Gul et al.:
'Longevity studies on the CMS-RPC system',
Journal of Instrumentation **14**, C05012 (2019).

97 G. Aielli, M. Alviggi, V. Ammosov et al.:
'New results on ATLAS RPC's aging at CERN's GIF',
Nuclear Science, IEEE Transactions on **53**, 567–571 (2006).

98 ALICE collaboration:
ALICE technical design report of the dimuon forward spectrometer,
tech. rep., https://t.ly/VLhb (Geneva, 1999).

99 G. Aad et al. (ATLAS collaboration):
'Performance of the ATLAS RPC detector and Level-1 muon barrel trigger at $\sqrt{s}$ = 13 TeV',
Journal of Instrumentation **16**, P07029 (2021).

100 B. Mandelli, R. Guida, M. Gagliardi and M. Marchisone:
'Gas mixture quality monitoring for the RPC detectors at the LHC experiments',
Journal of Instrumentation **14**, C09006 (2019).

101 E. Altuntas, M. Capeans, I. Glushkov et al.:
Long-term study of optimal gas purifiers for the RPC systems at LHC,
tech. rep. (CERN, Geneva, 2012).

102 R. Arnaldi, A. Baldit, V. Barret et al.:
'A low-resistivity RPC for the ALICE dimuon arm',
Nuclear Instruments and Methods in Physics Research Section A: Accelerators, Spectrometers, Detectors and Associated Equipment **451**, 462–473 (2000).

103 R. Arnaldi, a. Baldit, V. Barret et al.:
'Ageing test of RPC for the Muon Trigger System for the ALICE experiment',
in IEEE Symposium Conference Record Nuclear Science 2004. Vol. 4 (2004), 2072–2076 Vol. 4.

104 R. Arnaldi, A. Baldit, V. Barret et al.:
'Beam and ageing tests with a highly–saturated avalanche gas mixture for the ALICE p–p data taking',
Nuclear Physics B - Proceedings Supplements **158**, Proceedings of the 8th International Workshop on Resistive Plate Chambers and Related Detectors, 149–153 (2006).

105 G. L. Bencze, J. L. Bènichou, M. Della Negra et al.:
'Study of resistive plate chambers for muon detection at hadron colliders',
Nuclear Instruments and Methods in Physics Research Section A: Accelerators, Spectrometers, Detectors and Associated Equipment **340**, 466–473 (1994).

106 R. Arnaldi, A. Baldit, V. Barret et al.:
'Front-end electronics for the RPCs of the ALICE dimuon trigger',
IEEE Trans. Nucl. Sci. **52**, 1176–1181 (2005).

107 S. Agosteo, S. Altieri and G. o. Belli:
'A facility for the test of large-area muon chambers at high rates',
Nuclear Instruments and Methods in Physics Research Section A: Accelerators, Spectrometers, Detectors and Associated Equipment **452**, 94–104 (2000).

108 P. Dupieux:
RPCs of ALICE Muon Trigger: a saga of more than 20 years,
https://indico.in2p3.fr/event/17140/contributions/64153/attachments/50313/64188/DETGAZ-ALICE-RPC-DP-081018.pdf, 2018.

109 K. Aamodt et al. (ALICE collaboration):
'Charged-Particle Multiplicity Density at Midrapidity in Central Pb-Pb Collisions at $\sqrt{s_{NN}}$ = 2.76 TeV',
Phys. Rev. Lett. **105**, 11 (2010).

110 L. Quaglia, A. Bianchi, A. Ferretti et al.:
'Performance and aging studies for the ALICE muon RPCs',
Journal of Instrumentation **16**, C04002 (2021).

111 S. Manen, P. Dupieux, B. Joly et al.:
'FEERIC, a very-front-end ASIC for the ALICE muon trigger resistive plate chambers',
in 2013 ieee nuclear science symposium and medical imaging conference (2013 nss/mic) (2013), pp. 1–4.

112 A. Ferretti (ALICE collaboration):
'The upgrade of the RPC-based ALICE Muon Trigger',
JINST **14**, C06011 (2019).

113 J. Va'vra:
'Attempt to correlate the ionic model with observations in BaBar RPC chambers and R&D tests',
in 2003 ieee nuclear science symposium. conference record (ieee cat. no.03ch37515), Vol. 5 (2003), 3704–3708 Vol.5.

114 C. post:
Europe sees price rises for R134a,
https://www.coolingpost.com/world-news/europe-sees-price-rises-for-r134a/, 2021.

115 CERN:
Cern second environment report, scope one,
https://hse.cern/environment-report-2019-2020/emissions, 2020.

116 R. Guida, B. Mandelli and G. Rigoletti:
'Studies on alternative eco-friendly gas mixtures and development of gas recuperation plant for RPC detectors',
Nucl. Instrum. Meth. A **1039**, 167045 (2022).

117 R. Guida, M. Corbetta, B. Mandelli and G. Rigoletti:
'Strategies for reducing the use of greenhouse gases from particle detectors operation at the CERN LHC experiments',
PoS **ICHEP2020**, 979 (2021).

118 L. Benussi, S. Bianco, M. Ferrini et al.:
'A study of HFO-1234ze (1,3,3,3-Tetrafluoropropene) as an eco-friendly replacement in RPC detectors',
10.48550/ARXIV.1505.01648 (2015).

119 G. Proto:
'Study of the performance of the RPC detector with new eco-friendly gas mixtures',
Il nuovo Cimento C, 10.1393/ncc/i2021-21070-1 (2021).

120 A. Bianchi, S. Delsanto, P. Dupieux et al.:
'Characterization of tetrafluoropropene-based gas mixtures for the Resistive Plate Chambers of the ALICE muon spectrometer',
Journal of Instrumentation **14**, P11014 (2019).

121 G. Rigoletti, B. Mandelli and R. Guida:
'Characterization of RPC detectors with LHC-like background radiation and new eco-friendly gas mixtures',
Journal of Instrumentation **15**, C11003 (2020).

122 M. A. Shah, R. Hadjiska, A. Fagot et al.:
'The CMS RPC detector performance and stability during LHC RUN-2',
Journal of Instrumentation **14**, C11012 (2019).

123 X. Fan, L. Naumann, M. Siebold et al.:
'Precise measurement of gas parameters in a realistic RPC configuration: The currently used R134a gas and a potential alternative eco-gas',
Nuclear Instruments and Methods in Physics Research Section A: Accelerators, Spectrometers, Detectors and Associated Equipment **1024**, 166124 (2022).

124 M. Abbrescia, D. Benussi L.and Piccolo et al.:
'Eco-friendly gas mixtures for Resistive Plate Chambers based on tetrafluoropropene and Helium',
Journal of Instrumentation **11**, P08019 (2016).

125 A. Bianchi, S. Delsanto, P. Dupieux et al.:
'Studies on tetrafluoropropene-based gas mixtures with low environmental impact for Resistive Plate Chambers',
Journal of Instrumentation **15**, C04039 (2020).

126 M. Marchisone (ALICE collaboration):
'Performance of a resistive plate chamber equipped with a new prototype of amplified front-end electronics in the ALICE detector',
Journal of Physics: Conference Series **889**, 012011 (2017).

127 G. Proto, G. Aielli, E. Alunno Camelia et al.:
'Characterization of new eco friendly gas mixtures based on HFO for RPCs',
Journal of Instrumentation **16**, C02001 (2021).

128 D. Pfeiffer, H. Gorine G.and Reithler et al.:
'The radiation field in the gamma irradiation facility gif++ at cern',
Nuclear Instruments and Methods in Physics Research Section A: Accelerators, Spectrometers, Detectors and Associated Equipment **866**, 91–103 (2017).

129 National Library of Medicine:
PubChem, the world's largest collection of freely accessible chemical information,
https://pubchem.ncbi.nlm.nih.gov/, 2022.

130 R. Margraf and N. Charitonidis:
'Muon Beam Studies in the H4 beam line and the Gamma Irradiation Facility (GIF++)',
CERN-ACC-NOTE-2018-0029 (2018).

131 CERN:
The H4 Secondary Beam Line of EHN1/SPS,
https://sba.web.cern.ch/sba/BeamsAndAreas/H4/H4_presentation.html, 2017.

132 CERN:
How to control the North Area beam lines,
http://sba.web.cern.ch/sba/documentations/how2controlnabeams.htm, 2017.

133 L. Terlizzi (ALICE collaboration):
'Commissioning and first performances of the ALICE MID RPCs',
10.48550/ARXIV.2211.11254 (2022).

134 A. Fagot:
'Consolidation and extension of the CMS Resistive Plate Chamber system in view of the high-luminosity LHC upgrade',
PhD thesis (Universiteit Gent. Faculteit Wetenschappen, 2020).

135 M. Gagliardi:
'The ALICE muon spectrometer: trigger detectors and quarkonia detection in p-p- collisions',
PhD thesis (Università degli studi di Torino, 2007).

136 W. R. Leo:
'The NIM Standard',
in *Techniques for nuclear and particle physics experiments: a how-to approach* (Springer Berlin Heidelberg, Berlin, Heidelberg, 1994), pp. 257–261.

137 VITA: Open Standards, Open Markets:
Vmebus technology faq,
https://www.vita.com/VMEbus-FAQ, 2022.

138 ROOT Team:
Root reference guide: ttree class reference,
https://root.cern.ch/doc/master/classTTree.html, 2023.

139 L. Pizzimento (ATLAS collaboration):
'Performance of the BIS78 RPC detectors: a new concept of electronics and detector integration for high-rate and fast timing large size RPCs',
Journal of Instrumentation **15**, C11010 (2020).

140 G. Saviano, M. Ferrini, L. Benussi et al.:
'Properties of potential eco-friendly gas replacements for particle detectors in high-energy physics',
Journal of Instrumentation **13**, P03012 (2018).

141 CAEN:
Application Note AN3251: Time Measurements with CAEN Waveform Digitizers,
https://mobydick.mib.infn.it/brofferio/didattica/datasheet/CAEN%20AN3251_Time_Mes_CAEN_Digitizer.pdf, 2015.

142 R. Bailey and P. Collier:
Standard Filling Schemes for Various LHC Operation Modes,
tech. rep., http://cds.cern.ch/record/691782 (CERN, Geneva, 2003).

143 L. Quaglia et al. (ECOgas@GIF++ collaboration):
'Eco-friendly Resistive Plate Chambers for detectors in future HEP applications',
10.48550/ARXIV.2212.09572 (2022).

144 P. Crespo et al.:
'Resistive plate chambers in positron emission tomography',
Eur. Phys. J. Plus **128**, 73 (2013).

145 Grafana:
Grafana main webpage,
https://grafana.com/.

146 Rigoletti, G. and others (ECOgas@GIF++ collaboration):
'Studies of RPC detector operation with eco-friendly gas mixtures under irradiation at the CERN Gamma Irradiation Facility',
PoS **EPS-HEP2019**, 164 (2020).

147 M. Gagliardi:
'Commissioning and first performance of the resistive plate chambers for the ALICE muon arm',
Nuclear Instruments and Methods in Physics Research Section A: Accelerators, Spectrometers, Detectors and Associated Equipment **661**, X Workshop on Resistive Plate Chambers and Related Detectors (RPC 2010), S45–S49 (2012).

Acknowledgements

Although many times I felt quite lost, a few important people helped me find my way in the world of PhD. I owe you all a lot and this work wouldn't have been possible without your constant support.

I would like to thank the whole ecogas collaboration, for our weekly meetings and the fruitful discussions that we had in them. Thanks to Gianluca, Mattia, Beatrice, Amrutha, Giuliana, Liliana, Alessandra, Aldo, Barbara and Giorgia for all the precious help along the way and for the company during the long test beam nights.

Jan deserves an honorary mention; I truly owe you a lot; thank you for always being available to listen to my crazy ideas, for providing me with interesting feedback and for always suggesting the right thing to do. Thanks for all the coffees in R1, which inevitably turned into a physics symposium.

Special thanks also to Nikolas; your knowledge, wisdom and life-approach will always stick with me. Thank you for all the activities, lunches, dinners and trips that you always passionately organize and for the unbreakable bond that we managed to create. Lastly, thank you for welcoming me in 904 and treating me as part of the group.

I also fondly remember all the *facada no bombril* moments with Mapse and Kevin. I really hope that we will manage to see each other again soon.

Lastly, I would like to thank Chilo and Andrea, for the time they have invested in reviewing this work, for all the much appreciated suggestions and for the very kind and encouraging words they used in their evaluation.

Ringraziamenti

In primis vorrei ringraziare il mio supervisor, Martino Gagliardi. Ci tenevo a ringraziarti per tutto ciò che mi hai insegnato e per l'infinito tempo che mi hai dedicato sia durante la scrittura della la tesi che durante corso di questi tre lunghi anni. Grazie per avermi sempre dato ascolto e anche, soprattutto, per aver sempre valorizzato le mie idee e i miei progetti; tra cui questo ultimo anno al CERN. Grazie anche per avermi introdotto al CERN e nel meraviglioso mondo di ALICE, destreggiandoti abilmente tra l'essere un supervisor e un amico. A tal proposito non posso non ricordare le svariate fondue chinoise annaffiate da cannette di blonde al portoghese di Meyrin.

Un grazie speciale va anche ad Alessandro Ferretti, altro commilitone delle RPC di ALICE. Grazie non solo per l'interesse che ha sempre mostrato verso il mio lavoro e per la continua disponibilità a discuterne ma anche per avermi insegnato un approccio più *filosofico* alla fisica, cha va oltre ai semplici risultati e che punta a comprendere il vero messaggio nascosto dietro ai vari dati.

In sostanza, grazie Ale e Martino per condividere con me, ogni giorno, la vostra passione per la fisica (e per le grandi abbuffate).

Un ringraziamento speciale va a tutto il gruppo ALICE di-muoni e ZDC: ai pilastri del gruppo (Ermanno, Enrico, Chiara, Roberta, Livio, Nora, Giorgione) e ai junior: Edo, Sara, Tiziano, Luca, Andrea, Michele (purooo) e Stefan (best coinquilino). Grazie a tutti per la disponibilità sempre mostratami e per tutti i bei momenti (sempre immortalati da Edo) che abbiamo vissuto insieme in questi anni. #*fisicamentescarichi*

Grazie a Livia, compagna di avventure e sventure (perché si sa che in laboratorio, se qualcosa può andare storto, andrà sicuramente storto). Grazie per tutti i mesi di convivenza da Igor, al Carre d'Or, al Sejour, per tutti i momenti passati in control room ad aspettare i muoni e tutte le cene per celebrare il loro arrivo. Ti ringrazio per tutti il tempo che abbiamo condiviso (compreso questo giorno speciale) e per tutto quello che condivideremo.

Grazie a Dayron, grande compagno di test beam e di vita. Quello che è

iniziato come un test beam insieme è diventata una delle mie amicizie più care. Il tuo supporto è stato fondamentale nell'ultimo anno, sia lavorativamente parlando (tutte le volte che siamo stati alla GIF e al 904 fino a notte fonda) che non (tutte le nostre serate di birra+coddino e la convivenza in Rue La Fayette).

Grazie agli arfò: Ricci, Andre e Alby. Nonostante siamo sparsi in giro per il mondo, trovano sempre il tempo per una serata al bingo o una ciaspolata dell'ultimo minuto. Anche se non ci sentiamo ogni momento, vi porto sempre con me; letteralmente sul braccio. Un pensiero va anche a tutti i miei amici, con cui ho condiviso questi anni di dottorato. Grazie a tutta la 1727 gang: Agata, Brondy, Ele, Nora, Lauda, Cocca e Andreina. Grazie per aver allietato i pesanti giorni di quarantena, per tutte le serate e le bellissime vacanze estive nelle ville Astigiane. Grazie al boia, il più matto di tutti, per tutte le nottate di lavoro al 40; grazie agli altri matti del CERN (Fiorina, Antonello, Vincenzo, JJ e Mattia) per aver reso speciale l'ultimo anno; senza di voi non sarebbe stata la stessa cosa. Grazie anche ai guasconi: Fasce, Gio, il garden, dvrk, zio jieck e Matti, grazie per tutte le serate passate al parcheggio ad ammirare il *golfo d'Oro* di Casalborgone. Grazie a tutti coloro che mi sono stati vicini durante questi anni (e scusate se non vi ho elencati tutti), vi assicuro che un pezzetto del mio cuore è dedicato a ognuno di voi.

Chiara: savve (smack smack) e buongionno (smack smack). Per ringraziarti non bastano due righe (e non basterebbe nemmeno una tesi intera). Sei stata la luce che mi ha illuminato la strada nei momenti più difficili. Grazie per spingermi sempre a fare le scelte migliori per il futuro, anche se spesso non sono a nostro favore (se non fosse stato per te, non avrei inviato la domanda per il simil-fellow). Quest'anno lontani è stato duro, siamo dovuti diventare campioni di chiamate e cene virtuali ma, grazie ai tuoi meme e ai tuoi tormentoni (il migliore sarà sempre il "devo andare a fare le mie cose"), mi sembra di non esserci mai salutati e adesso siamo già di nuovo qui insieme, per festeggiare questo traguardo che, per gran parte, è anche tuo. Mi riempie di gioia saperti affianco a me e poter condividere con te questa momento così speciale. Ci sarebbero altri mille motivi per cui ringraziarti, non posso elencarli tutti ma tu sai quali sono; ti sono grato per ognuno, dal primo all'ultimo.

In ultimo (ovviamente non per importanza) vorrei ringraziare la mia famiglia. Grazie mille a mamma, papà e Chiara perché, nonostante io non sia sempre presente, voi riuscite sempre a trovare il tempo per chiedermi come sto e per informarvi sempre sul mio lavoro (e io con grane piacere vi

ammorbo con discussioni al limite della filosofia). Il vostro supporto silenzioso ma sempre presente è la cosa che mi aiuta a non arrendermi mai.